The Effect of Impurities and Geometry on the Corrosion and Thermodynamic Behavior of Molten Salts

A Dissertation

Presented in Partial Fulfilment of the Requirements for the

Degree of Doctor of Philosophy

with a

Major in Nuclear Engineering

in the

College of Graduate Studies

University of Idaho

by

Robin V. Roper

Approved by: Major Professor: Vivek Utgikar, Ph.D.

Committee Members: Richard Christensen, Ph.D.; Piyush Sabharwall, Ph.D.; Haiyan Zhao, Ph.D.; Toni Karlsson, Ph.D.

Department Administrator: Indrajit Charit, Ph.D., P.E.

August 2022

Abstract

Molten salt systems are highly relevant to the energy industry and have become a focus of much research in recent years, particularly in nuclear energy and thermal energy storage. Many types of molten salt are used for various systems, including fluoride, chloride, and nitrate salts. These types of salts have thermodynamic and chemical properties, which make them advantageous to energy production systems. Molten salt systems are superior to other systems in many ways, including design simplification, atmospheric operating pressures, higher heat capacities, safer operational parameters, and the possibility for on-line salt processing. Despite the advantages of a molten salt system, these concepts can also contain more complexity than many other energy storage systems due to the chemistry of the salt mixtures. In particular, molten salt systems can be particularly susceptible to corrosion. A risk assessment was performed as part of this dissertation, determining that corrosion risk is of particular concern in designing a molten salt system.

To address the risk of corrosion in molten salt system design, two phases of research were conducted, which are described in this work. The first phase aimed to determine the effect of corrosion on the thermodynamic behavior of molten salt. In particular, the melting behavior of two types of molten salt was investigated, with additions of impurities that could result from corrosion. The second phase of research aimed to determine the effect of system design on molten salt corrosion. By use of COMSOL multiphysics, four different basic geometries were modeled, which were representative of geometries that could be found in a large-scale system. Molten salt laminar flow was modeled in these geometries, with corrosion behavior coupled to the laminar flow physics. This model was first of its nature and thus was simple in form. It provided information on the general impact of design changes on the velocity profile and corrosion behavior in representative geometries.

The combination of experimentation and modeling determined that design changes can

be made to reduce the impact of corrosion on a molten salt system. Extending the system temperature to above the entire melting range of a molten salt will ensure an operating fluid that is entirely liquid in phase. Modifying geometry to reduce areas of peak velocity will reduce the intensity of local corrosion, and reducing the overall system velocity will also reduce corrosion. Incorporating system design changes such as these in preliminary phases of design can reduce overall corrosion risk, extending the lifetime of the system.

Acknowledgements

I would like to thank Kristen Geddes for her unwavering support and dedicated efforts, which have been invaluable in producing this work. Thank you also to Rich Christensen, for his mentorship and guidance for the last four years. Thanks to Larry Zirker, for his advice and general encouragement. Thank you to those other students who spent hours in the lab with me, seconding my tests, Silvino, Jan, and Trevor. Also thank you to Drew, for his instrumental support with COMSOL.

Dedication

In dedication to Leon Grayson Roper, who is my foundation, and greatest support.

Table of Contents

List of Tables

List of Figures

Acronyms

AHTR Advanced High-Temperature Reactor

ANL Argonne National Laboratory

ANOVA Analysis of Variance

ANP Aircraft Nuclear Propulsion

CSP Concentrated Solar Power

DSC Differential Scanning Calorimeter

FEM Finite Element Analysis

FHR Fluoride Salt-Cooled High-Temperature Reactor

FMEA Failure Mode and Effects Analysis

HTF Heat Transfer Fluid

HTREs Heat Transfer Reactor Experiments

INL Idaho National Laboratory

LWR Light-Water Reactor

MOSART Molten Salt Actinide Recycler and Transmuter

MSBR Molten Salt Breeder Reactor

MSFR Molten Salt Fast Reactor

MsNB Molten Salt Nuclear Battery

MSR Molten Salt Reactor

MSRE Molten Salt Reactor Experiment

NHES Nuclear Hybrid Energy System

ORNL Oak Ridge National Laboratory

PCM Phase Change Materials

PHA Preliminary Hazard Analysis

PISAs potential inadequacies in safety analysis

RGRS reactive gas recovery system

RPN Risk Priority Number

SAMOFAR Safety Assessment of the Molten Salt Fast Reactor

TES Thermal Energy Storage

TMSR Thorium-breeding Molten-Salt Reactor

CHAPTER 1

Introduction

Molten salt technology is an increasingly prevalent aspect of the energy industry. Beginning in the 1950s with the Aircraft Nuclear Propulsion program, molten salts have been expanded into many industries, including nuclear and solar energy, thermal energy storage, pyrochemistry, and more. Many different types of salts are used for these applications, but some types are more common, such as nitrate, fluoride, and chloride salts. These salts have chemical and thermodynamic properties which make them useful for different applications, such as high melting ranges, good heat transfer properties, and thermal/chemical stability at higher temperatures. However, salts can also be highly corrosive, and designs using molten salts will have a significant level of corrosion risk. To understand this risk, a qualitative risk assessment was performed on a sample molten salt system design.

1.1 Preliminary Risk Assessment of the Molten Salt Nuclear Battery

An Molten Salt Reactor (MSR) is an advanced type of reactor design which operates using liquid fuel rather than solid fuel. An MSR design utilizes molten salt with fissile material dissolved directly into the salt, combining the coolant and fuel. This concept was proved in the 1960s with the Molten Salt Reactor Experiment (MSRE). Currently, a MSR design is underway at the University of Idaho, called the Molten Salt Nuclear Battery (MsNB) [1].

Advanced nuclear reactor design is a complex process, involving modeling, experimentation, and demonstration of functionality and energy production. A crucial component of advanced reactor design is risk assessment, which is heavily involved in all stages of design.

Risk assessment aims to identify issues with a reactor design which pose a risk to both safety and equipment. Preliminary stages of risk assessment focus on identifying hazards and risks early in the design process so that design changes can be made to address major problems. In 2021, a preliminary risk assessment was performed on the MsNB, the results of which highlighted broader gaps in molten salt system designs. A full documentation of the MsNB preliminary risk assessment can be found in appendix A. Many risk assessment tools are available for preliminary risk analysis, and the described work utilized a Preliminary Hazard Analysis (PHA), and a Failure Mode and Effects Analysis (FMEA), to assess possible hazards and failures which may be detrimental to the early design of the MsNB.

There are many varying designs for a molten salt nuclear system, most of which can fall into two categories: liquid-fueled, and solid-fueled. A solid-fueled molten salt design operates similarly to typical commercial reactors: The molten salt acts as a coolant for solid nuclear fuel, removing the fission heat to a power cycle. Solid-fueled molten salt nuclear reactors are often referred to as an Fluoride Salt-Cooled High-Temperature Reactor (FHR). Conversely, a liquid-fueled molten salt reactor design, or an MSR, does not operate with a solid core. Instead, the fuel is dissolved into the coolant itself, and the reactor is designed to enable fission in the core region, heating the coolant and carrying that heat to a power cycle.

The MsNB is a 10 MW_{th} liquid-fueled MSR design, which uses Flinak (LiF-NaF-KF) salt with dissolved UF_4. The MsNB is a microreactor, intended for easy factory construction and transport to remote areas. The reactor is designed for a 10-year lifecycle, at which point it can be shipped back to a central location for waste processing and decommissioning. It is a unique design, because unlike other reactor designs of its type, the MsNB uses no pumps or valves. Instead, the MsNB coolant flow is driven by natural circulation. Density differences between hot and cooled salt in different regions of the reactor drive flow up and around the reactor geometry. Design details for this reactor were taken from reports generated at the University of Idaho [1, 2], as well as proprietary

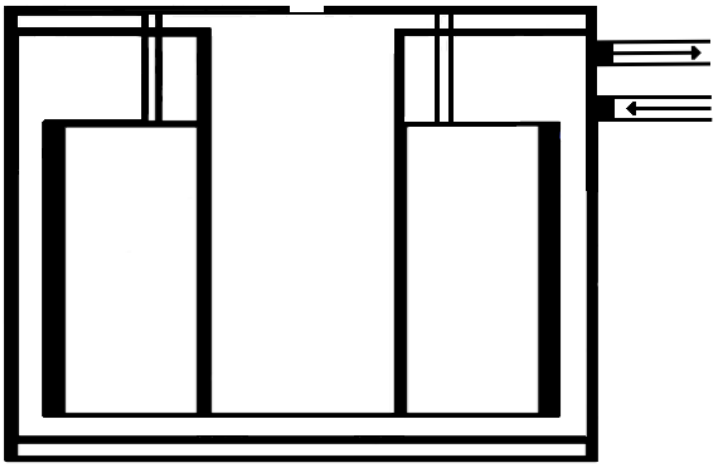

Figure 1.1: A simplified graphic of the MsNB

design documents. A simplified version of the MsNB main design is shown in figure 1.1. The reactor design is a 400-kW_{th} version of the original MsNB design, intended for operation in a testing facility to establish reactor behavior and model validity. The MsNB has two main system which control the salt flow and power generation: 1) a core region that produces 400 kW_{th} of heat, and 2) a circular heat exchanger region containing strip-fin heat exchangers paired to an air-Brayton or Helium-Brayton secondary cycle. The reactor design also originally includes proprietary core and reactor internals, which aid in natural circulation and thermal operation.

Before performing the PHA and FMEA, it was first necessary to establish boundaries for the analysis. The reactor boundary for this analysis is the reactor itself, with no designed secondary system. The analysis focused on general features, rather than minute detail, since the scope of this analysis is general hazards and failures. Since facility concerns are important for a risk assessment analysis of this type, a general facility with no specific design was assumed. This general facility includes a theoretical air-Brayton or helium-Brayton cycle. The reactor itself contains Flinak (LiF-KF-NaF) salt, with dissolved uranium tetrafluoride.

To simplify analysis, the reactor and analysis areas were separated into regions of focus, or 'nodes.' These nodes are important regions and systems within the analysis boundaries of the reactor. The PHA and FMEA focused on what is contained in the designated nodes. The nodes include the flow areas for the molten salt in the reactor, as well as the control drums, instrumentation, and general facility concerns. The nodes, pictured in figure 1.2 are as follows:

- Node 1: Core
- Node 2: Upper Distribution Region
- Node 3: Heat Exchanger Region
- Node 4: Downcomer
- Node 5: Lower Distribution Region
- Node 6: Control Drums
- Node 7: General Facility Concerns
- Node 8: Instrumentation

A separate PHA and FMEA table were constructed for each node. These are not included in this section, and the full report including these tables can be found in appendix A. The PHA and FMEA tables rank each hazard and failure, and therefore it is possible to filter the highest risks and examine them for common causes. PHA rankings of concern were those hazards with the category 'Extremely High Risk' or 'High Risk.' FMEA rankings of concern were those with an Risk Priority Number (RPN) of 9 or higher. These are risks which are unacceptably high, and there must be a level of mitigation before design can be completed.

The hazards ranked 'Extremely High Risk' were the following:

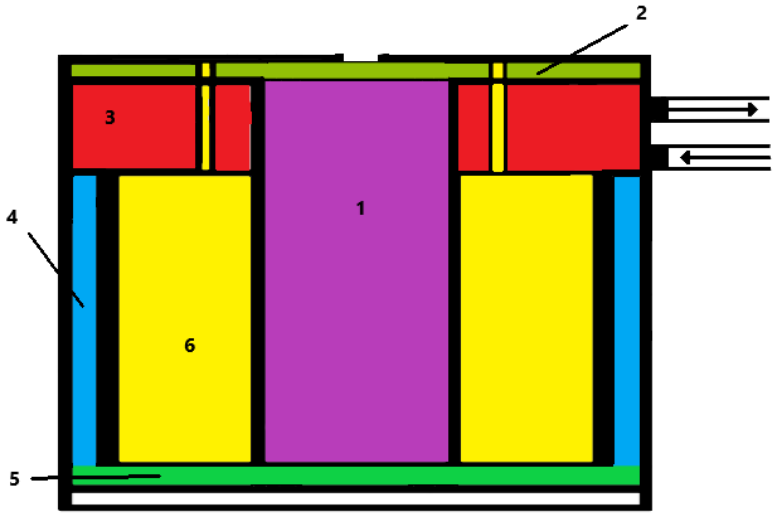

Figure 1.2: The MsNB, separated into risk assessment nodes.

- Corrosion of core wall
- Corrosion in Upper Distribution Region
- HX fin corrosion
- HX air leak into salt
- Corrosion of downcomer wall
- Blocked or partially blocked inlet to core

The hazards ranked 'High Risk' were the following:

- Corrosion of reactor internals
- Corrosion of core inlet structure
- Corrosion in lower distribution region
- Sensors exposed to salt by corrosion of reactor internals

The following failures had an RPN of 9 or greater:

- Internal damage: RPN = 9
- Corrosion of head intrusions: RPN = 16
- Containment breach: RPN = 15
- Holes in an air/salt interface: RPN = 12
- Outer wall breach: RPN = 15
- Inner wall breach: RPN = 12
- Clogging in core inlet region: RPN = 12
- Damaged core inlet region: RPN = 9
- Salt release: RPN = 15

The most obvious common trend in these risks is that of corrosion. A lack of corrosion control systems in the reactor design leads to high risk ratings on corrosion-related hazards and failures. All of the identified high-risk items are either directly or tangentially related to corrosion. Additional risks include depositing corrosion and fission products, and heat exchanger leakage into salt.

Causes of corrosion should be identified in a system such as this, but it is difficult to identify exactly what leads to corrosion. There are many possible causes and factors leading to corrosion, and all or just one can come into play at any time. Figure 1.3 shows a fishbone diagram illustrating this concept. Corrosion can be caused by material weakness, corrosion focal points, a reducing salt potential, or corrosion product deposition. Much has been reviewed on the topic of molten salt corrosion[3, 4, 5], and an in-depth discussion of corrosion mechanisms and behavior is not within the scope of this report. However, a further analysis of the corrosion mechanisms in this system will be necessary for a complete corrosion control system design.

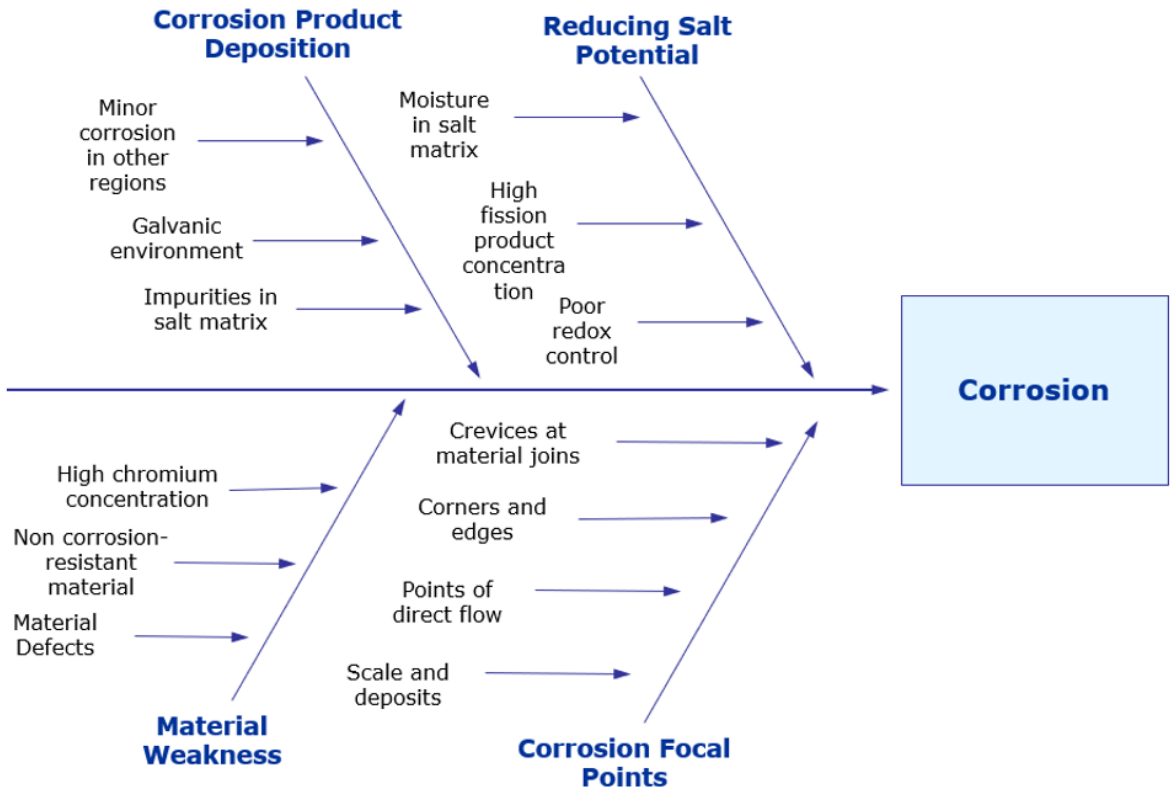

Figure 1.3: A fishbone diagram outlining possible factors involved in a corrosion-related hazard

The implication of the severity of corrosion in this system is that a corrosion control system will be key for long-term functionality of the MsNB. This is made more obvious when an event tree for corrosion is constructed, shown in figure 1.4. The event tree shows the possible intermediary events that occur between the initiation of corrosion and the eventual failures and damage to the MsNB structure. This specific event tree was constructed for wall corrosion specifically. The event tree shows the estimated probability for success and failure of each intermediary system, and the outcome of success or failure. The probabilities are estimates only, as no modeling or data has been done on this specific event.

As can be seen from the event tree, corrosion control is crucial to limiting major wall damage from corrosion. There are only two possible intermediary events; corrosion control,

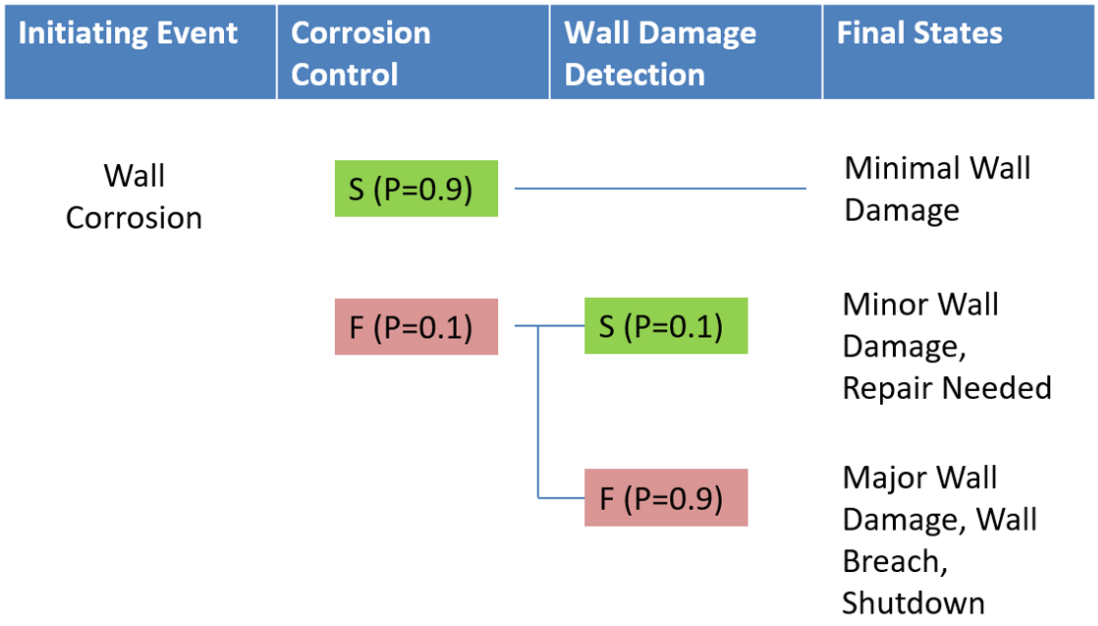

Figure 1.4: An event tree for corrosion in the MsNB, or a general molten salt system with an unspecified corrosion control system. Probabilities shown are qualitative estimates. S refers to a successful event, and F refers to a failed event.

and detection and repair of any damage. Detection and repair for this system is extremely unlikely. Not only is it impossible to view the internal walls of the reactor to detect corrosion, but it is also impossible to replace most parts of the MsNB. The integral design of the MsNB means replacing structure requires complete disassembly, an impossible task. The only components where this is remotely possible are components on the outer reaches of the reactor, such as the control drum drives, or external ports and apparatus. Thus, the only real barrier between initiation of corrosion and major damage is a corrosion control system. Thus, a design for a molten salt system requires both corrosion control system, and inherent design changes which reduce corrosion initiation.

1.2 Research Goals and Motivation

As shown in the risk assessment performed on a sample molten salt system design, corrosion is a major concern in molten salt system design. Without both inherent corrosion-ready

design, and corrosion control systems, molten salt corrosion may cause failure of crucial systems. Some corrosion control systems have been investigated [6, 7, 3, 8]. The goal of this dissertation is to evaluate the corrosion behavior of molten salt systems, in pursuit of the other main component of corrosion mitigation: corrosion-ready design. The main objectives of this research relate to two connected aspects of molten salt corrosion behavior:

- **Objective 1:** The effect of corrosion products on the salt, and
- **Objective 2:** The effect of the system on the corrosion behavior of the salt.

Investigating these two aspects provides information on how a system can be designed to minimize the severe impacts of corrosion. Objective 1 relates to designing a system to account for fluid changes due to corrosion products, and Objective 2 relates to system design changes that can reduce corrosion in the system. These system designs will provide valuable information for producing a more corrosion-ready molten salt system design. The objectives listed above were accomplished using modeling and experimentation, according to the following task breakdown:

- **Objective 1: Effect of Corrosion Products on the Salt**
  - Task 1: Experimental determination of the impact of corrosion products on the bulk melting point of molten salt
  - Taks 2: Evaluation of task 1 samples using a Differential Scanning Calorimeter (DSC), for higher resolution data.
- **Objective 2: Effect of a Molten Salt System on Corrosion Behavior of Salt**
  - Task 3: Modeling of corrosion in basic structural geometry and laminar flow
  - Task 4: Expansion of task 3 to include geometries representative of typical molten salt systems.

- Task 5: Variation of task 4 geometry to reduce corrosion risk.

The work supporting these tasks is described herein, with tasks 1 and 2 accomplished in chapters 3-4, and tasks 3-5 accomplished in chapters 5-6.

CHAPTER 2

Molten Salts - Literature Review

Sections 2.1 and 2.2 of this chapter are published in part, in Annals of Nuclear Energy, Vol 169, Robin Roper, Megan Harkema, Piyush Sabharwall, Catherine Riddle, Brandon Chisholm, Brandon Day, Paul Marotta, Molten Salt for Advanced Energy Applications: A review, Page 108924, Copyright Elsevier, (2022).

2.1 Molten Salts in Energy Applications

The primary uses of molten salt in energy technologies are in power production and energy storage. The physical characteristics and heat transfer properties of molten salt are well-suited to advanced high-temperature energy technologies, such as molten salt reactors or hybrid energy systems. This section discusses the two primary energy applications for molten salts: nuclear power production and thermal energy storage.

2.1.1 Power Production - Nuclear Energy

The molten salt cooled reactor is an advanced nuclear reactor concept that utilizes molten salt as either a coolant for solid fuel or as a fuel salt. The molten salt reactor concept originated in the 1940s and 1950s but has resurfaced as part of Generation IV advanced reactor initiative [4, 9, 10]. The main advantage that the concept presents is high-temperature single phase liquid operation on the order of 600 ° C at low, i.e., near atmospheric pressure. Light-Water Reactor (LWR) technology produces steam temperatures on the order of 300 ° C and requires that components withstand pressures that are 140 times atmospheric pressure. Thus, molten salt reactors have the inherent advantage of dramatically improved thermal performance due to high temperature, and at the same time reducing

cost since LWR components are extremely thick and expensive to produce/construct [4].

A liquid-fueled molten salt reactor has many potential advantages to LWR's, including safety, economic, nonproliferation, and environmental advantages [4, 10]:

- MSRs are safer because they can operate at low pressure, without concern of melting fuel or clad leaking fission products [11]. Separation of fission products and noble gases can occur continuously, reducing the source term in the case of an accident. The liquid state stability of the fuel salt at high temperature eliminates energetic source term vectors such as rapid steam expansions/explosions typical of LWRs.

- Economically, the MSR concept is advantageous due to:

  - Core design simplification and reduced manufacturing cost;

  - Reduction of structural section thickness due to reduced operating pressure;

  - The liquid nature of an MSR provides a higher heat capacity, which aids in the design of compact, less-expensive reactor designs;

  - Compact reactors can be mass-produced and shipped to reactor sites, which reduces construction costs; and

  - Used LWR fissile material could be used to start up a reactor, reducing waste materials.

- The MSR concept has the ability to breed thorium to produce fuel. Because thorium is much more abundant than uranium, [11] this would expand the global fuel

Figure 2.1: Two of the Heat Transfer Reactor Experiments (HTRE) [4]

supply. MSRs could also recycle or burn actinides, reducing the global stockpile of nuclear waste. Plutonium can also be recycled and burned in an MSR core, reducing plutonium inventory for nonproliferation purposes.

The Molten Salt Reactor Experiment

The MSRE originated in the 1950s with the Aircraft Nuclear Propulsion (ANP) program. The ANP program was developed to satisfy the United States' need for long-range aircraft solutions. On-board nuclear reactors were considered for aircraft propulsion, however, to accomplish the power required for jet engines, nuclear reactors would need to produce high-temperature superheated gas. The Heat Transfer Reactor Experiments (HTREs) were operated to demonstrate this ability. Two of these reactors are now displayed at Idaho National Laboratory (INL) (see Figure 2.1). [4]

The HTREs functioned well but had issues with the narrow fuel elements required for their compact design. At this point, it was proposed that the fissile material be dissolved into a liquid coolant, which would eliminate challenges with fuel-element structure. [4]

The MSR program was eventually developed, and the MSRE began construction in 1960.1 The MSRE consisted of a primary loop of $LiF-BeF_2-ZrF_4-UF_4$ (61.0:29.1:5.0:0.9 mol %), and a secondary loop of $LiF-BeF_2$ (66:34 mol %).1 The reactor core was a multi-

channel graphite structure, through which the salt flowed and became critical. Figure 2.2 shows a schematic of the MSRE. [9]

The MSRE successfully demonstrated the MSR concept, operating for 15,424 full power hours without significant incident. The experiment also demonstrated the ability of an MSR to operate on uranium-233, demonstrating the breeder concept. After this demonstration, design and development began on a Molten Salt Breeder Reactor (MSBR), but the project was eventually ended as funding was diverted to liquid metal breeder reactors. [4] Although the development of a full molten salt reactor was halted, interest has reignited in the last decade. At the beginning of the century, the Generation IV International Forum highlighted six nuclear reactor designs as next-generation designs. [9] The MSR concept is one of these Generation IV reactor concepts, and efforts around the globe have refocused on its development.

Although the MSRE ended, the facilities were not removed. In 1998, the decision was made to process fuel and flush fluoride salts from three MSRE drain tanks, to reduce risk from the salt to off-site and on-site locations. [12] This decision was made to address the uranium in the fuel salt, which was a potential hazard. The salt in the drain tanks was removed and processed to remove the uranium from the salt, and the remaining salt was placed in interim storage. In 2015 and 2016, Oak Ridge National Laboratory (ORNL) evaluated the MSRE facilities, identifying potential inadequacies in safety analysis (PISAs). These PISAs involved the potential corrosion in the reactive gas recovery system (RGRS) pump and piping, and the potential release of fluorine and hydrogen fluoride gases from the salt tanks and the spent sodium fluoride and alumina traps. [13] The PISAs were used to evaluate the ability to maintain the facilities safely until they are decommissioned and demolished, which is scheduled for the year 2060. [13]

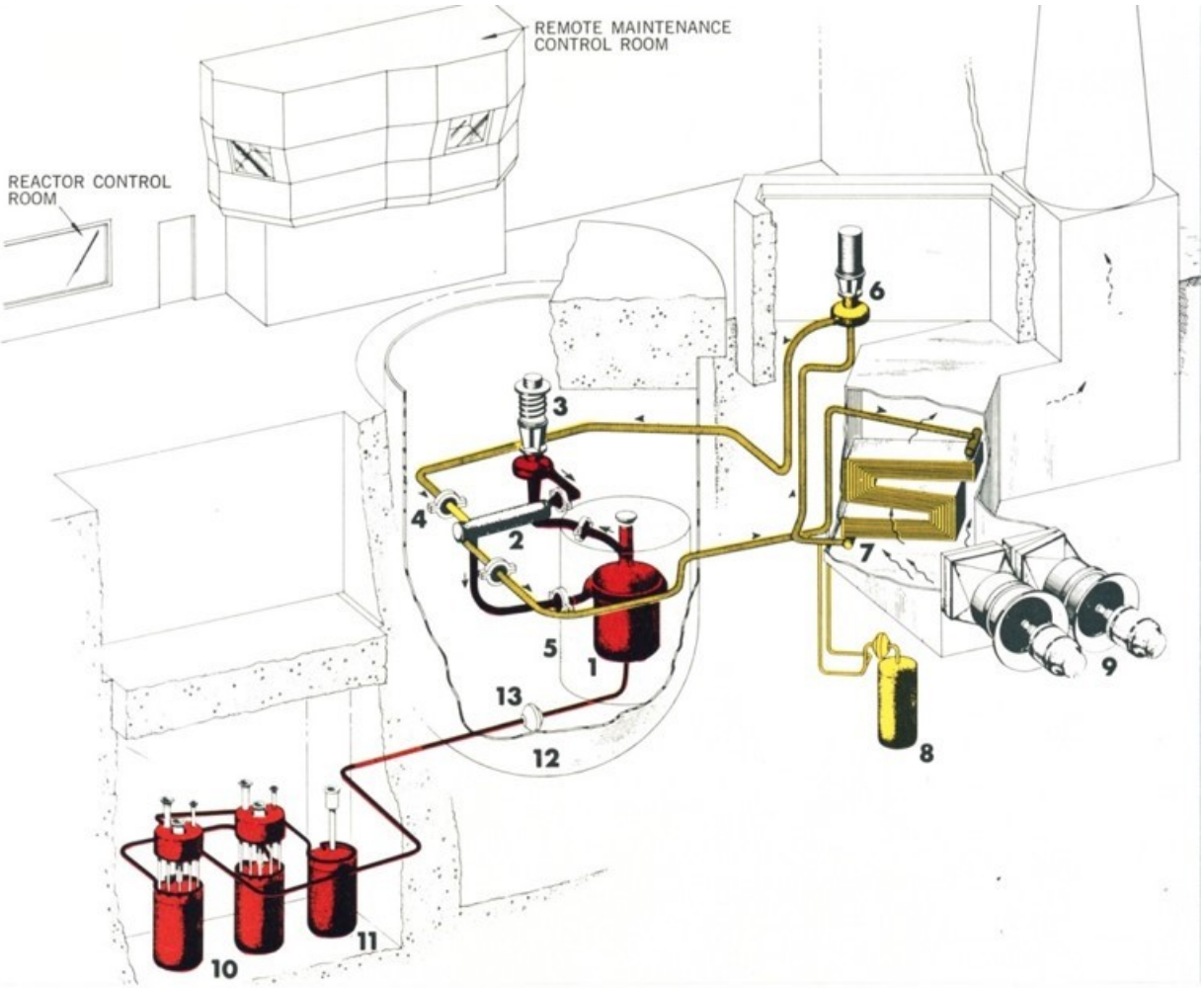

1. Reactor Vessel, 2. Heat Exchanger, 3. Fuel Pump, 4. Freeze Flange, 5. Thermal Shield,
6. Coolant Pump, 7. Radiator, 8. Coolant Drain Tank, 9. Fans, 10. Fuel Drain Tanks,
11. Flush Tank, 12. Containment Vessel, 13. Freeze Valve.

Figure 2.2: Schematic of the MSRE [9]

Pyrochemistry and Fuel Recycling

With the creation of nuclear power plants, one of the most significant issues that arose was what to do with the waste once the fuel rods were decommissioned. Before 1984, when the fission reaction had ceased in the fuel cells, the rods would be removed and stored in a water-containment vessel for an extended period before they were cool enough to store in an off-site facility. Additionally, not all the usable uranium was used during the fission process, but it was left unrecovered from the decommissioned rods. In 1984 INL and Argonne National Laboratory (ANL) pioneered a pyroprocessing method for recovering and recycling fissile material from used fuel. [14, 15]

Pyroprocessing uses high-temperature molten salts as the electrolyte for an electrochemical process. Molten salts have several advantages over other electrolytes: excellent heat transfer characteristics, large heat capacities, and stability at high temperatures ranging from 120 to 1000 ° C. Additionally, molten salts have large potential windows ($LiCl - KCl$ eutectic $-2.6 - 1.3VVs.Ag/AgCl$) which allows for a wider variety of elements to be reduced. Figure 2.3 shows a schematic of a pyroprocessing system.[16]

Once fuel rods have been decommissioned from the reactor, those that still have enough recoverable material, known as used (instead of spent) fuel rods, are sent for processing. Before being placed in the molten salt bath, they are sent to be sectioned up into smaller pieces to fit in a basket that behaves as the anode (i.e., the electrode where oxidation reaction occurs) for the process. Once the electrorefining begins, depending on the ionic state of the element, some uranium will be attracted to a cathode while the rest remains in the solution. Other elements, such as rare-earth elements, can also be attracted to the cathode and recovered along with the uranium. Afterward, the uranium will be refined and cast to be reused in fuel rods. The remainder of the elements from the fission process can be left within the solution or deposited on the cathode. These residual elements are processed through various means for storage. Noble metals are cast into ingots, while the salt and the elements contained within are turned into glass-bonded sodalites. Once this

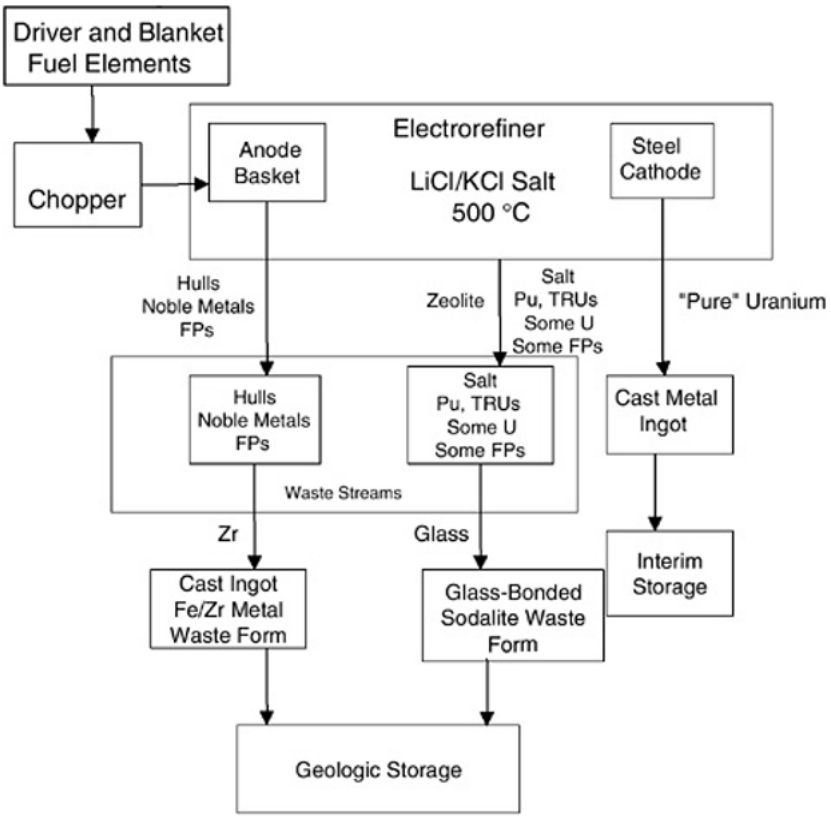

Figure 2.3: Pyroprocessing schematic [16]

process is completed, they are placed in a facility for long-term storage.

Actinide Burning

Nuclear power reactors typically operate commercially using a 'once-through' cycle. This means that spent nuclear fuel is unloaded from the reactor and stored as nuclear waste. Much of this waste contains materials which can be reused in another reactor, or that can be transmuted, thus reducing the amount of waste. Actinides, such as neptunium, americium, and curium, can be 'burned' or transmuted under certain reactor conditions. Fast reactors have a large ratio of fission-capture cross-sections and are effective at burning actinides. [17]

Modern Nuclear Technologies

With the resurgence of molten salt nuclear technology research, there are many molten salt nuclear technologies being developed in the modern day [10, 18, 19, 20, 21]. Researchers and institutions, in both government and private industrial sectors, are developing molten salt reactors or molten salt processing technology. These include liquid-fueled reactors, or solid-fueled reactors with molten salt as a coolant. Some of these designs are projected to be operational in the coming decade. The Molten Salt Fast Reactor (MSFR) is one such reactor. It is a liquid-fueled design with a closed thorium/uranium fuel cycle. [18, 19] It is under development by EVOL, a Euratom project by six participating European countries. The Safety Assessment of the Molten Salt Fast Reactor (SAMOFAR)) project is a molten salt development project in conjunction with the MSFR, with the goal of proving safety concepts of MSFR breeding and operation [18, 21].

The Advanced High-Temperature Reactor (AHTR), also known as the FHR, is a solid-fueled design with a graphite and solid fuel core structure. It utilizes molten salt as a coolant, rather than as a fuel. A prototype is currently under construction. [18] The Thorium-breeding Molten-Salt Reactor (TMSR) is a thorium-based reactor design program

under development in China, under the China Academy of Sciences, launched in 2011. [18] The TMSR program includes the AHTR/FHR reactor, as well as a second track of development for a liquid fueled reactor. The US department of Energy is collaborating with the China Academy of Sciences on the program. [18]

Another reactor design to note is the Molten Salt Actinide Recycler and Transmuter (MOSART) project. This project is under the MARS (minor actinide recycling in molten salt) program, which involves research organizations such as Riar and Kurchatov. The MOSART is a fast reactor fueled by transuranic fluorides from uranium and light-water reactor spent fuel [18, 20]. Many private companies are developing molten salt reactor technologies. These include companies such as Kairos Power, Moltex Energy, Flibe Energy, Terrestrial Energy, TerraPower, and Transatomic Power. [18] Many more organizations are in various stages of development, and are too numerous to list in this work. The contributions to the molten salt technology field from research organizations, both private and public, are quickly advancing the field of nuclear molten salt technology, and it is likely that the global energy sector will see functional molten salt reactors in the next decade.

2.1.2 Thermal Energy Storage

Thermal Energy Storage (TES) can be divided into three areas: sensible heat materials (solid and water), latent heat (phase change materials) and thermochemical (chemical reversible reactions). [22] Sensible heat is stored within a single-phase material with increasing or decreasing the temperature, and latent heat is stored using material phase change properties such as solid-liquid phase change by melting and solidification using either hot or cold Phase Change Materials (PCM). The heat from a heat-generating process is transferred to a heat-transfer medium and can be extracted later using a secondary power cycle.

There are several types of facilities that use thermal energy storage with molten salts. This work will focus on two types: Concentrated Solar Power (CSP) and the Nuclear

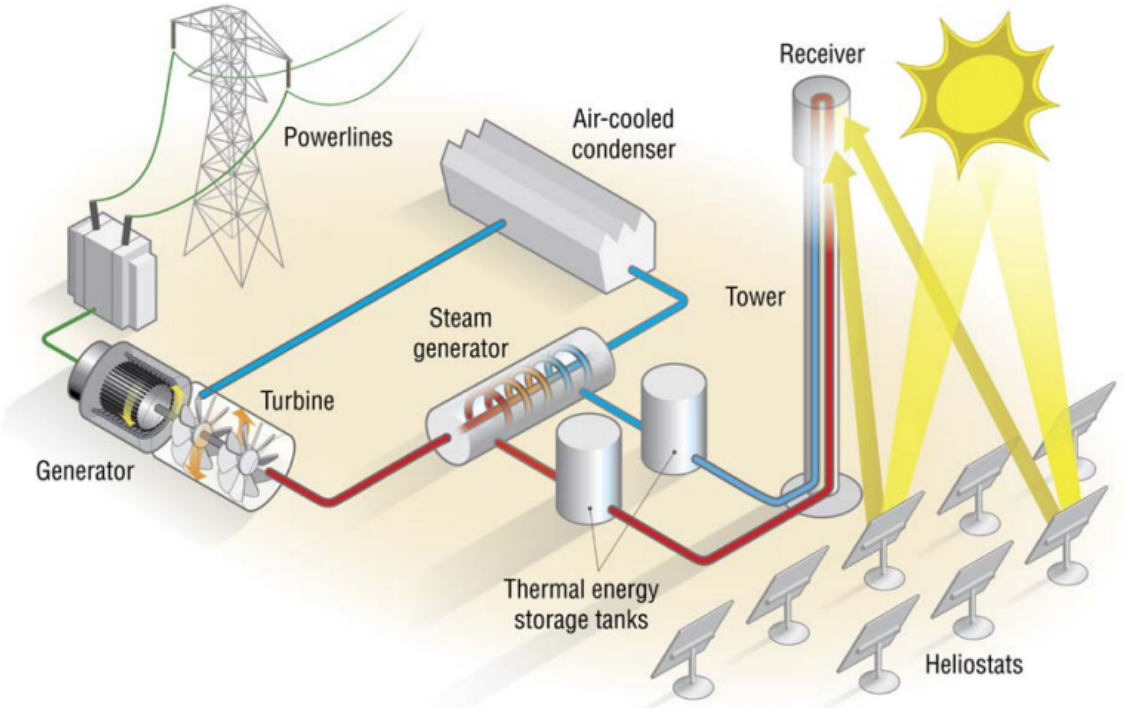

Figure 2.4: CSP plant with thermal energy storage tanks [23].

Hybrid Energy System (NHES).

Concentrated Solar Plants

A CSP plant is a power-production facility that uses a broad array of reflectors or lenses to concentrate solar energy onto a small receiver. Molten salt in the receiver is heated by solar energy and directed to thermal energy storage or a power cycle. Figure 2.4 shows a schematic of a CSP plant containing thermal energy storage systems and a power cycle. [23] In this type of system, cold molten salt is pumped to the top of the power tower containing the receiver, where it is heated by the concentrated solar power. It then flows to a hot storage tank, which stores the hot salt until it is needed for power production. After the power cycle, cold molten salt is stored in a cold storage tank until it is needed. Molten salt has excellent heat retention properties, meaning it can be stored for an extended period and retain the solar-generated heat for later use. [23]

The salt used in these types of CSP plants is called a Heat Transfer Fluid (HTF). The

salts selected for HTFs are typically chloride or nitrate salts. Chloride salts are promising due to their wide operating temperature ranges, but pose challenges with corrosion [24]. Nitrate salts are more common, particularly a blend of sodium and potassium nitrate, known as Solar salt.[25]

Solar Two

An example of a CSP plant with thermal energy storage is the Solar Two power plant, operated by the U.S. Department of Energy. The Solar Two program was operated to validate sophisticated CSP technologies using molten salt and was built using existing facilities from the Solar One pilot plant.

The Solar One pilot plant was a power-tower technology plant that operated from 1982 to 1988. In the 1990s, it was retrofitted to produce Solar Two, which demonstrated more advanced power-tower technology. [26] The primary difference between Solar One and Solar Two was the HTF used for the receiver. Solar One used water, and Solar Two used molten nitrate salt. Switching the power-tower to salt allowed the plant to have a more sophisticated thermal storage system, which meant the electricity generation and solar energy collection could be separated, and the power generation could become dispatchable.[26] Modifications to the Solar One plant required a new heat transfer system to accommodate the molten salt, as well as a new control system.[26] However, the turbine and generator, tower, and heliostat field only required minor modifications. Figure 2.5 shows a photo of the Solar Two plant during operation.[26] Solar Two operated from June 1996 to April 1999.[26]

Solar Two operated using a power tower system, which would collect solar energy from a field of heliostats. Figure 2.6 shows a schematic of the Solar Two plant's energy generation and thermal storage system.[26] The heliostat field reflected sunlight to a receiver at the top of the tower, which would heat a feed of cold (290 ° C) nitrate salt. The salt was then fed to a hot (565 ° C) thermal storage tank, where it could be pumped as needed through

Figure 2.5: The Solar Two power plant [27]

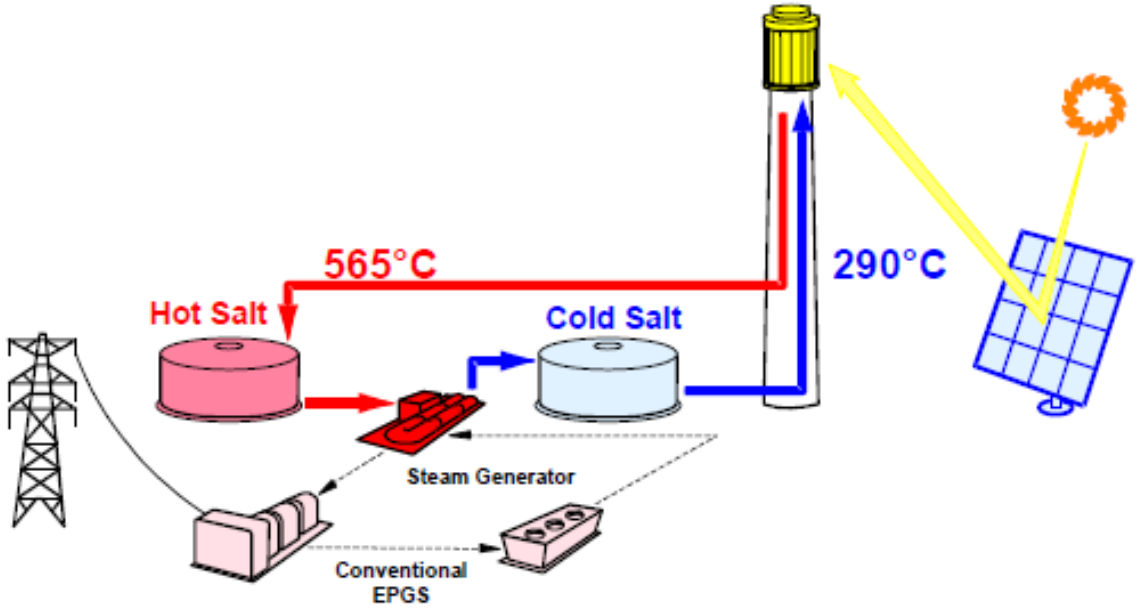

Figure 2.6: Schematic of the Solar Two power generation system [26].

a steam generator.[26]

The salt used for Solar Two consisted of approximately 3 million pounds (1300 tonnes) of 60 wt% $NaNO_3$, and 40 wt% KNO_3, which has a melting point of 205-220 ° C. [26] This salt is typically only stable up to temperatures of 600 ° C. [26] The nitrate salt mixture was chosen due to its heat transfer properties, which tolerated heat fluxes up to 1000 kW/m^2, and had properties conducive to the double-tank thermal storage system. Equipment used for the hot salt, including pipes and valves, was constructed of stainless steel, which is more resistant to nitrate salt corrosion at elevated temperatures. Equipment used for the colder salt was constructed from carbon steel, which is more cost-effective. The thermal energy storage system used at Solar Two used two tanks, a hot storage tank, and a cold storage tank. The cold storage tank was made from carbon steel, and the hot storage tank was made from stainless steel. Each tank was large enough to hold the entire plant's inventory of salt. Figure 2.7 shows a picture of the Solar Two plant's thermal energy storage tanks.[26]

Figure 2.8 shows the results of calculated and measured heat losses from the Solar Two

Figure 2.7: Thermal energy storage tanks at the Solar Two plant. On the left is the cold tank, and on the right is the hot tank. [26]

Figure 2.8: Thermal losses at the Solar Two plant [26]

Major Equipment	Calculated Thermal Loss, kW_t	Measured Thermal Loss, kW_t
Hot Salt Tank at 565°C	98	102 ±21
Cold Salt Tank at 290°C	45	44 ±6.6
Steam Generator System at 565°C	14	29 ±3.5
Receiver Sump at 290°C	13	9.5 ±1.0

.

plant. [26] As can be seen from the table, the heat loss from the thermal storage tanks was demonstrated to be very low, as compared to the thermal capacity of the system, which was 107 MWh (approx. 35 MW for three hours) [26]. Because of these results at Solar Two, it was predicted that commercial power plants with similar thermal storage systems would have an annual thermal storage efficiency of about 99%. [26]

Nuclear Hybrid Energy System

An NHES is a term referring to several energy systems combined to generate energy more efficiently. An NHES may include systems such as nuclear reactors, renewable energy sources, process heat applications, and energy storage.

An NHES design discussed by Green et. al [28] includes a high-temperature nuclear

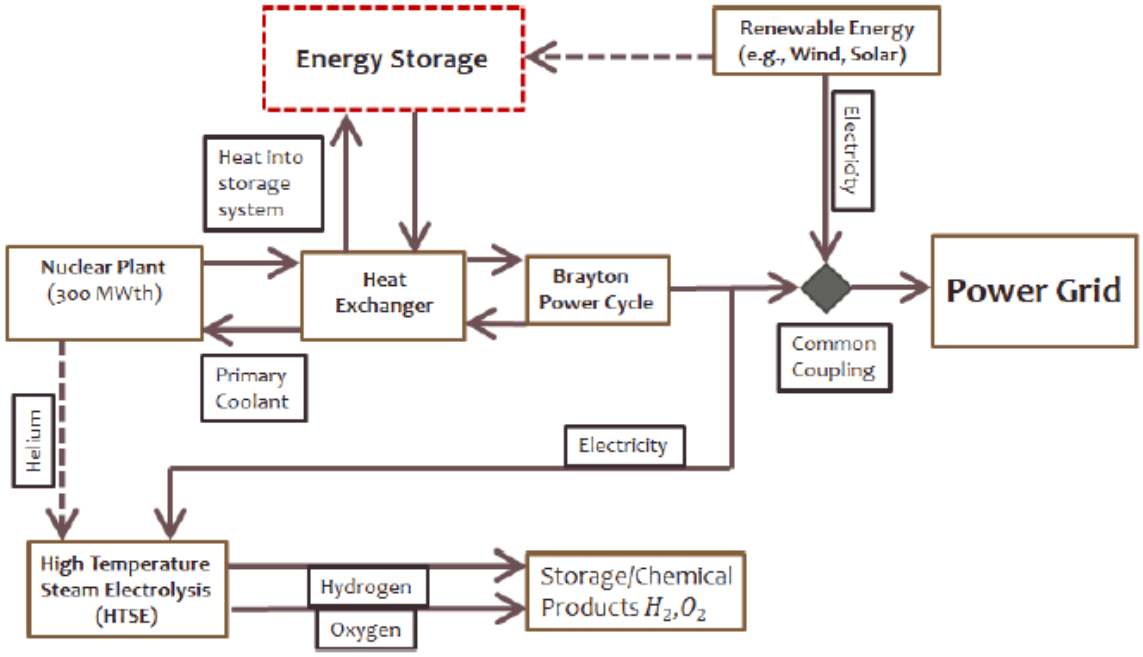

Figure 2.9: The Nuclear Hybrid Energy System [28]

reactor, which allows a portion of thermal energy to be used for process heat applications. This reduces the carbon footprint of the system. Figure 2.9 shows a schematic of the NHES. [28] An energy storage system is required to allow the NHES to respond to fluctuating energy needs.

This energy storage can be accomplished using molten salt thermal energy storage. Salt has a high temperature range and low viscosity, and there is existing experience in solar energy applications. Molten salt can be used in the NHES to store process heat from the nuclear plant, which can later be used when energy requirements increase. There are two different types of molten salt thermal storage options: a thermocline system, or a two-tank system. A two-tank system is like storage schemes used for CSP plants, in which a hot tank and a cold tank are used to store salt. A thermocline system uses only one tank, which contains both the cold and hot salt. The salt is separated by thermocline, which is a distinct layer of drastic temperature change. A thermocline prevents layers above and below it from mixing; therefore, the hot and cold salts do not mix in a thermocline storage tank. When the thermocline tank is charged, cold salt flows from the cold side of the

tank, through a heat exchanger, and into the hot side, filling the tank with stored thermal power. When the tank is discharged, the hot salt flows out, through a heat exchanger, and returns to the cold side.

One challenge present in working with molten salt thermal energy storage is salt freezing. Molten salt has a high melting point. Freeze protection is required to prevent the salt from cooling too much. Otherwise, the salt freezes within the system, causing blockage. Freeze protection is often provided by heaters, but could also be provided using gas turbines by directing hot exhaust to the molten salt systems. [28]

2.2 Molten Salt Chemistry

The chemical term "salt" refers to molecules that are ionically bonded. The components of salts consist of positively charged cations, and negatively charged anions, creating a bonded compound that has a neutral charge. A typical example of salt is sodium chloride ($NaCl$) or 'table salt,' which is widely used. Molten salts melt at very high temperatures, often over 400 ° C, because a lot of energy is required to break their ionic bond. Other salts, such as uranyl nitrate, which has a melting temperature of about 60 ° C, do not require as much energy to break their bonds. These types of salts are referred to as 'ionic liquids.' Energy production technologies, such as thermal energy storage or molten salt reactors, use molten salts because of their heat transfer and thermal properties at these high temperatures.

Salts are typically named for their anion, their negatively charged component. Salts typically used in energy applications include fluoride salts (LiF, NaF, KF, BeF_2), chloride salts ($NaCl$, $MgCl_2$, $CaCl_2$), and nitrate/nitrite salts ($Ca(NO_3)_2$, $NaNO_3$, KNO_3). Types of salts are mixed to produce salt eutectics with the properties desired for different applications. For example, 'Flibe' or $LiF - BeF_2$ (66:34 mol%) is a salt mixture often considered for molten salt reactor applications.

Chemicals interact with one another through either ionic or covalent interactions. In

solid states, most chemicals are primarily ionic, with only a small amount of covalent character. Molten salts are unique because, in their molten state, they exhibit a mixture of ionic and covalent interactions.[11] This fluctuates due to the changing nature of a molten salt system, such as the addition of components, fission-product generation, off-gassing, etc. This fundamental fluctuation of a molten salt system means that the chemical behavior and subsequent need for control can be complex.

Because molten salts are inherently ionic, they will disassociate into ions upon melting. Disassociation occurs when the thermal energy of each ion overcomes their bonding energy. Many salts disassociate at their melting point, or when dissolved into a solution. Lithium fluoride will disassociate at its melting point, forming the ions Li^+ and F^-. However, not all salts exhibit this disassociation behavior on their own. Beryllium fluoride will form a network of chained beryllium and fluoride atoms at its melting point, which can cause the salt to have a high viscosity. Zirconium fluoride also exhibits this non-disassociation behavior, causing a higher vapor pressure. 'Flibe,' a candidate MSR salt, was developed to combat the disassociation behavior of beryllium fluoride. Flibe is composed of lithium fluoride and beryllium fluoride. When beryllium fluoride melts, it can accept more fluorine atoms from an alkali fluoride, forming a tetrafluoroberylliate coordination complex (see Equation 2.1). Coordination complexes break the non-dissociative chaining behavior, allowing the salt mixture to have a lower viscosity. Zirconium fluoride also forms a similar coordination complex (see Equation 2.2).

$$BeF_2 + 2Li^+ + 2F^- \rightarrow BeF_4^{-2} + 2Li^+ \tag{2.1}$$

$$ZrF_4 + 2K^+ + 2F^- \rightarrow ZrF_6^{-2} + 2K^+ \tag{2.2}$$

Molten nitrate-nitrite salt decomposition is more complicated than that of chloride and fluoride salts. The thermal decomposition of these salts depends on the composition,

temperature, and experimental conditions. Some types of nitrite salts may form from nitrate in the melt, releasing oxygen according to the following reactions, where M is a cation. [29]

$$2MNO_3 \rightarrow M_2O + 2NO_{2(g)} + \frac{1}{2}O_{2(g)} \tag{2.3}$$

$$M(NO_3)_2 \rightarrow MO + 2NO_{2(g)} + \frac{1}{2}O_{2(g)} \tag{2.4}$$

Alkali metal oxide can form in the melt, releasing nitrogen or nitrogen oxide gas. The nitrate salts may also vaporize. These thermal decomposition behaviors are influenced by intrinsic salt properties, such as the metal-nitrate bond. Polarization is induced by the cation, distorting the electron distribution in the nitrate, which lowers the decomposition temperature. [29]

2.2.1 Selection of Salts for Energy Technologies

The selection of a salt type for a reactor or a thermal storage system requires careful consideration of the chemical and thermodynamic properties of the candidate salts. Different energy technologies will require different salt types, based on temperature and fluid property requirements. Molten salt reactors require salts that are both chemically and radiolytically stable at high temperatures and have low melting and high boiling points. For optimum thermodynamic behavior, molten salt reactors also require a large specific heat and thermal conductivity and a vapor pressure lower than that of water (<1 mmHg at 900°C). Low vapor pressure is required to allow for a molten salt reactor to operate at a high temperature without the working fluid volatilizing, which minimizes the vapor phase present in the system.

Fluoride salts are often the primary candidate salts for reactor systems. Lithium fluoride, beryllium fluoride, and sodium fluoride all have suitable melting ranges, and are often

considered as candidate salt components. Beryllium fluoride is especially compatible with a reactor system because it has the lowest thermal neutron cross-section of the fluoride salts ($\sigma \approx 0.010$ b). 'Flibe' or $LiF - BeF_2$ (66:34 mol%) was developed during the MSRE to combine the desired properties of beryllium and lithium fluoride, and was considered to have the most compatible properties for a reactor. [30] However, beryllium fluoride can be hazardous, and lithium fluoride can generate tritium in a neutron flux environment. Lithium material must be isotopically purified to 99.99% $Li-7$ to avoid tritium generation, which can be costly. [30]

'Flinak' or $LiF - NaF - KF$ (46.5:11.5:42 mol%) has been developed as a surrogate for Flibe. [30] Flinak has properties similar to Flibe but is not as toxic. $NaF - ZrF_4$ and $KF - ZrF_4$ are salt candidates that do not have the issue of tritium generation by lithium fluoride. However, these salts may have other undesirable fluid properties, such as the high melting point of $NaF - ZrF_4$ and the high vapor pressure of $KF - ZrF_4$.

Chloride salts are another category of candidate salt that have been considered for power production. Chloride salts often exhibit similar energy and behavior to fluoride salts and have similar corrosive effects. [30, 31] Candidates mixtures such as $KCl - MgCl_2$ (67:33 mol%) could be used as primary coolants if measures are taken to prevent the generation of $Cl - 36$ by nuclear transmutation.[32] If a candidate chloride salts contain lithium, similar problems arise as those seen in fluoride salts, where the lithium must be isotopically purified to avoid the generation of tritium in a neutron flux. Nitrate-nitrite salts contain NO_3 and NO_2 and are used in solar applications. A typical mixture is $NaNO_3 - NaNO_2 - KNO_3$, industrially known as Hitec. The stability of nitrate-nitrite salts in radioactive environments is mostly unknown. The salts may be stable, but this has not been tested because nitrate-nitrate salts lose stability at high temperatures ($\sim$ 550 to 600 °C). At higher temperatures, the salt will decompose to nitrites and oxides. This occurs at around 600°C in air, but under inert gas, the salt will decompose at even lower temperatures, depending on the temperature and impurities. Above 800°C, the

reaction is fast, forming so much gas that the salt appears to boil.[32] The products of the decomposition can be problematic because oxide impurities can contribute to corrosion. Nitrate-nitrite salts can also react with fuel, precipitating actinide oxides, and react with a graphite moderator.[33]

2.2.2 Chemistry Challenges

Tritium

Many salt candidates for molten salt reactors use lithium fluoride salt (LiF). Naturally occurring lithium consists of mostly the isotope $Li-7$ (92.58%)[11], with the remainder being $Li-6$. Tritium can be produced from lithium if a neutron is absorbed, by reactions 2.5 and 2.6 [11]:

$$Li^6 + n(thermal) \rightarrow He^4 + H^3 \tag{2.5}$$

$$Li^7 + n(fast) \rightarrow H^3 + He^4 + n \tag{2.6}$$

Tritium can be problematic in a reactor system because it can be a hazard to human operators. Tritium can permeate through metals to secondary systems, exposing workers to radiation.[34] If tritium permutates into water, humans can absorb tritiated water with severe consequences. Tritium is difficult to contain at high temperatures [4], and therefore the production of tritium needs to be prevented. Because only fast neutrons can cause $Li-7$ to absorb a neutron and produce tritium, the main concern for tritium production is with the less-common isotope $Li-6$. Even though there is only a small amount present in naturally occurring lithium, the salt would need to be isotopically purified to $Li-7$ to avoid tritium production. Isotopically purifying lithium can be an expensive process, which means that lithium enrichment could be a prohibitive cost to molten salt reactor development.

Corrosion and Materials Compatibility

Corrosion of structural materials is a significant concern in molten salt systems. Salt systems can be extremely corrosive, especially at the high temperatures present in reactor or thermal storage systems. Redox potential is an electrochemical property of materials that can be used to evaluate the corrosivity of a salt. Redox potential describes the tendency of a material to reduce or oxidize. A reducing material will have a more negative redox potential, and an oxidizing system will have a more positive redox potential. When a salt is reducing, it craves electrons and will gain them from a donor species through a reduction-oxidation (redox) reaction. When a salt is oxidizing, it will seek to donate electrons to an accepting species. When a species undergoes a redox reaction, its oxidation state will change. A typical example of a redox reaction is the reaction between hydrogen and fluoride:

$$H_{2(g)} + F_{2(g)} \rightarrow 2HF_{(g)} \tag{2.7}$$

In this reaction, hydrogen is oxidized from a state of 0 to +1, by losing one electron. Fluoride is reduced to an oxidation state of -1 from 0 by gaining an electron. The chemical composition of a material determines its redox potential. A more reducing salt will be less likely to corrode (oxidize) structural material.

Corrosion in a molten salt system differs from standard reactors systems due to the lack of a passive oxide film on the surface of structural materials. Typical alloys have an oxide film on their surface, which protects the alloy from corrosion from fluids. Reactions with air or moisture form these films. Gaseous fluorine can also form a protective fluoride layer. However, oxides and fluorides are soluble in fluoride salts, which will dissolve any protective layers that were present.

In their pure state, fluoride and chloride salts are naturally reducing, and are not likely to corrode surrounding material. The introduction of impurities in the salt increases the

redox potential, forming a more oxidizing mixture. Figure 2.10 shows an aggregation of corrosion studies on fluoride and chloride salts. [35] Impure salts show considerably more mass change than pure salts.

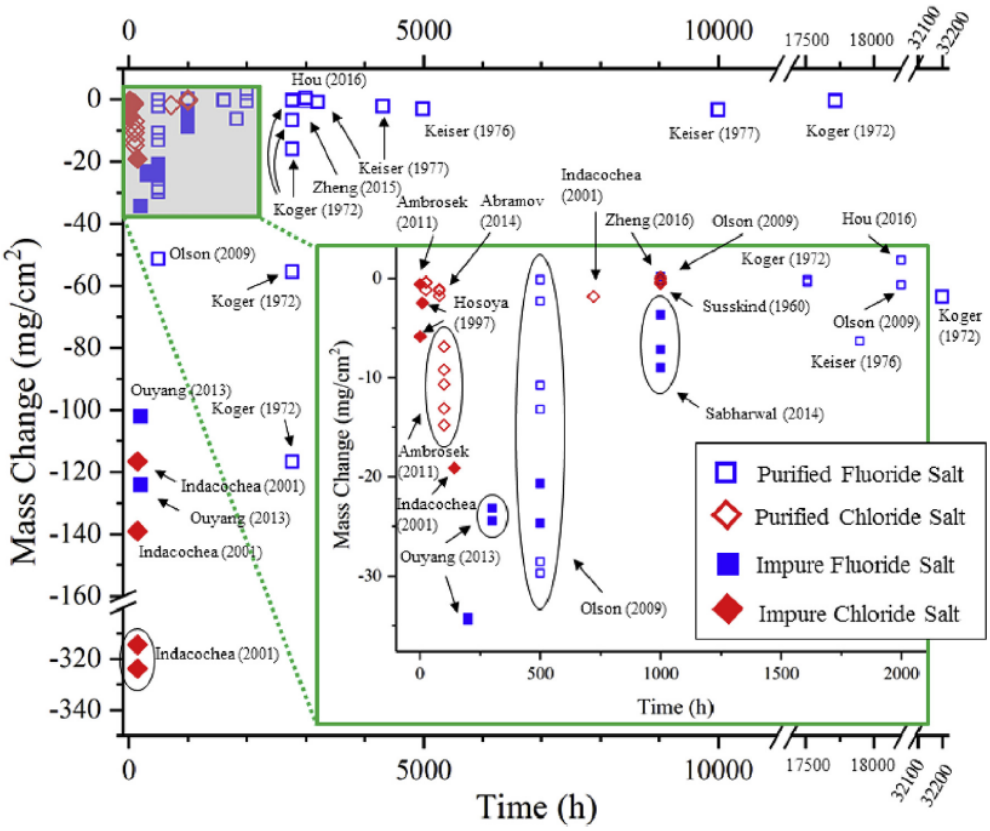

Figure 2.10: Aggregation of mass change data for impure and pure molten salts [35]

These data show that it is essential to remove impurities from molten salts to prevent the system from becoming too oxidizing and corroding structures. However, a salt should also not be kept in an overly reducing state, which can form metal suspensions that react with carbon to form metal carbides.[4] Therefore, the salt must be kept in a balanced, reduced state.

The metals most prone to attack in a molten salt system can be determined by Gibbs free energy of formation. Gibbs free energy indicates the energy available in a system to carry out chemical reactions and can be calculated using the activity of a species. A more negative free energy indicates that a metal is more prone to attack, and a more positive

free energy indicates a metal is less prone. From this information, it has been determined that structural alloy components are increasingly prone to attack in the following order: W, Mo, Ni, Co, Fe, Nb, Cr, Mn, Ti, Zr, and Al.[4] In corrosion-resistant alloys, the most prone element present is typically chromium, which is then attacked at grain boundaries. Because there is no passive film to protect the structural alloy, it is necessary to mitigate corrosion by either purifying the salt or by controlling the redox potential of the salt in a reducing state. Redox potential can be controlled through the use of reducing and oxidizing agents. These agents are chemicals that either reduce or oxidize the salt on addition, which can bring the salt to a more reducing or oxidizing state, thereby controlling the corrosion.

Redox buffers are another method of controlling molten salt corrosion. Buffers are chemicals which exist in two different oxidation states, such as U(IV/III), V(IV/III), Tm(III, II), Sm(III, II), Yb(III, II), Ce(IV, III), and Eu(III, II) [4]. They can be mixed with or suspended in a salt mixture, and will be preferentially oxidized or reduced in place of the salt. The above-listed elements are all viable options for redox buffers; however, the selection of a buffer is dependent on the system. A primary fuel salt can use uranium as a buffer, but if a salt is not a fuel salt, other options must be used. Some options are not viable due to high neutron cross-sections. If no buffer material is viable for use in a salt system, then other redox potential control methods must be used.

Chloride salts behave very similarly to fluoride salts. Similar to fluorides, pure molten chlorides are reducing; they therefore do not corrode alloying metals in contact with the salt. The impurities, such as metal oxides or water, therefore drive corrosion in molten chlorides in the salt. The presence of moisture in molten chlorides can lead to the formation of HCl, which will enhance corrosion rates dramatically. Like fluoride, chloride salts will dissolve passive protective films on structural alloys, but not as severely as fluoride salts.[5] Corrosion behavior in corrosion-resistant alloys is similar to that of fluoride; the salt selectively attacks chromium along grain boundaries. Nitrate-nitrite salts behave much differently from fluoride and chloride salts. Unlike fluorides and chlorides, nitrate-nitrites

have an oxidizing redox potential. These salts will form a protective oxide layer on metals, which becomes thicker as oxidation progresses [32]. Corrosion in molten salt system is discussed in greater detail in section 2.3 .

Irradiation and Fission Products

It is important to understand where fission products end up in MSR's and how they behave in order to determine what is dissolved, plated or insoluble in the MS and which fission products will need to be removed. The detailed chemical behavior of many fission products remained uncertain at the conclusion of the MSBR program in 1976, and there have been few studies since then. Loss of criticality is as much an issue in molten salt reactors as it is in LWRs. Fuel recycling for molten salt, also known as fuel salt cleanup, has renewed interest since the removal of fission products such as neodymium (Nd) and Cesium (Cs) contribute almost 50% to the loss of criticality making it vital that they are separated during molten salt recycling schemes. In addition to the separation of Cs and Nd, it is advantageous to remove zirconium (Zr) and samarium (Sm) from the salt since they supply nearly 80% of the fission products that could also contribute to loss of criticality.[36]

Four classes of fission products have been identified based on previous MSR work.[37] The four species, shown in Figure 2.11, are: gaseous (noble gases); soluble (alkali, rare earths, active refractories and halogens); insoluble (transition metals between Nb and Te); and sometimes soluble (Nb, Te and Zn periodic columns).[37] The 'sometimes soluble' group tends to change with the redox state of the MS. The chemistry of the interaction and transition of the insoluble and sometimes soluble phases is not completely understood. The majority of the fission product remain as salt soluble species; however, the decay behavior of the fission product chain is complex and can result in longer lived isotopes partitioning after the short-lived isotopes. This scenario occurs in some of the noble metal fission products as well as key isotopes such as Cs-137, Mo-99, and I-131.

Molten salt reactor fuel will require comprehensive investigation into its resistance to

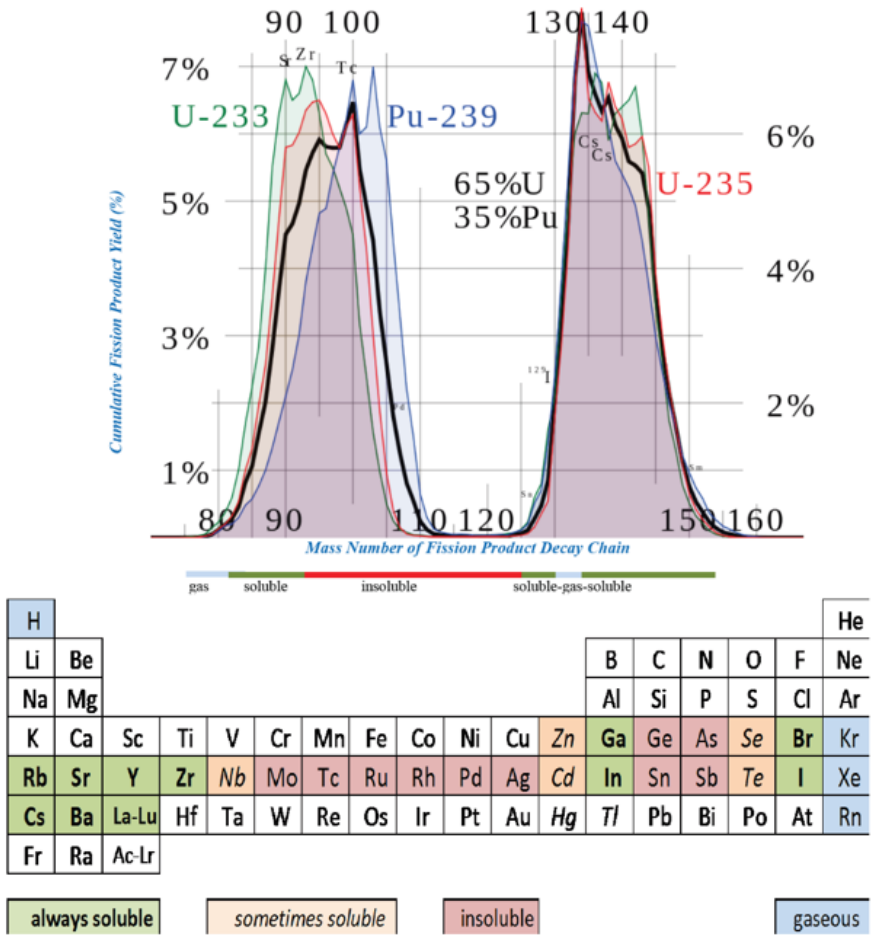

Figure 2.11: Fission product classes identified during MSR operation highlighted as groups in the periodic chart and the fission-yield curve. [37]

radiolysis damage due to the irradiation of the salt fission products. The current understanding of radiolytic effects in chloride salts is based on experience within the reprocessing industry which uses molten salt media to dissolve solid used nuclear fuels in preparation for separation. Experiments are yet to be conducted to confirm the stability of molten chlorides under the more intense conditions of irradiation as a fuel salt and studies conducted on solid fluoride and chloride salts using alpha, beta, gamma, and x-ray irradiation; however, data collected from interim storage solid salts showed radiolytic damage and chemical changes associated with dissolved fission and activation products.[37] The impact from fission and activation product distribution due to the nature of the molten salt as well as the impact of irradiation will also need further analysis since areas of the molten salt could receive more or less radiolysis effects depending on the ebb-and-tide of the salt flow. There are many areas of focus requiring study related to fission products and irradiation and ultimately both areas are tied together with one effecting the other in the molten salt.

2.3 Corrosion in Molten Salts

As discussed in section 2.2.2, corrosion of structural materials is a significant concern in molten salt systems. The purpose of this section is to provide more detail than that which was provided in section 2.2.2.

In the most basic sense, corrosion occurs when components of a system are reduced or oxidized. In a molten salt system, there are multiple routes corrosion could occur: Reduction of salt component cations, or oxidation of structural material components. Corrosion in molten salt systems could possibly occur when cations of major salt constituents, such as lithium, potassium, or beryllium, are reduced. However, the reduction potentials of these major salt cations are significantly less than the oxidation potentials of structural materials. This suggests that direct reduction of salt-component cations is not likely to be the source of structural material corrosion. [31]

Actinides in a molten salt mixture may also act as oxidants, causing metal corrosion.

Actinides may be present in a molten salt system with fissile material, such as the primary loop of a molten salt reactor design. Evaluating what actinides are likely to corrode metals depends on the reduction potential of the actinide. Fission products, which are dissolved in the mixture in the form of fluorides or chlorides, may act as oxidants. Under certain conditions, U(IV) may be an effective oxidiant to iron and chromium. Tritium fluoride, a byproduct of irradiation of lithium, is highly corrosive. The actinide and lanthanide cations U(IV), Np(IV), Zr(IV), Sm(III), and Eu(III) are thermodynamically more corrosive than other elements. [31]

Since fluoride and chloride salts are quite hygroscopic, they will readily absorb atmospheric moisture, forming water and oxide impurities [31]. Water contamination in molten salt reacts to form oxides, and hydrofluoric or hydrochloric acid. These acids can be extremely corrosive. The formation of these corrosive byproducts is by the following reactions [31]:

$$H_2O(g) + 2F^- \leftrightarrow O^{2-} + 2HF(g) \tag{2.8}$$

$$H_2O(g) + 2Cl^- \leftrightarrow O^{2-} + 2HCl(g) \tag{2.9}$$

While equation 2.8 is more thermodynamically favorable due to its more negative gibbs energy of formation, both reactions are possible in their respective fluoride or chloride salt mixtures [31]. The products of these equations are HF and HCl, which are both highly corrosive contaminants.

Hydrofluoric Acid, or HF, although it is considered a weak acid, is extremely reactive. This is due to the fluoride ion, which is an extremely reactive ion. In general, weak acids partially dissociate into their ions when they are in an aqueous solution. In contrast, a strong acid will completely dissociate in aqueous solutions. In molten salt mixtures, HF doesn't dissociated to H^+ and F^- ions, as it would in an aqueous solution. Rather, it

will strongly associate with F^- ions and form HF_2^- [31]. Hydrogen ion concentration is inversely proportional to the pH value of a solution, which has a significant impact on the corrosivity of the mixture. In general, the corrosion rate of metals will increase with a decrease in pH, which is accomplished through an increased concentration of hydrogen ions [31]. An increase in hydrogen ions will increase the cathodic reduction reaction rate. Therefore, an increase in the amount of HF and HCl will, through dissociation, produce more corrosive conditions.

When hydrogen ions are present in a solution, it is possible that they will be reduced to form H_2. This hydrogen evolution can proceed in fluoride salts through the reduction of HF, through the following reaction [31]:

$$HF + e^- \rightarrow \frac{1}{2}H_2 + F^- \tag{2.10}$$

In chloride salt melts in which HCl forms, contrary to HF, HCl will completely dissociate [31]. This is due to the favorability of the formation of Cl^-, which is a weak conjugate base. Thus hydrogen evolution proceeds through the reduction of the resultant hydrogen ion:

$$H^+ + e^- \rightarrow \frac{1}{2}H_2 \tag{2.11}$$

Corrosion through anodic metal dissolution can be increased through the production of OH^- ions, which form through the addition of water contaminants in a salt mixture [31]. Experimental evidence supports the hypothesis that the OH^- ions are involved in this increase in anodic metal dissolution, through the formation of hydroxylated metal compounds [31]. Thus, an increase in OH^- concentration in a molten salt solution will increase the anodic metal dissolution rate.

Oxide impurities in molten salts can be formed through oxygen and water contaminants. O^{2-} can be formed through reactions with moisture, such as reactions 2.8 and

2.9. The ion itself is not necessarily oxidizing toward metals, but through the formation of oxide corrosion products, the presence of the ion can influence the corrosion of structural materials [31]. Reaction 2.12 shows the formation of the corrosion product, where M represents the metallic element.

$$M + \frac{n}{2}O^{2-} \leftrightarrow MO_{\frac{n}{2}} + ne^{-} \tag{2.12}$$

The resultant oxide corrosion product, $MO_{\frac{n}{2}}$, may also dissolve in a fluoride or chloride salt, as shown in reaction 2.13 [31], in which X represents the fluoride or chloride ion.

$$MO_{\frac{n}{2}} + nX^{-} \leftrightarrow MX_n + \frac{n}{2}O^{2-} \tag{2.13}$$

Equilibrium potentials can be calculated for the oxide reactions above, and resultant equilibrium lines plotted in $E - pO^{2-}$ diagrams can indicate the thermodynamic behavior of different metallic elements in these oxide reactions. The diagrams, shown in figure 2.12, display potential as a function of $pO^{2-} = -log_{10}(a_{O^{2-}})$, and can indicate the domains in which the oxide metal compounds are stable [31]. These figures show that Ni will experience less corrosion at positive potentials than Fe and Cr. The oxide formation window for Cr is wider than Ni, which means chromium oxides can form at lower O^{2-} concentrations than nickel oxides. Typically this would indicate the formation of a dense, protective oxide layer, formed of chromium oxides. However, this oxide layer is not likely to form in chloride and fluoride salt systems [31]. Therefore, the alloys exposed to the salt mixture require thermodynamic stability to lessen the severity of corrosion [31]. This can be accomplished through redox potential control.

2.3.1 Effect of Fluid Velocity on Corrosion

The effect of fluid velocity on corrosion has been widely studied in general, for many fluids [38, 39, 40, 41, 42, 43]. A study evaluating the corrosion behavior of 13CrSS under ultra-

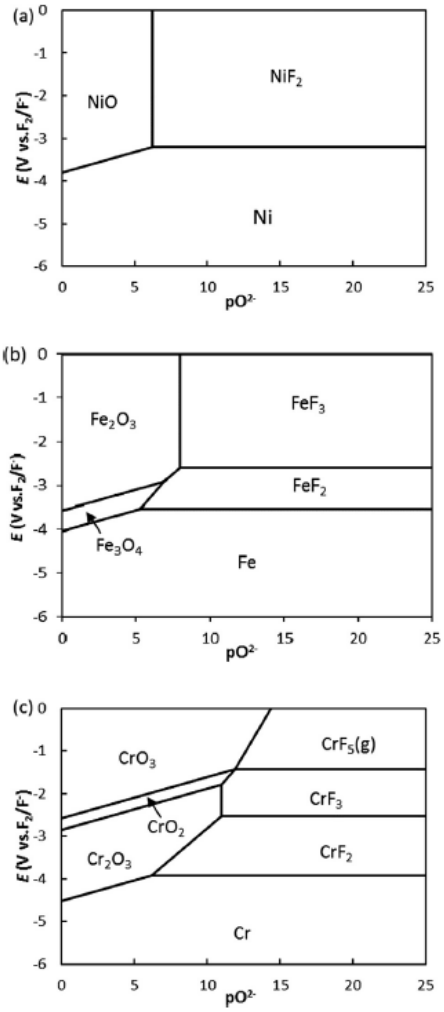

Figure 2.12: $E - pO^{2-}$ diagrams calculated by [31] at 700 ° for Ni, Fe, and Cr in FliBe.

HTHP $CO_2 - H_2S$ fluid flow found that a flow velocity delayed the deposition of corrosion products, and promoted the development of pitting [43]. An evaluation of fluid flow effect on CO2 corrosion in carbon steels found that flow facilitated corrosion, by augmenting the mass transfer rate of species between bulk and steel surface [41]. A 2020 analysis of erosion-corrosion in two-phase CK45 steel showed that increasing the fluid velocity from 5 m/s to 16 m/s increased the corrosion rate by 4-6 times, depending on microstructure [40].

The impact of velocity on molten salts is less known. There is some research on the subject [44, 45, 46, 47, 48], however most of these studies evaluate carbonate or nitrate

salts, not fluoride or chloride salts. Not much is known on the specific effect of velocity on fluoride and chloride salt corrosion. Parallels can be made between the information that exists for nitrate and carbonate salts and fluoride and chloride salts.

Experimentation on nitrate salts show that corrosion increases with increasing velocity [44, 48, 47]. A comparative review by Ma et. al [46] identified many more studies which come to a similar conclusion. This is due to a specific type of corrosion which occurs when the metal alloy and the solution have relative movement. This corrosion phenomenon, called erosion-corrosion, couples fluid erosion and electrochemical corrosion mechanisms, which leads to a far greater corrosion rate than either of the mechanisms separately [46]. Fluid in a flow state disrupts adherent surface films and deposits, which would otherwise offer protection against corrosion [49]. Flowing fluid also promotes material and charge transfer processes of corrosive components, and lends to the diffusion of oxidation reaction components, both of which increase corrosion [48]. In a system with no passive layer, such as fluoride and chloride salt systems, although no experimental data exists in these systems, it is reasonable to assume that increases in flow rate would increase the corrosion rate. Erosion-corrosion is also called 'impingement attack', and is accelerated in geometries such as elbows, turbines, constrictions, and other flow geometries which alter flow direction or velocity [49].

2.3.2 Corrosion Control in Molten Salt Systems

Corrosion in molten salt systems is significantly impacted by the purity of the salt. Corrosion in molten salt systems is driven by oxidizing impurities, such as oxides or moisture. Metal deposits and sulfur can also cause corrosion. Therefore, the best method for minimizing corrosion in a molten salt system is through purification of the salt. However, many purification methods are difficult to perform on a large scale. As an example of this difficulty, hydrofluorination is the most effective purification method for fluoride salts [4], and involves bubbling a mixture of hydrogen and hydrofluoric acid through the molten salt.

This process is effective, but hydrofluoric acid is extremely dangerous, and many expensive and complex procedures and systems must be put in place for the safety of operators. This kind of system may not be worth the effort, and other systems for purification and corrosion control may be necessary.

During the MSRE, it was determined that corrosion can be successfully minimized by controlling the redox potential of the salt [4]. Since the redox potential within a molten salt reactor can constantly be changing due to fission product production, constant measurement and control of the redox potential of the salt is crucial for minimizing corrosion. A salt mixture that is too oxidizing due to impurities will corrode structural materials, attacking chromium in corrosion resistant alloys. Additionally, a salt that is too reducing can form metal suspensions, which will attack carbon, which could be present in some structural components, such as graphite or carbon steel materials [4]. If a fuel salt is too reducing, uranium may react with carbon according to the following reaction [6]:

$$2U^{3+} + xC \rightarrow 3U^{4+} + UC_x \tag{2.14}$$

Therefore, a molten salt mixture needs to remain in a careful redox potential state, one that is not too reducing, and not too oxidizing. This carefully maintained state can reduce corrosion.

Redox Potential Measurement

Measurement of the redox potential of a solution can be accomplished through simple electrochemical methods, by evaluating the potential of a redox couple reaction within the salt at a certain temperature [3]. Redox couples, such as Eu^{3+}/Eu^{2+}, are related to the redox potential of a salt through the Nernst equation [50]:

$$E_{\frac{Eu^{3+}}{Eu^{2+}}} = E^{*}_{\frac{Eu^{3+}}{Eu^{2+}}} + \frac{RT}{nF} ln(\frac{c_{Eu^{3+}}}{c_{Eu^{2+}}}) \tag{2.15}$$

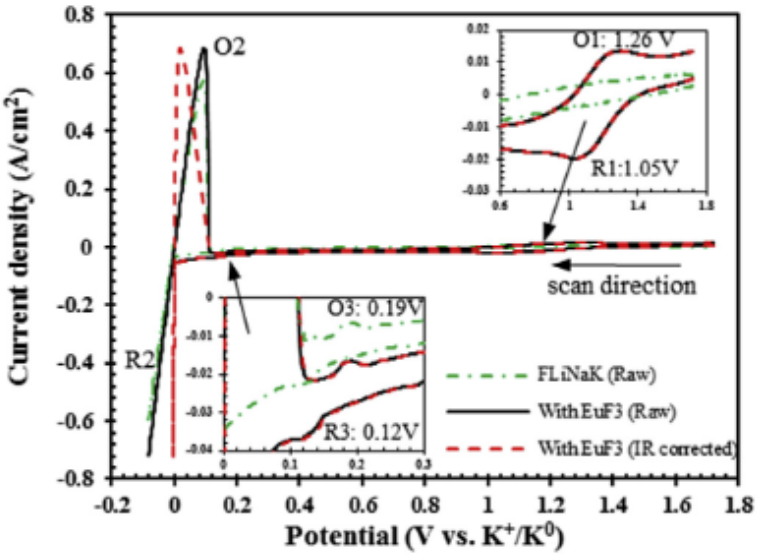

Figure 2.13: Cyclic voltammogram of flinak salt with dissolved EuF_3, from Guo et. al [51].

The couple U^{4+}/U^{3+} can be measured for fuel salts, or Eu^{3+}/Eu^{2+} can be used for other fluoride salts. These redox couples are often referred to as 'redox buffers,' and can be used to control the redox potential of the salt. The ratio of the redox species can be determined by an electrochemical sensor.

An electrochemical sensor designed for redox potential measurement of the salt is simply a three-electrode cell, consisting of a working electrode, a reference electrode, and a counter electrode, connected to a potentiostat. Through this three-electrode cell, cyclic voltammetry is performed to determine the concentration ratio of the relevant redox couple, and thus determine the redox potential. Figure 2.13 from Guo et. al shows an example cyclic voltammogram plot performed in flinak salt with dissolved EuF_3 at 700Â°C [51]. The peaks R1/O1 represent the reduction and oxidation of the Eu^{3+}/Eu^{2+} redox couple. Peaks O2/R2 are due to the decomposition of K+ in flinak salt, and peaks R3/O3 are due to impurities in the salt [51].

Cyclic voltammetry performed on the salt will produce a peak potential difference corresponding to the reduction and oxidation of the redox couple. The concentration ratio fo

the redox couple can then be determined using a method developed by Keightley et. al, referenced in Guo et. al [51]. If the diffusion coefficients D_{red} and D_{ox} are known, peak current densities and potentials can be predicted at varying concentration ratios using the above set of equations. This prediction shows that the concentration and diffusion coefficients solely depend on the peak potential difference. A correlation between concentration and peak potential difference is formed from the prediction, and therefore the concentration ratios can be calculated from the resultant correlation [51]. This method was developed to determine concentrations of redox couples in a solution where both members of the couple are present. Another method, the Randles-Sevcik equation, was used during the MSRE to determine the redox couple concentration ratio; however, this method has since been proven to only be valid when only one member of the redox couple is present [51].

One issue with setting up a three-electrode cell within molten salt is selection of a stable reference electrode. A reference electrode should have a reproducible and well-known potential. Fluoride and chloride salts are highly reactive, and therefore metal and ceramic reference electrode design can be challenging. Alternative reference electrodes include thermodynamic redox electrodes, gas electrodes, and dynamic electrodes. Thermodynamic reference electrodes use a half-cell reaction with a material stable in salt, separated from the main salt solution by an ion barrier. Zhang et. al [3] references several examples from literature. Some designs use a nickel rod suspended in fluoride salt with dissolved nickel fluoride. This design utilizes the Ni_{2+}/Ni redox couple. A gas reference electrode consists of a tube with a platinum or palladium tip suspended in the salt melt, and a gas is bubbled through the tube at a fixed ratio to the noble metal tip. For fluoride salts, $HF - H_2$ gas is often used.

Dynamic reference electrodes were developed as a method to associate a quasi-reference electrode with a thermodynamic reference. These dynamic reference electrodes apply a pulse current on a solid inert electrode to determine the potential of the salt solvent.

Duran-Klie et. al[52] developed a dynamic reference electrode using a potassium electrode for flinak salt. The current is applied in a controlled range, which deposits the potassium ions on a tungsten wire, enabling the redox potential of the potassium ions to be measured, serving as a well-known reference potential.

Redox Potential Control Methods

To minimize corrosion, the redox potential of the salt needs to be carefully monitored and controlled. Control of the redox potential is done through adjusting the concentration ratio of the redox couple of interest within the salt. When the concentration ratio of the redox couple is adjusted, the redox potential can be adjusted. This redox couple can be the uranium redox couple in fuel salt, or another couple such as europium in coolant salts. Control of this ratio can be done by directly adding a redox couple component, or by oxidizing/reducing agents and redox buffers. The ratio must be maintained at a careful reducing state; a too oxidizing salt will corrode structural materials, and a too reducing salt will form metal suspensions or attack carbon.

The redox potential of a molten salt system can be controlled through the addition of a reducing agent. A reducing or oxidizing agent is a material that changes the salt redox potential when it is added to the salt, either as a dissolved metal or a metal rod or plate suspended in the salt. The material changes the redox potential of the salt by reacting with a member of the redox couple of interest, reducing or oxidizing a component to change the ratio. This is often more desirable than directly adjusting the concentration ratio of the redox couple in the salt, because the redox agents can be easier to produce. During the MSRE, beryllium metal was added in small capsules to the flibe salt, which reacted with UF_4 to form UF_3, reducing the salt and lowering the U^{4+}/U^{3+} concentration ratio [51]. Other reducing agents include zirconium, or any other metal capable of accepting electrons from fluoride. When a salt becomes too reducing, it is necessary to add an oxidizing agent to raise the redox potential to an acceptable level. Hydrogen fluoride is an acceptable

oxidizing component but any fluoride species capable of donating electrons to the salt is viable, such as chromium fluoride or nickel fluoride.

A redox buffer is a species capable of existing in two oxidation states. The redox couple of interest in a salt can exist as a redox buffer. The redox buffer, denoted as Xn+/Xm+, brings the reduction-oxidation reaction to equilibrium through reactions 2.16 and 2.17, where M represents structural material [51]:

$$M + Ox \leftrightarrow M^{n+} + Red \tag{2.16}$$

$$X^{m+} + Ox \leftrightarrow X^{n+} + Red \tag{2.17}$$

Reaction 2.16 shows the corrosion of structural material M. The redox buffer, X, acts as a sacrificial material, oxidizing in place of the structural material in reaction 2.17. The concentration ratio of X^{n+}/X^{m+} is maintained to favor reaction 2.17, preventing the formation of M^n+. If the salt becomes too oxidizing, the buffer is oxidized before corrosion occurs. If the salt becomes too reducing, the buffer is reduced before the salt forms a suspension. Possible redox buffers include U(IV/III), V(IV,III), Tm(III,II), Sm(III,II), Yb(III,II), Ce(IV,III), and Eu(III,II) [4]. Uranium is a convenient material for use in a primary salt, since it is both a fuel and a buffer. Other options are less desirable for use as a primary salt, because of high neutron cross sections. If the salt is to be used as only a coolant, other buffers must be used instead of uranium. Use of a redox buffer still requires control of the concentration ratio of the redox couple, but it is important to use a redox buffer to provide an intrinsic defense to changes in the redox potential.

CHAPTER 3

Experimental Methodology

3.1 Introduction and Scope

Design of molten salts systems requires a thorough understanding of how the salt will behave, not only during initial operation, but over the entire lifetime of the system. Although it is possible to include corrosion control systems in a system design, eliminating corrosion entirely is not possible, particularly in fluoride and chloride salts systems. This means that over the system's operational lifetime, there will be inevitable corrosion, leading to degradation of internals, and the addition of corrosion products to the salt mixture. Many fluid thermophysical properties are correlated with the composition of the fluid mixture. Addition of impurities, such as corrosion and fission products, changes this chemical makeup, possibly altering the thermodynamic behavior of the salt [4]. In a molten salt reactor design, significant changes in thermophysical properties can have severe impacts on reactor operation, such as coolant flow, and core neutronics. Two forms of experimentation were conducted to investigate this type of corrosion-product-driven behavior change.

The purpose of this experimentation was to examine the impact of corrosion products on the melting point of molten salts. The melting point was chosen as a focal thermophysical property, due to the simplicity of measurements, and the relevance to reactor design. A molten salt reactor operates using a molten matrix, and therefore the design relies heavily on predictable melting/freezing point data. Two forms of experimentation were conducted for this research. The first set of tests evaluated the melting temperature in bulk, using an apparatus constructed in-house. The second set of tests used a DSC, to

evaluate the melting temperature on a smaller, more sensitive scale. The same samples were used for both tests, with the purpose of evaluating the efficacy of the bulk testing with the results of the DSC.

Two types of salt were examined: 'Flinak' ($LiF - KF - NaF$) and 'Solar salt' ($NaNO_3 - KNO_3$), with corresponding corrosion products of FeF_3 and Fe_2O_3. The salts were chosen due to their use in nuclear and solar applications. Flinak salt is a candidate salt for molten salt reactor applications, and is often used as a surrogate for other, more hazardous fluoride salts. Solar salt is used in solar applications, but is also a candidate salt for thermal energy storage applications, which can be coupled to a nuclear system. The corrosion products for this study were chosen to correspond to each salt. Common corrosion products in molten salt systems include both iron and chromium derivatives [53, 31]. Chromium in particular is selectively attacked at grain boundaries. Iron is the main constituent in steel alloys, therefore iron fluoride and iron oxide were selected as the focus of these experiments. Both of these chemicals are iron derivatives, and possible corrosion products in molten salt systems.

3.2 Sample Preparation

The Solar salt was organized into 10 samples, with corrosion product concentrations of 0, 0.5, 1, 2, and 5 wt%, for a total of 2 samples for each concentration. The Flinak salt was organized into 8 samples, with corrosion product concentrations of 0, 1, 2, and 5 wt%, for a total of 2 samples for each concentration. Each sample was given a corresponding letter code. Prior to experimentation, each group of samples (Flinak and Solar) was randomized using a random number generator, to produce a randomized testing order for each group. Tables 3.1, 3.2, and 3.3 show this sample organization. After all planned Solar salt samples were evaluated, surplus stock allowed for additional samples to be added. Therefore, two additional Solar salt tests (not included in table 3.1) were conducted, with iron oxide concentrations of 3.5 wt%. These additional samples were labeled X and Y, and the

results of these are included with the Solar salt results, outlined in chapter 4.

Table 3.1: Sample organization and Fe_2O_3 addition amounts for the Solar salt tests.

Fe_2O_3 **wt%**	0	0.5	1	2	5
Set 1	I	J	K	L	M
Set 2	N	O	P	Q	R

Table 3.2: Sample organization and Fe_2O_3 addition amounts for the Flinak set 1 salt tests.

Fe_2O_3 **wt%**	0	1	2	5
Set 1	A	B	C	D
Set 2	E	F	G	H

Table 3.3: Sample organization and FeF_3 addition amounts for the Flinak set 2 salt tests.

FeF_3 **wt%**	0	1	2	5
Set 1	AA	BB	CC	DD
Set 2	EE	FF	GG	HH

Each sample was prepared according to the same procedure. Solar salt and Flinak were prepared from component materials (e.g. Flinak was prepared from stock of LiF, KF, and NaF), which were in a powdered form. Corrosion products (also in powdered form) were added to each sample according to the sample ID. Procedural controls ensured each sample received the same amount of air exposure during preparation. Samples were mixed by adding components to a container, stirring the mixture for a preset amount of time, and then sealing the container. The container was then shaken for a preset amount of time to further stir the mixture. Samples for the bulk and DSC testing were taken from the resultant stock of each sample. Throughout all sample preparation and handling, a timer was used to ensure equal air exposure per sample.

Due to experimental limitations, sample preparation and bulk testing took place in open air, rather than in a glove box environment. Fluoride and chloride salts in particular are very hygroscopic, and therefore it was assumed that moisture uptake would occur during sample preparation and testing, adding an indeterminate amount of impurities to the samples. To account for this impurity, samples were treated as identically as possible during preparation and testing. Procedural limitations on exposure time and mixing allowed a reasonable assumption that the salt samples would have the same exposure time per sample, and therefore a similar amount of moisture uptake per sample. Therefore, the samples produced are comparable, in that the difference between each sample is the addition of corrosion product impurities, which were varied per sample. The implication of this procedure is that the melting points determined in this study are not absolute, and the data gathered in this study is only comparable to literature to a small degree. This is acceptable in this study, because the objective of these experiments is inter-comparison between samples, to evaluate a change in behavior. In addition, moisture uptake in molten salts is more relevant to real-world applications. Large-scale molten salt systems may not have the ability to maintain atmospheric isolation for salts, and atmospheric exposure is a possibility.

3.3 Bulk Testing Methodology

Initially, the melting tests were planned to be done using a customized melting vessel, designed for corrosion resistance in a molten salt environment. Figure 3.1 shows the melting vessel. The vessel was constructed by welding a nickel plate to the bottom of a 3-inch nickel 200 pipe. A stainless steel 316 flange was welded to the top. The vessel was designed to be placed into a 110V Tabletop QuikMelt Top-Loading furnace, shown in Figure 3.2. The furnace operates using electric heating coils, which were connected to a Tempco TPC-1000 temperature control console. A customized insulation ring with an insulation lid was used to extend the insulated length to the top of the vessel, since the

Figure 3.1: Initial melting vessel, constructed from a nickel-200 pipe with a nickel plate welded to the bottom, and a SS-316 flange welded to the top.

furnace itself was not tall enough. The heated length of the vessel, the bottom 6 inches, was sufficient for the salt sample volumes.

Although the melting vessel was effective, after initial pre-experimental tests of the vessel it was decided to forgo its use. This decision was made based on the difficulty of extracting completed salt samples from the vessel. Due to safety concerns, it was not permitted to pour molten salt from the vessel. Therefore, it was necessary to allow salt samples to cool to room temperature before attempting removal. The depth of the vessel made it very difficult to access the salt sample. In addition, as the salt slowly cooled, it tended to crystallize, adhering to the sides and bottom of the vessel, and making removal extremely difficult. Because of this difficulty, an alternative design for a melting vessel was required.

The final apparatus for melting tests is shown in Figures 3.3 and 3.4. Due to the

Figure 3.2: The furnace used for bulk testing

difficulty of extracting solid salt out of containers, this design was created to have an insertable cup, which would be replaceable with an identical cup. The cups had a height of 3.5 inches, a diameter of 2 inches, and were constructed of stainless steel. Twenty of these cups were constructed, which made it possible to test multiple samples in a shorter time period, because solid samples could easily be removed from the furnace. The insertable cups were designed to be shorter, to allow easier removal of the solid salt. Once the salt was removed, the cups could be reused.

The salt samples, with a mass of 50g, were placed in the steel cup, which was placed in a graphite crucible in the furnace. The furnace was then topped with a circular insulating disk, to contain heat from escaping out of the top of the furnace. Two type K thermocouples protruded through the insulation into the salt melt, one type K thermocouple penetrated between the crucible and the heating coils for temperature control, and one type K thermocouple remained outside the furnace for ambient temperature measurements.

Type K thermocouples were used for this testing, which have a temperature range of -200 to 1260 ° C. The thermocouples were calibrated using a Fluke Calibration 9170 Field

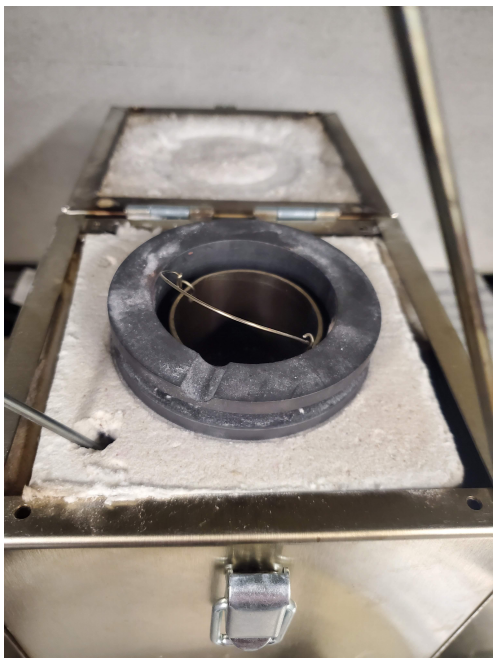

Figure 3.3: The bulk testing apparatus, without insulating lid. The test sample is contained in an insertable steel cup, which rests in the graphite crucible

Figure 3.4: The bulk testing apparatus, with insulating lid and thermocouples.

Metrology Well, which is a dry-well calibrator with a temperature accuracy of approximately 0.01-0.03 ° C.

The melting procedure consisted of raising the temperature of the salt from room

temperature, through the salt's melting range (200-250 ° C for Solar salt, 450-500 ° C for Flinak). The temperature controller was kept at the same prescribed ramp rate (10 °/min) for each test. A 30-minute 'baking' time was included for Flinak tests, to allow time for moisture bake-off. After the temperature passed through the melting range, reaching approximately 50 °C above the expected melting point (determined from literature), the test was complete, and the test was shut down. The shutdown procedure included shutting off the furnace, removing the insulation cover from the furnace, and removing the sample-containing cup from the furnace using tongs. The cup was placed to the side of the furnace on a steel plate to cool. This process effectively quenched the salt, and also allowed the furnace to be quickly cooled, ready to be reused for the next sample.

3.3.1 Bulk Testing Data Evaluation

Data were collected using the aforementioned two type K thermocouples, which were placed in the salt melt during melting. As the temperature of the salt reaches melting, the thermal energy from heating is put into the phase change, rather than the temperature increase of the salt. A plot of salt temperature vs. time reveals a flat region at this point, which can be used to determine the melting point by averaging over the temperature data points in the flat region. Figure 3.5 shows an example of this melting curve.

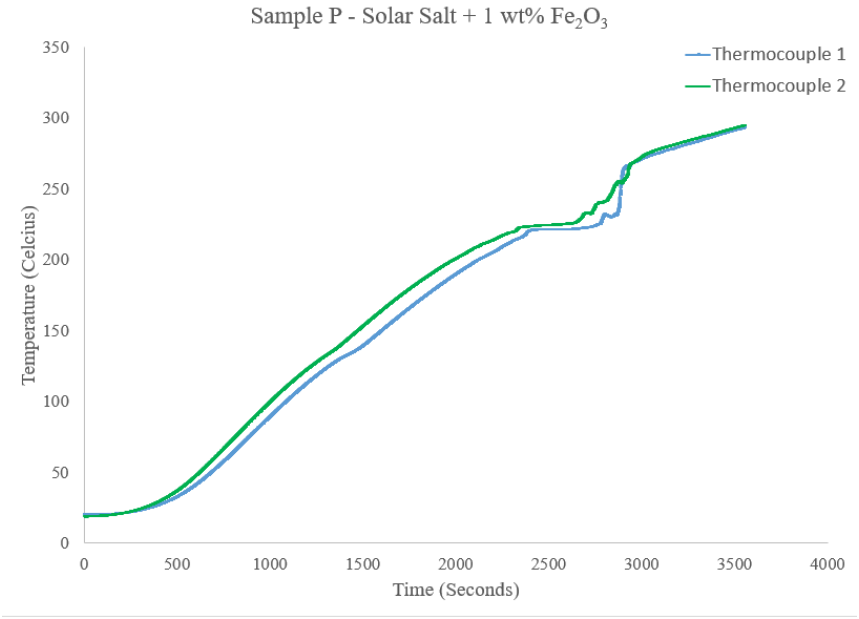

Figure 3.5: A melting curve obtained from one of the bulk melting tests (Solar salt, sample P). Note the flat region at approximately 222 degrees.

Determining the melting point by averaging over the flat region of the plot can yield an estimation of the melting point, within $\pm 5°C$. However, the analysis method has limitations, in that determining what regions are flat requires some level of visual inspection. A more accurate evaluation can be done using the first derivative of the data. A first derivative of the data shows the slope of the data, which approaches zero as the curve flattens. The data can then be narrowed to values of the melting point to which the first derivative is closest to zero. This method relies on numerical determination of melting point,

rather than visual inspection, reducing possible error. Figure 3.6 shows a sample of the first derivative of the temperature vs. time plot. This plot was typical of the general first derivative behavior of all samples. The slope decreases until it reaches zero, representing the gradual leveling of the temperature of the sample.

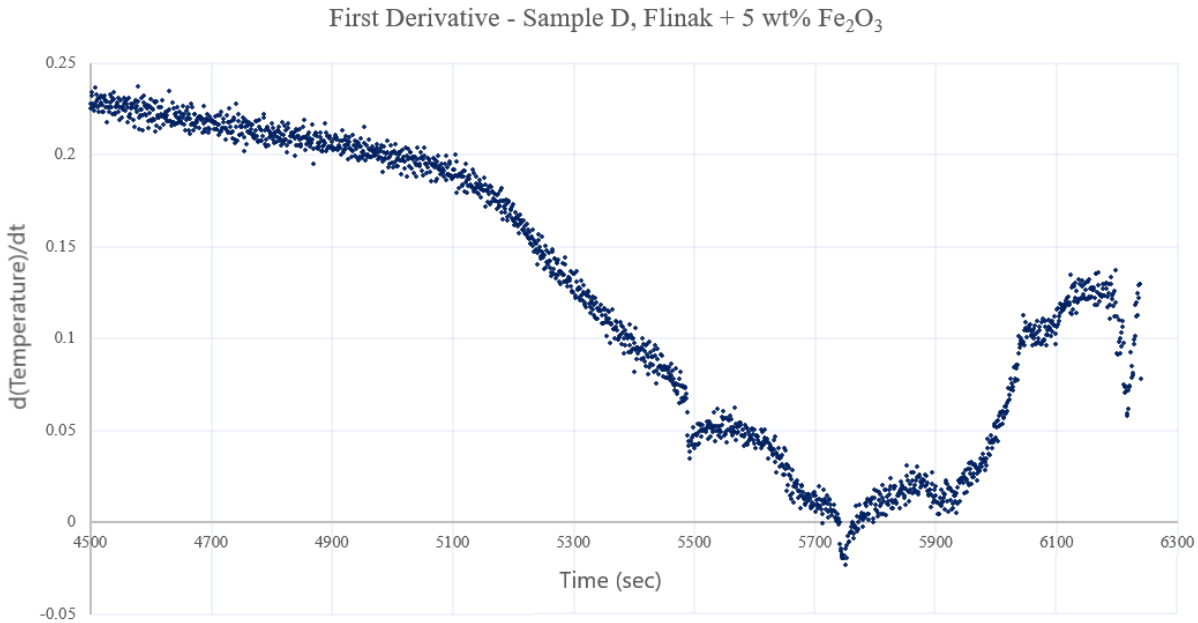

Figure 3.6: The first derivative plot of one of the temperature readings for sample D. Note the gradual decrease of slope until it approaches zero, representing the approach to the melting range.

Each bulk melting test was evaluated using a first derivative procedure. The first derivative of each dataset was evaluated using a central finite difference method. The resultant data was filtered, to identify the data points that were within a threshold of ± 0.05 of zero. An average was taken of the longest consecutive range of values that met this threshold. Since there were two thermocouples measuring the salt temperature during each test, two melting point values were taken for each sample. These two values were averaged to determine an overall melting point for the sample.

An Analysis of Variance (ANOVA) was performed for each set of melting point data. An ANOVA is a statistical analysis that evaluates the differences among means, providing a statistical test of population means (given some treatment), determining whether or not

they are equal. An ANOVA of a group of data will determine if the data points have a statistically significant variation. Significant metrics from an ANOVA are the F statistic (or F-ratio), and the p-value. The F-ratio is the result of the test of the null hypothesis that all of the treatment means are the same. When this null hypothesis is true, the F-ratio will have a value close to 1 [54]. The p-value is a metric which can help evaluate the significance of the F-ratio. The p-value is the probability of observing an F-ratio as large or larger than the one that was observed. Small p-values are indicative that the null hypothesis may be incorrect. Traditionally, p-values less than 0.05 are considered 'statistically significant', and p-values less than 0.01 are considered 'highly statistically significant' [54].

In the case of the ANOVA performed on the bulk melting point test data, the null hypothesis is that there is no variation between melting points with the treatment of impurity variation. A p-value of approximately less than the threshold of $p = 0.05$ would indicate statistical significance, and the null hypothesis would be rejected, indicating a variation of melting temperature with impurity concentration.

3.4 Differential Scanning Calorimeter Fundamentals

Calorimetry is a branch of scientific characterization which measures heat. The exchange of heat relates to many types of processes, including melting, freezing, chemical reactions, and many others. When heat is exchanged, caloric measurements can be used to investigate the process. Differential Scanning Calorimetry (DSC) is a process or machine which uses caloric measurements to evaluate heat flow difference using a temperature-controlled program, and a differential method of measurement [55]. Two types of DSC exist, a heat flux DSC and a power compensation DSC. The type used for this study is a heat flux DSC, and will be described here.

A heat flux DSC uses a defined exchange of heat to be measured in a well-defined heat conduction path with a set thermal resistance [55]. A signal is generated by a temperature

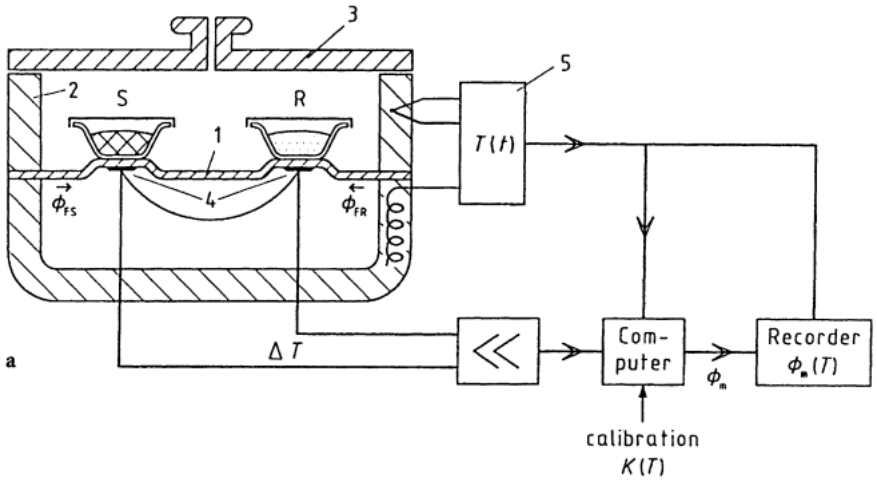

Figure 3.7: A heat-flux DSC with a disk-type measurement system, from [55]. Labeled parts are as follows: 1- Disk, 2- Furnace, 3- Lid, 4- Differential Thermocouples, 5- Programmer and Controller, S- Sample substance in crucible, R- Reference, $\theta_F S$- Heat flow rate from furnace to sample, $\theta_F R$- Heat flow rate from furnace to reference, θ_m - Measured heat flow rate, K- Calibration factor.

difference; the intensity of the heat flow and the heat flow rate are proportional to that difference [55]. Several measuring types exist for heat flux DSC's; the type used in this study was a disk-type measuring system. A schematic of a disk-type DSC is shown in figure 3.7. In this type of DSC, the main heat flow from the furnace to the samples passes symmetrically through a disk of medium thermal conductivity [55]. A reference (typically an empty crucible identical to the sample crucible, or a known reference substance) and an experimental sample are positioned on the disk symmetrically. When the furnace is heated, heat flows through the disk, equally heating the sample and reference. The temperature difference between the samples is zero, unless disturbed by a sample transition, such as melting or crystallization.

3.4.1 Interpretation of DSC Curves

A DSC generates data in the form of a signal, which is generated when there is a difference between the sample and reference. When the signal difference between the reference and sample consumes heat, a signal peak can be observed. Melting behavior of a substance will

generate an endothermic peak. An example of a basic dsc peak, in this case an exothermic peak, is shown in figure 3.8 [55]. In this figure, ΔT represents the measured signal, R the thermal resistance between furnace and sample, β the heating rate, ΔC the difference between the heat capacities of the reference and sample, 1 the peak area (exothermic), and 2 the area below the baseline. The baseline is a measure of the heat required to heat the sample between t_1 and t_2.

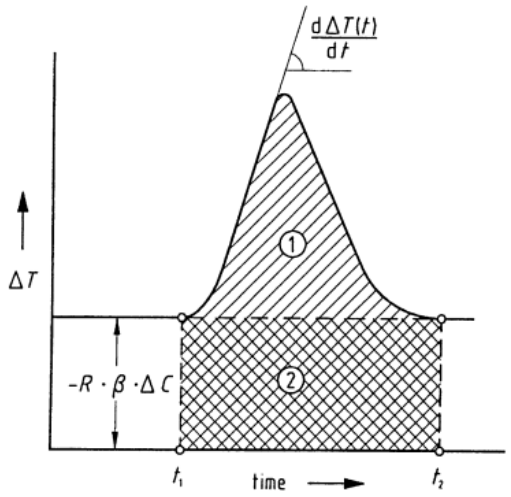

Figure 3.8: A sketch of a measured curve of a heat flux DSC [55] with an exothermic peak, indicating heat is released inside the sample.

A sample DSC curve from this study is shown in figure 3.9. This figure is evaluating Flinak salt with 1 wt% Fe_2O_3. Exothermic and endothermic peaks both appear in this plot. The direction of exothermic peaks is indicated in the top left portion of the plot; in this case exothermic peaks are oriented downwards. In this plot, peaks pointing upward represent points where melting phase transitions occurred, and peaks oriented downwards represent points where crystallization occurred. Melting is considered complete after the final endothermic peak has occurred; in figure 3.9 this takes place at approximately 665-668 ^{c}irc C.

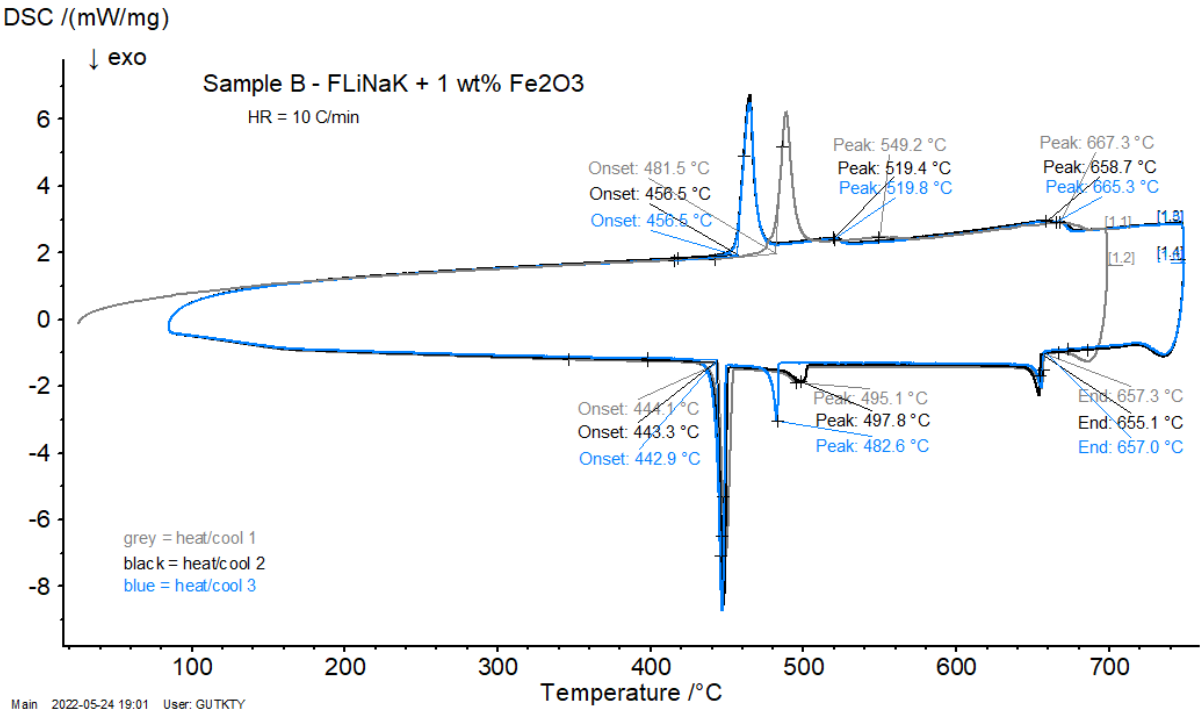

Figure 3.9: DSC curve for sample B from this study

3.5 DSC Test Methodology

After completion of bulk testing, some select samples were evaluated using a DSC. The purpose of the additional testing was to obtain more accurate results for previously tested samples, for comparison to the bulk testing. Since the bulk testing methodology has some limitations (open-air testing, limited temperature range), DSC testing will allow for a wider picture of the salt behavior with impurity additions.

Six samples were evaluated for the DSC test phase. The samples are shown in Table 3.4. The samples were chosen to evaluate three sample concentrations from each of the Flinak sample sets.

Two samples, sample A and sample AA, were both selected for DSC evaluation, although they are both essentially the same composition (no added impurities). Sample A was initially tested with a lower heating range, and behavior was observed which indicated a larger temperature evaluation range was required. The remaining samples were

Flinak Sample	Impurity	wt% Impurity
A	None	0
B	Fe_2O_3	1
D	Fe_2O_3	5
AA	None	0
BB	FeF_3	1
DD	FeF_3	5

Table 3.4: Samples selected for DSC evaluation

tested in a larger temperature range, but because sample A was not tested with this larger temperature range, more data was required for a sample with no added impurities.

The DSC parameters held constant for all samples are listed in Table 3.5. Several parameters varied from sample to sample, including sample size range (approximately 4-7 mg), and sample temperature range. As stated, the initial sample temperature range was determined to not be large enough to capture sample behavior, and thus the temperature range was increased for the remainder of the samples. The temperature ranges for each sample are shown in Table 3.6.

Parameter	Setting
Crucible Material	Glassy Carbon (Netzsch)
Purge and Protective Gas	Argon
Purge and Protective Gas Flow Rate	50 ml/min
Furnace Atmosphere	Argon
Furnace Material	High Temperature Rh (0 to 1650 ° C)
Sample Carrier Material	DSC Cp
Thermocouple Type	Type S
Calibration	Temperature, Sensitivity
Heating/Cooling Rate	10 ° C/min

Table 3.5: DSC Parameters

The reference and sample crucibles were placed on the sample carrier on the DSC furnace, having a temperature range of from room temperature to 1650 ° C. Argon gas was purged through the furnace during experiments. The sample and reference crucibles were subjected to the desired temperature program, and data acquired and saved on the instrument computer. Data acquired includes information about the reference, sample cru-

Sample	Cycle 1	Cycles 2 and 3
A	22-700 °	150-520°
B	22-750°	50-750°
D	22-750°	50-750°
AA	30-775°	25-775°
BB	45-750°	50-750°
DD	25-775°	50-775°

Table 3.6: Temperature ranges used for each sample during DSC testing

cible weights, sample weight, argon purge flow rate, protective gas flow rate, calibrations, heating rates, and temperature ranges.

3.5.1 DSC Calibration

Two types of calibration were performed for this work: temperature, and sensitivity. A temperature calibration determines the accuracy of the DSC temperature measurements, and a sensitivity calibration ensures the accuracy of quantitative evaluation of DSC peak areas (i.e. enthalpy). These calibrations require standard materials of high purity, with known transformation temperatures. Calibrations were run using these high purity materials, under identical test conditions.

A calibration must be run using no less than three standards, and must encompass the temperature range in which the experimental samples will be analyzed. The calibrations must also be run using the same set of conditions as the experimental samples, including purge flow rate, sample size, crucible material, and heating rate. Temperature and sensitivity calibrations were run using a set of six, high purity metal standards, at a heating rate of 10 °/min.

Each standard was subject to four heating/cooling cycles. A representative calibration curve for indium with a 10 °C/min heating rate is shown in Figure 3.10. There is only one peak, because indium has only one phase transition, solid to liquid. The average of the onset temperatures for the latter three cycles was used for the onset temperature of the calibration file. Table 3.7 shows the average onset transition temperature values for the

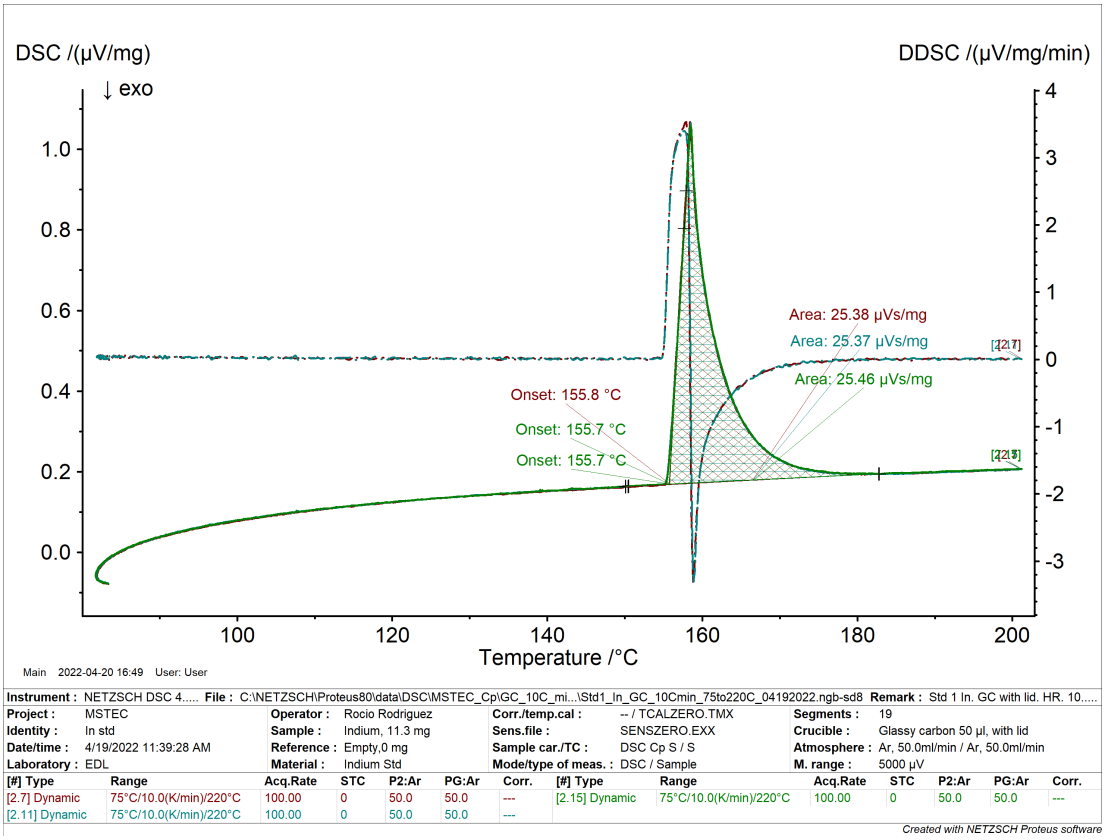

Figure 3.10: DSC curve for Indium standard, with first derivative.

six standards used in this calibration. Table 3.7 also shows the peak area values for each standard, used in the sensitivity calibration.

Standard	Literature Transition Temperature (° C)	Average Onset Transition Temperature (° C)	Peak Area (μVs/mg)
Indium	156.6	155.73	25.403
Bismuth	271	270.8	41.85
Zinc	419.5	418.53	61.32
Aluminum	660.3	659.35	150.05
Silver	961.8	959.7	26.033
Gold	1064.2	1061.27	11.947

Table 3.7: Standard literature transition temperature values, calibration transition temperature values, and sensitivity calibration peak areas.

Using the average values in Table 3.7, temperature and sensitivity calibration curves were constructed for the 10 °C heating rate. These curves can be seen in Figures 3.11 and

3.12. The sensitivity of the system is defined as the ratio between the change of the measurement and the change of the measured quantity, or heat flow rate. Sensitivity changes with temperature, and is automatically applied within the DSC software. A calibration curve, constructed from the calibration data, determines the temperature-dependant proportionality factor between peak area and enthalpy, and is automatically applied to the data by the DSC software, using uploaded calibration files. The sensitivity calibration curve shown in Figure 3.12 indicates that as temperature increases, the sensitivity of the instrument decreases. The sensitivity calibration curve was loaded into the software to correct for the decreased sensitivity at higher temperatures.

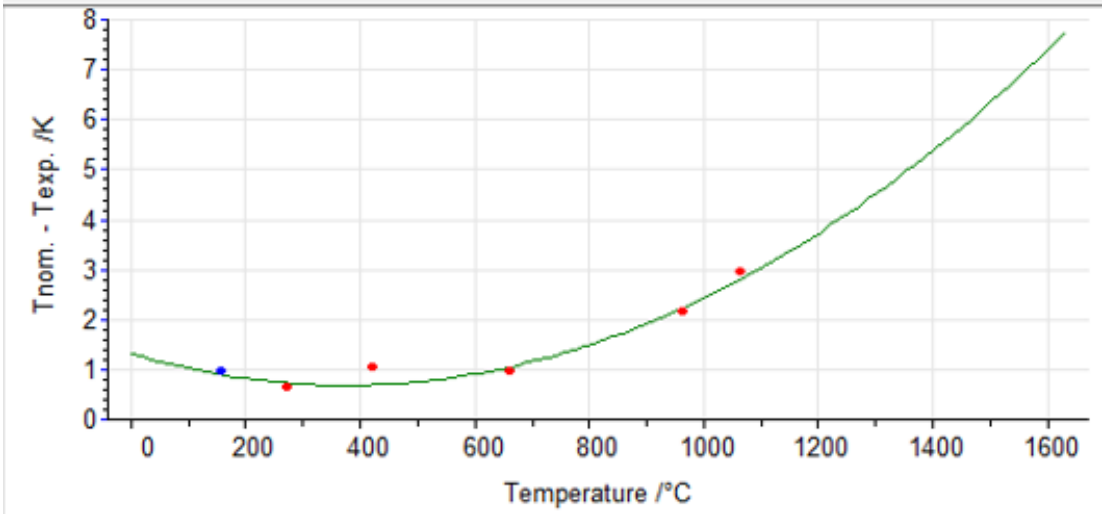

Figure 3.11: Temperature calibration curve for the DSC, at 10 ° C/min.

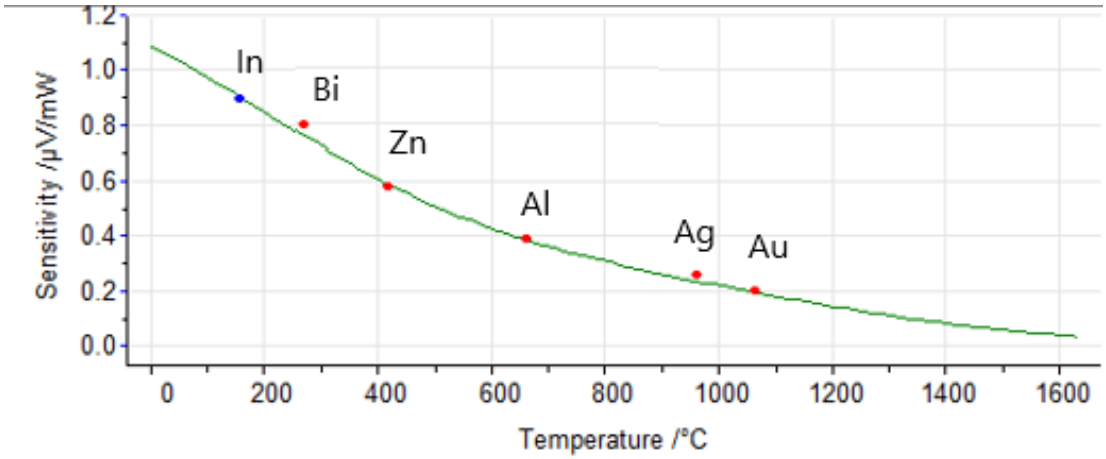

Figure 3.12: Sensitivity calibration curve for the DSC, at 10 ° C/min.

CHAPTER 4

Experimentation Results

Two phases of testing were completed for this study: bulk testing, and DSC testing. In this chapter, the results from each phase will be presented separately, and then compared.

4.1 Results of Bulk Testing

The bulk testing consisted of three test sets, wherein samples were heated through a melting range, and temperature data were taken as a function of time. The resultant temperature curve was used to determine a melting temperature. As outlined in chapter 3, the three test sets consisted of the following:

- Solar salt with varied Fe_2O_3 impurities
- Flinak salt with varied Fe_2O_3 impurities
- Flinak salt with varied FeF_3 impurities

Data were gathered in the form of temperature curves, which will be presented in the following sections for each test set. In addition to the temperature curves, completed samples were extracted from sample containers, and cracked in half. Pictures of the cracked samples will show the profile of the salt samples after they have melted and solidified.

Uncertainty analyses were conducted for each set of data, including standard deviation from averages, and system-induced uncertainty. Uncertainty from the system was in the form of thermocouple measurement uncertainty, and the temperature controller accuracy. This uncertainty can be seen in figure 4.1, which shows error for every 100th data point of the sample P dataset. Sample P was from the Solar Salt tests, and contained 1 wt% Fe_2O_3. The full dataset for sample P was shown previously, in figure 3.5. When averages

were calculated for each sample metling point value, this system-induced uncertainty was included along with standard deviation values.

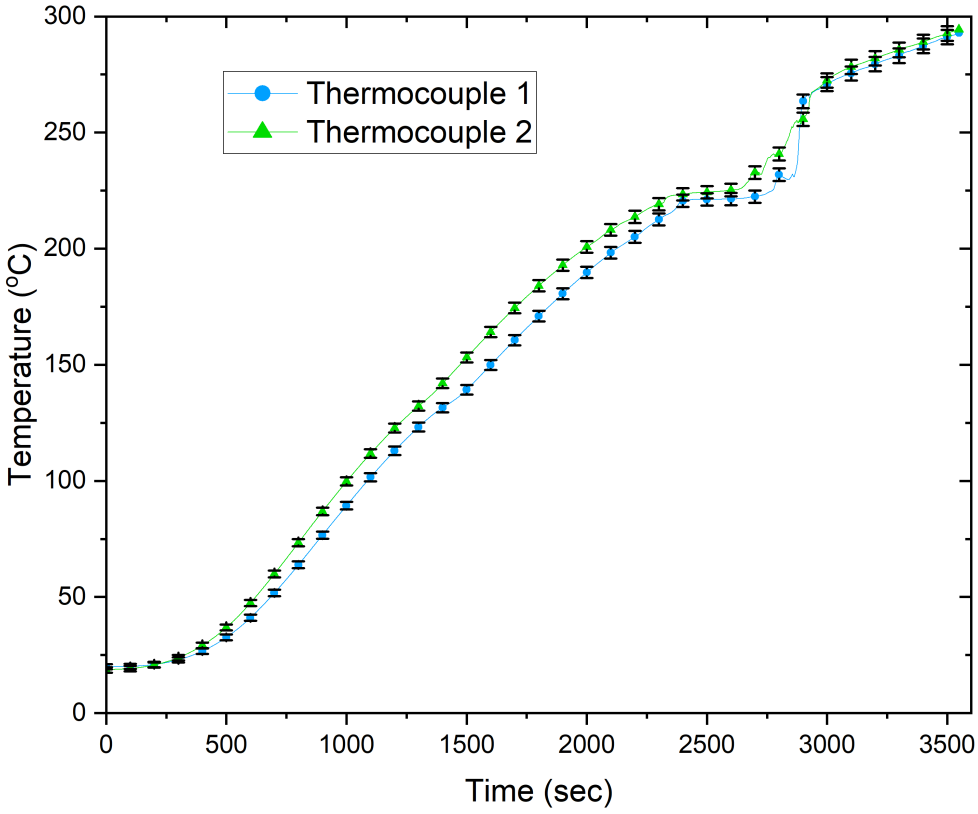

Figure 4.1: Error bars showing the system-induced uncertainty in temperature measurements

4.1.1 Solar salt

Prior to evaluation of the Solar salt sample set, an equipment test was conducted, using $NaNO_3$ as a surrogate. This equipment test was performed to evaluate the reliability of the furnace, camera, and measurement system. As the sodium nitrate was melted, pictures were taken at random intervals, beginning at 20 degrees before the expected melting temperature, and ending approximately 15 degrees after melting. The pictures show the progression of the phase change from solid to liquid, and are shown in Figure 4.2.

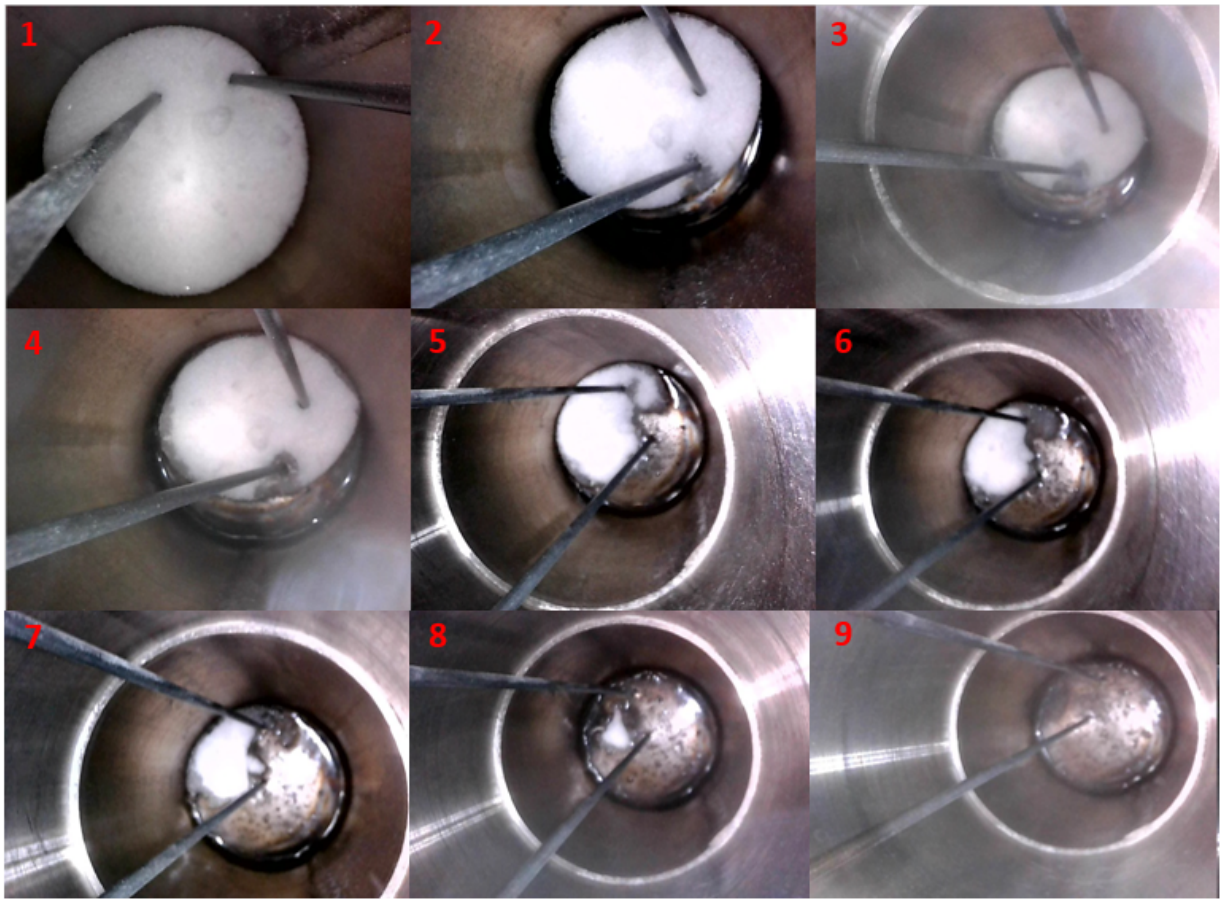

Figure 4.2: Progression of melting during an equipment test using sodium nitrate. Frames are labeled in order of capture.

During the actual Solar salt testing phase, additional picture series were taken in similar fashion to the equipment test - pictures taken at random intervals for the temperature range surrounding the expected melting range. Due to the repetitive nature of the tests combined with camera limitations, only two samples were chosen for picture series capture; samples R and P (R contained 5 wt% Fe_2O_3, and P contained 1 wt% Fe_2O_3). Select pictures from these series can be seen in Figures 4.3 and 4.4. It was observed during testing that the appearance of the melted samples was not of a pure liquid, as compared to frame 9 of Figure 4.2. Rather, the samples tended to form a heterogeneous suspension of solid and liquid material, as can be seen in the final frames of Figures 4.3 and 4.4. This would indicate that the mixture was not entirely melted, although the temperature curve for the sample passes through a melting region of the sample.

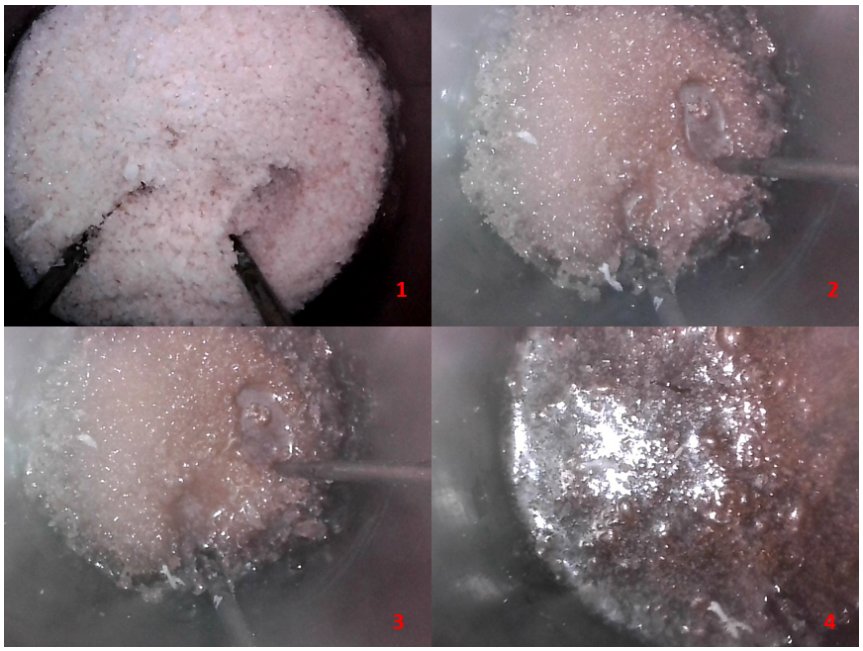

Figure 4.3: Progression of melting during Solar salt test P, which contained 1 wt% Fe_2O_3. Frames are labeled in order of capture.

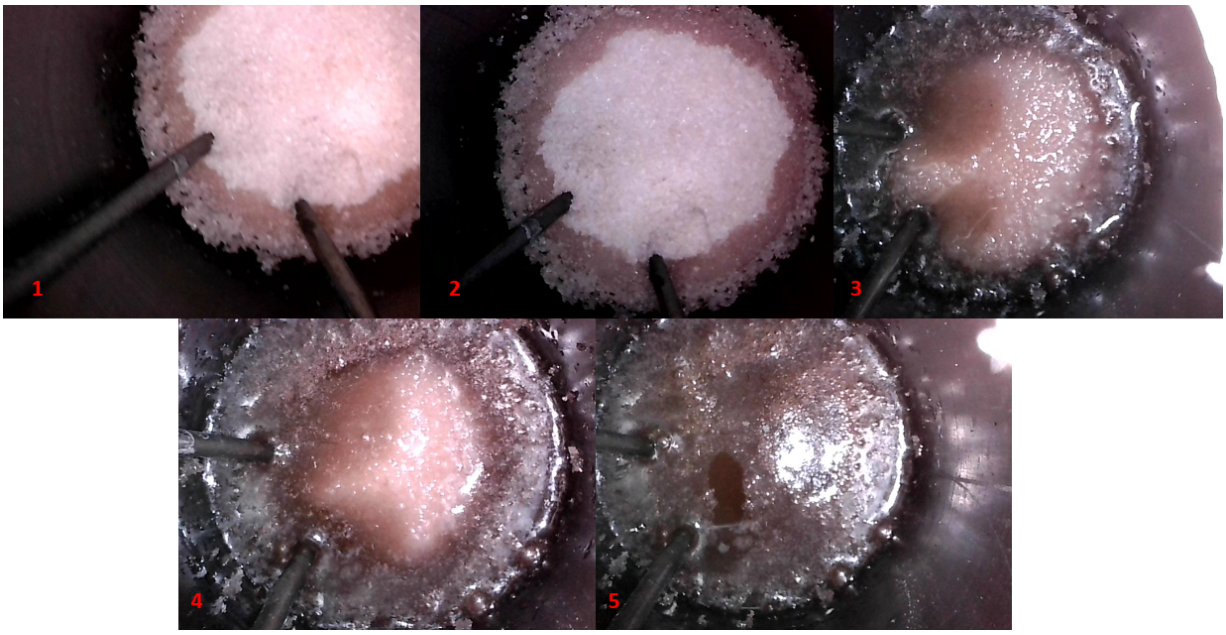

Figure 4.4: Progression of melting during Solar salt test R, which contained 5 wt% Fe_2O_3. Frames are labeled in order of capture.

The results for the Solar set of bulk testing can be seen in Table 4.1, which are displayed in sample alphabetical order. The table displays the individual temperatures captured by each thermocouple, and the average melting temperature of the sample. Two data points are missing, for samples Q and Y. This is due to a thermocouple failure during the last samples. After Solar salt testing was complete, the thermocouple was replaced.

Sample	Fe_2O_3 wt%	TC1 (°C)	TC2 (°C)	Avg T (°C)
I	0	220.1	219.0	219.6
J	0.5	219.8	224.3	221.8
K	1	220.0	221.3	220.6
L	2	220.1	218.3	219.2
M	5	217.8	220.7	219.2
N	0	224.5	224.1	224.3
O	0.5	220.7	219.7	220.2
P	1	221.1	224.3	222.7
Q	2	-	221.5	221.5
R	5	225.0	225.6	225.3
X	3.5	225.4	225.8	225.6
Y	3.5	-	220.0	220.02

Table 4.1: Results of Solar salt melting point testing

The results from the Solar salt tests can also be seen in Figure 4.5. An uncertainty analysis was performed on the data, including standard deviation and system-induced uncertainty. This uncertainty can be seen in the scatter plots, in the form of error bars.

Upon initial observation of the data, both in tabulated form, and within the scatter plots, it seems as if there is insignificant variation in melting temperature with impurity concentration. This is further confirmed by the statistical analysis of the data, in the form of an ANOVA. A one-way ANOVA revealed that there was no statistically significant difference between mean melting point values with different impurity concentrations, both for the individual thermocouple results, and the average values. This implies there is no significant effect on the melting point from Fe_2O_3 concentration. The values for F and p can be seen in table 4.2.

Data set	Degrees of Freedom	F	p
TC1 and TC2	(5,16)	0.4967	0.7742
Average	(5,6)	0.1805	0.96

Table 4.2: Values for the degrees of freedom (between groups, within groups), F statistic, and p-value for a one-way ANOVA for the Solar salt bulk testing.

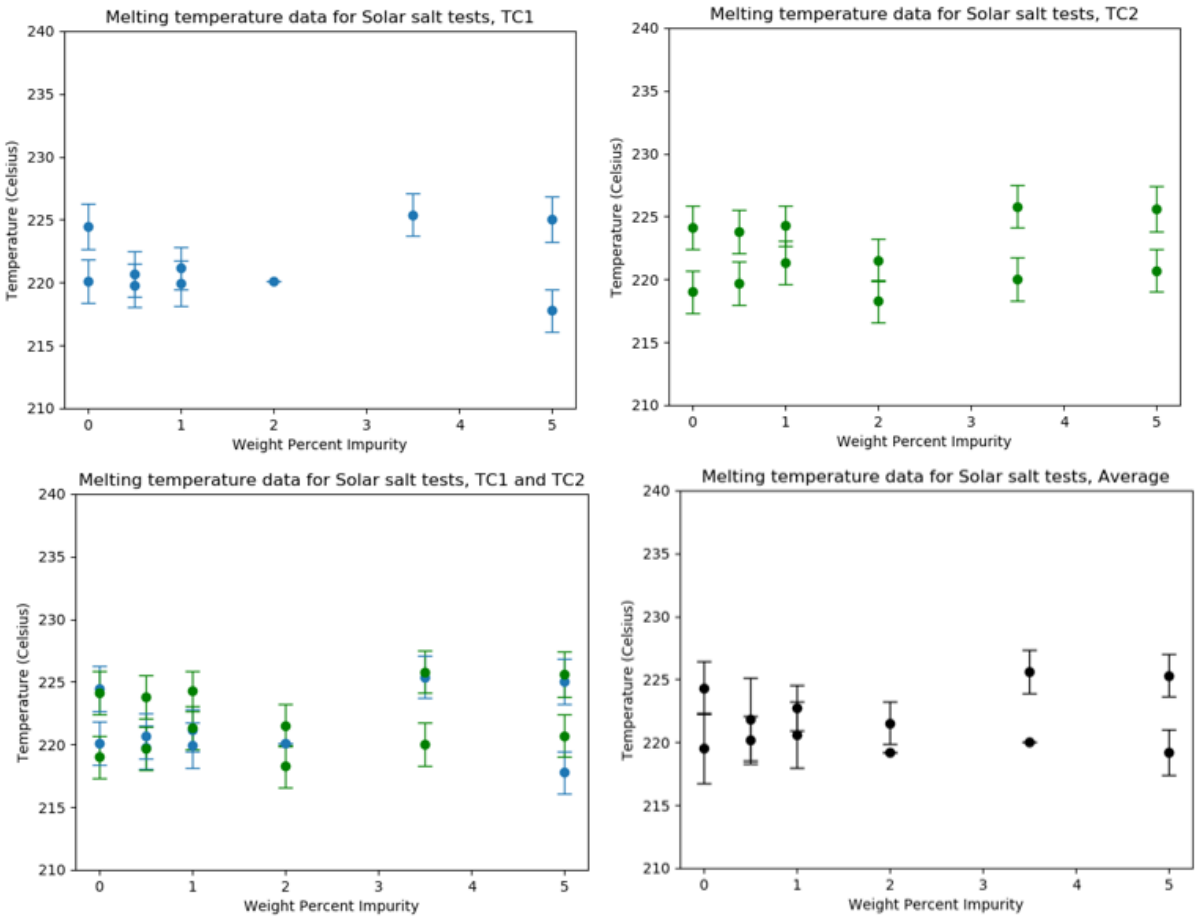

Figure 4.5: Scatter plots of Solar salt results

4.1.2 Flinak and Iron Oxide

Flinak, or LiF-KF-NaF, melts at significantly higher temperatures than Solar salts. Unfortunately, the camera used to capture melting progressions did not have substantial capability to withstand these high temperatures except for very short periods of time. Only one series of pictures was captured for the Flinak sample sets, for sample C (2 wt%

iron oxide), and can be seen in figure 4.6. Similar to what was observed in the Solar salt testing, the final melted state (at approximately 500 °C) did not appear to be uniformly liquid. Rather, as can be seen in frame 7 of figure 4.6, the appearance of the melted sample was of a suspension, with small unmelted solids in the salt mixture. As in the Solar salt testing, this indicates that the sample is not entirely molten. Due to experimental limitations, it was not possible to heat the sample beyond 500 ° C, therefore a final liquid state was not achieved.

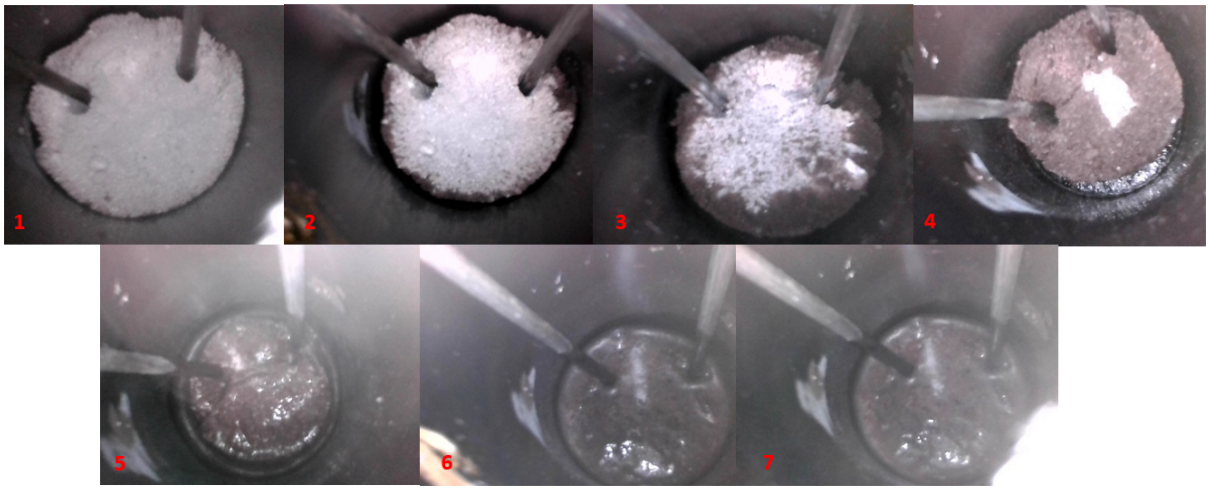

Figure 4.6: Progression of melting during Flinak set 1 salt test C, which contained 2 wt% Fe_2O_3. Frames are labeled in order of capture.

The results for the Fe_2O_3 set of Flinak bulk testing can be seen in Table 4.3, which are displayed in sample alphabetical order. The table displays the individual temperatures captured by each thermocouple, and the average melting temperature of the sample. An uncertainty analysis was performed on the data, including standard deviation and system-induced uncertainty, and is displayed with the data in the form of error bars, in Figure 4.7.

The scatter plots of the iron oxide Flinak bulk results show no obvious trend dependent on impurity concentration. A one-way ANOVA performed on the results also displays no statistically significant correlation between impurity concentration and melt temperature. The results of the ANOVA can be seen in table 4.4, which show p-values above the

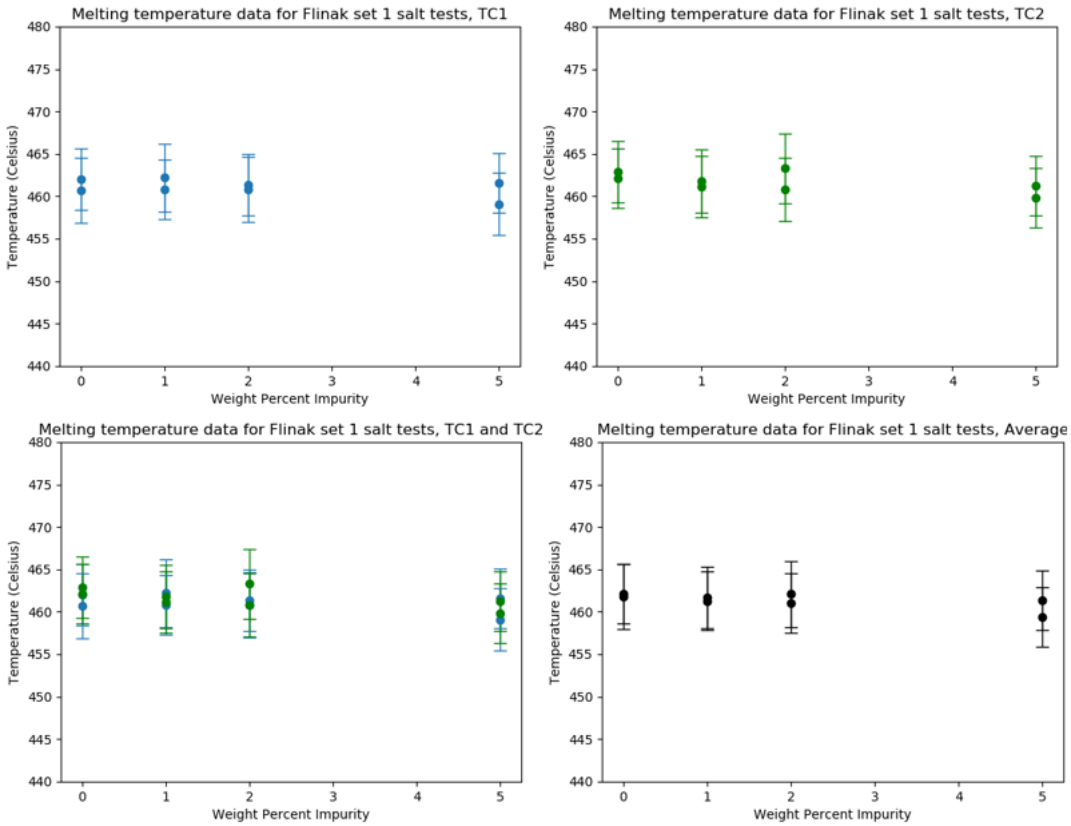

Figure 4.7: Scatter plots of the Flinak-Fe_2O_3 bulk test results

Table 4.3: Results of Flinak Set 1 melting point testing - Fe_2O_3 impurities

Sample	Fe_2O_3 wt%	T1 (C)	T2 (C)	Avg T (C)
A	0	460.7	462.9	461.8
B	1	460.8	461.8	461.3
C	2	460.8	463.3	462.1
D	5	459.1	459.8	459.5
E	0	462.0	462.1	462.1
F	1	462.2	461.1	461.7
G	2	461.3	460.8	461.0
H	5	461.6	461.3	461.4

traditional threshold of $p = 0.05$

4.1.3 Flinak and Iron Fluoride

The results for the FeF_3 set of Flinak bulk testing can be seen in table 4.5, which are displayed in sample alphabetical order. The table displays the individual temperatures

Data set	Degrees of Freedom	F	p
TC1 and TC2	(3,12)	1.5618	0.25
Average	(3,4)	1.2959	0.39

Table 4.4: Values for the degrees of freedom (between groups, within groups), F statistic, and p-value for a one-way ANOVA for the Flinak-Fe_2O_3 salt bulk testing.

captured by each thermocouple, and the average melting temperature of the sample. Two samples, sample BB, and sample HH, were neglected from the statistical analysis due to experimental error. The temperature curves for those data samples did not have a clear distinguishable melt region. Although the central finite difference method described in chapter 3 yielded values, the points are not reliable as melt temperature values. It is unknown why these readings failed, although a possible explanation is that the salt matrix contained air pockets, or regions of unmelted suspension, which caused too much variation of temperature on the thermocouple to capture a reliable reading.

Table 4.5: Results of Flinak-FeF_3 bulk testing

Sample	FeF_3 wt%	T1 (C)	T2 (C)	Avg T (C)
AA	0	470.54	461.65	466.1
BB	1	483.02	524.8	503.91
CC	2	465.64	469.97	467.8
DD	5	465.56	473.8	469.7
EE	0	461.43	462.8	462.1
FF	1	466.74	468.6	467.67
GG	2	463.8	464.63	464.22
HH	5	474.37	-	474.37

A scatter plot of the data can be seen in Figure 4.8, which includes error bars derived from an uncertainty analysis, just as in the previous two sample sets. Because of the smaller sample size in this set due to the neglected data points, the error for these samples was slightly larger, since a decrease in sample size increases the value of the standard deviation.

Similar to the first two sample sets, the scatter plots show no apparent deviation in melt temperature due to impurity concentration. This is confirmed by a one-way ANOVA,

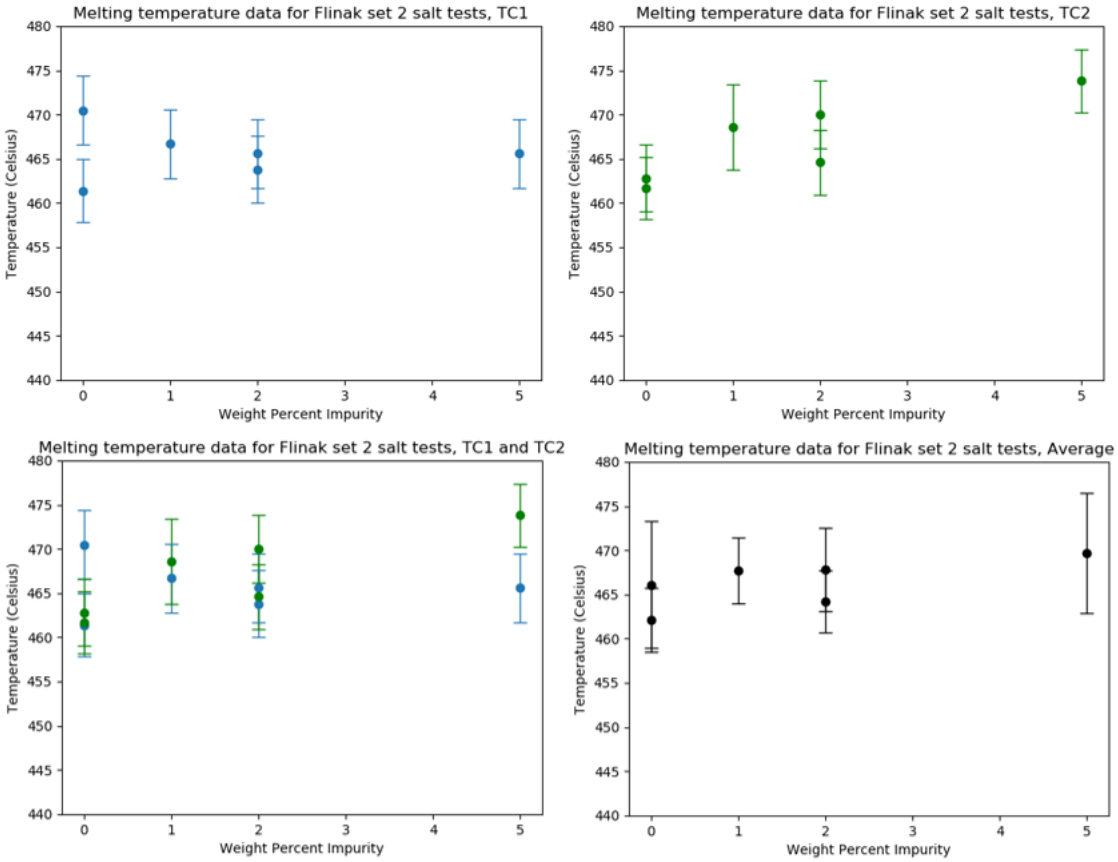

Figure 4.8: Scatter plots of Flinak-FeF_3 bulk test results.

performed on the results. The results of the analysis are shown in table 4.6, which shows the values for the F-statistic and the p-value for the data. The p-values for this sample set were above the traditional threshold of $p = 0.05$, indicating no statistically significant correlation of means.

Data set	Degrees of Freedom	F	p
TC1 and TC2	(3,8)	0.7787	0.538
Average	(5,6)	1.076	0.515

Table 4.6: Values for the degrees of freedom (between groups, within groups), F statistic, and p-value for a one-way ANOVA for the Flinak-FeF_3 bulk testing.

4.1.4 Post-melt sample evaluation

When bulk testing was completed, samples were extracted from containers for disposal. Extraction was accomplished by heating the outside of the sample can with a torch, allowing the bulk sample to loosen and be removed from the can. The extracted samples were broken in half, and photos of each were taken. The center of each bulk sample was unmelted from the extraction process, and therefore the pictures of the extracted samples are a glimpse of what the bulk sample looks like upon cooling after the test was completed. Because of the extraction process, the edges of the samples where the salt contacted the container became blackened or discolored. Therefore when observing color variations in the pictured samples, discoloration along edges should be disregarded.

Figure 4.9 shows extracted samples A, and AA. Sample A was part of the Flinak-Iron Oxide sample set, and sample AA was part of the Flinak-Iron Fluoride sample set. Both samples did not have any added impurities, and thus are included in the same figure. Observation of the cut sample shows that there is no discernable visible variation in color throughout. The sample is white in appearance, and appears fairly homogeneous. There are small holes, which indicate the presence of air pockets. These air pockets could have arisen during any phase of the testing, and therefore don't necessarily indicate anything significant, other than the presence of gaseous elements during some phase of the experiment, or density changes during cooling. It is possible that these air pockets were formed due to the oxygen impurities that would have come from air exposure. However, it is impossible to determine this without further experimental characterization, and no further speculation will be made on the air pockets.

Figure 4.10 shows sample C, which contained Flinak and 2 wt% Fe_2O_3. The photo compilation shows the sample before and after cracking. Initial observation of the sample shows some color variation throughout the sample. It appears that the sample is not homogeneous, with various spots of white or red appearing throughout the sample. The

Figure 4.9: Pictures of extracted samples A and AA. The top right photo is sample AA, and the remaining photos are sample A. These samples were both pure Flinak, with no added corrosion products.

red color within the sample comes from the iron oxide, which when pure is dark red. A closer view of the color variations in sample C is displayed in Figure 4.11, which also shows the figure with red markings, outlining areas of color variations.

Figure 4.12 shows sample DD, which contained Flinak with 5 wt% FeF_3. Figure 4.13 shows a closer view of sample DD, with markings identifying areas of color variation. Similar to sample C, sample DD also shows a lot of color variation, indicating the sample was not homogeneous on cooling. It can be assumed that different phases formed in the salt, and the mixture was not homogeneous, with FeF_3 rich phases.

It should also be noted that there is a distinct red color that can be observed in sample DD. The iron fluoride additive was originally white-green in color, before sample preparation and experimentation. There was no possible accidental addition of iron oxide during sample preparation. It is plausible that the iron fluoride, during melting and cooling, reacted with oxides present in the melt or with air, to form iron oxide compounds, which may explain the red color. Although what products are forming cannot be determined for certain without experimental characterization, it can be concluded that chemical reactions are occurring during melting which result in impurities not initially present in the mixture.

Figure 4.10: Pictures of extracted sample C, Flinak + 2 wt% Fe_2O_3. Note the variation of color, indicating there were different phases present.

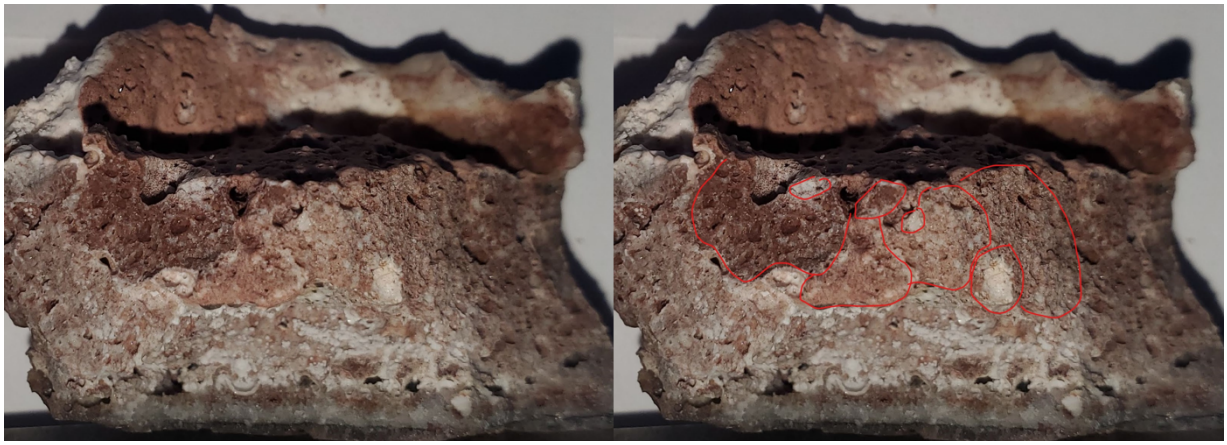

Figure 4.11: A larger view of the color variations within sample C. On the right is a duplicate picture, with markings identifying different zones of color.

Thermodynamic analysis of possible reactions that could result in iron oxide components shows that several reactions are viable. Figure X shows the results of a Gibbs energy

calculation using HSC Chemistry [56]. A more negative Gibbs energy indicates that the reaction can occur spontaneously. Several proposed reactions have a negative Gibbs energy, particularly at high temperature. Therefore, it is plausible that the pink/red color variation in the Flinak + FeF_3 sample comes from iron oxide, formed by FeF_3 reacting with oxygen or moisture impurities.

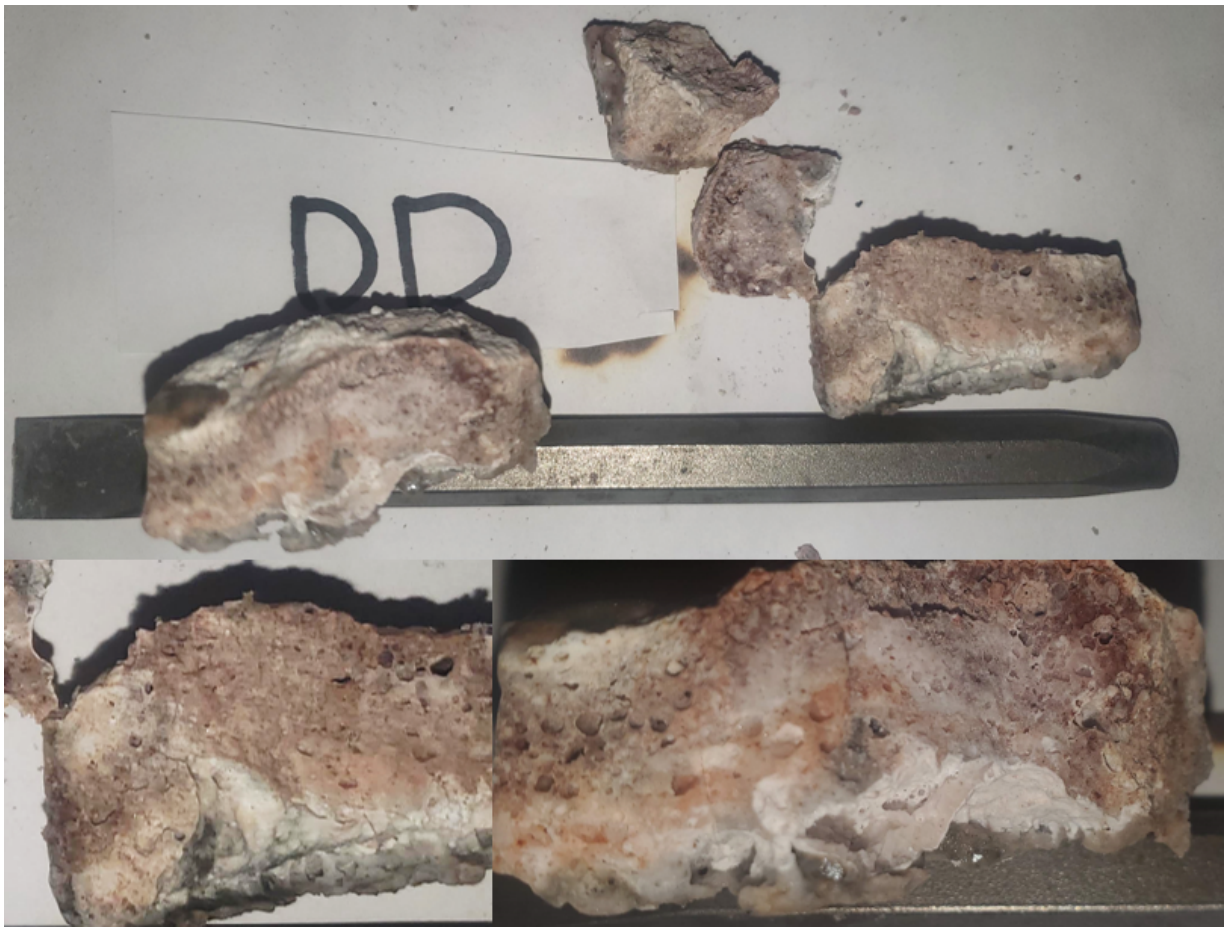

Figure 4.12: Pictures of sample DD, Flinak + 5 wt% FeF_3. Note the presence of red color variations.

In this work, only pictures for the cooled and cracked samples C and DD are displayed. Pictures were taken of each sample after it was extracted from the sample container. The same type of color variation seen in samples C and DD are observed in each sample with an added impurity. The same lack of homogeneity was not observed as clearly in samples with no added impurity.

Figure 4.13: A larger view of the color variations within sample DD. The lower pictures are duplicates, with markings identifying different zones of color.

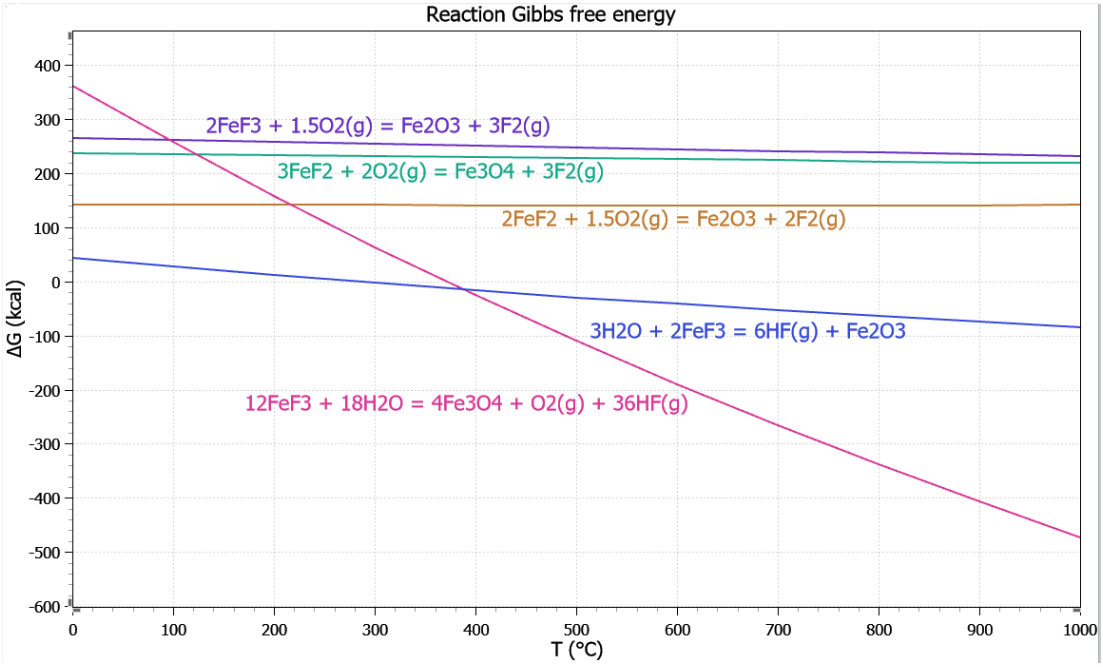

Figure 4.14: A diagram of Gibbs energy for several proposed reactions which form iron oxide in the Flinak melt.

4.2 Results of DSC Testing

As described in chapter 3, the DSC test set consisted of six samples, three from each of the Flinak sample sets used in the bulk testing phase. DSC curves were generated for each sample, and all six DSC curves can be found in appendix 7.

A detailed summary of the interpretation of DSC curves can be found in Section 3.4. Each DSC test consisted of three heat/cool cycles. Upon loading into the apparatus, the samples were in a powdered form, and therefore the first heat/cool cycle melts the powder into a more homogenized mixture. Because of this, only the second and third cycles are considered for accurate temperature values. The first cycle is considered a pre-melting cycle, and behavior different from standard is expected during this initial cycle.

It was expected that the results would provide a eutectic melting temperature, which would remain constant throughout the samples. This is considered standard behavior, the eutectic temperature of samples does not change. This eutectic peak shows the onset of melting, and the melting of the sample is not complete until the final peak on the DSC curve. Thus, the eutectic peak and the final peak show the temperature range over which melting occurs.

One of the samples (Sample A) was tested at a smaller temperature range than the rest of the samples. Sample A was initially tested with a smaller heating range, and behavior was observed which indicated a larger temperature evaluation range was required. As a result, the DSC curve for sample A is not comparable to the rest of the curves. Since sample AA has the same composition (Flinak with no added impurities), sample AA was used in place of sample A for the Fe_2O_3 sample set, providing the 'pure' comparison for the other samples with added impurities.

The DSC curve for sample AA can be seen in Figure 4.15. The onset temperatures indicate a eutectic melting temperature of approximately 456-459 ° C. An additional disturbance within the onset peak indicates a possible impurity in the salt mixture. Also

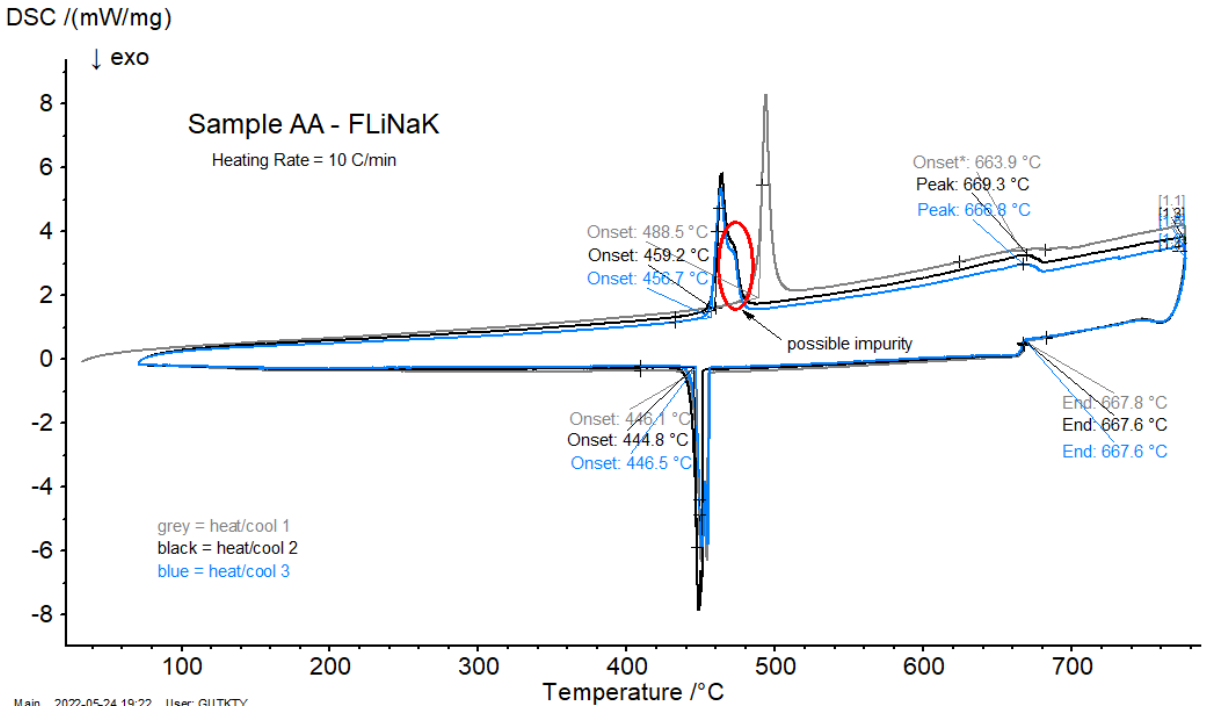

Figure 4.15: DSC curve for sample AA, Flinak with no added impurities

indicated in the DSC curve is a final melting peak at approximately 669 ° C. No other disturbances or peaks were observed between the eutectic onset and the end peak.

The DSC curve for sample D can be seen in Figure 4.16. Sample D contained Flinak, and 5 wt% added Iron Oxide. The onset temperatures indicate a eutectic melting temperature of approximately 455 ° C. Additional disturbances were observed between the onset and the final peaks, particularly on the cooling portion of the heat/cool cycles. The curve also indicated a final melting peak at approximately 661 ° C. Similar behavior was observed in the DSC curve for sample B, the other sample which contained Fe_2O_3 impurities.

The DSC curve for sample BB can be seen in figure 4.16. Sample BB contained Flinak, with 1 wt% added FeF_3. The onset temperatures indicate a eutectic melting temperature of approximately 455 ° C. The curve also indicated a final melting peak at approximately 669-676 ° C. Similar behavior was observed in the DSC curve for sample DD, the other sample which contained Fe_2O_3 impurities. A notable difference between sample BB and

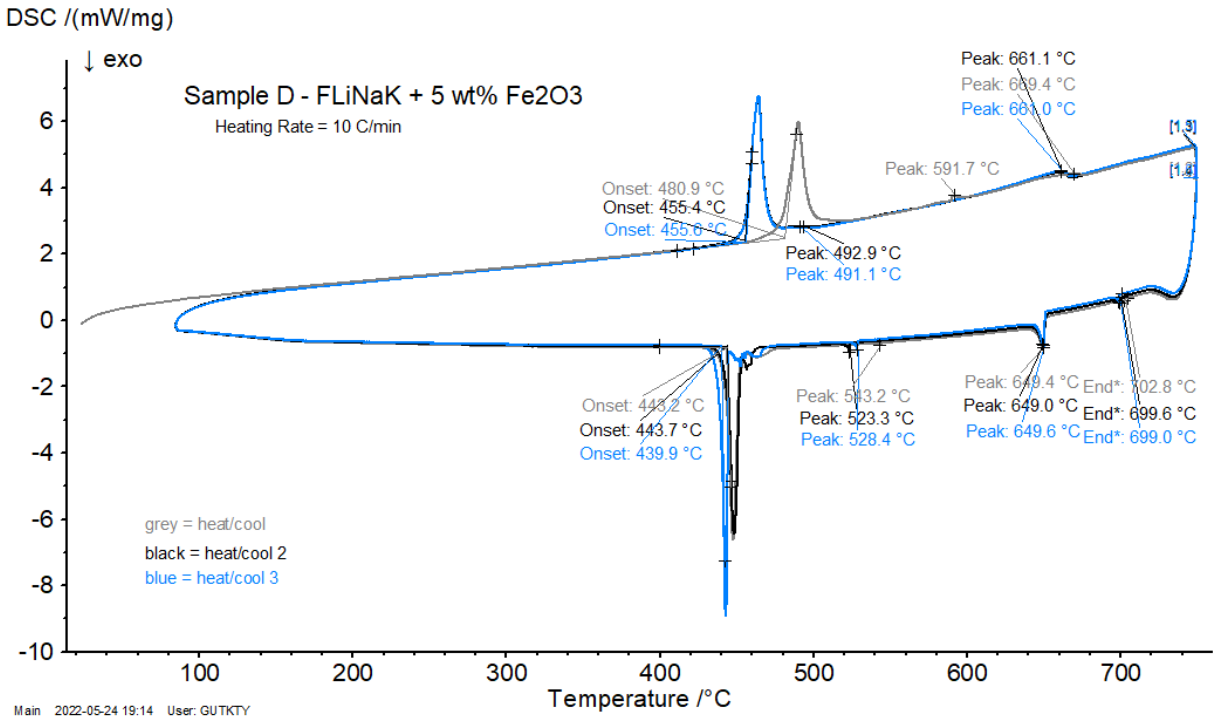

Figure 4.16: DSC curve for sample D, Flinak with 5 wt% Fe_2O_3.

sample DD was the presence of additional disturbances in sample DD, whereas there were none in sample BB.

The eutectic onset and end peak temperatures were recorded from each sample, and can be seen for the Fe_2O_3 sample set in table 4.7, and for the FeF_3 sample set in Table 4.8. As expected, there is no significant variation in eutectic onset temperature. There is some possible variation that can be seen in the final peak temperature, which is also visible when the values are plotted. Scatter plots of the results can be seen in figures 4.18 and 4.19. The iron fluoride sample set in particular shows variation in the end peak temperatures, with a slight downward trend.

A one-way ANOVA performed on the results from the DSC testing shows that there is no statistically significant variation between the eutectic temperatures and impurity concentration. There also was no statistical significance shown between the end peak temperature and impurity concentration for the iron oxide sample set. However, for the iron

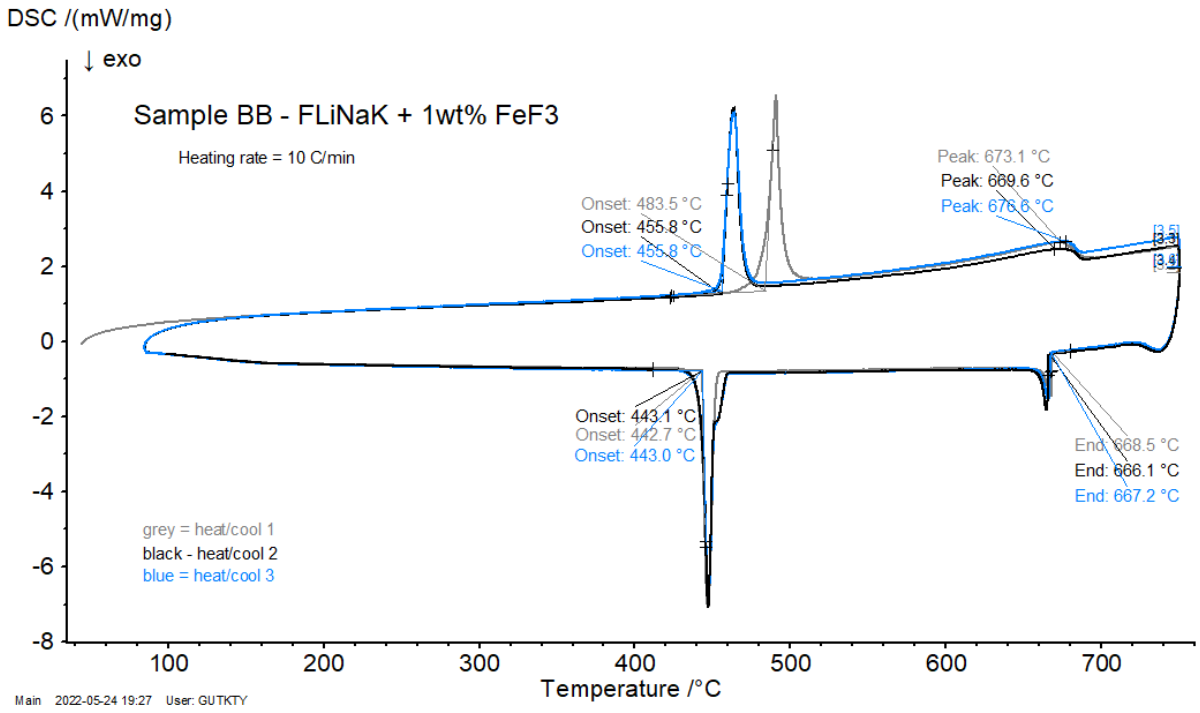

Figure 4.17: DSC curve for sample BB, Flinak with 1 wt% FeF_3.

Sample	wt% Fe_2O_3	Heat/Cool Cycle	Eutectic Onset	Final Peak
AA	0	2	459.2	669.3
AA	0	3	456.7	666.8
B	1	2	456.5	658.7
B	1	3	456.5	665.3
D	5	2	455.4	661.1
D	5	3	455.6	661.0

Table 4.7: Temperature values for the eutectic onset and end peaks for the second and third heat/cool cycles, for the Fe_2O_3 Flinak sample set.

Sample	wt% FeF_3	Heat/Cool Cycle	Eutectic Onset	Final Peak
AA	0	2	459.2	669.3
AA	0	3	456.7	666.8
BB	1	2	455.8	669.6
BB	1	3	455.8	676.6
DD	5	2	456.1	652.4
DD	5	3	458.9	647.9

Table 4.8: Temperature values for the eutectic onset and end peaks for the second and third heat/cool cycles, for the FeF_3 Flinak sample set.

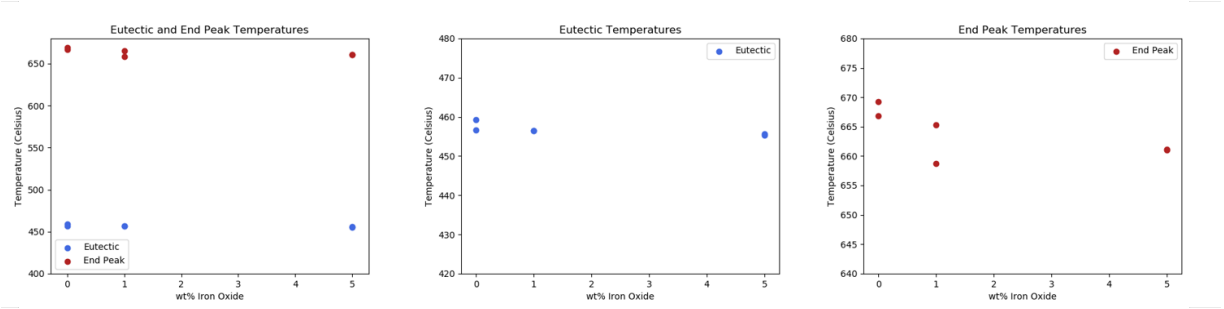

Figure 4.18: Scatter plot for the results of DSC testing for the Flinak-Fe_2O_3 sample set.

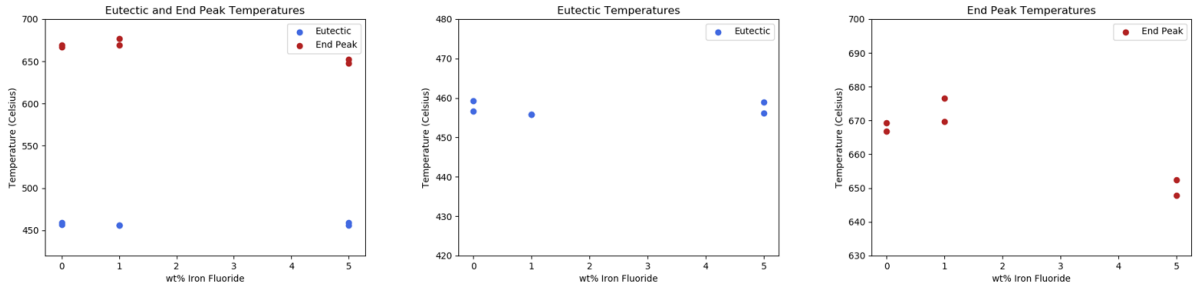

Figure 4.19: Scatter plot for the results of DSC testing for the Flinak-FeF_3 sample set.

fluoride set, the p-value for the variation between groups was calculated to be approximately $p = 0.015$, which is less than the traditional threshold of significance. Therefore, for the iron fluoride sample set, there is a statistically significant variation between the final melting temperature and the iron fluoride concentration.

Data set	Degrees of Freedom	F	p
Eutectic	(2,3)	2.895	0.1994
End Peak	(2,3)	3.473	0.1657

Table 4.9: Values for the degrees of freedom (between groups, within groups), F statistic, and p-value for a one-way ANOVA for the Flinak-Fe_2O_3 DSC Tests.

Data set	Degrees of Freedom	F	p
Eutectic	(2,3)	1.095	0.4394
End Peak	(2,3)	23.116	0.01504*

Table 4.10: Values for the degrees of freedom (between groups, within groups), F statistic, and p-value for a one-way ANOVA for the Flinak-FeF_3 DSC Tests.

4.3 Implications and Limitations

The results of the bulk testing indicated that there was no statistically significant variation between the bulk melting temperature and the impurity concentration. However, in the DSC tests, a variation was found for the final melting temperature of the iron fluoride group. It was also determined during the DSC testing that the melting of the Flinak samples does not occur in its entirety near the eutectic melting temperature. During DSC testing, the melting range needed to be adjusted to a larger range, because behavior was observed far above what was initially expected to be the final melting range. The melting of Flinak salt occurs over a range of temperatures between 450 - 700 ° C, with the bulk of the melting occurring during the eutectic onset, and small portions of the salt finally melting at approximately 650-670 ° C.

The bulk testing procedure was limited in temperature range, and at the time of testing, it was not known that behavior above 500 ° C was expected. The bulk testing captured melting behavior at the eutectic onset, but was not sensitive to detect other phase transitions. The bulk testing determined that the eutectic melting temperature does not vary with added impurities. This is confirmed by the DSC testing results, which show eutectic melting temperatures in the same approximate range as the bulk test results. Behavior after eutectic melting can occur for many reasons, and further testing is needed. Because of the impurities inherent in open-air sample preparation and testing, it is possible that oxides and moisture reacted with salt components, or that Fe_2O_3 is not soluble in the salt, causing the extension of the melting range. Because a final melting peak in the 650-670 ° C range was observed on the 'pure' (no added impurities) sample as well as the 'impure' (added impurities), impurities inherently present in open-air samples are a possible origin of the extended melting range. However, the exact cause cannot be determined without further experimental characterization. The DSC results also show disturbances present between onset and final melting, on samples B, D, and DD. It was

not possible to determine what the cause of these disturbances is without further testing, but it can be concluded that there is some enthalpy change detected by the DSC for the samples. This activity could be reacting compounds, oxide impurities, or the added impurities. Additional sample characterization would be required to determine the cause of these disturbances.

The behavior observed in the DSC testing can be further confirmed by the bulk melting progression photos and the post-test sample photos presented earlier in this chapter. The melting progression of the samples showed that the final melted state of the samples had an appearance of a suspension, rather than a transparent liquid. After the samples had cooled and been cracked open, the samples exhibited color variation, showing the presence of different phases during cooling. These visuals support the conclusion that there is a portion of the salt samples that does not melt at the eutectic melting temperature, or is insoluble in Flinak.

4.4 Conclusions

Bulk testing and DSC testing was performed on three sets of salt samples, with varying amounts of added impurities. The first set of salt samples consisted of Solar salt with Fe_2O_3 impurities. No DSC testing was conducted on these samples. The second and third sample sets consisted of Flinak salt with Fe_2O_3 and FeF_3 impurities.

The bulk testing performed on the samples captured the eutectic melting temperature of each sample, and statistical analysis showed no variation between the melting temperature and added impurity concentration, for all three sample sets.

DSC testing confirmed that the eutectic melting temperature does not vary with added impurity, as expected. However, behavior was observed in DSC testing that showed there is a melting range in which the bulk of the salt melts at the onset of the eutectic melting temperature, and the salt does not reach a uniformly liquid state until approximately 650-680 $^\circ$ C. Portions of the salt remain solid throughout this melting range, melting at different

temperatures throughout. The exact components which melt during this extended melting range cannot be determined without further experimental analysis, but could arise from oxide impurities inherent in open-air samples, from the added impurities, or a combination of both.

In molten salt systems, it is difficult to maintain an entirely pure salt mixture, particularly in a nuclear system, which generates fission products. Although open-air testing in experimentation-scale work is undesirable and leads to uncertainty, it is more realistic, and applicable to a large-scale system. Large systems, due to the scale of molten salt involved, will inevitably have some level of atmospheric exposure, leading to moisture and oxide impurities. Corrosion, although it can be reduced, is also inevitable in a large-scale system, which will add corrosion products to the melt. Thus in a large-scale system, impurities should be expected, including corrosion products, moisture and oxides from air exposure, and fission products. Therefore it is expected that in a large-scale molten salt system, Flinak salt will experience a melting range similar to what was observed in this study. Other salt types will also have a melting range, although the quantification of those ranges is not within the scope of this work. Bulk melting will occur at the expected melting temperature of the salt, but for a uniformly liquid salt system it will be required to maintain the system at a temperature above the salt's melting range. If the system temperature is within the melting range, the salt may contain suspended solid phases, which could have an impact on fluid flow, heat transfer, corrosion, and in the case of nuclear systems, neutronics.

CHAPTER 5

Modeling of Molten Salt Corrosion using COMSOL Multiphysics

The experimental results described in chapter 4 show results of salts which are stagnant, and not under any type of flow conditions. Experimental determination of melting point is not effected by fluid flow conditions, since melting point is an intrinsic property of the material and is not dependent on velocity. However, corrosion is an extrinsic behavior, dependent on many external conditions, including temperature and fluid velocity. In general, realistic molten salt systems will have fluid flow conditions, and this will impact the corrosion conditions of the system. It is desired to limit or minimize corrosion in molten salt systems, to avoid irreversible damage to the system. In some areas of a molten salt system, it may be difficult or impossible to access certain areas for repairs, which means the barriers between initial corrosion and corrosion-induced failure are few.

The impact of fluid velocity on corrosion in fluid-flow systems is discussed in detail in section 2.3.1 of this work. It has been stated that an increase in fluid velocity will increase the corrosion rate, due to a process called erosion-corrosion. Flow geometries which cause changes to fluid direction, velocity, or turbulence, can be particularly vulnerable to attack. Therefore, it is desired to optimize flow geometries to maintain a steady velocity. Perpendicular intrusions, such as an intruding pipe, will cause flow to impinge on the upstream side of the intrusion, which will increase corrosion.

Many active methods for limiting corrosion in a molten salt system exist, as have been described earlier in this work. However, active methods may not be applicable or possible in all designs, and require outside intervention to apply. Passive methods for corrosion control would allow the minimization of corrosion without active intervention. Passive methods of corrosion control include salt purification, redox buffers, and geometry modifications. The efficacy of salt purification and redox buffers has been studied [4], but

the influence of geometry on a flowing molten salt system has significantly less information. Some modeling efforts have been done in COMSOL evaluating corrosion in molten salt systems, but to date, none of these included coupled fluid flow physics.

The purpose of this modeling study is to evaluate the efficacy of geometry changes on reducing the magnitude of corrosion. In particular, this study seeks to look at geometry modifications that are effective in flowing conditions, rather than stagnant conditions. The modeling described in this chapter evaluates the corrosion behavior of several different geometrical configurations in molten Flinak salt, under laminar flow conditions. The geometrical configurations are then modified to determine what can be done to reduce corrosion. The modeling effort was performed using COMSOL Multiphysics, which allowed for the coupling of corrosion and fluid mechanics. The results obtained in this study evaluate the fluid flow through various geometry cases, which are representative of the geometries which may be found in a typical molten salt system. Each case is evaluated in its initial state, and then the geometry of each case is modified to maintain a steady velocity.

5.1 COMSOL Multiphysics

COMSOL Multiphysics is a finite-element based modeling tool, which uses graphic user interfaces and multiple physics modules to model common and advanced engineering and applied science scenarios [57]. COMSOL includes many features, including material databases, PDE/ODE solving capabilities, CAD interfaces, and many others.

Finite Element Analysis (FEM), is a common computational method in applied science fields. FEM is accomplished by dividing the geometry of the problem at hand into smaller divisions, by a process called *meshing*. These divisions make up small elements that are simple geometric shapes, which contain nodes. At these nodes, sets of algebraic equations are obtained from the governing partial differential equations (PDEs) to form a global system of algebraic equations, that can be solved, producing solutions at each node. These

nodal values can be used to determine a desired quantity at any point in each element, and therefore the entire domain of the model [57]. COMSOL Multiphysics software generates a mesh for a model by either *free* meshing or *mapped* meshing, which are unstructured and structured meshing methods, respectively [57]. The mesh can be modified for resolution for different regions of geometry, and the software can adjust the mesh during computation to adapt to complex geometry and physics. Figure 5.1 shows a geometry with a mesh generated by COMSOL, which was used for the base case of this modeling effort (described later in this chapter).

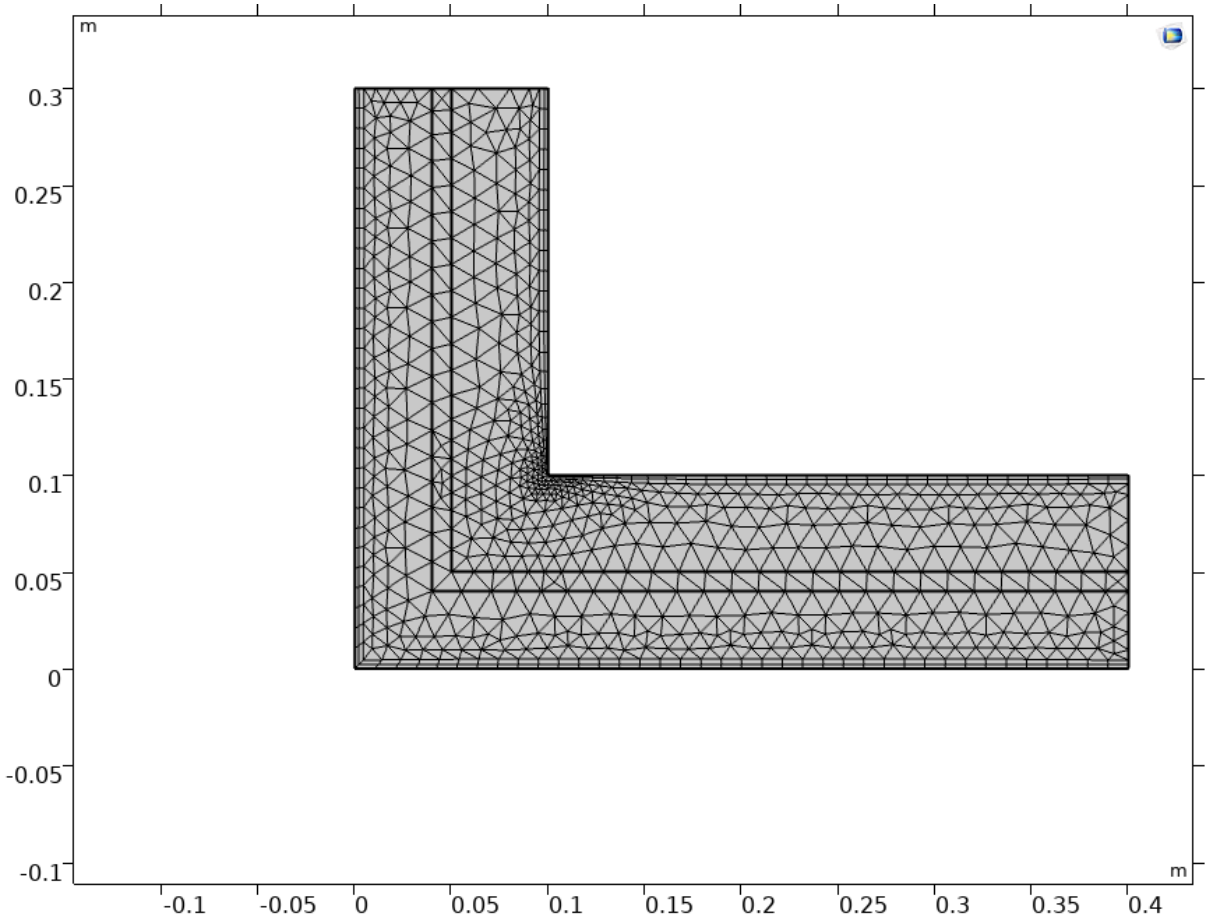

Figure 5.1: A mesh generated for the base case model of this study. A mesh is generated for FEM

The COMSOL interface functions using a *model tree*, which functions according to a nodal structure. Branches of the model tree can be added, with global definitions,

model components, and computational parameters. Subbranches are added beneath their respective branches, which include items such as a geometry branch for a component, or branches related to physics interfaces for components, such as laminar flow, or current distribution. Nodes and subnodes are then added under the subbranches, which designate parameters for their parent branch/node.

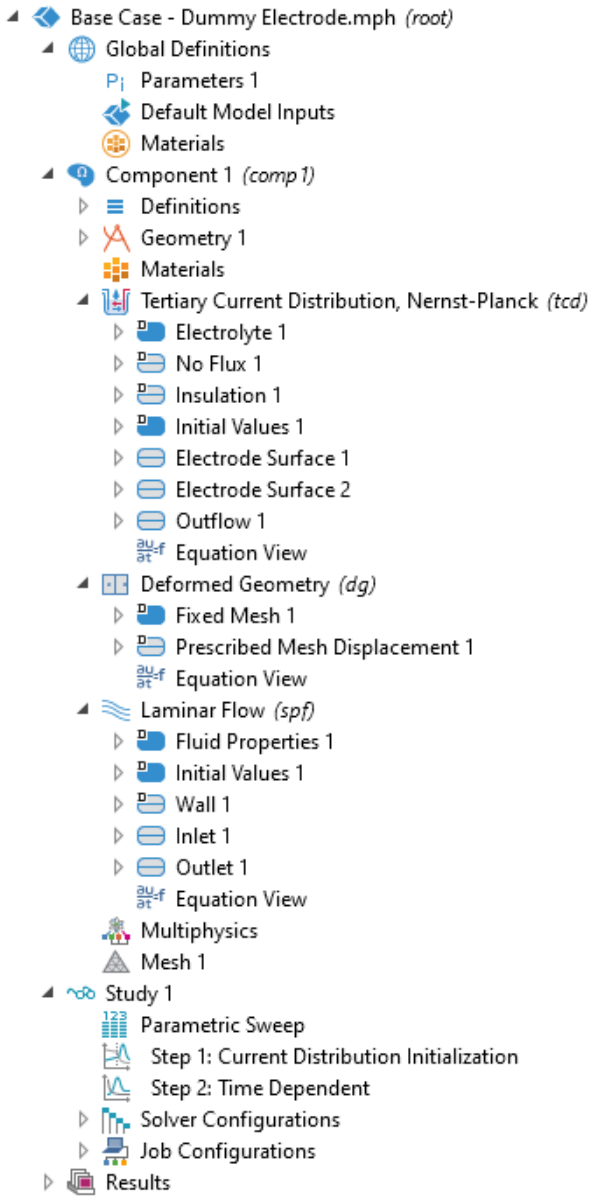

Figure 5.2: Model tree for the base case model of this study. A model tree consists of main branches, with subbranches, nodes, and subnodes relating to their respective parent.

The model tree for the base case of this study is shown in figure 5.2. Note the main branches of this model tree (under the 'component 1' label), which are *Global Definitions*, *Component 1*, *Study 1*, and *Results*. There are many subbranches for these branches, and those under *Component 1* and *Study 1* are shown in the figure. The branch for component 1 designates the geometry and physics for the study, and includes a *Geometry* subbranch, and physics subbranches. The *Tertiary Current Distribution, Nernst-Planck* subbranch designates the corrosion physics for the model. *Deformed Geometry* is paired with current distribution physics for corrosion models, and controls mesh displacement and deformation. *Laminar Flow* is the final physics subbranch added to this model, and controls the fluid flow physics for this study. The subbranches contain nodes, and subnodes, which designate parameters such as inlet and outlet specifications, electrode surface reactions, and more.

The subbranches and nodes in COMSOL multiphysics relate to the geometry by declaration of domains and boundaries. Applicable subbranches, nodes, and subnodes, can be assigned to a boundary or domain within the geometry, which then assigns the specific parameters to that location. Domains are regions of 2D or 3D geometry, and boundaries are regions of 1D geometry, such as an edge. Figure 5.3 shows an example of a domain assignment for the base case model of this study. The domain shown is the *Laminar Flow* subbranch domain, which shows that the subbranch is assigned to the entirety of the geometry (highlighted blue), meaning that the parameters included within this subbranch will apply to the entire geometry.

Boundary selection functions identically to domain selection. A boundary is assigned to an applicable branch or node, which declares the applicable parameters assigned to that location. Figure 5.4 shows an example of a boundary assignment for the base case model of this study. The node *Inlet 1* is underneath the *Laminar Flow* subbranch, meaning the node is declaring inlet parameters for the laminar flow physics. Since an inlet is geometry-dependent, a boundary must be assigned assigning an inlet location. The highlighted boundary (blue line) shows the boundary assigned to the node. In this model, a similar

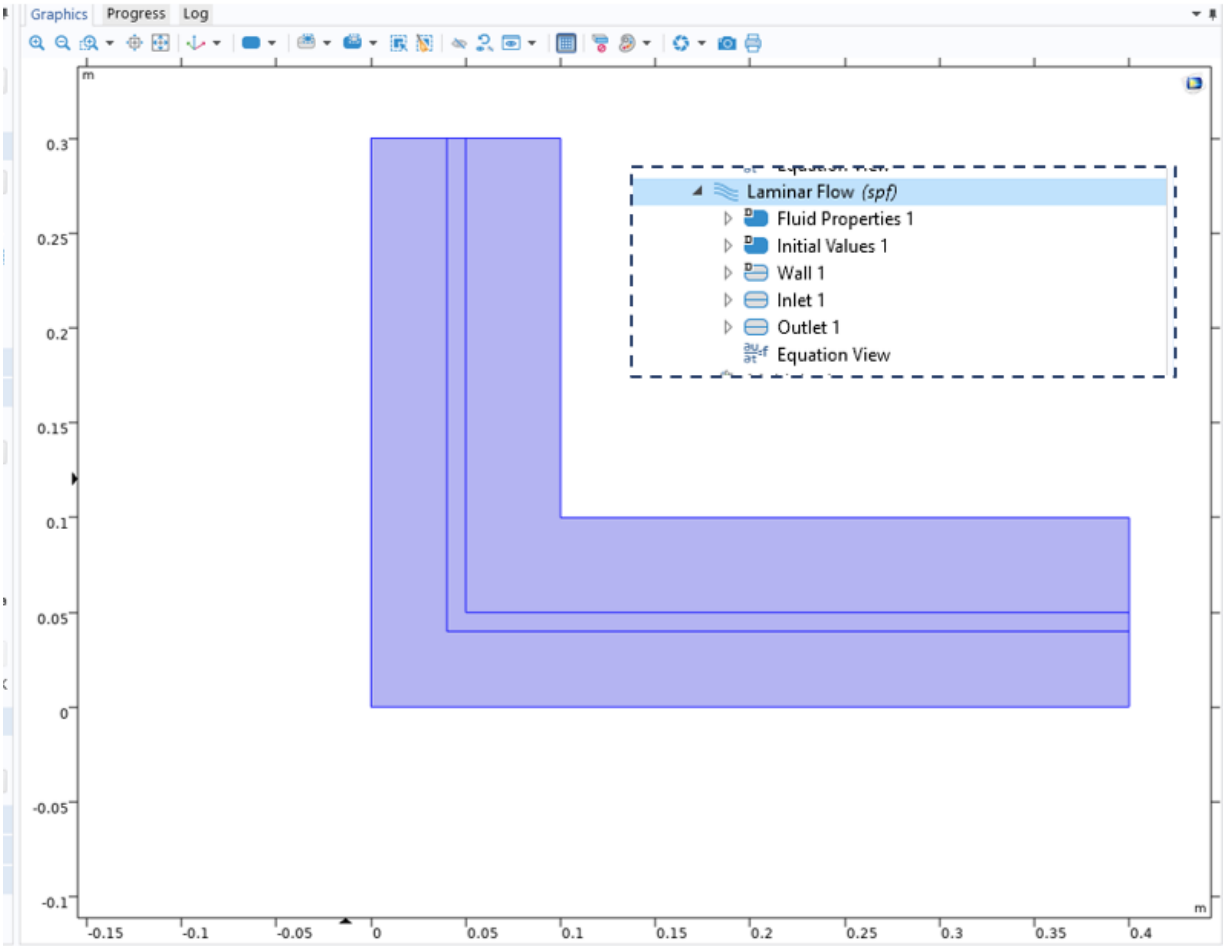

Figure 5.3: A domain is assigned to the *Laminar Flow* subbranch, declaring that the subbranch parameters apply to the entire highlighted area.

assignment was made for the outlet, on the lower right of the structure.

5.1.1 Corrosion in COMSOL Multiphysics

The corrosion module of COMSOL Multiphysics uses current distribution interfaces to model a system. This is based on basic electrochemical principles, in which an electrochemical cell with two electrodes experiences transfer of electrons from an *anode* to a *cathode*. When modeling a corrosion system, assumptions need to be made to refine the model, and this is accomplished using the different current distribution interfaces. The following current distribution interfaces are available under the corrosion module [58]:

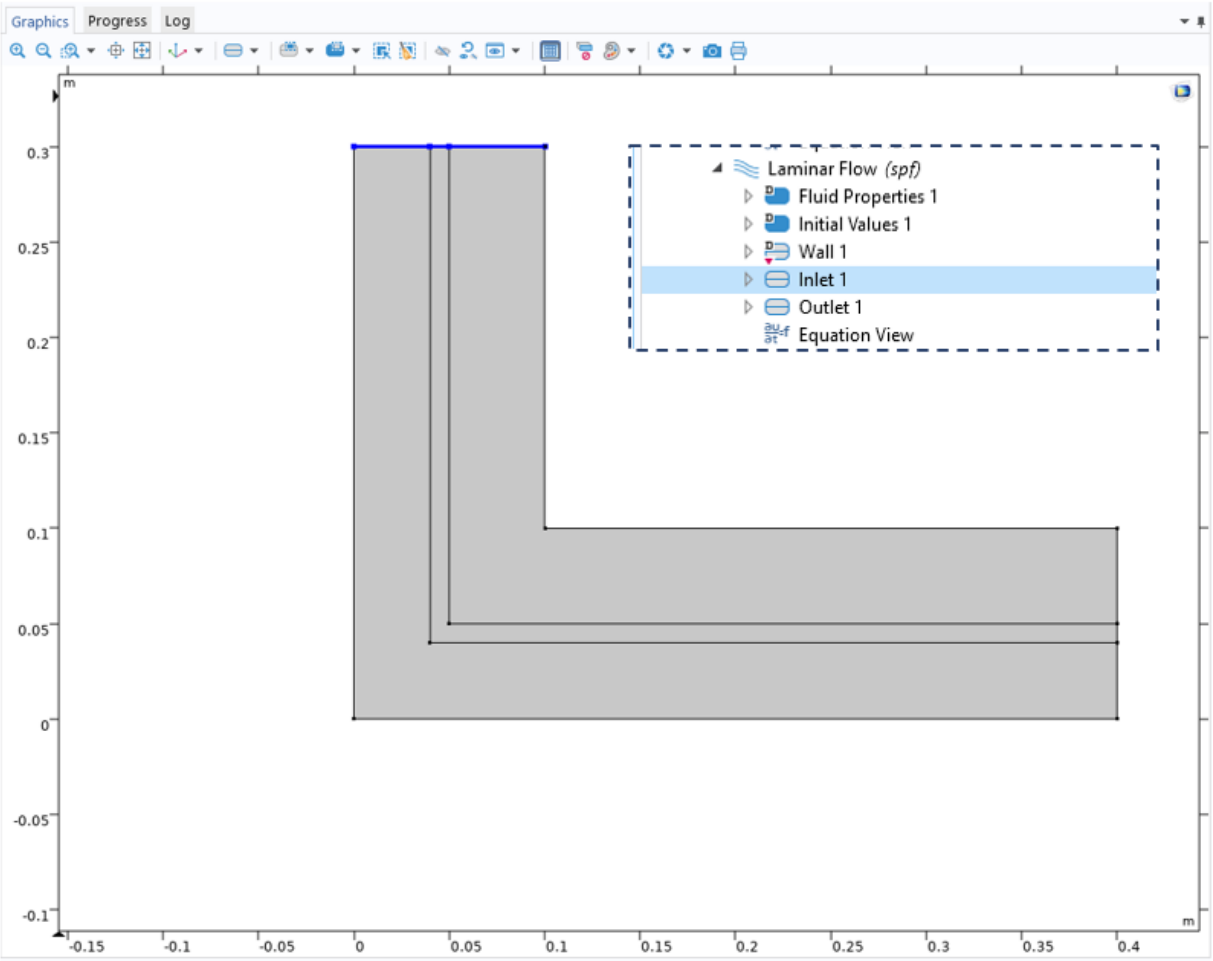

Figure 5.4: A boundary is assigned to the *Inlet 1* node of the *Laminar Flow* subbranch, declaring the inlet location for the laminar flow physics.

- *Primary Current Distribution:* A linear relationship is assumed between current density and electric field, and Ohm's law is obeyed for the electrolyte current.
- *Secondary Current Distribution:* Electrode kinetics proceed at a finite rate.
- *Tertiary Current Distribution:* Advanced nonlinear charge conservation equations are required, and electrode polarization is concentration-dependent.
- *Electroanalysis:* Potential gradients are so small that the spatial distribution is negligible.

The current distribution interface selected for this study is the tertiary current distri-

bution, which was recommended for this model [59]. This interface uses the Nernst-Planck equations, which neglect ion-ion interactions [58]:

$$\mathbf{N}_i = -D_i \Delta c_i - z_i u_{m,i} F c_i \Delta \phi_l + c_i \mathbf{u} \tag{5.1}$$

The tertiary current distribution, Nernst-Planck interface also uses an electroneutrality restraint, which sets a boundary condition in which

$$\sum z_i c_i = 0, \tag{5.2}$$

which determines the electric potential in the Nernst-Planck equations, in place of the full Poisson equation. This is because the Poisson equations uses the Debye length, a value which typically relatively small. The electroneutrality assumption holds at much larger distances from a charged surface [58].

The current flow in the model is given by:

$$\mathbf{i}_l = F \sum z_i \mathbf{N}_i \tag{5.3}$$

Where $\mathbf{N}_i$ is substituted by the Nernst-Planck expressions, and subsequently the laws of conservation of mass and charge combine to satisfy conservation of current.

Electrochemical reactions are modeled within the current distribution interfaces by use of 'Electrode Reaction' nodes. These reactions are determined by stoichiometry, thermodynamics, and kinetics [58]. A Butler-Volmer relationship was used to describe the electrode kinetics, which takes into account a reference exchange current density, i_0.

Electrolyte velocity is a parameter within the Nernst-Planck relationship, and is a parameter that can be declared within the COMSOL distribution interface. The velocity parameter can be set as a number, mathematical relationship, or be set as a parameter from another physics subbranch. In the case of this study, the coupling of laminar flow and tertiary current distribution was accomplished by declaring the Nernst-Planck velocity

$$\frac{\partial \rho}{\partial t} + \nabla \cdot (\rho \mathbf{u}) = 0$$

$$\rho \frac{\partial \mathbf{u}}{\partial t} + \rho(\mathbf{u} \cdot \nabla)\mathbf{u} = \nabla \cdot [-p\mathbf{I} + \tau] + \mathbf{F}$$

$$\rho C_p \left(\frac{\partial T}{\partial t} + (\mathbf{u} \cdot \nabla) T \right) = -(\nabla \cdot \mathbf{q}) + \tau : \mathbf{S} - \frac{T}{\rho} \frac{\partial \rho}{\partial T} \bigg|_p \left(\frac{\partial p}{\partial t} + (\mathbf{u} \cdot \nabla) p \right) + Q$$

ρ is the density (SI unit: kg/m^3)
$\mathbf{u}$ is the velocity vector (SI unit: m/s)
p is pressure (SI unit: Pa)
τ is the viscous stress tensor (SI unit: Pa)
$\mathbf{F}$ is the volume force vector (SI unit: N/m^3)
C_p is the specific heat capacity at constant pressure (SI unit: J/(kg·K))
T is the absolute temperature (SI unit: K)
$\mathbf{q}$ is the heat flux vector (SI unit: W/m^2)
Q contains the heat sources (SI unit: W/m^3)
$\mathbf{S}$ is the strain-rate tensor:

Figure 5.5: The Navier-Stokes equations, used for fluid flow in COMSOL.

parameter to be the same velocity parameter resulting from the laminar flow calculations. Thus, each point in the mesh has a velocity calculated by the laminar flow physics interface, which is then fed into the Nernst-Planck calculations, determining the effect of the fluid flow on the current distribution.

5.1.2 Flow in COMSOL Multiphysics

Fluid flow in COMSOL multiphysics is defined using the Navier-Stokes equations, shown in figure 5.5 [60].

The Navier-Stokes equations describe fluid flow in a single-phase system, and are used in COMSOL for the laminar flow interface. This can be accomplished in several gemoetric configurations, including 2D, 2D axisymmetric, and 3D configurations. This work used a 2D geometric configuration, to reduce computational load.

5.2 Model Parameters

Table 5.1 shows parameters used in the model, which are constant for all modeled geometries. The values used were either obtained from literature [31, 32, 61], or calculated from Flinak salt properties. The model was time-dependent, and the simulation time was set as t = 500 hours. Temperature dependent properties, such as density and viscosity, were approximated at 700 ° C.

Parameter	Value	Description
X_{Cr}	$1E-4$	Initial Chromium Fraction in the Salt
C_{Cr}	1.587 $\frac{mol}{m^3}$	Initial Chromium Concentration in the Salt
z_f	-1	Charge of Fluoride Ions
z_s	2.19	Average Charge Number for SS316 Steel
C_{F-}	47,611 $\frac{mol}{m^3}$	Fluoride Ion Concentration
α	0.32	Anodic Transfer Coefficient
i_0	9.6e-6 A/cm^2	Exchange Current Density
E_{ref}	-3.6 V	Reference Equilibrium Potential
F	96,485 $\frac{C}{mol}$	Faraday's Constant
MW_salt	126.02 $\frac{g}{mol}$	Molecular Weight of Flinak
ρ_{salt}	2000 $\frac{kg}{m^3}$	Density of Flinak
μ_{salt}	0.01 $Pa*s$	Viscosity of Flinak
T	700 °C	System Temperature
d	0.2 m	Out-of-plane thickness
v_{set}	0.05 m/s	Inlet Fluid Velocity

Table 5.1: Parameters constant for all geometries in the COMSOL multiphysics model study.

The redox reaction of concern in this case was kept simple. This model is a first-steps model, and therefore complex redox reactions are not within the scope of the model. Since chromium is particularly susceptible to attack by oxygen impurities in molten salt systems,

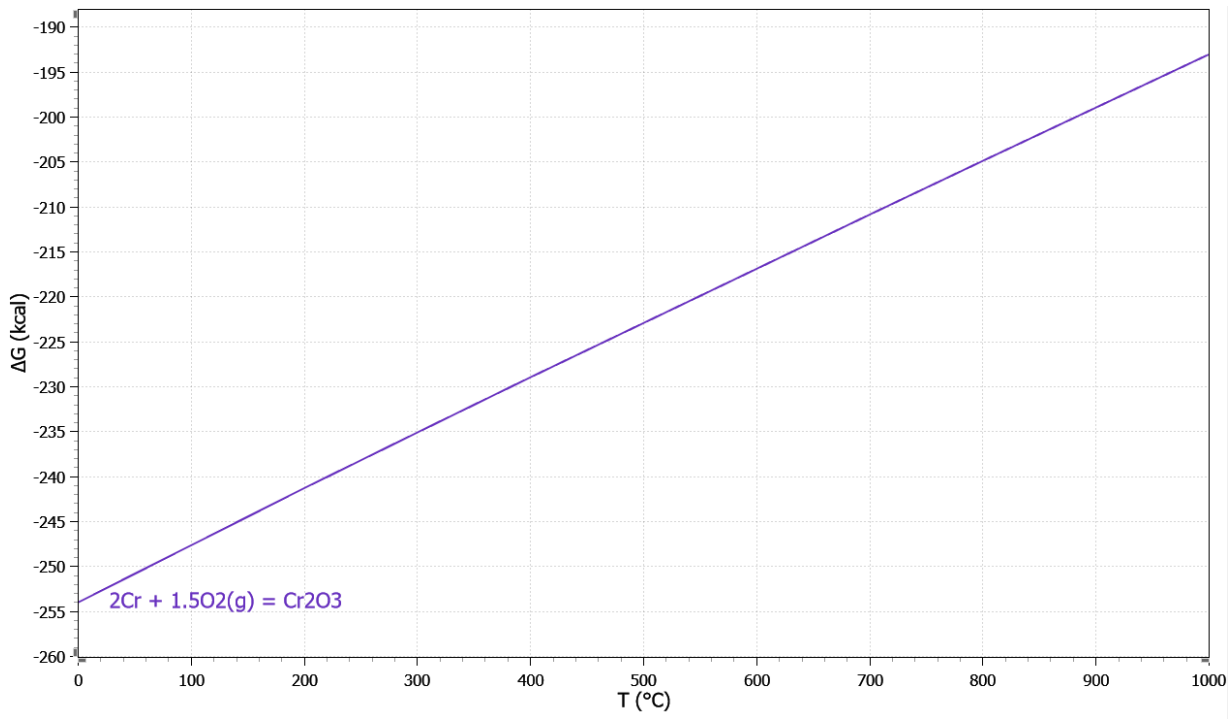

Figure 5.6: Gibbs Energy for the reaction of Chromium with Oxygen, calculated using HSC Chemistry software [56].

a simple chromium-oxygen redox reaction was considered for this model:

$$2Cr(s) + 1.5O_2 \rightarrow Cr_2O_3 \tag{5.4}$$

A simple Gibbs energy calculation using HSC chemistry software [56] shows that this reaction can proceed spontaneously (see figure 5.6). This is a very simplified version of the complex corrosion mechanics that would be occurring in a realistic molten salt system, but is within the scope of this work. Using this corrosion reaction, the severity of corrosion dependent on geometry can be estimated. The stoichiometry of this reaction was used for the electrode surface node of the COMSOL tertiary current distribution interface.

5.2.1 Geometry Selection

Several different geometric configurations were chosen for this study, representative of various types of geometries which would be found in a typical molten salt system. This

includes the following:

- Flow around a sharp right-angle corner
- Flow around a right-angle corner with fillets
- Flow over a perpendicular cylindrical intrusion
- Flow over a fin

Figure 5.7 shows sketches of each geometric configuration. Each model was constructed in a two-dimensional space, to reduce computational load. Perpendicular intrusions and fins were represented by cross-sectional shapes, as seen in frames C and D of figure 5.7. In figure 5.7.C, a perpendicular circular intrusion is represented by a circle, and in figure 5.7.D, a fin is represented with a convex composite curve

The geometry was modeled in laminar flow conditions, due to the computational load turbulent conditions would impose. Laminar flow is often present in molten salt systems, and is present in the MsNB design from the University of Idaho, discussed in chapter 1 of this work. A velocity was calculated for the diameter of the system which would result in a Reynolds number of approximately $Re \approx 1300$, at system temperature.

After initial evaluation of the base geometry selection, a parametric sweep was used to evaluate the effect of velocity on the model. The model was evaluated at inlet velocities of $v_{set} = [0.05, 0.06, 0.07] m/s$. The results of this parametric sweep are discussed in chapter 6.

Finally, modifications were made to the models to optimize the geometry, with the goal of minimizing corrosion rates. These modifications included parametric sweeps to determine optimal fillet radius, altering the radius of intrusions, and modifying fin-type and round-type geometry of intrusions. The results of these changes are also discussed in chapter 6.

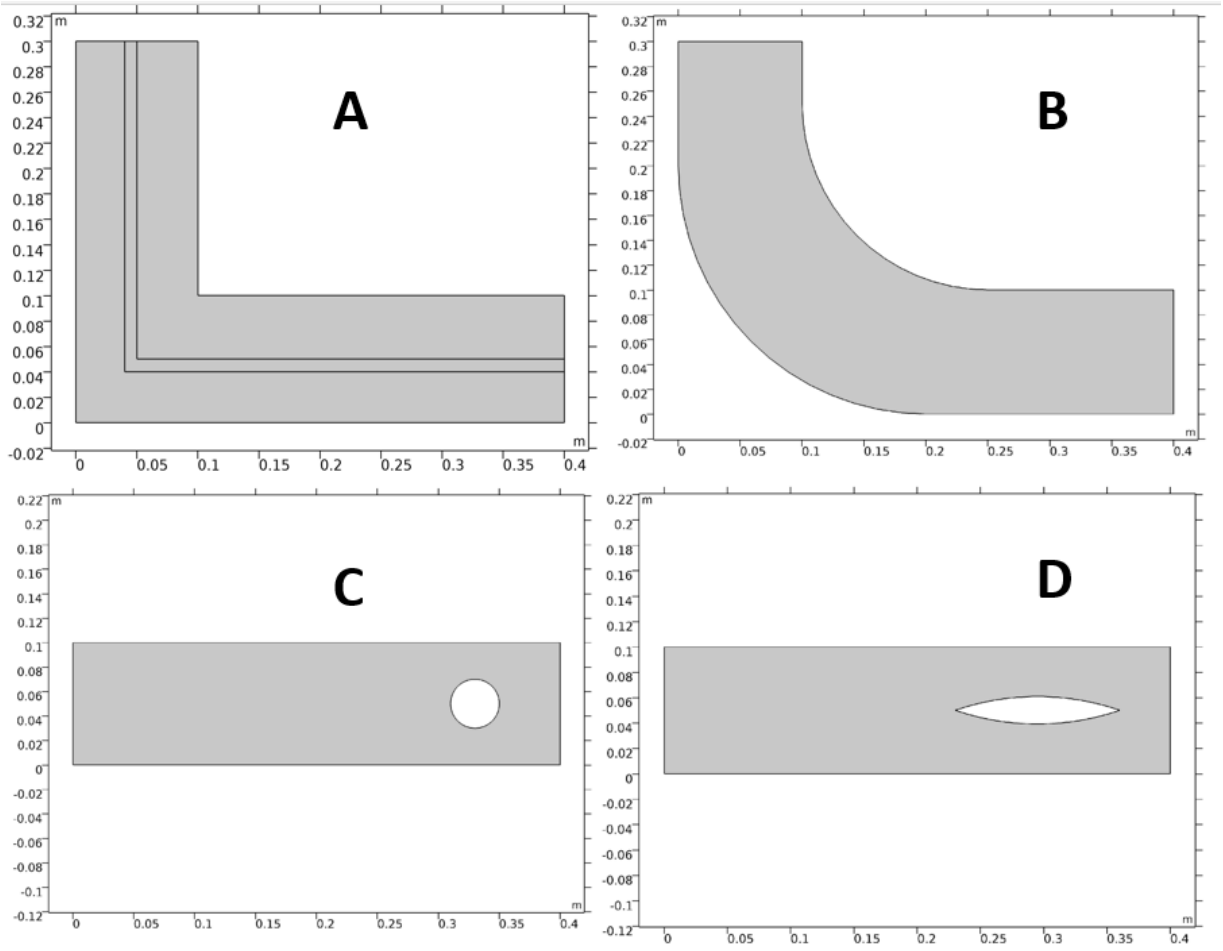

Figure 5.7: Basic geometric configurations used for the COMSOL study, in units of meters. A - right angle corner, B - right angle corner with fillets, C - flow over a vertical intrusion, and D - flow over a fin.

5.3 Model Limitations and Uncertainty

This modeling effort has several limitations. This modeling effort, a corrosion-laminar flow coupling for a molten salt system in COMSOL multiphysics, has not previously been accomplished in literature. As such, there was little previous literature to base the model on, and therefore this model is a first-steps type of effort. The corrosion chemistry in the model has been simplified, and the geometrical configurations are represented in two dimensions. Because the model does not model an entire system, the corrosion model is limited in its representation of an entire molten salt system. A large-scale molten

salt system has many additional system-wide behaviors, including chemical, nuclear, and corrosion reactions. In a system with differing materials, galvanic corrosion reactions would occur. A system-wide model is out of the scope of this work. The objectives of this model are to determine design changes which can reduce corrosion intensity, and to provide a foundation for future molten salt modeling efforts in COMSOL multiphysics.

Another limitation to this model is the limitation that is inherent in all current molten salt modeling. Many thermophysical properties of molten salts are still under investigation, or are unknown [37]. Estimations exist for some properties, and correlations and data are available for some types of salts, or for certain properties. However, data are limited, and this uncertainty reflects in this model. Values such as exchange current density, and equilibrium potential, were estimated from literature, in some cases from molten salt systems which were similar, but not identical to the model scenario.

In addition to the inherent limitations described above, the modeling efforts required some modification to accurately represent the expected corrosion behavior. Initially, the model was constructed to include an anodic reaction on the surface/walls of the model, with the cathodic reaction occurring in the bulk flow. However, this proved difficult to accomplish successfully given the initial geometric parameters. Figure 5.8 shows a plot of the resultant electrode thickness change rate vs. time, in the base case. The initial model parameters caused the software to direct electron flow from one wall to the other, arbitrarily picking a surface to dissolve chromium, and another surface to deposit chromium. This is reflected in the plot by the rates of two opposite points being mirror images of each other. This was clearly a fundamental flaw in the model design, producing unreliable results.

After some investigation, it was determined that the cause of this issue was the cathodic reaction in the bulk flow was not being represented. In a molten salt system, metal oxides and impurities provide the cathodic side of the redox reaction, and dissolved corrosion products are carried downstream. Essentially, the expected behavior in a large-scale system is a dissolution reaction taking place on the wall, with the products being carried

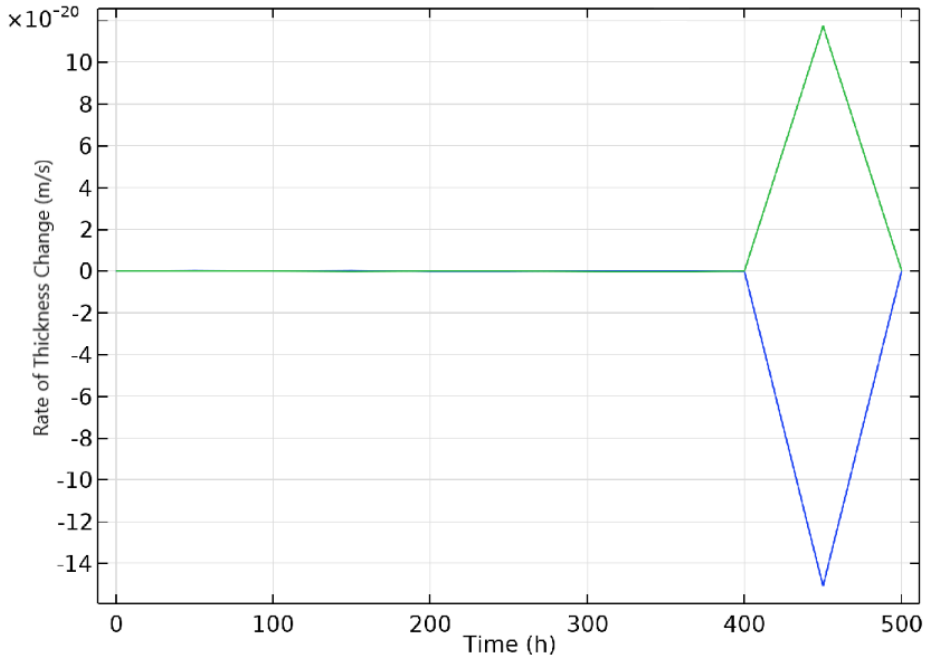

Figure 5.8: Rate of electrode thickness change for two opposite points on the right-angle base case. Note that the rates are mirror images of each other.

downstream, to elsewhere in the system. It is possible that this behavior could be modeled by constructing a COMSOL model of an entire molten salt system, with all of its components. However, this would be a very complex endeavor, and was not within the scope of this work.

Because of the limitations of this model design, it was necessary to simulate this bulk cathodic reaction with a 'dummy electrode', which can be seen in figure 5.9. This dummy electrode served to 'collect' electrons to the center of the geometry, simulating the bulk behavior. The fluid aspect of the model was adjusted to ignore the dummy electrode. This was accomplished by declaring the laminar flow domain as the entirety of the geometry, which caused the laminar flow subbranch to ignore the boundaries of the dummy electrode. This essentially made the dummy electrode 'invisible' to the fluid calculation, and only applicable for the current distribution calculation. This allowed for the corrosion reaction to take place on the wall surfaces, effectively simulating the corrosion products being taken

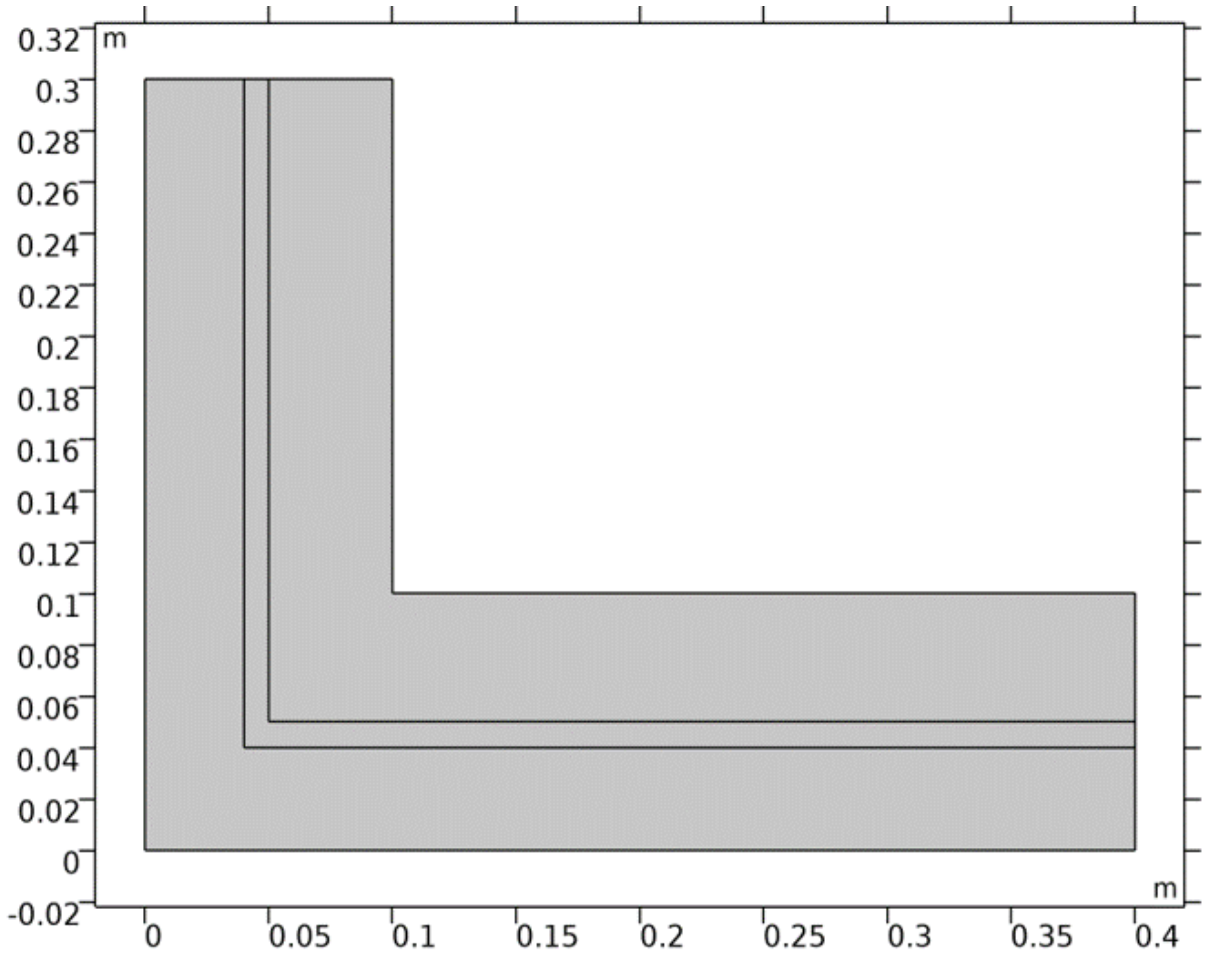

Figure 5.9: Geometry of the base case model, a right-angle corner, with units in meters. Note the lines running down the center of the 2D pipe, which constitute the dummy electrode.

up by the bulk flow.

Once the dummy electrode was incorporated into the model, results were as expected from the objective scenario. The walls of the system experienced dissolution, which was carried into the bulk fluid via the dummy electrode. Figure 5.10 shows a plot generated by the model, which shows the current density vector, or in other words, the direction of electron flow. The figure shows that the electrons flow from the dissolution reactions on the walls of the system, to the reaction in the bulk fluid, simulated by the dummy electrode.

It should be noted that the addition of this dummy electrode means that the results

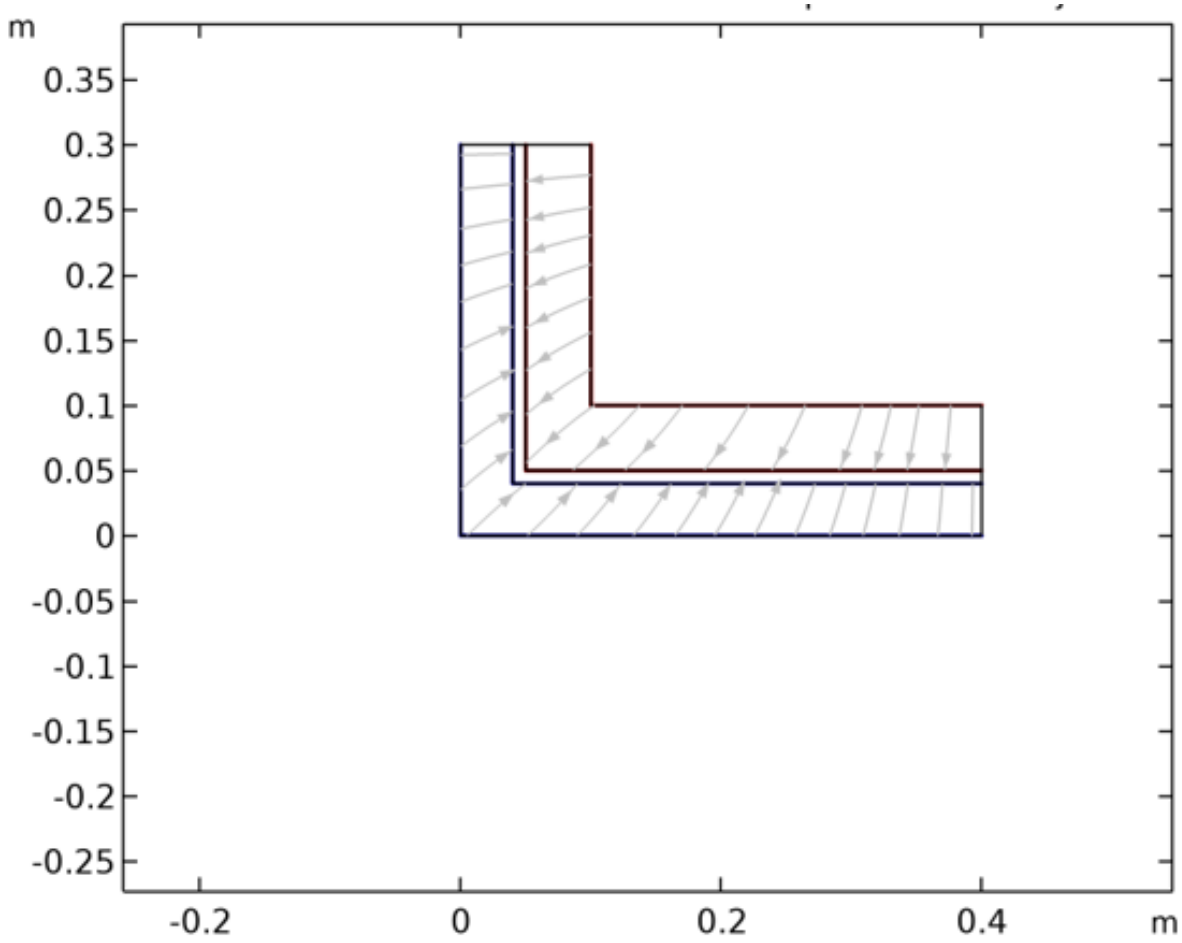

Figure 5.10: Current density vectors, of the base case model, with a dummy electrode.

from this model are limited in their application to a realistic molten salt system, and some results may not be useful on a specific scale. The requirement for a dummy electrode means that the objectives of the model need to be limited, because some results will not be reflective of realistic scenarios. The applicable results of the model were as follows:

- 2D representations of the fluid velocity
- Thickness change of the surface, after dissolution takes place.
- Rate of thickness change of the surface, determined by taking the derivative of the surface thickness change by time.

These main results will provide a simplified look at the relation between geometry and corrosion. Greater thickness change corresponds to more intense corrosion, and thus geometry changes which lessen the degree of thickness change are more advantageous. Since this model is first of its nature, without any basis to work from, simplicity was required, producing simple results. Future work on this modeling effort can refine the model parameters to provide information with a higher degree of accuracy.

CHAPTER 6

Modeling Results - Geometry Impact on Corrosion in a Molten Salt System

The results from the modeling efforts are presented in this chapter. These results consist of figures showing the intensity of corrosion depending on geometric location, as well as the effect of velocity. A generated report containing the entirety of the model parameters and results of the base case can be found in appendix C.

6.1 Base Case - Right Angle Corner

The base case for this model was a 2D representation of flow around a right-angle corner, as seen in figure 6.1. The geometry consists of a 2D right angle, with the flow inlet at the top left horizontal surface, and the flow outlet at the bottom right vertical surface. Two lines run through the center of the flow, acting as dummy electrodes to simulate bulk electrolyte behavior. Fluid flow ignores the domain of the dummy electrode, treating the system as a simple corner.

The velocity profiles for the base case can be seen in figure 6.2. A parametric sweep was conducted with three inlet velocity values, $v_{set} = 0.05, 0.06, 0.07 m/s$, and all three velocity profiles are displayed. In all three velocity profiles, regions of higher flow exist. The bottom horizontal wall in particular experiences higher flow velocities along its length.

The effect of the increase in velocity along the bottom horizontal wall can be seen when the total thickness change is plotted versus its location. Figure 6.3 shows the total thickness change of each outer wall, by its x or y coordinate, for the case with an inlet velocity of $v_{set} = 0.05 m/s$. The total thickness change represents how much thickness loss was seen over the total time of the simulation, in this case 500 hours. A more negative value

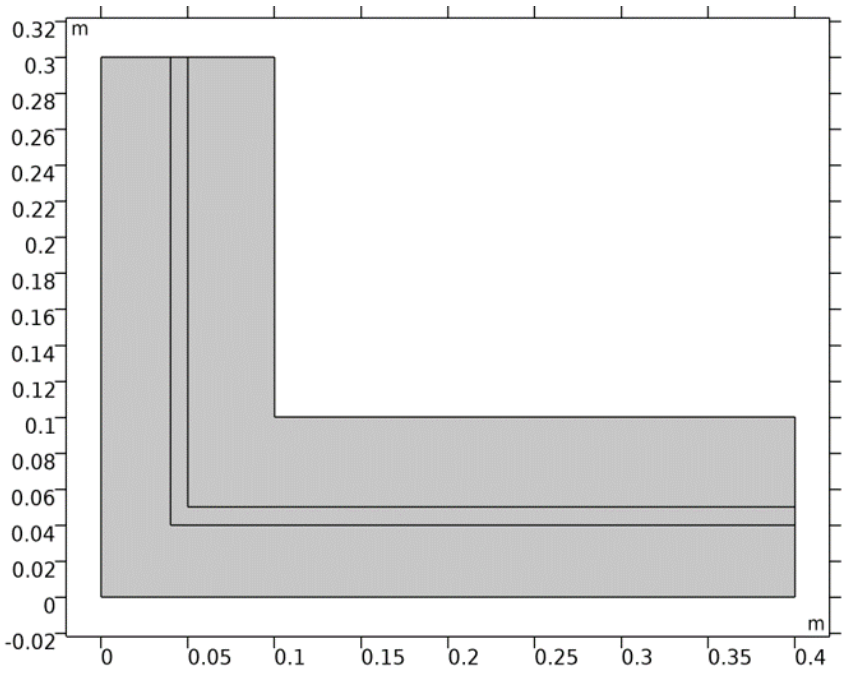

Figure 6.1: Geometry of the Base Case with a right-angle corner, with units in meters. Note there are four wall surfaces, two horizontal, and two vertical.

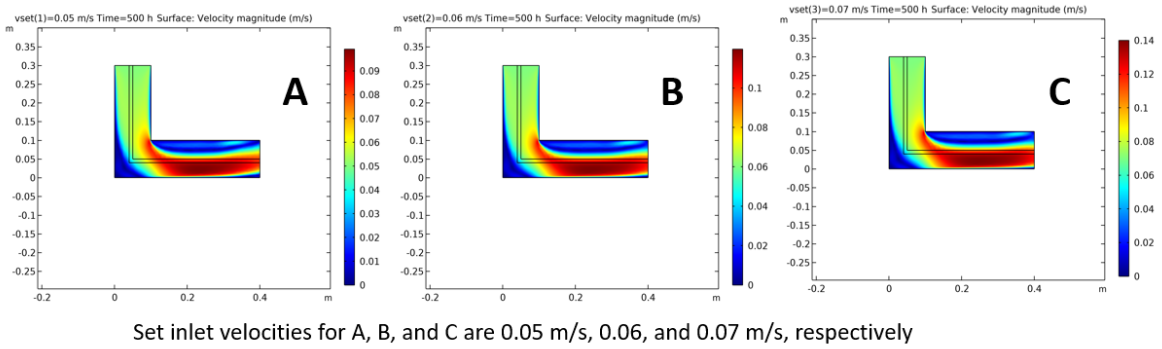

Figure 6.2: Results of a parametric sweep of three different inlet velocities

indicates more corrosion intensity in that location. Frame B in figure 6.3 corresponds to the bottom horizontal wall, which experienced more corrosion. The total thickness loss is increasingly negative along the length of the wall, corresponding to the increase in velocity. Frame D also shows this behavior; along the y-coordinate of the left vertical wall, a more negative value is shown closer to the inlet, where the velocity is higher relative to the corner region of the left vertical wall. Interestingly, although the region of greater velocity on the bottom horizontal wall experiences relatively greater thickness change than its

corresponding lower-velocity coordinate, when comparing the values between other walls, the bottom horizontal wall experienced slightly less thickness change than the right vertical wall, and the top horizontal wall.

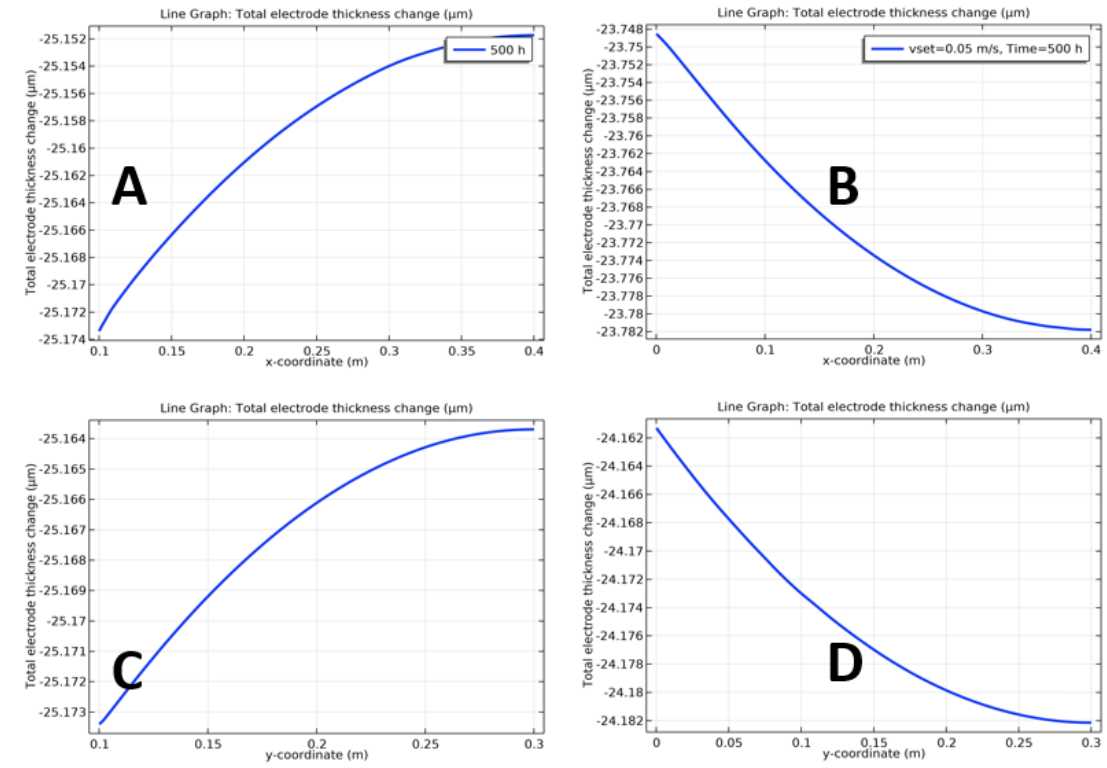

Figure 6.3: The total thickness change of each wall surface, by x or y coordinate, expressed in μm.

The total thickness change by coordinate was also evaluated through the parametric sweep of velocities, the results of which are in figure 6.4. It is clear from these results that as the velocity of the system is increased, the corrosion becomes more intense - on each wall, the higher velocities results in a more negative value.

Though informative, the plots shown in figure 6.3 show only the total thickness change over time. To achieve a value for the rate of thickness change, or the corrosion rate, a derivative was taken by time of the total thickness change. The derivatives are plotted in figure 6.5 for each wall, by x and y coordinate. The rates show the same behavior

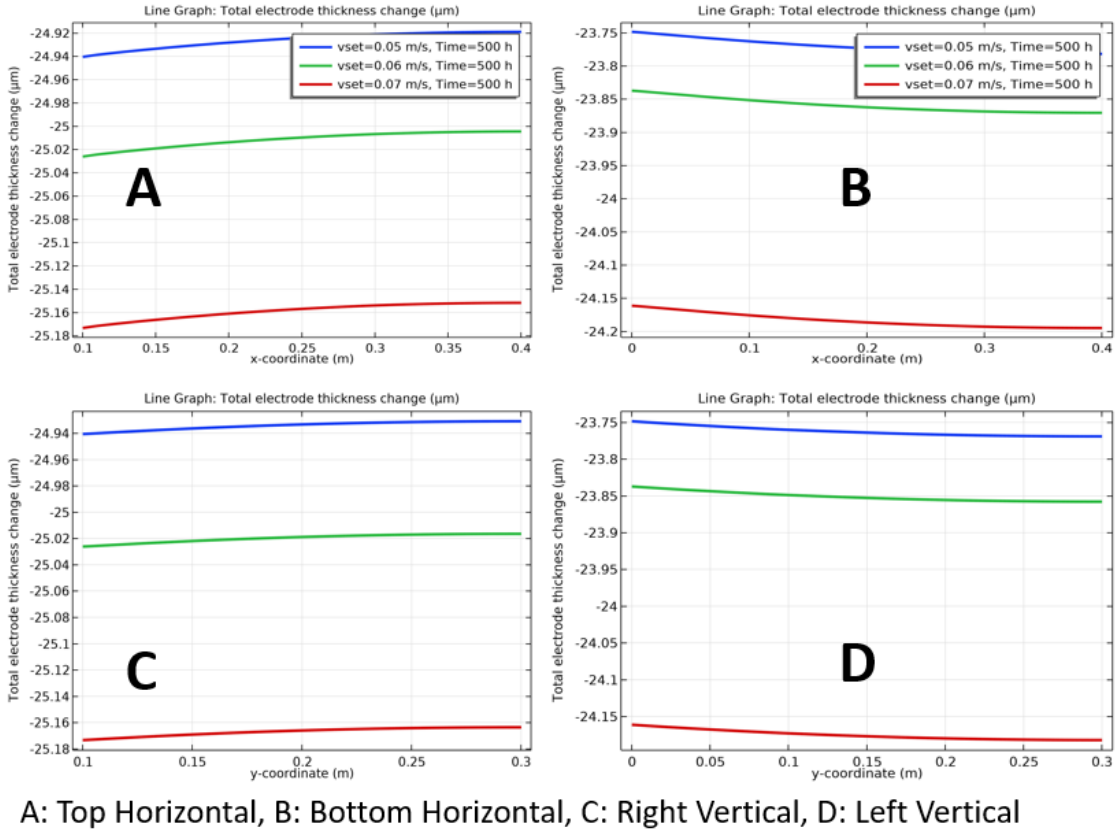

Figure 6.4: The total thickness change of each wall surface by x or y coordinate, for each velocity in the parametric sweep.

previously seen with the total thickness change. There is an increased rate of thickness change at higher velocities, and the top horizontal and right vertical walls show higher rates than the bottom horizontal and left vertical walls. This appears to be due to a higher value of current density magnitude on these walls, as seen in figure 6.6. It is unclear whether this current density difference between the walls is the corrosion behavior, or a difference caused by uncertainty in the model (which has been described in section 5.3). A possible explanation for the difference in current density on the walls is the presence of the stagnant region on the corner, which decreases the corrosion rate in that area. The right vertical and top horizontal walls have a fairly consistent flow along their lengths, whereas the bottom horizontal and left vertical walls have a greater difference along their lengths of

stagnant and low-flow regions. It is also possible that the continuous stagnant/low-flow region along the top horizontal wall increased the current density in that region, due to a longer residence time. However, it is difficult to determine the cause of this behavior without further refinement of the model.

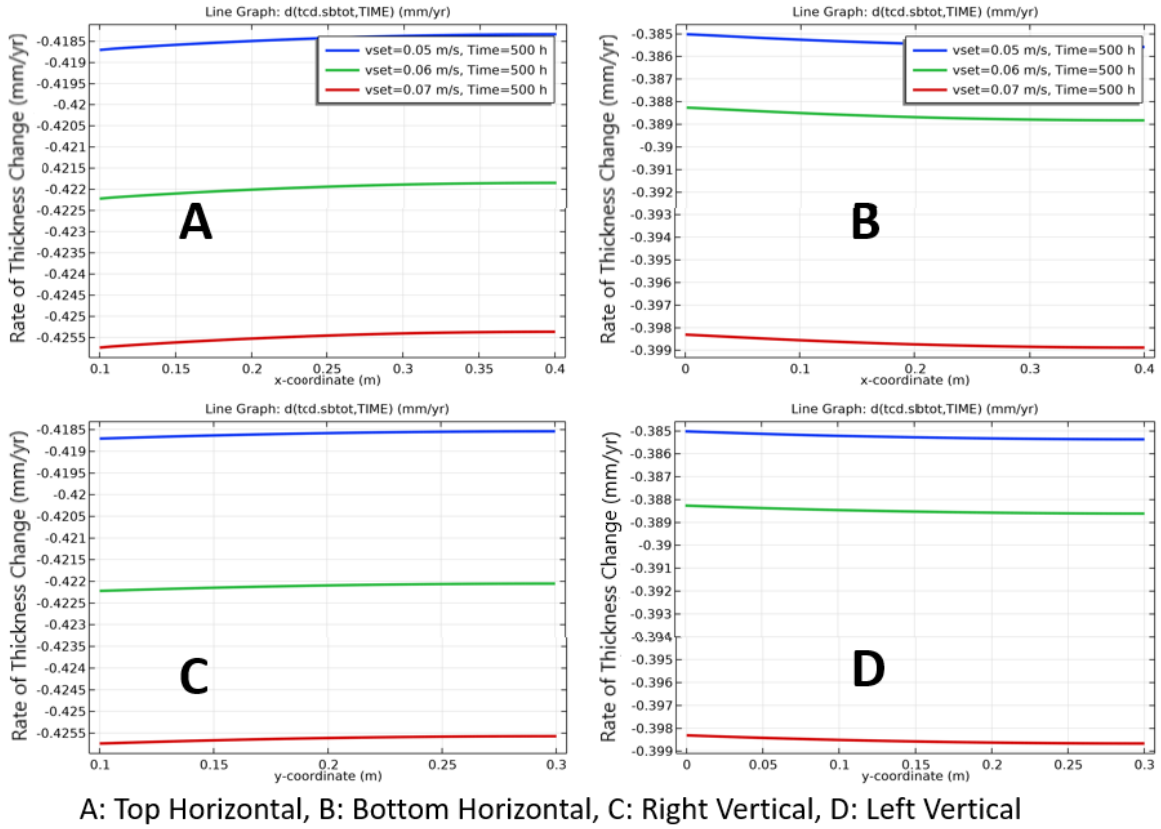

Figure 6.5: The rate of thickness change for each wall surface by x or y coordinate, for each velocity in the parametric sweep.

It was also possible to evaluate specific points on the wall over the duration of the simulation time. The inner and outer corner points were evaluated for total thickness change, and rate of thickness change (expressed by the derivative of the total thickness change by time). This information is displayed in figure 6.7. The plot on the left shows the total thickness change by time, which decreases as time progresses. This is to be expected - as time progresses, the total thickness change would increase, since dissolution is occurring. The plot on the right shows the rate of thickness change by time, which

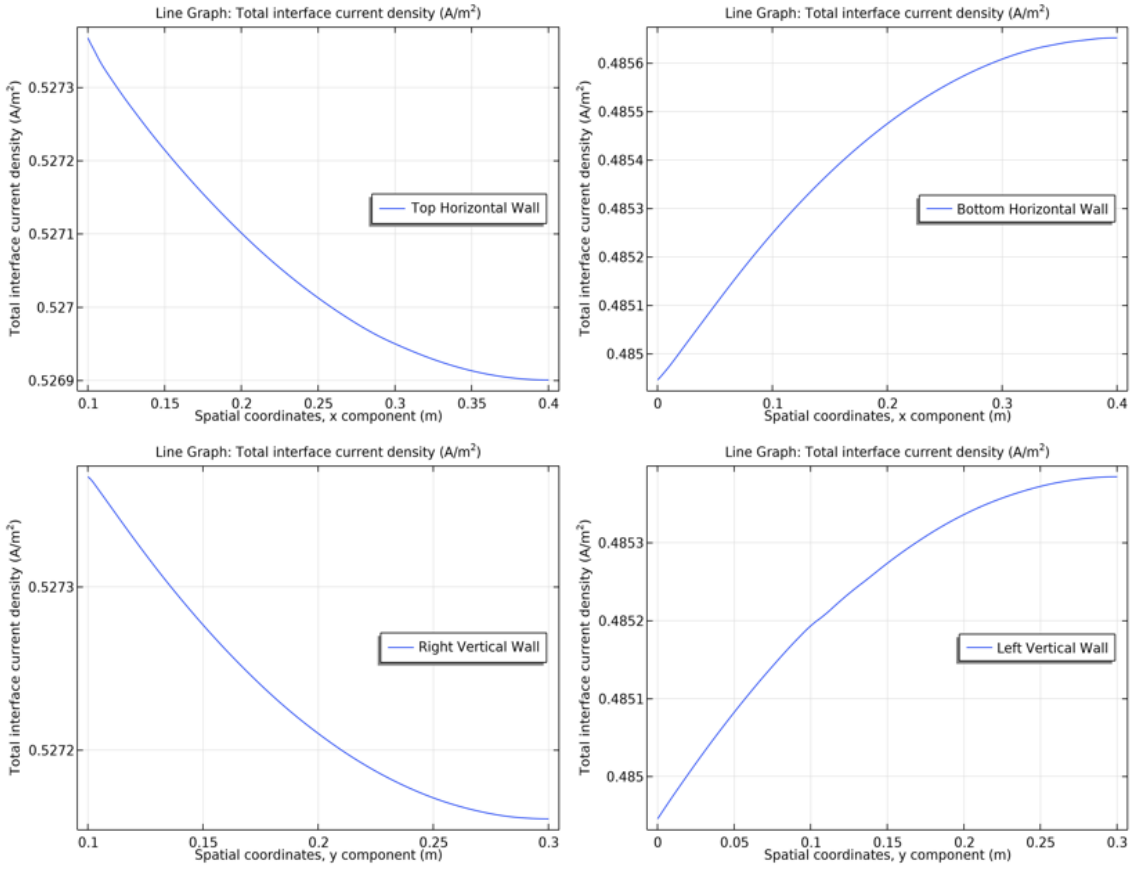

Figure 6.6: The current density magnitude of each wall surface, by x or y coordinate,

decreases as time progresses. From this model it appears that the corrosion rate will decrease as time progresses. In addition, the rate of thickness change for the bottom left point is less intense (more positive) than the inside corner point. This corresponds to the velocity profile; the inside corner point experiences higher velocities than the outer corner.

As described in section 2.3.1, it is known what the general relationship is between velocity and corrosion; as velocity increases, corrosion intensity will increase. This is supported by the results of the base case model, which showed that an increase in inlet velocity increased the total thickness change, and the rate of thickness change. Therefore, adjusting the fillet radius of each corner to decrease disturbances and higher-velocity regions will, in theory, decrease the corrosion intensity.

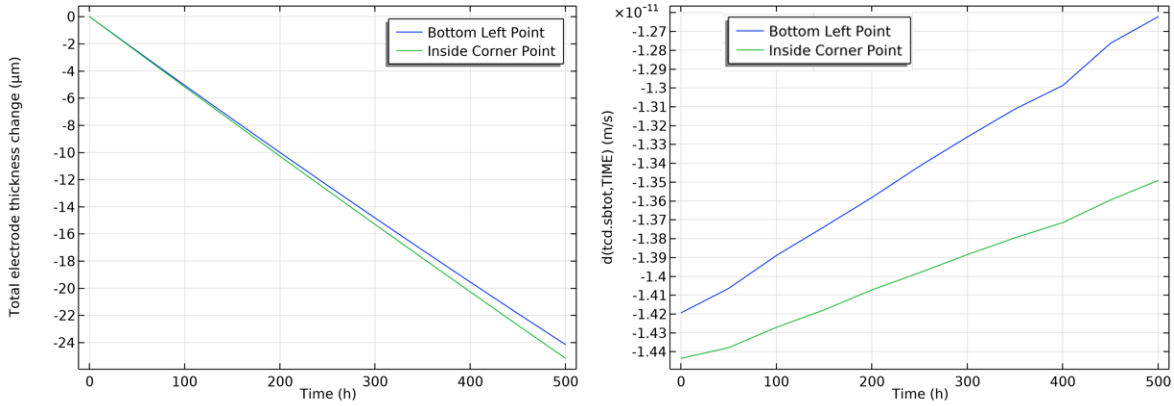

Figure 6.7: The total thickness change (left) and rate of thickness change (right) for the corner points, by time.

6.2 Right Angle Corner with Fillet

To evaluate the effect of a fillet on corrosion behavior, the base case was modified to contain two fillets on each of its sharp corners. A fillet is simply a rounding of a corner, based on a set radius value, called the fillet radius. To adjust the rounding of the corner, the fillet radius is varied.

The geometry of the fillet model is shown in figure 6.8. It is simply the base case with a fillet radius established for each of the sharp corners. Flow enters the top, and exits the bottom right, just as in the base case. The fillet radius was varied in two different phases. First, each corner's fillet radius was varied at equal values, at $r = 0.01m$, $0.05m$, and $0.1m$. Second, the fillet radii were varied separately, at 6 different combinations, which are displayed in table 6.1.

Frame	r_{inner} (m)	r_{outer} (m)
A	0.2	0.24
B	0.2	0.22
C	0.2	0.2
D	0.1	0.22
E	0.08	0.22
F	0.01	0.2

Table 6.1: Inner and Outer fillet radii for each frame in figure 6.11.

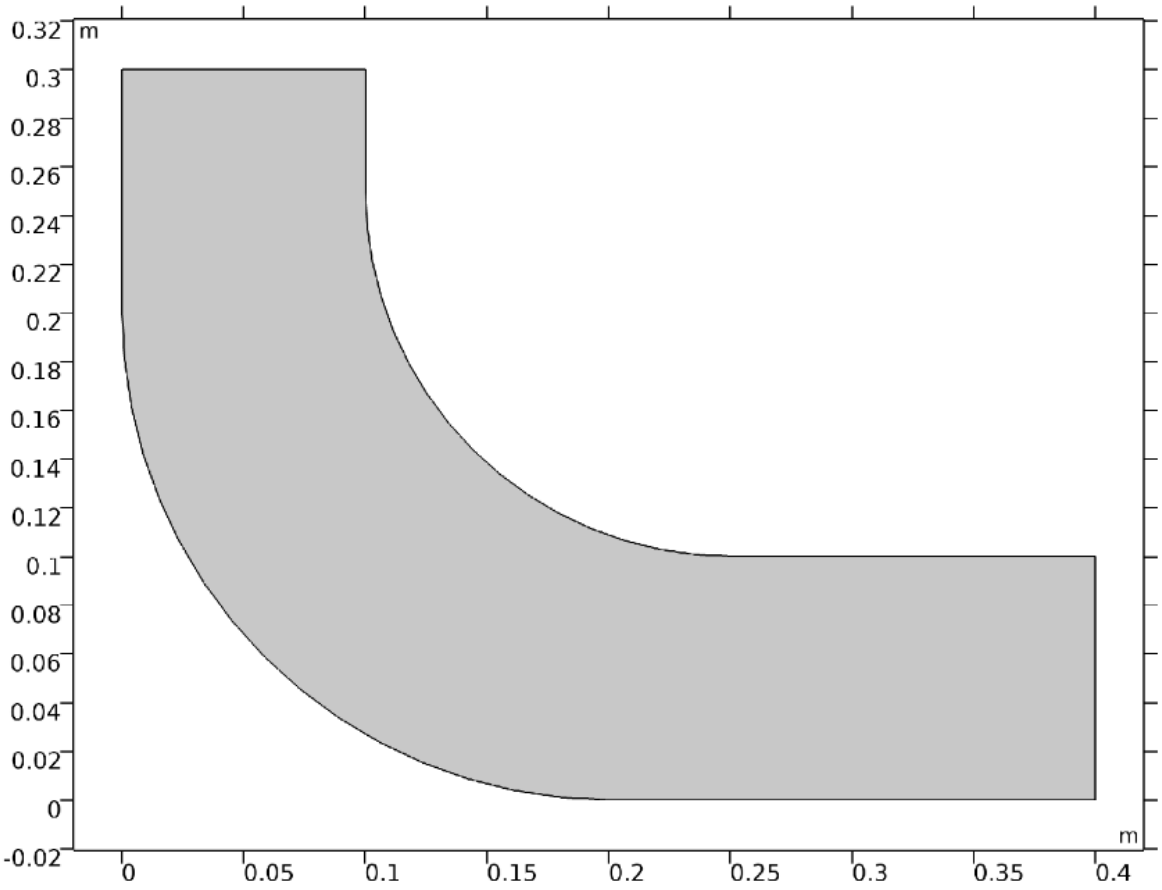

Figure 6.8: Geometry of the right angle corner with fillets on both the inner and outer corners.

The velocity profiles for the equal fillet radius variation are shown in figure 6.9. It appeared that a larger fillet radius was more conducive to a steady velocity. Frame C shows that the region of highest velocity in the profile was less than the regions of highest velocity in frames A and B.

Figure 6.10 shows the rate of thickness change (mm/yr) for each of the walls, at each of the varied fillet radii. On each of the walls, it can be seen that the magnitude of the thickness change rate increases with an increase in fillet radius. Although the increase of fillet radius was shown to decrease the peak velocity, this increase in fillet radius also produces areas where high-velocity fluid (relative to the rest of the system) comes closer to the walls, particularly in frame C. The increase in fillet radius also left a larger stagnant

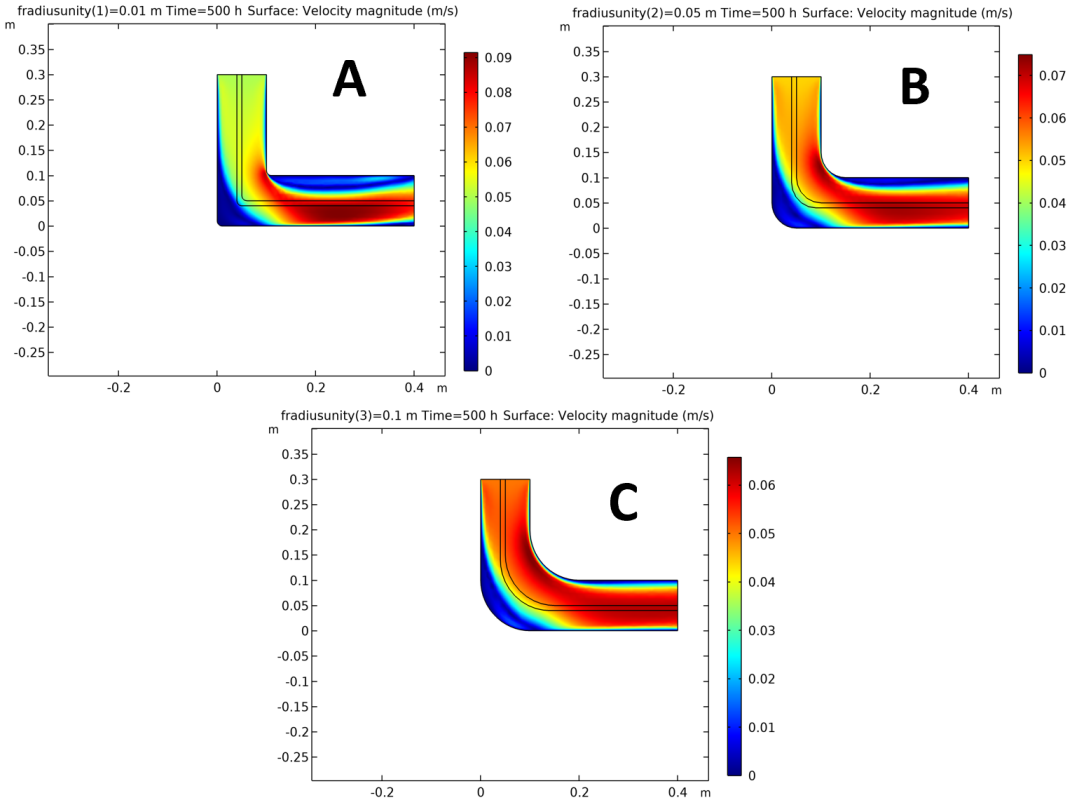

Figure 6.9: Velocity profiles of fillet variations, where the two fillet radii were kept equal. Fillet radii are A: 0.01m, B: 0.05m, and C: 0.1m

region, which may also influence the corrosion magnitude.

Because the fillet radii were varied with the same values for both corners, it is possible a different effect can be obtained by separately varying the fillet radii, obtaining an optimized velocity profile with less variation. Figure 6.11 shows the six separately varied fillet radius velocity profiles. Frames A and B had larger fillet radii, which were selected to form to the bulk flow pattern. Adjusting the fillet radius in this fashion created a steady flow pattern, with no particular regions of higher or lower flow. Conversely, frames E and F had a much larger outer fillet radius than inner fillet radius, which created stagnant regions along the top horizontal wall, and higher flow velocities which impinge on the inner corner. This behavior is particularly severe in frame F, which has a peak velocity of double the inlet velocity of 0.05 m/s.

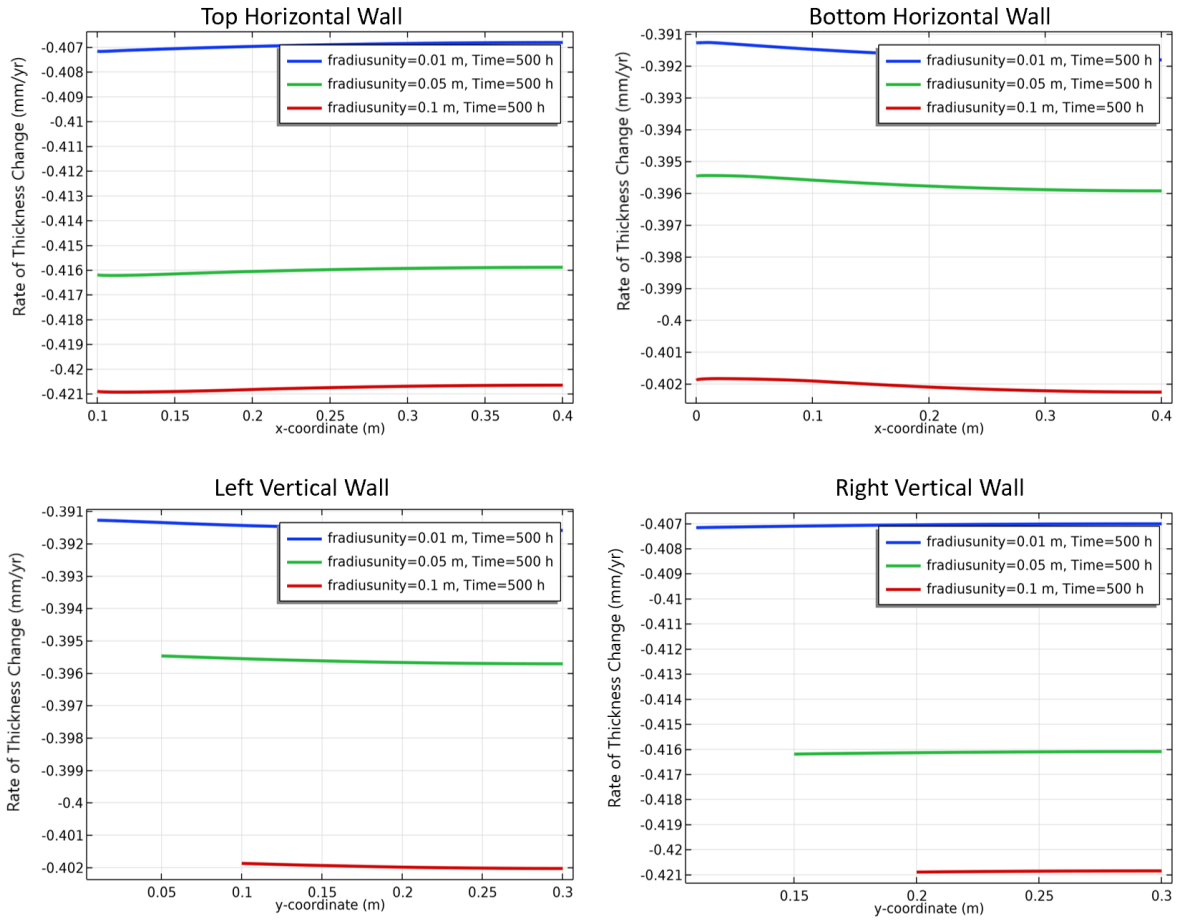

Figure 6.10: The rate of wall thickness change by x or y coordinate, for each of the three varied fillet radii.

The results of the fillet radius variations show that a steadier velocity profile can be obtained by using larger fillet radii, which can be tuned to the bulk flow pattern using fluid flow modeling techniques.

The frame in figure 6.11 with the steadies flow pattern appeared to be frame A. A comparison of the rate of thickness change of frame A with the base case (no fillet) and the fillet case is shown in figure 6.12. The fillet case improved on the base case only on the smallest fillet radius, which had a lesser corrosion magnitude than the highest velocity base case. However, frame A of the separately varied fillet cases showed a lesser magnitude than both the base case and the fillet case. This shows that it is not enough to simply increase the fillet radius of both corners, as that was shown to also increase the corrosion

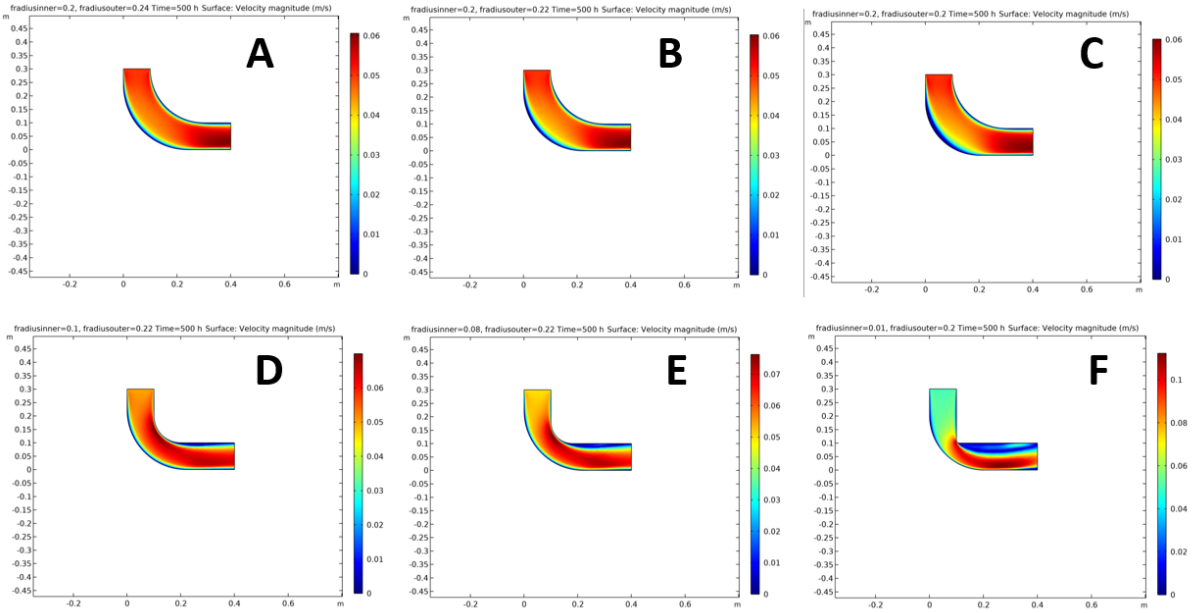

Figure 6.11: Velocity profiles of fillet variations, where the two fillet radii were varied separately. Fillet radii are shown in table 6.1

magnitude. Rather, optimizing the velocity profile by altering the fillets of the right-angle corner to match the velocity profile of the bulk fluid is effective for reducing corrosion magnitude.

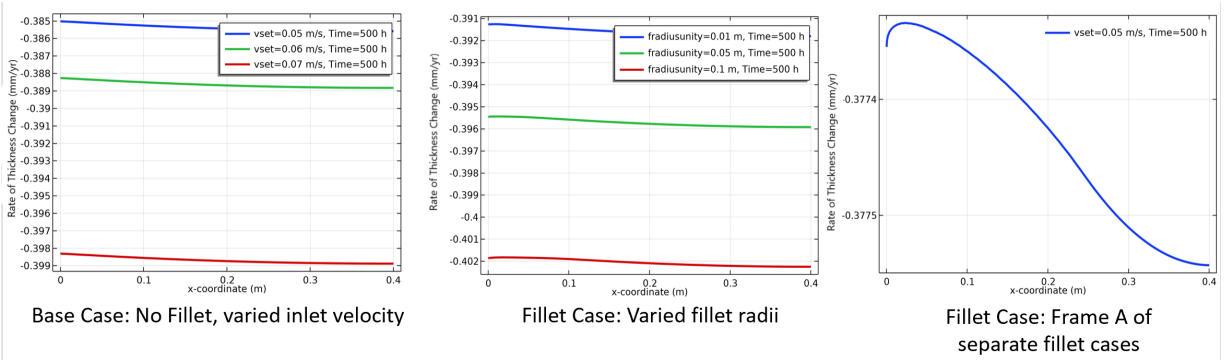

Figure 6.12: A comparison of the rate of thickness change of the right-angle corner case, the fillet case with varied radii, and frame A of the separately varied fillet radii case.

6.3 Flow over a Cylindrical Intrusion

Flow over a cylindrical intrusion was approximated by a flow over a circle, as can be seen in figure 6.13. The fluid enters on the right side, and exits on the left, flowing over the circle in the process. Two different circle radii were evaluated, $r = 0.02m$, and $0.03m$.

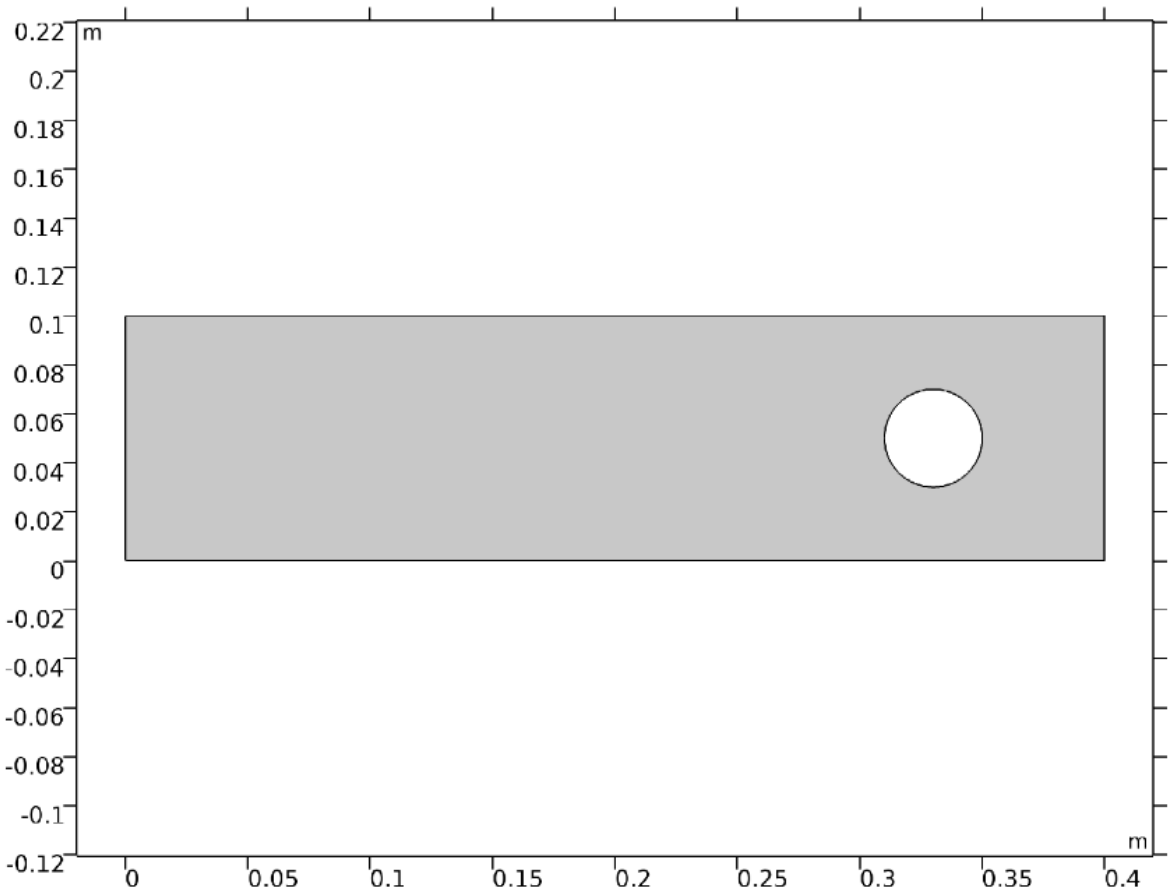

Figure 6.13: Geometry of the flow over a cylindrical intrusion, represented by a circular flow impedance.

The velocity profiles for the two circle radius variations can be seen in figure 6.14. For both variations, the bulk flow remains close to the inlet value for the undisturbed length of the geometry, and then impinges on the circle, creating a tiny region of stopped flow, and a subsequent higher velocity region of flow around the circle. The peak velocity around the circle for the larger radius was much larger than the peak velocity for the smaller radius.

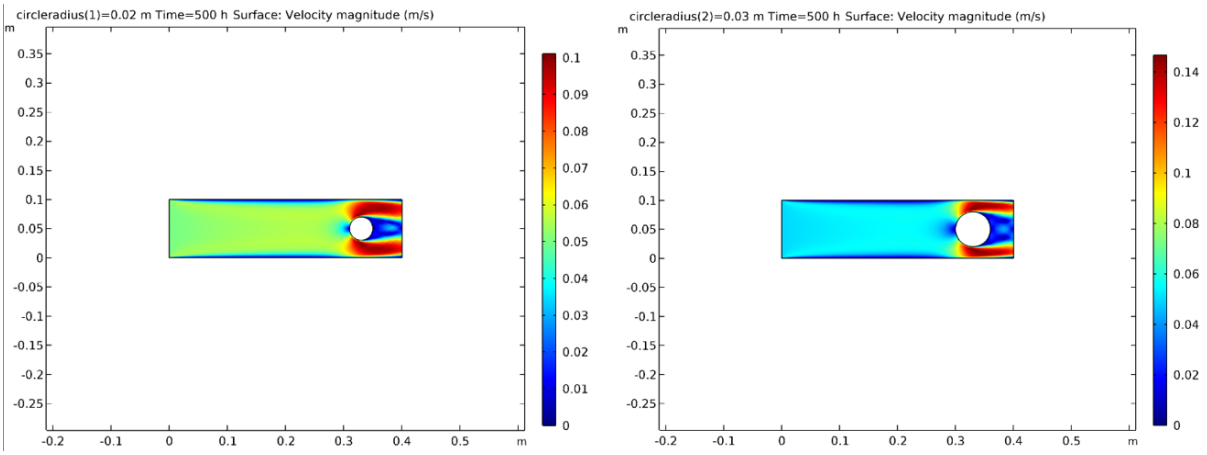

Figure 6.14: Velocity profiles of the two circular flow impedance radii, which are left = 0.02 m, right = 0.03 m.

Figure 6.15 shows the total thickness change, and the rate of thickness change of the upper side of the circle geometry. Only the top side of the circle, as the values for the top and bottom of the circle were identical. This is due to the symmetrical nature of the geometry. In Figure 6.15, it can be seen that the circle with a smaller radius experienced a greater magnitude of corrosion. There are many possible reasons this could occur. The smaller radius leads to a much smaller surface area, which could increase the corrosion rate. In addition, although the peak velocity was higher in the larger radius case, the smaller radius velocity profile showed a slightly larger 'red' area, meaning there were larger regions of fluid flow with higher velocity, which could also lead to a higher corrosion rate. Further modeling is required to determine the cause of this behavior, but it is clear that a smaller radius increased the magnitude of corrosion on the circular geometry.

Figure 6.16 shows a more detailed plot of the total thickness change for the two radius variations. Separating the plots for the radii allows a view of where the focal points for corrosion are on the circle. Each plot is shown by x-coordinate. It can be seen that each plot starts with a slightly larger magnitude of thickness change on the left side of the plot, moving to a smaller magnitude of corrosion on the right side. This follows the direction of flow: the upstream flow being on the left side of the circle, and the downstream flow

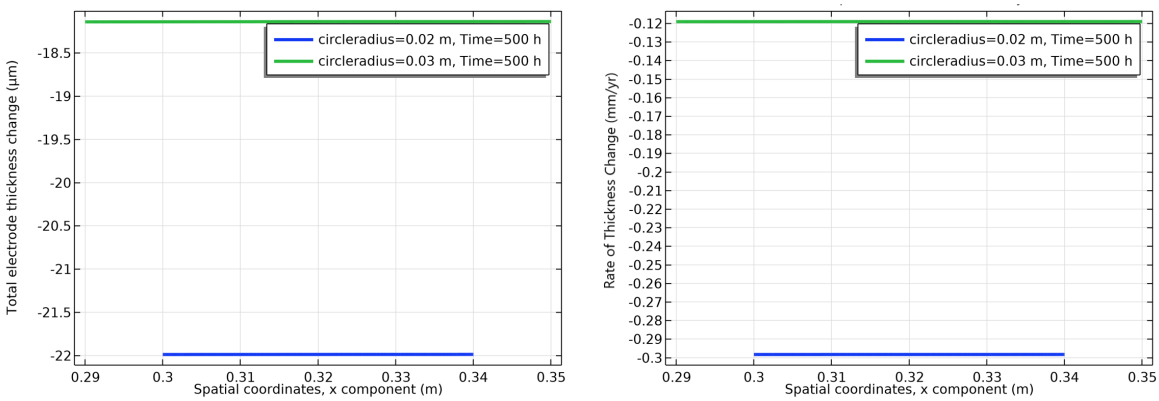

Figure 6.15: The total thickness change, and the rate of thickness change of the upper side of the circle geometry.

on the right. These figures show that a slightly higher magnitude of corrosion is seen on the upstream side of the circle, regardless of radius. The upstream side of the circle is where the fluid impinges on the object, creating both stagnant and high-velocity regions. However, the difference in magnitude between the upstream and downstream sides is on the order of 0.002 μm, an extremely small difference when compared to the difference made by altering the circle radius.

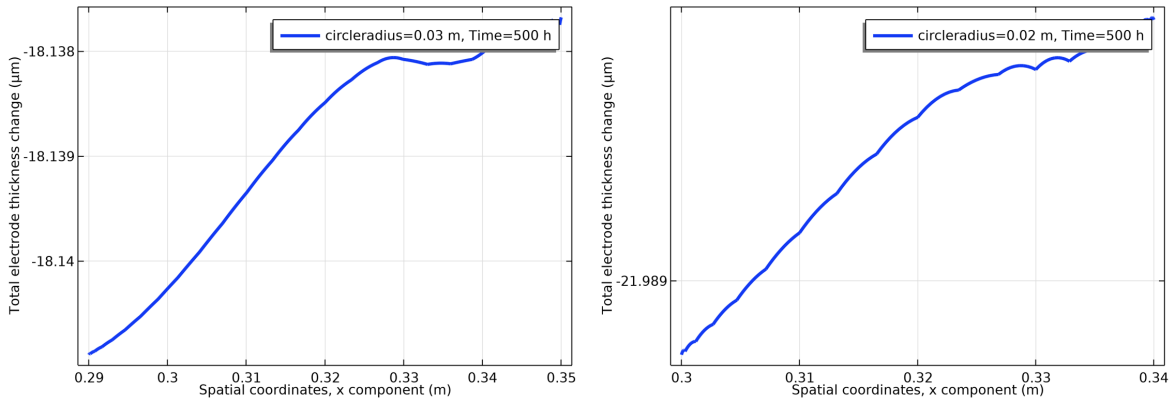

Figure 6.16: A comparison of the total thickness change between the two circle radii - the larger radius on the left, and the smaller on the right. Each plot is for the upper arc of the circle.

6.4 Flow over a Fin

Fins are designed to be conducive to flow patterns. Where in the case of a cylindrical intrusion, there was impingement on the upstream side of the circle, and stagnant flow on the downstream, fins can be designed to reduce such regions. Four different fin designs were evaluated for this study, and can be seen in figure 6.17. The top left frame in this figure is a fin which is pointed on both ends, and approximates the most basic type of fin geometry. This fin was also varied by the radius of concavity of its sides.

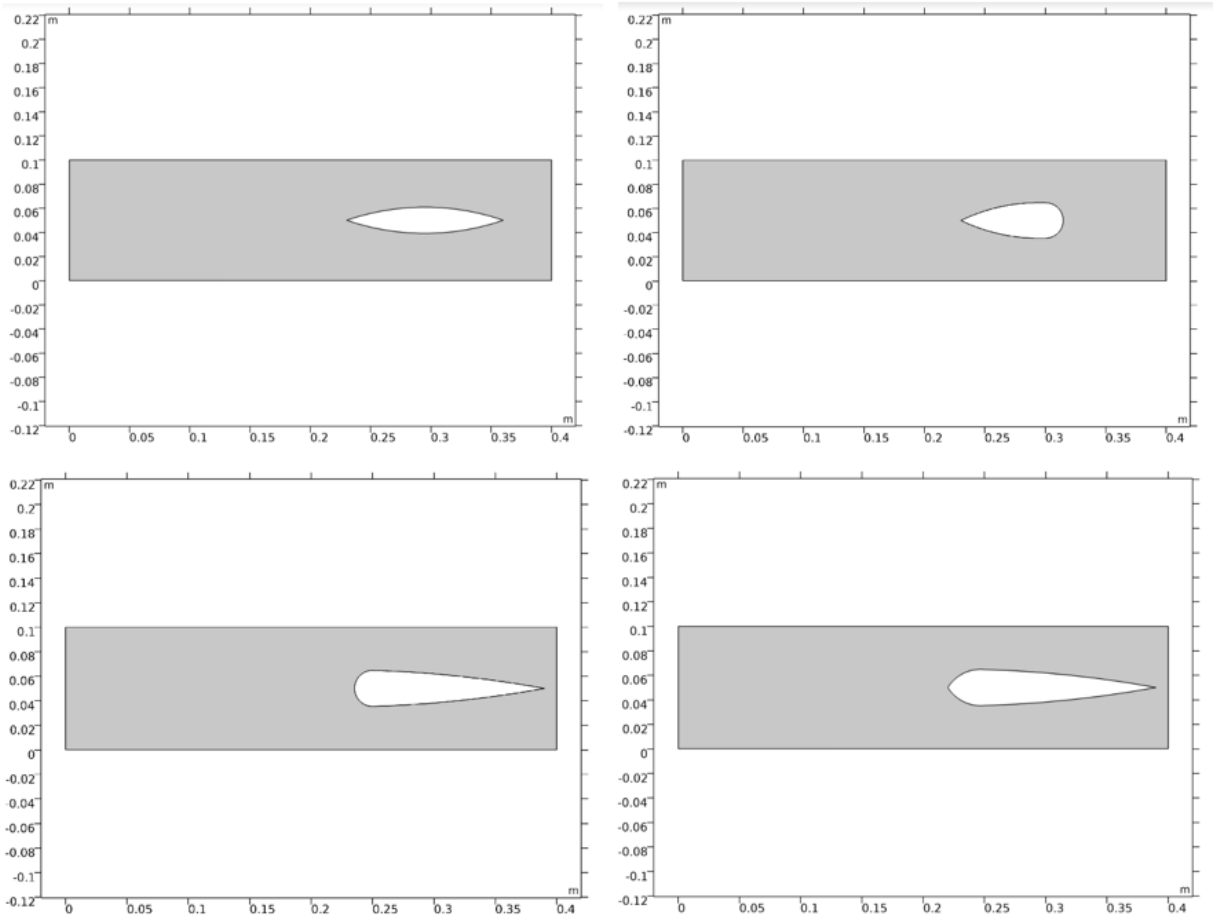

Figure 6.17: Geometries of the various fin types evaluated

The results of varying the basic fin design by concavity radius can be seen in figure 6.18. The fin was effective in reducing the impingement point on the upstream side, but still had minor stagnancy on the downstream side. Increasing the concavity radius (and

therefore reducing the size of the fin) was effective in streamlining this behavior. The points of highest velocity decreased in magnitude as the concavity radius was increased.

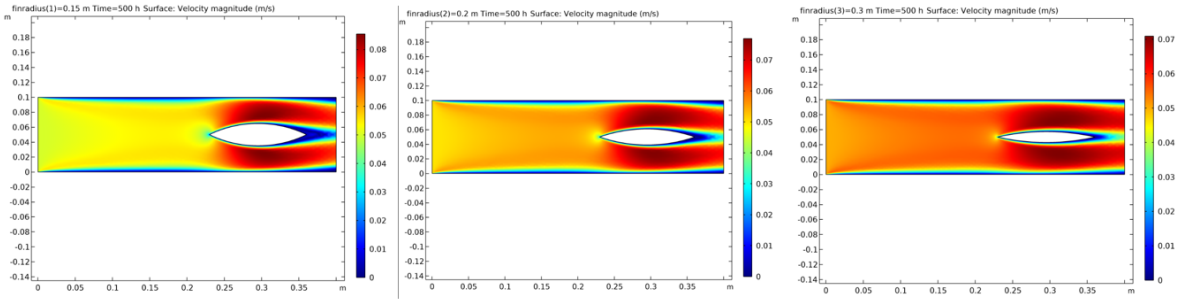

Figure 6.18: Velocity profiles for the three different fin radii, which are from left to right are r = 0.15m, r=0.2m, and r=0.3m.

The rate of thickness change for each of the three fillet radii is shown in figure 6.19. It seems for this model, a disturbance or error occurred for the fin radius of 0.15 m, the largest fin size, which caused a widely varied and positive rate of thickness change for the length of the fin. Due to this behavior, it is difficult to see what effect the fin radius has by looking at the rate of thickness change.

The effect of the fin radius on the corrosion magnitude can still be evaluated through side-by-side plots of the total thickness change, as shown in figure 6.20. When viewed in this form, the results for the fin of radius 0.15 m seems to mostly be at a steady value of -14 μm. However, due to the possible error, this value may be unreliable. The comparison between all three fin radii shows that the thinnest fin (with the largest fin radius of 0.3 m) has the most severe magnitude of thickness change. The medium sized fin thickness has the lowest thickness change of the three, suggesting a mid-range fin thickness is better for reducing corrosion rates.

Figure 6.21 shows the velocity profiles of the four different fin types. The top left frame is the fin with the smallest concavity radius of the three radial variations. The top right fin was kept at the same radius, but rounded on the back. The only difference between this and the basic fin was some resulting downstream stagnancy, which is less ideal. The

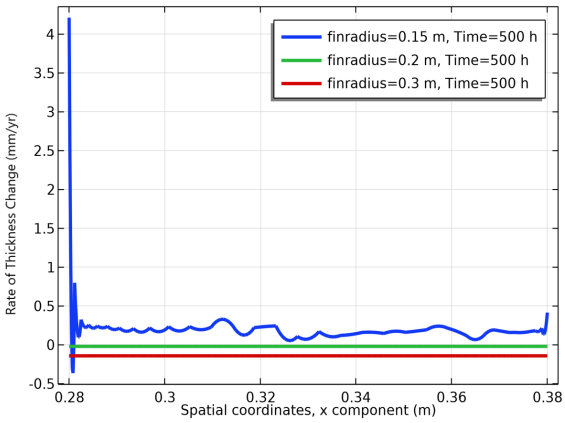

Figure 6.19: The rate of thickness change along the top boundary of the fin, for each fin radius.

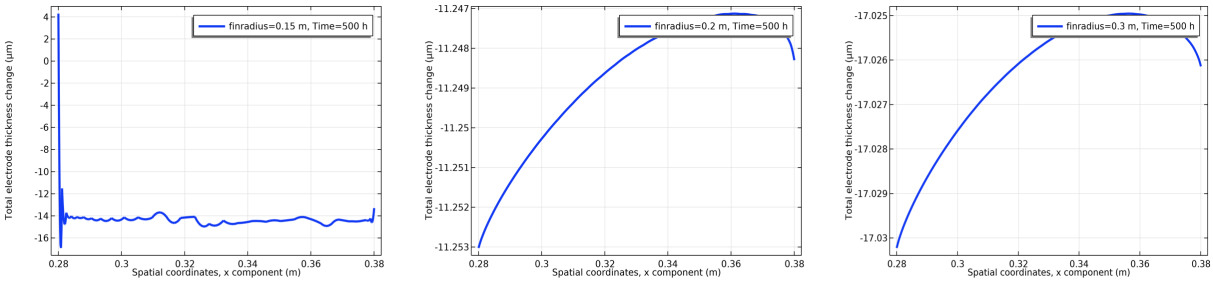

Figure 6.20: The total thickness change along the top boundary of the fin, for each fin radius, side by side for comparison.

bottom right geometry reverses this design, rounding the upstream side of the fin, and at the same time increasing the length of the downstream fin side. This shows a lesser region of stagnancy, but creates an impingement point on the upstream side of the fin. Finally, the bottom right geometry adjusts the bottom left geometry to include a pointed tip, which appeared to reduce the impingement point, while still minimizing the downstream stagnancy. The bottom right fin design appeared to be the most conducive to steady flow conditions.

Because the bottom right fin showed the most steady flow conditions, the geometry was evaluated for corrosion effect in comparison with the basic fin shape. Figure 6.22 shows the velocity of the standalone model, which includes the 'dummy electrode' method used for corrosion in this study. The fin has slight size variations from the one shown earlier in

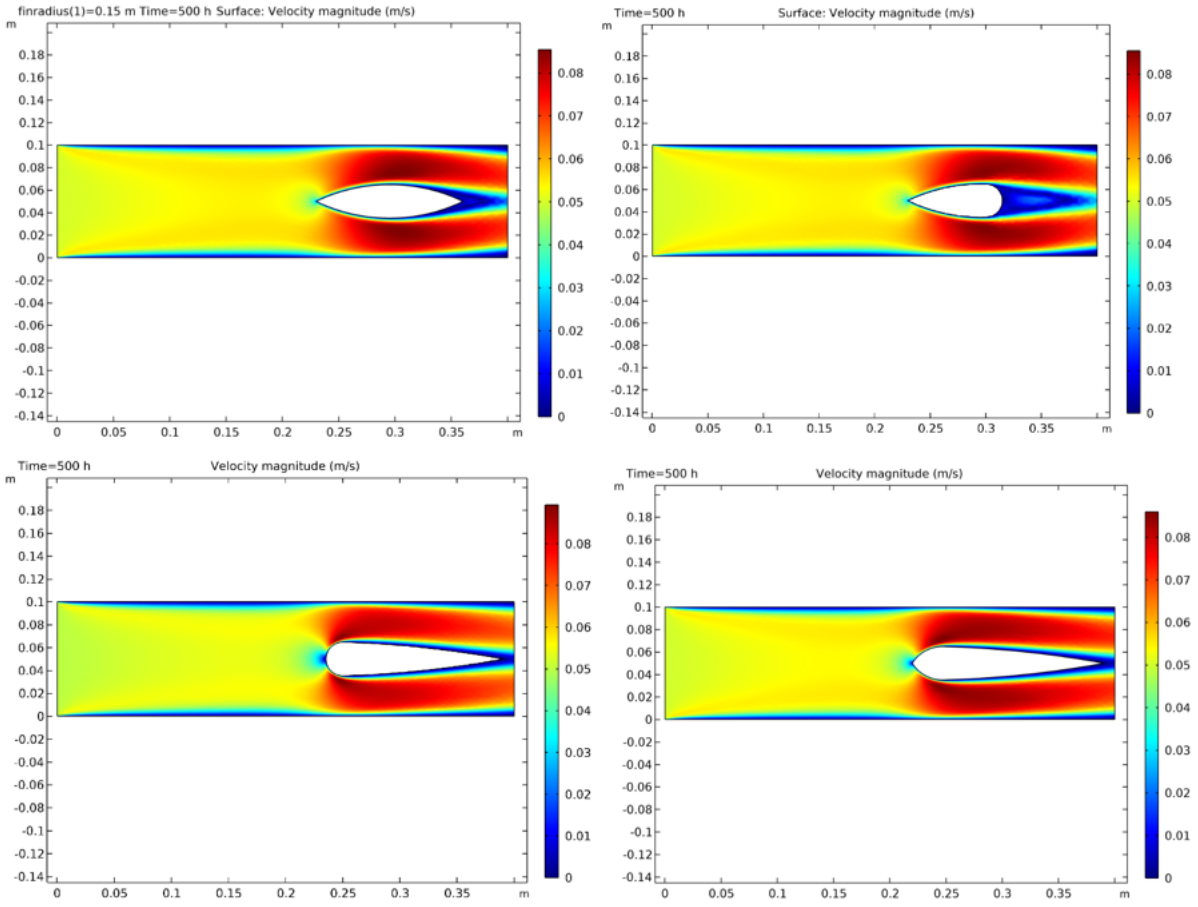

Figure 6.21: Velocity profiles for each fin type

conjunction with the other fin designs, but uses the same basic shape, with a blunt pointed upstream tip, and a lengthened downstream tip. For the purposes of the standalone model of this geometry, the shape is referred to as an 'airfoil'.

Figure 6.23 shows a comparison of the rate of thickness change between two basic fin sizes, and the airfoil. Each fin had the same shape of thickness change plot, with a more severe magnitude of corrosion toward the upstream end of the fin. Figure 6.24 shows the same plots with equalized y-axes, to show the magnitude of difference between the fin types. Although the adjustment of the fin to suit the velocity profile removed stagnant areas, it appears that this adjustment was not effective. The airfoil shape appears to have a larger magnitude of thickness change rate than both of the other fin cases. This comparison shows that the medium-sized fin (radius of 0.2 m) had a much less severe

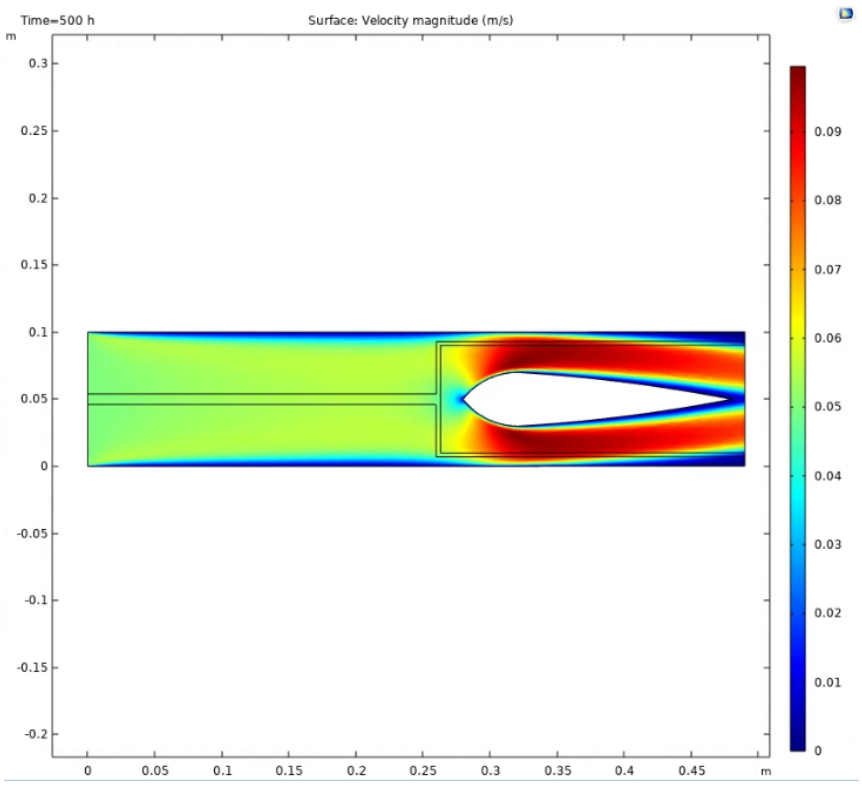

Figure 6.22: Velocity profile for the fin type optimized by velocity profile.

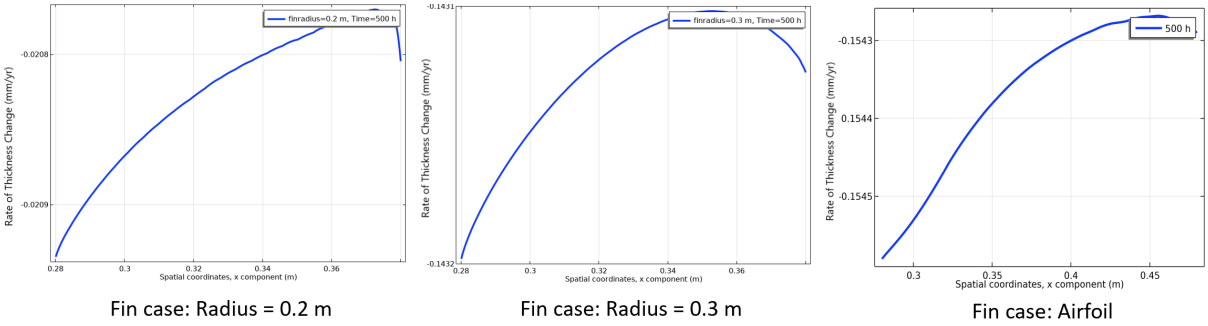

Figure 6.23: Comparison of the rate of thickness change between the fins with radius of 0.2m and 0.3m, and the airfoil shape.

corrosion magnitude than both the thinner fin, and the airfoil. The implication from this data is that adjusting the fin shape to accommodate a steadier flow is not necessarily effective for reducing corrosion magnitude. The most effective strategy in this case was to instead optimize the fin thickness.

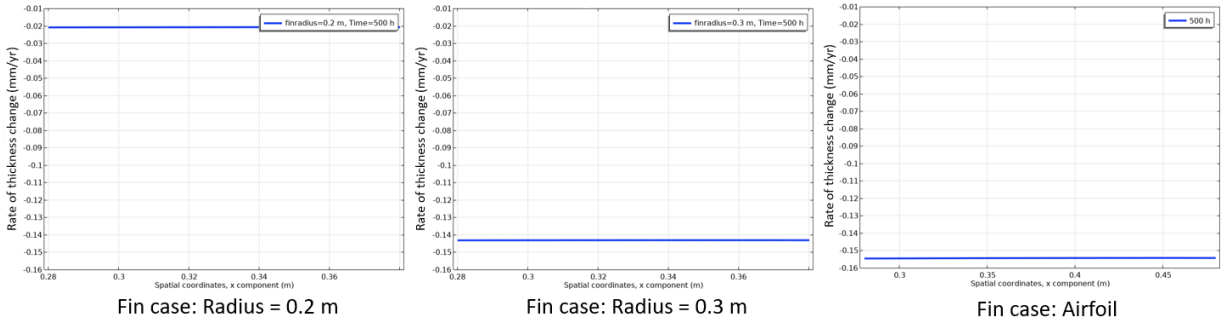

Figure 6.24: Figure 6.23, with the y-axes equalized to show the magnitude of difference between fin types.

6.5 Conclusions

The corrosion and fluid flow behavior was investigated for several different geometries, including a right-angle corner, a filleted corner, a cylindrical intrusion, and fins. The base case model has some limitations, and therefore the conclusions that can be drawn are limited. However, it can be seen that higher velocities increase the intensity of corrosion in the system. In the base case, it was seen that the total and rate of thickness change became more intense along the wall in the direction of higher flow. This is as expected, as it has been established in the literature that higher flow velocities correspond to higher corrosion rates. The base case also displayed some behavior which suggests that regions of stagnancy may also experience more corrosion intensity. Subsequently, model geometries were evaluated to attempt to optimize the velocity profiles to maintain a steady velocity, without regions of particularly high velocity, and without regions of stagnancy/low-flow.

In the case of the filleted corner, it was found that larger fillet radii resulted in a greater magnitude of corrosion. Although the increase of fillet radius appeared to reduce peak velocity, the mirroring of fillet radii across the corner resulted in areas of high-velocity fluid on the walls, as well as areas of stagnancy. When the fillet radii were adjusted separately, to conform to the general flow pattern, the velocity profile became more steady. The fillet radius combination with the steadiest flow pattern was evaluated for corrosion effect, and showed a reduced magnitude of corrosion. This behavior can be used in general design to

reduce corrosion risk. By conducting fluid modeling of a system with flow over corners, the radius of the corners and corner fillets should be adjusted to conform to the flow pattern, not just by altering the fillet radius to be more rounded, but rather by optimizing the velocity profile.

In the case of the cylindrical intrusion, represented by 2D flow over a circle, the circle with the smaller radius experienced smaller peak velocity values than the larger radius. However, adjusting the radius in the case of a circular flow disturbance did not eliminate regions of stagnant or accelerated flow. Corrosion analysis for the cylindrical intrusions showed that the circle with the smaller radius experienced greater corrosion. It was also shown that the corrosion magnitude was more dependant on the radius of the circle, rather than the location on the intrusion.

Fins are geometries designed to avoid the type of fluid impingement seen in the cylindrical intrusion case. Fins of different concavity radius and shape were evaluated for flow and corrosion magnitude. Fins with a greater concavity radius experienced lower peak velocities. However, the largest and the smallest fins both had more severe magnitudes of corrosion than the medium-sized fin. The fin geometry with the greatest success in reducing areas of impingement, stagnancy, and accelerated velocities appeared to be a fin with a slightly blunter pointed tip, and an extended downstream pointed length. Although this fin geometry appeared to produce a steadier velocity profile, the corrosion results showed that the fin shape experienced more corrosion than the basic fin shape. Thus, optimizing the fin size was more effective at reducing corrosion magnitude than optimizing the fin shape.

CHAPTER 7

Summary and Conclusions

Molten salt systems, such as molten salt nuclear reactors, solar power systems, and thermal energy storage, use molten salts for energy generation. Molten salts are extremely advantageous for these types of systems, due to their chemical and thermodynamic properties. However, research and development efforts on molten salts are recent, and some data is lacking on the behavior of salts in different types of systems. Risk analysis shows that corrosion behavior is of particular concern when designing a molten salt system, and thus it is crucial to understand molten salt corrosion behavior, in terms of system design.

In this work, the effect of corrosion on molten salt behavior was studied experimentally, and the effect of geometry on molten salt corrosion behavior was studied using COMSOL multiphysics. Experimentation included bulk testing to determine the melting temperature of molten salt samples with added corrosion-related impurities. Additional testing in a DSC was conducted to provide clarity on the bulk testing results. Modeling in COMSOL included a base case, with flow in a simple geometry with laminar flow and corrosion physics. Subsequent models were constructed with additional geometries.

Experimentation on the melting point of fluoride and nitrate molten salts showed that the eutectic melting temperature remains the same despite the addition of corrosion products (as expected). However, it was shown that as corrosion products are added, impurities can form different phases, forming a suspension of liquid and solids as the salt melts. This was clear in the visual documentation of the bulk experimentation. During melting, the liquid salt had the appearance of 'slush' or a suspension with small amounts of solids present. After cooling, the samples showed a lack of homogeneity, showing regions of color variation.

During DSC testing, this behavior was confirmed. The DSC testing showed that there

is an initial bulk melting which occurs at the eutectic melting temperature, but final melting does not occur until far above the initial melting temperature. This means that there is a range in which the molten salt is not entirely liquid, with solids remaining that have a higher melting temperature. Additional experimentation is required to determine exactly what the composition is of these solids, but it is likely that they arise from a combination of the added corrosion product impurities, and the impurities inherent in open-air sample preparation and testing. Although this open-air testing creates uncertainty in experimentation, the conditions of open-air testing are more applicable to real world systems. A large-scale molten salt system will inevitably have salt-to-air exposure, since complete isolation from atmosphere is difficult to accomplish on a large scale. Thus, it can be expected that real molten salt systems will have a level of impurities inherent in the molten salt composition. Subsequently, it can be expected that the salt will show similar behavior to the bulk melting behavior that was experienced in these tests - different phases of impurities and salt mixtures, resulting in a range of melting temperature significantly above the expected melting temperature. Molten salt system designs should account for this extended range; if a system temperature is set in the middle of the melting range, there will be small portions of the fluid that remain solid, forming a suspension, and possibly altering the flow mechanics and thermodynamic balance of the system.

Since impurities in a molten salt system can impact the melting range of the molten salt, it is desirable to minimize impurities. Corrosion can introduce impurities o to the system in the form of corrosion products, and therefore reducing corrosion can reduce system impurities. In addition, it is desireable to reduce corrosion risk, due to the severity of the consequences of corrosion in a molten salt system. A preliminary risk assessment outlined in this work determined that the most likely way to reduce corrosion risk is through corrosion control methods, or through system design changes. Modeling in COMSOL multiphysics in this study determined geometry changes which can reduce flow. The model included both laminar flow and corrosion physics, and is a first-steps model, since

a coupled flow-corrosion model has not previously been done for molten salt in COMSOL. Because of the first-steps nature of the model, some limitations were inherent in the results. However, it was determined that a flow velocity profile can be telling in where corrosion will be more intense, particularly in regions of peak fluid velocity, or possibly in regions of stagnancy/low-flow compared to the bulk flow. Higher system velocities also tended to increase corrosion rate, indicating that a lower overall system velocity can reduce corrosion risk. Geometries investigated were a right-angle corner with and without fillets, a perpendicular cylindrical intrusion, and four different fin types. Geometry changes which were most effective at reducing corrosion were:

- Optimizing fillet radius to suit velocity profile
- Increasing the radius of circular shapes
- Optimizing the size of a fin, rather than the shape of a fin

To conclude, from this work was determined several design considerations which can reduce the overall corrosion risk of a molten salt system. First, impurities inherent in molten salt systems may extend the melting range of the salt, and so it is necessary to have a system temperature above the melting range to maintain an entirely liquid phase. Second, geometric changes to a system can reduce corrosion, in particular where the geometric changes are made to optimize the velocity profile.

Bibliography

[1] D. Blight, E. Engmann, J. Peterson, J. Richards, W. Sowah, and J. Warner, "Design of the Molten Salt Nuclear Battery - in fulfillment of the course requirements for NE 575," tech. rep., University of Idaho, 2019.

[2] J. P. Carter, T. Casper, K. Geddes, D. Haar, T. Lasley, and S. Lucas, "Microscale Nuclear Battery Shielding and Fuel Cycle (Front-to-Back End)," in fulfillment of course requirement for NE 575, University of Idaho, 2021.

[3] J. Zhang, C. W. Forsberg, M. F. Simpson, S. Guo, S. T. Lam, R. O. Scarlat, F. Carotti, K. J. Chan, P. M. Singh, W. Doniger, K. Sridharan, and J. R. Keiser, "Redox potential control in molten salt systems for corrosion mitigation," *Corrosion Science*, vol. 144, pp. 44–53, Nov. 2018.

[4] B. C. Kelleher, *Purification and Chemical Control of Molten Li2BeF4 for a Fluoride Salt Cooled Reactor*. Dissertation, University of Wisconsin-Madison, 2015.

[5] K. Sridharan and T. Allen, "Corrosion in Molten Salts," in *Molten Salts Chemistry*, pp. 241–267, Elsevier, 2013.

[6] M. Gibilaro, L. Massot, and P. Chamelot, "A way to limit the corrosion in the Molten Salt Reactor concept: the salt redox potential control," *Electrochimica Acta*, vol. 160, pp. 209–213, Apr. 2015.

[7] G. Yamazaki, J. Yagi, T. Tanaka, T. Watanabe, and A. Sagara, "Corrosion Mitigation of Ferritic Steels in HF-Containing FLiNaK by Titanium Sacrificial Anodes," *Plasma and Fusion Research*, vol. 13, pp. 3405079–3405079, June 2018.

[8] N. D. Bull Ezell, R. Kisner, N. Russell, F. K. Reed, P. Champlin, J. Keiser, A. Martin, and D. Holcomb, "Development of a Corrosion Monitoring System for Molten Salt Reactors," Tech. Rep. ORNL/TM-2019/1273, Oak Ridge National Laboratory, Aug. 2019.

[9] D. F. Williams and P. F. Britt, "Technology and Applied R&D Needs for Molten Salt Chemistry," tech. rep., Oak Ridge National Laboratory, Apr. 2017.

[10] Serp, "The molten salt reactor (MSR) in generation IV: Overview and perspectives," *Progress in Nuclear Energy*, vol. 77, pp. 308–319, Nov. 2014.

[11] T. J. Dolan, *Molten Salt Reactors and Thorium Energy*.

[12] "EPA Superfund Record of Decision," DOE/OR/02-1671&D2, Oak Ridge National Laboratory, Oak Ridge Reservation (USDOE), Molten Salt Reactor Experiment, Sept. 1998.

[13] "STJ-02MSRE-D992 / Molten Salt Reactor Experiment Engineering Evaluation and Extended Life Study, URS | CH2M Oak Ridge LLC, Oak Ridge, Tennessee," p. 157.

[14] M. F. Simpson, "Developments of Spent Nuclear Fuel Pyroprocessing Technology at Idaho National Laboratory," Tech. Rep. INL/EXT-12-25124, Idaho National Laboratory, Mar. 2012.

[15] M. F. Simpson and J. D. Law, "Nuclear Fuel Reprocessing," Tech. Rep. INL/EXT-10-17753, Idaho National Laboratory, Feb. 2010.

[16] V. Utgikar, "Pyroprocessing schematic," 2019.

[17] C. Yu, X. Li, X. Cai, C. Zou, Y. Ma, J. Han, and J. Chen, "Analysis of minor actinides transmutation for a Molten Salt Fast Reactor," *Annals of Nuclear Energy*, vol. 85, pp. 597–604, Nov. 2015.

[18] World Nuclear Association, "Molten Salt Reactors," May 2021.

[19] "Europe - evol's molten salt fast reactor." https://www.daretothink.org/europe-evols-molten-salt-fast-reactor/, Feb. 2015. Accessed: 2022-3-19.

[20] V. Ignatiev, O. Feynberg, I. Gnidoi, S. Konakov, M. Kormilistyn, A. Merzliakov, A. Surenkov, V. Uglov, and A. Zagnitko, "MARS: Story on Molten Salt Actinide Recycler and Transmuter Development by Rosatom in Co-Operation with Euratom," Tech. Rep. NEA/NSC/R(2015)2, NRC Kurchatov Institute, Russian Federation, 2015.

[21] "Samofar." http://samofar.eu/. Accessed: 2022-04-27.

[22] L. F. Cabeza, *Advances in Thermal Energy Storage Systems: Methods and Applications*. Elsevier, Oct. 2014.

[23] U.S. Department of Energy, "2014: The Year of Concentrating Solar Power," Tech. Rep. DOE/EE-1101, May 2014.

[24] W. Ding, H. Shi, A. Jianu, Y. Xiu, A. Bonk, A. Weisenburger, and T. Bauer, "Molten chloride salts for next generation concentrated solar power plants: Mitigation strategies against corrosion of structural materials," *Solar Energy Materials and Solar Cells*, vol. 193, pp. 298–313, May 2019.

[25] C. S. Turchi, J. Vidal, and M. Bauer, "Molten salt power towers operating at 600-650 c: Salt selection and cost benefits," *Solar Energy*, vol. 164, pp. 38–46, Apr. 2018.

[26] R. W. Bradshaw, D. B. Dawson, W. De La Rosa, R. Gilbert, S. H. Goods, M. J. Hale, P. Jacobs, S. A. Jones, G. J. Kolb, J. E. Pacheco, M. R. Prairie, H. E. Reilly, S. K. Showalter, and L. L. Vant-Hull, "Final Test and Evaluation Results from the Solar Two Project," Tech. Rep. SAND2002-0120, 793226, Jan. 2002.

[27] J. Pacheco, "Final Test and Evaluation Results fromt he Solar Two Project," Tech. Rep. SAND2002-0120, Sandia National Laboratory, 2002.

[28] M. Green, P. Sabharwall, G. Mckellar, S.-J. Yoon, C. Abel, B. Petrovic, and D. Curtis, "Nuclear Hybrid Energy System: Molten Salt Energy Storage," Tech. Rep. INL/EXT-13-31786, Idaho National Laboratory, Nov. 2013.

[29] T. Bauer, N. Pfleger, D. Laing, W.-D. Steinmann, M. Eck, and S. Kaesche, "High-Temperature Molten Salts for Solar Power Application," in *Molten Salts Chemistry*, pp. 415–438, Elsevier, 2013.

[30] R. Roper, P. Sabharwall, and R. Christensen, "Chemical Overview of Molten Salts," (Minneapolis, Minnesota).

[31] S. Guo, J. Zhang, W. Wu, and W. Zhou, "Corrosion in the molten fluoride and chloride salts and materials development for nuclear applications," *Progress in Materials Science*, vol. 97, pp. 448–487, Aug. 2018.

[32] Manohar S. Sohal, Matthias A. Ebner, Piyush Sabharwall, and Phil Sharpe, "Engineering Database of Liquid Salt Thermophysical and Thermochemical Properties," Tech. Rep. INL/EXT-10-18297, 980801, Mar. 2010.

[33] M. Rosenthal, P. Haubenreich, and R. Briggs, "The Development Status of Molten Salt Breeder Reactors," Tech. Rep. ORNL 4812, Oak Ridge National Laboratory, 1972.

[34] C. Wang, H. Qin, W. Tian, S. Qiu, and G. H. Su, "Transient analysis of tritium transport characteristics of thorium molten salt reactor with solid fuel," *Annals of Nuclear Energy*, vol. 141, p. 107337, June 2020.

[35] S. S. Raiman and S. Lee, "Aggregation and data analysis of corrosion studies in molten chloride and fluoride salts," *Journal of Nuclear Materials*, vol. 511, pp. 523–535, Dec. 2018.

[36] B. Merk, D. Litskevich, R. Gregg, and A. R. Mount, "Demand driven salt clean-up in a molten salt fast reactor - Defining a priority list," *PLOS ONE*, vol. 13, p. e0192020, Mar. 2018.

[37] "Report for the US Department of Energy Office of Nuclear Energy Workshop, Molten Salt Chemistry Workshop: Technology and Applied R&D Needs for Molten Salt Chemistry," tech. rep., Apr. 2017.

[38] A. Badiea and K. Mohana, "Effect of temperature and fluid velocity on corrosion mechanism of low carbon steel in presence of 2-hydrazino-4,7-dimethylbenzothiazole in industrial water medium," *Corrosion Science*, vol. 51, pp. 2231–2241, Sept. 2009.

[39] R. Alonso Gil and A. Igual Munoz, "Influence of the sliding velocity and the applied potential on the corrosion and wear behavior of hc cocrmo biomedical alloy in simulated body fluids," *Journal of the Mechanical Behavior of Biomedical Materials*, vol. 4, pp. 2090–2102, Nov. 2011.

[40] S. a. Zadeh and P. Rashidi, "The effect of fluid velocity and microstructure on erosion corrosion of two-phase CK45 steel," *Results in Materials*, vol. 6, p. 100077, June 2020.

[41] R. Elgaddafi, R. Ahmed, and S. Shah, "The effect of fluid flow on CO2 corrosion of high-strength API carbon steels," *Journal of Natural Gas Science and Engineering*, vol. 86, p. 103739, Feb. 2021.

[42] J. Yang, S. Wang, J. Wang, and X. Tang, "Effect of high flow velocity on corrosion behavior of Ni based and Ni-Fe based alloys in supercritical water oxidation environment," *The Journal of Supercritical Fluids*, vol. 170, p. 105126, Apr. 2021.

[43] Y. Wang, B. Wang, X. Xing, S. He, L. Zhang, and M. Lu, "Effects of flow velocity on the corrosion behaviour of super 13Cr stainless steel in ultra-HTHP CO2-H2S coexistence environment," *Corrosion Science*, vol. 200, p. 110235, May 2022.

[44] X. Zhang, C. Zhang, Y. Wu, and Y. Lu, "Experimental research of high temperature dynamic corrosion characteristic of stainless steels in nitrate eutectic molten salt," *Solar Energy*, vol. 209, pp. 618–627, Oct. 2020.

[45] L. Gonzalez-Fernandez, M. Intxaurtieta-Carcedo, O. Bondarchuk, and Y. Grosu, "Effect of dynamic conditions on high-temperature corrosion of ternary carbonate salt for thermal energy storage applications," *Solar Energy Materials and Solar Cells*, vol. 240, p. 111666, June 2022.

[46] L. Ma, C. Zhang, Y. Wu, and Y. Lu, "Comparative review of different influence factors on molten salt corrosion characteristics for thermal energy storage," *Solar Energy Materials and Solar Cells*, vol. 235, p. 111485, Jan. 2022.

[47] A. Mallco, F. Pineda, M. Mendoza, M. Henriquez, C. Carrasco, V. Vergara, E. Fuentealba, and A. G. Fernandez, "Evaluation of flow accelerated corrosion and mechanical performance of martensitic steel T91 for a ternary mixture of molten salts for CSP plants," *Solar Energy Materials and Solar Cells*, vol. 238, p. 111623, May 2022.

[48] L. Ma, C. Zhang, Y. Wu, and Y. Lu, "Effect of flow rate and SiO2 nanoparticle on dynamic corrosion behavior of stainless steels in molten salt for thermal energy storage," *Corrosion Science*, vol. 194, p. 109952, Jan. 2022.

[49] D. Jones, A., *Principles and Prevention of Corrosion.* Prentice Hall, 2nd ed., 1996.

[50] J. Zhang and S. Guo, "Rare Earth Electrochemical Property Measurements and Phase Diagram Development in a Complex Molten Salt Mixture for Molten Salt Recycle," Tech. Rep. 14-6489, 1432448, Mar. 2018.

[51] S. Guo, N. Shay, Y. Wang, W. Zhou, and J. Zhang, "Measurement of europium (III)/europium (II) couple in fluoride molten salt for redox control in a molten salt reactor concept," *Journal of Nuclear Materials*, vol. 496, pp. 197–206, Dec. 2017.

[52] G. Duran-Klie, D. Rodrigues, and S. Delpech, "Dynamic Reference Electrode development for redox potential measurements in fluoride molten salt at high temperature," *Electrochimica Acta*, vol. 195, pp. 19–26, Mar. 2016.

[53] T. Warchilova, V. Dillingerova, R. Skoda, T. Simo, O. Matal, T. Vaculovic, and V. Kanicky, "Corrosion of nickel-based structural materials for nuclear reactors by molten fluoride salt: From bulk content of corrosion products to elemental imaging of corrosion changes," *Spectrochimica Acta Part B: Atomic Spectroscopy*, vol. 148, pp. 113–117, Oct. 2018.

[54] G. W. Oehlert, *A first course in design and analysis of experiments*. New York: W.H. Freeman, 2000.

[55] G. Hohne, W. Hemminger, and H.-J. Flammersheim, *Differential scanning calorimetry*, vol. 380. Springer, Oct. 2004.

[56] Metso:Outotec, "Hsc Chemistry." https://www.hsc-chemistry.com/. Accessed: 2022-07-08.

[57] M. Tabatabaian, *COMSOL for engineers*. Dulles, Virginia: Mercury Learning and Information, 2014.

[58] COMSOL Multiphysics, *Corrosion Module User's Guide*. 5.4 ed., 2018.

[59] COMSOL Multiphysics Support Center, "Personal Communication," Mar. 2022.

[60] "COMSOL Multiphysics Reference Manual," p. 1742.

[61] W. Wu, S. Guo, and J. Zhang, "Exchange Current Densities and Charge-Transfer Coefficients of Chromium and Iron Dissolution in Molten LiF-NaF-KF Eutectic," *Journal of The Electrochemical Society*, vol. 164, no. 13, pp. C840–C844, 2017.

Appendix A: Risk Assessment of a Molten Salt System Design

The following is the full report for a risk assessment conducted on a sample molten salt system, in 2021.

Risk Assessment of a Molten Salt Reactor Design - Conducted in Spring 2021 in Fulfillment of NE 529 at the University of Idaho

Note: This report has been modified for the purposes of this dissertation appendix. Changes from its original form have been made to remove proprietary and/or irrelevant information.

Executive Summary

Molten salt reactors (MSRs) are an advanced type of reactor design which operates using liquid fuel rather than solid fuel. A MSR design utilizes molten salt with fissile material dissolved directly into the salt, combining the coolant and fuel. This concept was proved in the 1960s with the Molten Salt Reactor Experiment (MSRE). Currently, a MSR design is underway at the University of Idaho, called the Molten Salt Nuclear Battery, or MsNB.

The MsNB is a 10MWth molten salt microreactor, which has been designed to allow for easy factory construction and transport to remote areas to support critical infrastructure with electricity and heat. It utilizes molten Flinak salt (LiF-NaF-KF) with dissolved uranium tetrafluoride. The MsNB is unique in design, containing no pumps or valves. Instead, the MsNB uses natural circulation to drive coolant flow. This unique design adds a level of inherent safety to the already inherently safe MSR concept. The MsNB has finished its preliminary design stages, and is moving to a secondary design stage of validation and testing. To test the MsNB, DOE authorization and NRC licensing will be necessary. However, to accomplish authorization and licensing, the MsNB design will need to be assessed for safety and functionality of design. To this end, a preliminary risk assessment was performed on the MsNB, to assess major hazards and possible failures that could occur in the current reactor design.

The risk assessment of the MsNB in this work consisted of a preliminary hazard analysis (PHA) and a failure modes and effects analysis (FMEA). These analyses were performed using the most current version of design documents provided. The boundaries of the analysis focused primarily on the reactor itself, excluding any secondary systems. General facility concerns were accounted for, including general accident scenarios. The MsNB was divided into regions, or 'nodes', for ease of analysis. The PHA and FMEA were performed on each node, identifying and ranking the hazards and possible failures at each node. Hazards which ranked above an unacceptability threshold were identified for further discussion.

The results of the PHA and FMEA showed that a primary concern for the current stage of reactor design is corrosion. The current design for the MsNB does not include any type of corrosion control system, which means corrosion hazards were ranked particularly high. In

addition to corrosion, other hazards which ranked highly were containment breach, salt release, deposit buildup, and heat exchanger damage.

Possible mitigations for the identified hazards and failures were investigated to lower overall risk. Corrosion control methods such as redox control, sacrificial anodes, and molten salt purification would reduce the likelihood of corrosion in this system. In addition, a maintained positive pressure differential from the salt to the air in the heat exchanger would lessen the severity of a breach in the heat exchanger. Other alternative mitigations to identified hazards include minor geometry and design changes, use of corrosion-resistant materials, and molten-salt-specific emergency response procedures. The PHA and FMEA results were reevaluated based on these possible mitigations. It was shown that a corrosion control system would be highly effective in reducing risks in this design, and a layered and thorough corrosion control system will be crucial for future design phases of the MsNB.

Phase I - Risk Assessment

1 Introduction

Advanced nuclear reactor design is a complex process, involving modeling, experimentation, and demonstration of functionality and energy production. A crucial component of advanced reactor design is risk assessment, which is heavily involved in all stages of design. Risk assessment aims to identify issues with a reactor design that pose a risk to both safety and equipment. Preliminary stages of risk assessment focus on identifying hazards and risks early in the design process so that design changes can be made to address major problems. The work detailed in this report is a preliminary risk assessment of an advanced reactor design, that of the Molten Salt Nuclear Battery (MsNB). Many risk assessment tools are available for preliminary risk analysis, and this work utilized a preliminary hazard analysis, and a failure mode and effects analysis, to assess possible hazards and failures which may be detrimental to the early design of the MsNB.

1.1 Motivation

The Molten Salt Nuclear Battery (MsNB) is a molten salt microreactor design currently in progress at the University of Idaho, in collaboration with MicroNuclear LLC. The MsNB is designed to allow for easy factory construction and transport to remote areas to support critical infrastructure with electricity and heat. The MsNB project is currently moving from a preliminary design phase into testing implementation, and therefore requires DOE authorization and NRC licensing. As part of the regulatory process, the MsNB needs to be demonstrated as a safe, functional reactor design. A preliminary risk assessment is a crucial tool to identifying design deficiencies which will require changes before DOE authorization is possible, and therefore a preliminary risk assessment was performed for the current MsNB design, to aid in the transition to secondary design and testing phases.

1.2 Goals

The goals of this analysis was to perform a preliminary hazard analysis (PHA) and a failure mode and effects analysis (FMEA) for the MsNB, for the purpose of identifying design deficiencies in the early MsNB design. The following workscopes and tasks were submitted in the proposal for this project:

Workscope 1. Qualitative Hazard Review.

Task I. Literature Review and Boundary Establishment. A review of design documents and existing literature will be conducted to establish system boundaries, as well as to discover previous work in similar areas.

Task II. Hazard Identification and Review. Hazards, accidents, and accident sequences will be identified for the system, including the reactor vessel and the preliminary facility design.

Workscope 2. PHA, FMEA, and Safety Feature Documentation.

Task III. Preliminary Hazard Analysis. The hazards identified in task II will be assessed qualitatively using a preliminary hazard analysis.

Task IV. Failure Mode and Effects Analysis The PHA developed in task III will be expanded into a FMEA, focusing on the MsNB and its immediate facilities.

Task V. Documentation and Assessment of Safety Features. Safety features and recommendations will be identified to address the results of tasks III and IV. A report will be generated with the results of workscope 2.

2 Background

The Molten Salt Nuclear Battery (MsNB) is a liquid-fueled MSR design, which uses Flinak (LiF-NaF-KF) salt with dissolved UF_4. The MsNB is a microreactor, intended for easy factory construction and transport to remote areas. The reactor is designed for a 10-year lifecycle, at which point it can be shipped back to a central location for waste processing and decommissioning. It is a unique design, because unlike other reactor designs of its type, the MsNB uses no pumps or valves. Instead, the MsNB coolant flow is driven by natural circulation. Density differences between hot and cooled salt in different regions of the reactor drive flow up and around the reactor geometry. Section 3.1 of this work contains a detailed description of the MsNB design. Design details for this risk assessment were taken from reports generated at the University of Idaho (1; 2), as well as proprietary design documents. A simplified schematic of the design of the MsNB is shown in figure 1. The reactor design analyzed for this risk assessment was a smaller version of the original MsNB design, intended for operation in a testing facility to establish reactor behavior and model validity. The MsNB has two main system which control the salt flow and power generation: 1) a core region which produces 400 kW_{th} of heat, and 2) a circular heat exchanger region containing offset strip-fin heat exchangers paired to an air-Brayton or Helium-Brayton secondary cycle. The reactor design also contains proprietary core and reactor internals, to aid in neutronic and flow function.

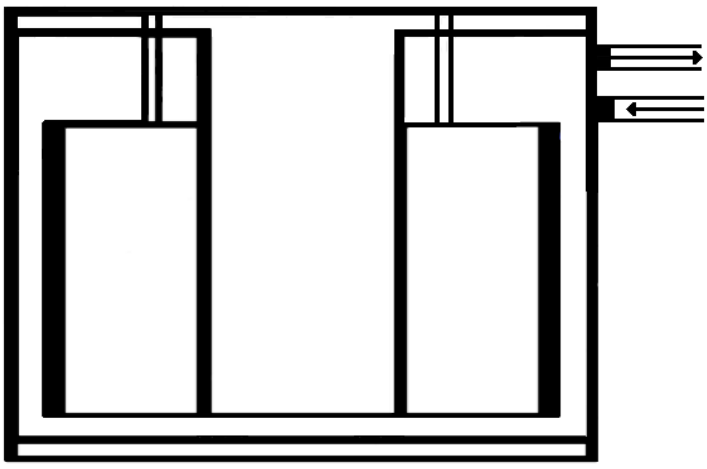

Figure 1: Schematic of the MsNB, simplified to remove proprietary design details.

3 Methodology

3.1 Assumptions

Before performing the PHA and FMEA, it was first necessary to establish boundaries for the analysis. The reactor boundary for this analysis is the reactor itself, with no designed secondary system. The analysis focused on general features, rather than minute detail, since the scope of this analysis is general hazards and failures. Since facility concerns are important for a risk assessment analysis of this type, a general facility with no specific design was assumed. This general facility includes a theoretical air-Brayton or helium-Brayton cycle. The reactor itself contains Flinak (LiF-KF-NaF) salt, with dissolved uranium tetrafluoride.

Referring to the simplified reactor schematic shown in figure 1, the flow travels up the center core region, across the top, and down through the heat exchanger and downcomer. The reactor operates using natural circulation, which is driven by the density difference between the hot and cold regions of fluid. The entire structure at this stage is assumed to be constructed of 316 stainless steel. The control scheme for the reactor is large control drums, which operate in the internal space of the reactor between the inner and outer flow regions. The control drums are the only moving part in the entire reactor structure. The heat exchanger is an offset strip-fin heat exchanger (HX), with air or helium as a secondary coolant.

3.2 Analysis Structure

Two analyses were conducted; a preliminary hazard analysis (PHA) and a failure mode and effects analysis (FMEA). The purpose of the preliminary hazard analysis is to assess the hazards of a system, causes of those hazards, and what effect those hazards will have on the system. The FMEA is similar, but focuses on a 'what can go wrong?' system of evaluating the hazards, and determines what type of failures will occur, and the effect of those failures.

The structure of the PHA follows recommendations from the CCPS manual for hazard evaluation procedures (3). Figure 2 shows the risk matrix used for the PHA and FMEA analysis. The structure for the PHA is as follows:

- Identify hazards at each node
- Identify the cause of each hazard
- Identify the major effects of each hazard
- Rank the severity and likelihood of each hazard using the risk matrix.
- Using the risk matrix, label the hazard as low, moderate, high, or extremely high risk.

The FMEA followed a similar procedure, using the same risk matrix shown in figure 2. The FMEA procedure is as follows:

- Identify possible failures at each node
- Identify the effect of the failure
- Rank the severity of the failure, using the risk matrix
- Rank the possible occurrence of the failure, using the risk matrix
- Calculate the Risk Priority Number (RPN) by multiplying the severity and occurrence rankings.

0 – 5 = Low Risk 6 – 10 = Moderate Risk 11 – 15 = High Risk 16 – 25 = extremely high unacceptable risk		Severity of the potential injury/damage				
		Insignificant damage to Property, Equipment or Minor Injury **1**	Non-Reportable Injury, minor loss of Process or slight damage to Property **2**	Reportable Injury moderate loss of Process or limited damage to Property **3**	Major Injury, Single Fatality critical loss of Process/damage to Property **4**	Multiple Fatalities Catastrophic Loss of Business **5**
Likelihood of the hazard happening	Almost Certain **5**	5	10	15	20	25
	Will probably occur **4**	4	8	12	16	20
	Possible occur **3**	3	6	9	12	15
	Remote possibility **2**	2	4	6	8	10
	Extremely Unlikely **1**	1	2	3	4	5

Figure 2: Risk matrix used for the PHA and FMEA. The PHA used the qualitative legend categorizations, and the FMEA used the numerical categorizations in each box.

After the PHA and FMEA are complete for the system, the highest risk failures and hazards were collected and assessed for common trends and causes. Preventative measures and possible mitigations were assessed, and the effect of these preventative measures was evaluated by recalculating the risk level and RPN for the hazards. The threshold for considering a hazard or failure differs for the PHA and the FMEA. It is impossible to mitigate all hazards, so an acceptability level needs to be set for which hazards and failures are acceptable or unacceptable. For the PHA results, a hazard that is rated 'high' or 'extremely high' is unacceptable. This means that the severity, likelihood, or both is high enough that the hazard cannot be allowed to go unmitigated in the system. For the FMEA, an RPN of 9 or higher indicates the same level of unacceptable risk.

To simplify analysis, the reactor and analysis areas have been separated into regions of focus, or 'nodes'. These nodes are important regions and systems within the analysis boundaries of the reactor. The PHA and FMEA will focus on what is contained in the designated nodes. The nodes include the flow areas for the molten salt in the reactor, as well as the control drums, instrumentation, and general facility concerns. The nodes are as follows:

- Node 1: Core
- Node 2: Upper Distribution Region
- Node 3: Heat Exchanger Region
- Node 4: Downcomer
- Node 5: Lower Distribution Region
- Node 6: Control Drums
- Node 7: General Facility Concerns
- Node 8: Instrumentation

Figure 3 shows the location of nodes 1-6 in the reactor.

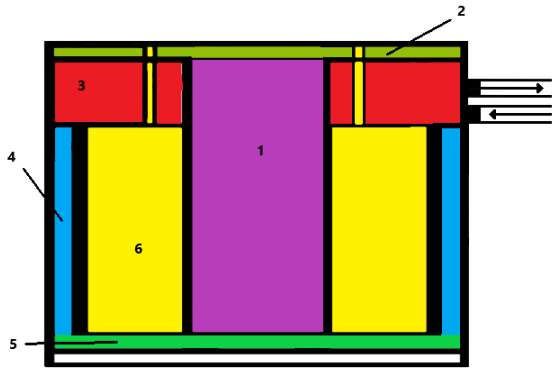

Figure 3: Location of nodes 1-6 in the MsNB. Labels are as follows: (1)-Core (2)-Upper Distribution Region (3)-Heat Exchanger Region (4)-Downcomer (5)-Lower Distribution Region (6)-Control Drums

3.2.1 Node 1: Core

The core region is a cylindrical chamber through which the molten salt flows, becomes critical, and heats up. There are no moving parts in the core, and additional proprietary reactor internals are located in the core, constructed of stainless steel 316, and graphite.

3.2.2 Node 2: Upper Distribution Region

The upper distribution is a disk-shaped region. The flow from the core comes from the outlet of the core and flows outward, toward the outer HX region and annulus. The upper distribution region contains intrusions through the top of the core, allowing access for controls and instrumentation.

3.2.3 Node 3: Heat Exchanger

The heat exchanger (HX) is an offset strip-fin heat exchanger.The heat exchanger includes fins of SS316, with alternating air and salt layers. The salt flow goes through the heat exchanger, downwards toward the downcomer region.

3.2.4 Node 4: Downcomer

The downcomer region is the thin annular region between the HX and the lower distribution region. It contains no extra structures, and is simply a narrow, circular flow region.

3.2.5 Node 5: Lower Distribution Region

The lower distribution region is similar to the upper distribution region, but with no intrusions. The region includes the core inlet, which contains a SS316 proprietary inlet structure.

3.2.6 Node 6: Control Drums

The control drums are large rotating cylinders, which can be rotated to move moderating material toward or away from the core. The control drums are buried in the internal structure of the MsNB, and do not contact the salt flow. The drives penetrate through the top of the core, and are protected from the salt flow in the intrusion area by SS316 'cans' surrounding the intrusion.

3.2.7 Node 7: General Facility Concerns

Since no facility design yet exists for the MsNB, only general facility concerns will be addressed in this analysis. The secondary cooling system is at this stage considered part of this general facility. The purpose of the secondary cooling system is to remove heat from the reactor by way of the heat exchangers (node 3). Hazards and failures within the facility could cause the secondary cooling system to malfunction, affecting the heat removal from the reactor. Hazards and failures within a general facility could also include natural disasters such as earthquakes, flooding, or power loss. These are the types of failures and hazards which will be considered at this node.

3.2.8 Node 8: Instrumentation

An instrumentation system has not yet been designed for the MsNB, but concerns of instrumentation are still important to consider for this analysis. A very basic instrumentation structure will be considered for this analysis, which includes thermocouples (TCs) and self-powered neutron detectors (SPNDs) embedded in reactor internals.

4 Results

4.1 Preliminary Hazard Analysis

A separate table was constructed for each node. This section contains the tables for the PHA at each node, consisting of tables 1-9.

Hazards for the PHA were decided based on the structure of the reactor, and included things such as corrosion of specific structures, freezing or overheating of the fuel salt, or failures of moving or electrical parts. Corrosion hazards are particularly prevalent at places referred to as 'focal points'. These focal points for corrosion are places where corrosion is more likely to occur, such as bends, right angles, areas where flow is directed at a material or particularly strong, or places where there is a defect or existing damage.

Table 1: PHA for node 1: Core

Hazard	**Cause**	**Major Effects**	**Severity and Likelihood**	**Hazard Category**
Overheating	Supercriticality, loss of cooling, loss of flow, stagnant flow	wall damage, reactor shutdown, damage to reactor internals	3/1	Low Risk
Salt Freezing	Lack of core heating, loss of flow, stagnant flow	Blockage, focal points for corrosion	2/1	Low Risk
Corrosion of reactor internals	Corrosion control failure, salt impurities, defect or damage in SS316 cladding	Damage to reactor internals, instrumentation damage, impurity addition to salt by corrosion products	3/4	High Risk
Corrosion of core wall	Corrosion control failure, salt impurities, defect or damage creating focal point	Wall damage, possible wall breach, addition of corrosion products to salt	4/4	Extremely High Risk
Outlet Buildup	Corrosion and fission product deposit, impurity deposit	Corrosion of core outlet, possible blockage or flow impedance	3/3	Moderate Risk

Table 1 shows hazards for the core region. The major hazards for this region are overheating, salt freezing, and corrosion. Overheating is a typical hazard for a reactor core. The severity and likelihood of this hazard is lower due to the neutronics of the core. By inherent design, molten salt reactors have a negative reactivity coefficient, meaning an undesired increase in temperature will lead to a reactor shutdown. This prevents damage or loss of property, and decreases the likelihood of a severe overheat. A loss of flow or loss of coolant incident could cause an overheat,

but again, due to the inherent reactor properties, overheating will automatically shut down the reactor. Stagnant pockets of molten salt could create localized regions of overheated salt, which could cause wall damage or damage to the WHIP device.

Salt freezing is also unlikely in the core region. The core is the hottest location in the reactor, and therefore it is extremely unlikely there will be any salt at a temperature low enough to freeze. In addition, the core does not contain any areas small enough for blockage to be a major concern, thus the severity is not as high.

Corrosion of both the wall and the reactor internals is a major hazard. Because there is not yet any corrosion control system designed for the MsNB, the likelihood of corrosion is very high for both the core wall and the WHIP device. Any small grain defect in the steel will create a focal point for corrosion to begin, particularly if a defect in the SS316 cladding on graphite structures exposes the graphite beneath. Impurities in the salt will also increase the likelihood of corrosion, which will be compounded by the addition of corrosion product impurities. The severity of corrosion is very high in this case, because the core region will be difficult to monitor and repair corroded materials. If a wall begins to corrode, the damage must be noticed and repaired before a wall breach occurs. However, there is no way to monitor the walls inside the core for corrosion, and there is no way to repair the wall of the core without entirely disassembling the MsNB. Reactor internals may be slightly more replaceable, but will still cause severe damage and loss of property if corroded beyond use.

Table 2: PHA for node 2: Upper Distribution Region

Hazard	**Cause**	**Major Effects**	**Severity and Likelihood**	**Hazard Category**
Overheating	Loss of cooling, loss of flow, stagnant regions	Damage to containment, damage to intrusions or instrumentation ports	3/2	Moderate Risk
Salt Freezing	Localized stagnant regions, loss of flow	Blockage, focal points for corrosion	2/2	Low Risk
Corrosion	Corrosion control failure, salt impurities, defect or damage, crevice or corner regions	Wall damage, reactor breach, damage to control drum containment, salt leakage into internals, Corrosion product addition to salt	4/4	Extremely High Risk
Salt Release	Corrosion or damage of intrusions or ports through reactor top	Radioactive material release, damage to facility, damage to environment, risk of injury	4/2	Moderate Risk

Table 2 shows hazards for the upper distribution region. The major hazards for this region are overheating, salt freezing, corrosion, and salt release.

Overheating in this region can be caused by loss of flow, loss of cooling, or by stagnant regions of salt. In this region, it is somewhat more likely that stagnant regions of salt could occur, due to the large disk-like area the salt is flowing through. Intrusions through the top of the reactor could create localized regions of low flow, trapping hot salt. It is unlikely that the salt would become hot enough to cause damage, however the damage that could occur would be moderately severe.

Salt freezing can occur similarly to overheating; in this region it is somewhat more likely for

localized stagnant regions to occur which could cool and freeze. The narrowness of the region means a minor blockage could occur.

Corrosion is an extremely high risk for this node. As explained previously, the lack of a corrosion control system severely increases the likelihood of corrosion. The severity in this case is also high due to the critical damage which corrosion could cause in this region. Causes of corrosion in this region are similar to the core region, with the addition of region geometry. Crevices and corners can create focal points for corrosion. Crevices and corners can occur in locations where intrusions come through the region. If there are improper welds, or localized areas where fittings come into contact but are not welded, this can create crevices, which are more likely to corrode.

Salt release is a hazard in this region due to the regions location. This regions contains walls on the outside of the reactor, and thus a wall breach could create a salt release. It is unlikely that a salt release would occur, however the damage that could occur from a release of fuel salt could be quite severe, particularly since a salt release would require an extended reactor shutdown, and possibly require dismantling of the reactor to repair the breach.

Table 3: PHA for node 3: Heat Exchanger

Hazard	**Cause**	**Major Effects**	**Severity and Likelihood**	**Hazard Category**
Fin Corrosion	Corrosion control failure, salt impurities, defect or damage creating focal point	Fin damage, possible hole in fin, subsequent ingress of air into salt	4/4	Extremely High Risk
HX inlet corrosion	Corrosion control failure, salt impurities, defect or damage, and inlet is a focal point for corrosion	Altered flow, deposit buildup and restricted flow	2/4	Moderate Risk
Air leak into salt	Damage to one or more fins causing a hole	Impurity addition to salt causing increased corrosion rates system-wide. Increase in pressure in system, multi-phase flow, unpredictable flow, slowed or halted natural circulation, decreased heat removal	5/4	Extremely High Risk

Table 4: PHA for node 3: Heat Exchanger, continued from table 3

Hazard	**Cause**	**Major Effects**	**Severity and Likelihood**	**Hazard Category**
Salt freezing	stagnation or over-cooling by HX	Blocked fin regions, decreased heat removal, corrosion focal point	2/2	Low Risk
Air side HX corrosion	Particulates or moisture in secondary system	fin damage, corrosion product addition to secondary system, possible hole in fin and air leakage into salt	3/1	Low Risk

Tables 3 and 4 show the PHA for the HX region. The primary hazards for this region involve corrosion of the inlet or fin, as well as air leaking into the salt, or the salt freezing and plugging the HX. Fin corrosion in this region is extremely likely, due to the 1-mm thickenss of the fins. Any defect or corrosion focal point in the fin will lead to corrosion, which will penetrate through the fin much quicker than any other region of the MsNB, due to the thinness of the fin. This is also particularly severe due to the effects of air ingress to the salt. Air leaking into the salt has the highest severity rating, because this would severely compromise the salt matrix. Air or helium from the secondary side, unless it is kept extremely pure, would inevitably introduce moisture and oxide impurities into the salt, which would make it much more corrosive (4).This would increase the corrosion rate throughout the entirety of the reactor. The addition of air would also create a two-phase system, impacting the flow and neutronic balance of the reactor. The cascading effects of the air introduction to the reactor could compromise the salt, making the reactor possibly inoperable. In contrast to the salt side, corrosion on the air side of the heat exchanger is unlikely. Air is not as corrosive as salt, and there is no relation between impurity concentration and corrosiveness. And unlike fluoride salts, air does not dissolve protective passive films on structural alloys, and therefore there would be an additional layer of protection on the air side of the heat exchanger.

Table 5: PHA for node 4: Downcomer

Hazard	**Cause**	**Major Effects**	**Severity and Likelihood**	**Hazard Category**
Outlet buildup	Corrosion and fission product deposit, and impurity deposit	Outlet corrosion, possible blockage or flow impedance	3/3	Moderate Risk
Corrosion of inner wall	Corrosion control failure, salt impurities, defect or damage creating focal point	Wall damage, possible breach, salt leakage into control drum assembly and internals	4/4	Extremely High Risk
Corrosion of outer wall	Corrosion control failure, salt impurities, defect or damage creating focal point	Wall damage, possible breach, possible salt release and personnel exposure	5/4	Extremely High Risk
Salt Freezing	Loss of flow, heat exchanger malfunction	Blockage, focal points for corrosion	2/2	Low Risk

Table 5 shows the PHA for the downcomer region. The primary hazards for this region are buildup of deposits at the outlet of the downcomer, corrosion of the inner and outer wall, and blockage due to salt freezing.

The biggest of these hazards is the corrosion of the inner and outer wall. The likelihood and severity of these hazards is high due to the lack of corrosion control in the current design boundaries. In addition, corrosion of the outer wall would be particularly severe, since a significant amount of corrosion could lead to a breach of the outer wall, leading to a release of fuel salt.

In a typical molten salt design, salt freezing is of most concern as it leaves a heat exchanger, since that is when the salt is at its coldest point. However, in this region, frozen salt is unlikely to cause significant enough blockage to stop flow, since the salt would need to freeze in the entire 360 degrees of the annulus. Since this is unlikely, salt freezing in the annulus is not as high of a risk.

Table 6: PHA for node 5: Lower Distribution Region

Hazard	**Cause**	**Major Effects**	**Severity and Likelihood**	**Hazard Category**
Blocked or partially blocked inlet to core	Frozen salt, corrosion/fission product deposits	Loss of flow or flow impedance, focal point for corrosion of inlet structure	4/4	Extremely High Risk
Corrosion of core inlet structure	Corrosion control failure, salt impurities, inlet structure creates focal points for corrosion	Change in flow, stagnant flow regions, possible loss of natural circulation	3/5	High Risk
Wall corrosion	Corrosion control failure, salt impurities, defect or damage creating focal point	Wall damage, possible breach, corrosion product addition to salt matrix	3/4	High Risk
Salt Freezing	loss of flow, stagnant regions	Blockage, focal points for corrosion	2/2	Low Risk

Table 6 shows the hazards for the lower distribution region. In this region, the highest hazard is in the inlet region to the core. Since this region contains a structure to direct the flow, it contains many possible focal points for corrosion. In addition, the flow of salt changes direction at the inlet region, which could exacerbate any corrosion occurring. Because of this, the likelihood of corrosion at the core inlet structure was ranked as almost certain.

The lower distribution region also has an extremely high risk of blocking or partial blocking of the inlet region to the core. The area is small, and at the lowest point in the reactor. It is possible that sediment or impurities could collect in this region, left behind as the flow travels back up the reactor. Corrosion products and fission products could deposit on the inlet structure. These factors all combined leave a high possibility of blockage in the inlet structure.

Table 7: PHA for node 6: Control Drums

Hazard	**Cause**	**Major Effects**	**Severity and Likelihood**	**Hazard Category**
Electrical Failure	Salt leakage into electrical systems, shorted wires, worn out systems, power overload, fault in manufacturing or assembly	Loss of drive control, loss of sensors and instrumentation, reactor shutdown for repair	3/2	Moderate Risk
Salt Exposure	Corrosion through barriers and subsequent wall breach and salt leakage, salt leakage through intrusions in upper dist. region	Corrosion and damage of drives, drums, and electrical systems, reactor shutdown for repair	3/2	Moderate Risk
Operational Error	Operator error of control drum drives	Reactor overheats and/or shuts down, possible control drum damage	2/1	Low Risk

Table 7 shows the hazards for the control drums. These drums are the only moving part within the analysis boundaries, and do not have any intentional salt exposure. Thus, the hazards in this region are different from the rest of the reactor. The main hazards in this region are electrical failure, salt exposure, and operational error. None of these risks are high enough to pose a serious problem.

It should be noted that this region is one of the only two regions containing human factors. All other regions rely on automation and natural fluid behavior to operate. Thus, this region has an inherent risk stemming from human reliability. Operational error is always a risk in regions where human control may be necessary. In this region, it is likely that a level of automation will

be present to assist in control drum operation, which means the likelihood of an operational error is low. However, this is an estimate based on general assumptions, and it is recommended that a human reliability analysis be performed when this region has a more comprehensively designed control scheme.

Table 8: PHA for node 7: General Facility

Hazard	**Cause**	**Major Effects**	**Severity and Likelihood**	**Hazard Category**
Salt exposure to water	Salt leakage, water in zone close to reactor, failure of water-containing secondary systems, fire response involving water	Possible steam explosion, rapid release of salt and radioactive steam, injury and severe facility damage	5/1	Low Risk
Secondary system load change	System removes too much, or not enough heat, but still functioning	Reactor oscillation and response	1/5	Low Risk
Structural material failure	Radiation damage, corrosion damage	Reactor or secondary system damage, possible reactor shutdown, major repairs or loss of reactor functionality	4/1	Low Risk
Widespread facility damage	Natural disaster, attack by aggressive forces	Reactor scram and shutdown, possible salt release and major reactor damage	5/1	Low Risk
Fire	Accident in facility, hot salt leakage, electrical failure	Facility damage, possible damage to reactor structure, secondary loop, or control systems	5/2	Moderate Risk

Table 8 shows the hazards for the general facility region. This region was assumed to con-

tain general facility hazards, such as water systems, a secondary cooling system, and general hazards such as fire and natural disaster. None of these hazards had a concerning risk category. Secondary system load changes could cause concern, but the inherent properties of the reactor mean any overheating will cause a reactor shutdown, not a meltdown. The only hazard with a ranking above 'low' was fire. This was given a high severity rating, because of the possibility of fire to cause severe damage to crucial systems. The severity of a fire would be particularly high if water were used as an extinguishing method, since molten salt is incompatible with water. However, it is unlikely that water would be used to extinguish fire close to the reactor, since this incompatibility is well known, and procedures would be in place to avoid water use.

Table 9: PHA for node 8: Instrumentation

Hazard	**Cause**	**Major Effects**	**Severity and Likelihood**	**Hazard Category**
Sensor exposed to salt	Corrosion of instrumentation casing	Sensor damage	3/4	High Risk
Sensor Failure	Corrosion, electrical failure, radiation damage	Faulty data on core conditions, possible reactor shutdown for repairs	3/2	Moderate Risk
Corrosion of TC sensor casing	TC exposure and damage	Faulty TC readings and sensor failure	3/3	Moderate Risk

Table 9 shows the hazards for the instrumentation. The only concerning hazard in this region is the possibility that the sensors are exposed to salt, causing sensor failure. This is a high risk because it of its high likelihood, due to the corrosive nature of the reactor and lack of control systems. However, the severity of a sensor-salt exposure is not high, because no crucial reactor systems would be compromised.

4.2 Failure Mode and Effects Analysis

This section contains the results of the FMEA. There is some redundancy to the PHA, due to the similarity of the types of analysis. Similar to the PHA, the possible failures were decided based

on the structure of the reactor, possible corrosion focal points, and where the salt flows.

Table 10: FMEA for node 1: Core Region

Failure	**Effect**	**Severity Rating**	**Occurrence Rating**	**RPN**
Damage to reactor internals	Altered core flow, sensor failure	3	3	**9**
Overheating	Reactor shutdown, core material damage	4	2	**8**
Core outlet blockage	Altered exit flow, natural circulation impedance, decreased power, overheating in core	4	2	**8**
Loss of flow through core	Reactor overheat and eventual shutdown, loss of power	5	1	**5**

Table 10 shows the failures for the core region. The failure that ranked the highest in this region was WHIP damage. This is a high-ranked failure because if the cladding on the reactor internals is corroded enough to expose any of the internal graphite, the corrosion would become much more severe. Overheating of the core did not score highly, because it is unlikely due to the inherent properties of the reactor, which would cause a shutdown before serious damage could occur.

Table 11: FMEA for node 2: Upper Distribution Region

Failure	**Effect**	**Severity Rating**	**Occurrence Rating**	**RPN**
Minor Blockage	Restricted flow, decreased flow to HX	2	3	**6**
Major Blockage	Restricted flow, loss of flow, loss of circulation and reactor shutdown	4	1	**4**
Loss of flow	Overheating, loss of circulation and reactor shutdown	4	1	**4**
Corrosion of head intrusions	Damaged control drum drives, salt leakage to internals	4	4	**16**
Containment breach	Salt release to facility/environment, loss of fuel salt, reactor shutdown	5	3	**15**

Table 11 shows the failures for the upper distribution region. The highest ranked failures in this region were the corrosion of the head intrusions, and a breach of containment.

The head intrusions through the top of the reactor create a large amount of corrosion focal points in this region. Flow is perpendicular to these intrusions, which means corrosion could be more pronounced on areas with flow directed straight onto them. In addition, intrusions through the reactor head create right angles, which are another type of possible corrosion focal point. Improper welds on these intrusions could also create crevices, which are highly vulnerable to corrosion. The effect of damage to these intrusions could be quite severe, possibly causing salt exposure to the control drum drives, shutting down reactor control systems.

A breach of containment is also possible in this region, due to its location on the outer shell of the reactor. A breach of containment in this region could be caused by corrosion of the head intrusions, particularly if there are intrusions for instrumentation or salt loading. Although a breach is more unlikely, the severity of a breach is extreme, giving the failure a high RPN.

Table 12: FMEA for node 3: Heat Exchanger Region

Failure	**Effect**	**Severity Rating**	**Occurrence Rating**	**RPN**
Single fin failure	Minor decrease in heat removal, reactor power oscillation and stabilization, minor power loss	2	3	**6**
Multiple fin failure	Major decrease in heat removal, if reactor unable to stabilize, overheating and eventual shutdown	4	2	**8**
Single hole in a air/salt interface	minor air flow into salt, impurity addition and minor salt pressure increase, salt will plug hole evenutally	3	4	**12**
Multiple holes in air/salt interfaces	Major air flow into salt, major impurity addition and possible pressure increase. Major loss of heat removal and possible shutdown required	4	3	**12**

Table 13: FMEA for node 3: Heat Exchanger Region, continued from table 12

Failure	**Effect**	**Severity Rating**	**Occurrence Rating**	**RPN**
HX inlet blockage	Major loss of heat removal, reactor shutdown	4	1	**4**
HX single panel inlet blockage	Minor loss of heat removal, reactor power oscillation and response, possible corrosion focal point	2	2	**4**
Loss of air flow	Heat exchanger failure, reactor overheat and shutdown	4	2	**8**

Tables 12 and 13 shows the failures for the HX region. There are a significant number of possible failures in this region, because of its intricate structure. However, not many of them ranked very severely. The highest ranked failures in this region were the possibility of a hole in an air/salt interface. A hole would be caused by corrosion of a fin between air and salt flow. Interestingly, although the severity and occurrence of a single hole versus multiple holes are different, the two failures have the same RPN, meaning the failures have the same level of risk. A single hole is more likely, but less severe. Multiple holes is less likely, but more severe. Both are high risks, because a hole in an air/salt interface would mean air leakage into the salt, which is a large concern, as addressed in table 3.

Table 14: FMEA for node 4: Downcomer

Failure	**Effect**	**Severity Rating**	**Occurrence Rating**	**RPN**
Minor blockage	Minor disruption to flow, stagnant region and possible corrosion focal point	2	1	**2**
Major blockage	Major disruption to flow, power decrease, overheated regions, possible reactor shutdown	4	1	**4**
Outer wall breach	Salt release to facility/environment, loss of fuel salt, reactor shutdown, major damage	5	3	**15**
Inner wall breach	Salt leakage to internals, internal damage and control drum failure, reactor shutdown	4	3	**12**

Table 14 shows the failures for the downcomer region. The only possible failures in this region are wall breaches or blockage. Blockages, as discussed previously, are unlikely in this region due to the 360 degree design. Wall breaches however, are much more likely, due to the lack of a corrosion control system. Since corrosion is quite likely, a wall breach is likely as well. An outer wall breach is more severe than an inner wall breach, but both failures would be unacceptable, and therefore have high RPN's.

Table 15: FMEA for node 5: Lower Distribution Region

Failure	**Effect**	**Severity Rating**	**Occurrence Rating**	**RPN**
Minor blockage	Flow restriction, power loss, reactor power oscillation and response	2	2	**4**
Major blockage	Loss of flow, overheating and reactor shutdown	4	1	**4**
Clogging in core inlet region	restricted flow, possible loss of flow	3	4	**12**
Damaged core inlet region	restricted flow, possible blockage, particulates in salt matrix	3	3	**9**

Table 15 shows the failures for the lower distribution region. The failures in this region are similar to the hazards identified in the PHA. Blockage and damage to the core inlet region are possible, with clogging and damage in the core inlet region having the highest RPN ratings.

Table 16: FMEA for node 6: Control Drums

Failure	**Effect**	**Severity Rating**	**Occurrence Rating**	**RPN**
Single drive failure	Compensation with other drums, reactor shutdown for repair	3	2	**6**
Multiple drive failure	Loss of sufficient reactor control, scram and/or shutdown	4	2	**8**
Operational error	Over or under moderation, overheat or loss of power, eventual reactor shutdown	3	2	**6**
Electrical failure	Control drum failure, possible reactor shutdown	3	2	**6**

Table 16 shows possible failures in the control drums. Similar to the PHA results, none of the failures in this region are severe enough to be past the unacceptable level of 9 or higher. The highest possible failure in this region is a multiple drive failure, which would cause a reactor shutdown.

Table 17: FMEA for node 7: General Facility

Failure	**Effect**	**Severity Rating**	**Occurrence Rating**	**RPN**
Secondary system removes too much heat	Initial power decrease response, power oscillation and eventual stabilization	1	5	**5**
Secondary system removes too little heat	Initial power increase, power oscillation, and eventual stabilization	1	5	**5**
Secondary system removes no heat	Reactor temperature increase, eventual shutdown	5	1	**5**
Water/salt contact	Steam explosion, significant reactor and facility damage, injury, death	5	1	**5**
Salt release	Personnel and environmental radiation exposure, loss of fuel salt, facility damage, reactor shutdown	5	3	**15**
Unintentional unmanned conditions	failure to respond to accident scenario, failure to operate control drums, possible damage and/or reactor shutdown	4	1	**4**

Table 17 shows the failures for the general facility. This FMEA contains possible accident scenarios involving the secondary system. The possible variations from the secondary system

pose a risk, with the highest severity being that of the secondary system removing no heat, rendering the heat exchangers ineffective. However, due to the inherent properties of the reactor, this would only result in a reactor shutdown.

If there are load changes to the heat exchanger, caused by the secondary system removing too much or too little heat, modeling has shown that the reactor would respond to these disturbances with temperature oscillations and eventual stabilization(2).

The possibility of a salt release is the highest rated failure in this region. The RPN of 15 is very high, stemming from the severity of 5. A salt release would be extremely severe, even if it is a small amount. This would expose workers and the environment to radioactive material, and if it is still hot enough to be slightly molten, poses additional hazards to the facility and personnel. With corrosion risks, the likelihood of a breach causing a salt release is high enough to make salt release an unacceptable risk.

Table 18: FMEA for node 8: Instrumentation

Failure	**Effect**	**Severity Rating**	**Occurrence Rating**	**RPN**
TC Failure	Faulty temperature monitoring	1	3	**3**
Self-Powered Neutron Detector failure	Lack of neutron flux monitoring	2	3	**6**

Table 18 shows possible failures for the instrumentation. Similar to the PHA, there is no severe concern with the instrumentation. None of the possible failures pose a severe risk, with the highest risk being that of a SPND failure, with an RPN of 6.

4.3 Common trends

The PHA and FMEA tables rank each hazard and failure, and therefore it is possible to filter the highest risks and examine them for common causes. Of most concern are those hazards with the category 'Extremely High Risk'. These are risks which are unacceptably high, and there must be a level of mitigation before design can be completed.

The hazards ranked 'Extremely High Risk' were the following:

- Corrosion of core wall
- Corrosion in Upper Distribution Region
- HX fin corrosion
- HX air leak into salt
- Corrosion of downcomer wall
- Blocked or partially blocked inlet to core

The hazards ranked 'High Risk' were the following:

- Corrosion of reactor internals
- Corrosion of core inlet structure
- Corrosion in lower distribution region
- Sensors exposed to salt by corrosion of reactor internals

The following failures had an RPN of 9 or greater:

- Internal damage: RPN = 9
- Corrosion of head intrusions: RPN = 16
- Containment breach: RPN = 15
- Holes in an air/salt interface: RPN = 12
- Outer wall breach: RPN = 15
- Inner wall breach: RPN = 12
- Clogging in core inlet region: RPN = 12

- Damaged core inlet region: RPN = 9
- Salt release: RPN = 15

The most obvious common trend in these risks is that of corrosion. A lack of corrosion control systems in the reactor design leads to high risk ratings on corrosion-related hazards and failures. All of the identified high-risk items are either directly or tangentially related to corrosion. Additional risks include depositing corrosion and fission products, and HX leakage into salt. Mitigation for these risks will be discussed in part 2 of this report.

5 Discussion

5.1 Major takeaways

The most apparent takeaway from this analysis is that corrosion control is key to reducing risk in this reactor design. Every single major risk identified is related to corrosion, and thus it is important to look deeper at the impact of corrosion on the system. Risk assessment tools can be used to look more in-depth at the corrosion behavior of the reactor system.

Causes of corrosion should be identified in a system such as this, but it is difficult to identify exactly what leads to corrosion. There are many possible causes and factors leading to corrosion, and all or just one can come into play at any time. Figure 4 shows a fishbone diagram illustrating this concept. Corrosion can be caused by material weakness, corrosion focal points, a reducing salt potential, or corrosion product deposition. Much has been reviewed on the topic of molten salt corrosion(5; 4; 6), and an in-depth discussion of corrosion mechanisms and behavior is not within the scope of this report. However, a further analysis of the corrosion mechanisms in this system will be necessary for a complete corrosion control system design.

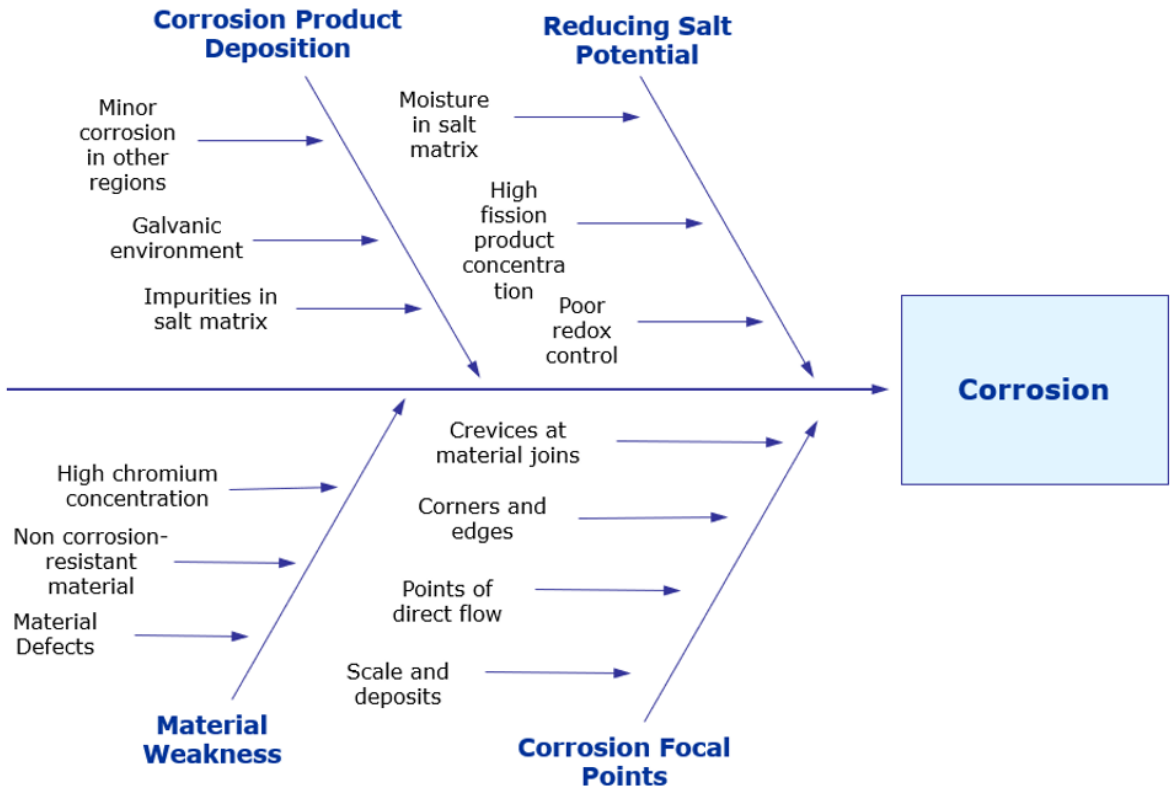

Figure 4: A fishbone diagram outlining possible factors involved in a corrosion-related hazard

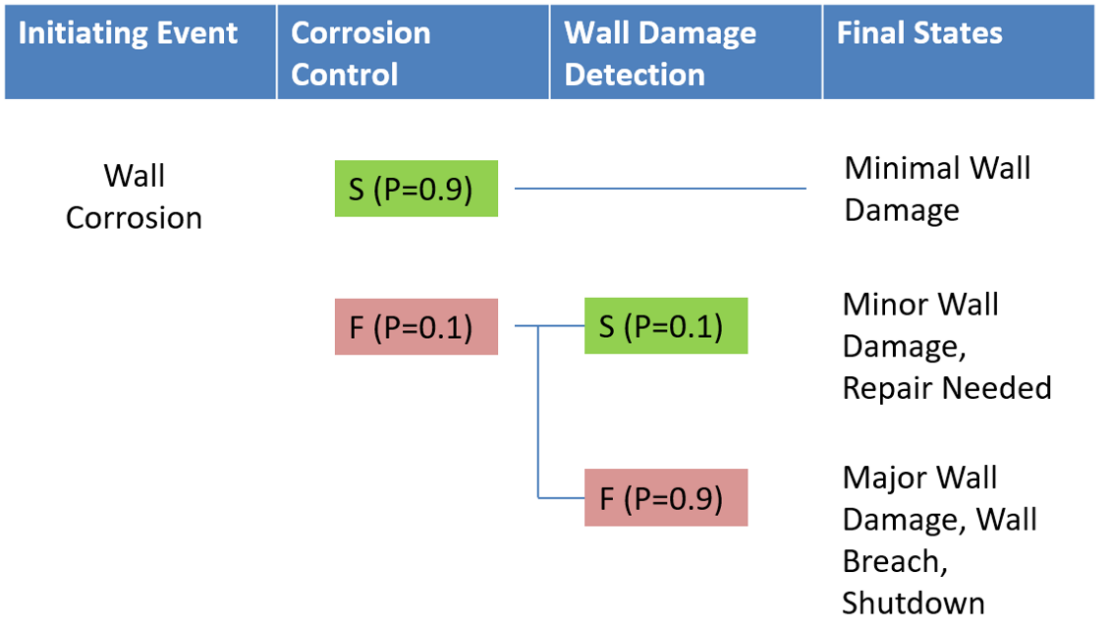

Figure 5: An event tree for corrosion in the MsNB

5.2 Implications

The implication of the severity of corrosion in this system is that a corrosion control system will be key for long-term functionality of the MsNB. This is made more obvious when an event tree for corrosion is constructed, shown in figure 5. The event tree shows the possible intermediary events that occur between the initiation of corrosion and the eventual failures and damage to the MsNB structure. This specific event tree was constructed for wall corrosion specifically. The event tree shows the estimated probability for success and failure of each intermediary system, and the outcome of success or failure. The probabilities are estimates only, as no modeling or data has been done on this specific event.

As can be seen from the event tree, corrosion control is crucial to limiting major wall damage from corrosion. There are only two possible intermediary events; corrosion control, and detection and repair of any damage. Detection and repair for this system is extremely unlikely. Not only is it impossible to view the internal walls of the reactor to detect corrosion, but it is also impossible to replace most parts of the MsNB. The integral design of the MsNB means replacing structure requires complete disassembly, an impossible task. The only components where this is remotely possible are components on the outer reaches of the reactor, such as the control drum drives, or external ports and apparatus. Thus, the only real barrier between initiation of corrosion and major damage is a corrosion control system.

5.3 Limitations

Although a corrosion control system can be highly effective in preventing corrosion damage, this prevention is not unlimited. No corrosion control system is going to be perfect, and corrosion is an ever-present fact of fluid systems. Some level of corrosion is inevitably going to occur; it is the responsibility of the corrosion controls to keep that corrosion to an acceptable level. The reactor does not need to withstand corrosion forever, it just needs to withstand corrosion through its operating lifetime of about 10 years.

Phase II - Risk Management

6 Mitigation

6.1 Risks

The most major risks identified in the analysis, as discussed in section 4.3, all relate to corrosion, either directly or indirectly. However, corrosion isn't the only hazard present in the system. Based on the results of section 4.3, the following risks require mitigation in the MsNB design. These are the main themes identified from the highest risk hazards and failures:

- Corrosion, particularly of vulnerable regions such as the HX, reactor internals, and outer annulus.
- HX air leakage into salt
- Deposits from corrosion or fission products
- Exposure of sensors to molten salt
- Wall breach and salt release
- Damaged core inlet region (or other internal damage)

Corrosion is the biggest and most concerning of these risks, but all of these themes ranked highly in the risk analysis. Risks such as the leakage of air into salt from the heat exchanger, exposure of sensors to salt, and wall breach all relate to corrosion, but additional measures other than direct corrosion control can also be taken to address these risks. It is important to explore multiple avenues of risk mitigation, to ensure the success of the mitigation.

6.2 Goals

The goal of risk management is to take the results of the risk assessment performed and apply mitigation strategies to lower the risk. Because the PHA and FMEA both ranked hazards based on likelihood and severity, risk management strategies aim to reduce the risk by reducing either the likelihood, or severity of a hazard. In some instances, such as corrosion, it is difficult to reduce the severity of an incident. However, reducing the likelihood is effective at reducing the risk to acceptable levels.

The goal of this section is to outline possible methods for reducing the identified highest risks and hazards. The threshold for classifying a hazard as unacceptable was a ranking of 'high' or

'extremely high', and the threshold for an unacceptable failure was an RPN of 9 or greater. These thresholds will be applied in the risk reduction discussion - an effective risk reduction strategy will reduce the selected hazard to values below the acceptability threshold. Because no single strategy is unilaterally effective, it is likely that a combination of risk reduction strategies will be required for each hazard.

7 Methodology

7.1 Assumptions

There are many possible risk reduction strategies which could be applied to the identified hazards. However, not all strategies are possible. For this discussion, it will be assumed that minor design changes are possible, but major design changes are not. For example, one major issue that arose in analyzing the risk in the reactor was the inability to access and repair certain systems. Although changing the design to allow for repairs would reduce a lot of risk, this would involve drastic design changes, fundamentally altering the MsNB design. This is an undesirable level of design change, as it would revert the design process to preliminary stages. Thus, only minor design changes will be considered in risk reduction strategies.

7.2 Risk Reduction Strategies

7.2.1 Corrosion

Corrosion of crucial systems was a hazard which impacts many systems in the MsNB, and therefore a comprehensive and effective risk reduction strategy is required to address corrosion in the system. There are many ways to reduce the risk of corrosion in a reactor system, including corrosion control methods, material changes, and minor design changes.

Corrosion control methods refer to the monitoring and control of redox potential. Redox potential is a fundamental property of electrolytes, referring to the materials tendency to either reduce or oxidize a material. It is a function of composition, and changes only with changing composition of a mixture. The molten salt reactor experiment (MSRE) in the 1960s determined that monitoring and controlling redox potential was an effective way of limiting corrosion in a molten salt system (4). Much has been reviewed on the subject of redox potential control (7; 5). Redox potential control systems can include redox buffers, reduction and oxidation agents, or purification systems. Corrosion in a molten salt system has also been demonstrated through use of a sacrificial anode (8). These systems can be deployed in a combined system to limit corrosion and monitor redox potential in the MsNB.

Redox potential control is not the only method for controlling corrosion. Minor design and material changes can also reduce corrosion risk in some regions. Corrosion-resistant alloys such as inconel, hastelloy, or nickel-based alloys can reduce the likelihood of corrosion in a molten salt system. Minor design changes to smooth corners, redirect flow, and eliminate focal points for corrosion may also lower the risk of corrosion. It is important when considering material changes to consider the new risk of galvanic corrosion. Galvanic corrosion occurs when two dissimilar metals are connected electrically while both immersed in an electrolyte solution. In

a reactor environment, any dissimilar metals in contact with molten salt would be subject to galvanic corrosion. Currently, the MsNB design is uniformly SS316 steel. This eliminates the risk of galvanic corrosion, and therefore galvanic corrosion was not considered in the PHA and FMEA. If minor material changes are made in the MsNB design, the selected materials must be evaluated for their tendency to corrode galvanically with the SS316 in the main structure of the MsNB.

To evaluate a materials tendency for galvanic corrosion, one can refer to the galvanic series. Shown in figure 6, the galvanic series is a list of corrosion potentials for various alloys and pure metals (9). The larger the difference between corrosion potentials is, the more likely the metals are to undergo galvanic corrosion. In a galvanic corrosion cell, the metal with the more active corrosion potential will corrode. For example, in the galvanic series shown, stainless steel type 316 has a corrosion potential range of about -0.4, and graphite a range of about 0.2. These are quite different, and if the two metals were in electrical contact with the molten salt, the SS316 would be subject to galvanic corrosion, particularly at boundaries between the graphite and SS316. This is particularly relevant on the WHIP device, if the SS316 were to corrode enough to expose the graphite internal structure of the WHIP. Nickel alloys are not as dissimilar as SS316/graphite, but if they are employed in the MsNB, it will be necessary to model the system to determine the magnitude of the possible galvanic corrosion that could occur.

A corrosion control system for corrosion mitigation should not rely on just one method. Because of the importance of corrosion control systems in halting the progression of corrosion, a control system needs to have multiple layers. Layers of different control methods can be put in place, and different layers will make up for deficiencies in other layers. This system is often called a 'Swiss cheese model' of safety systems, called so because each layer of control has holes, which are covered by other layers. An effective and layered corrosion control system will reduce the likelihood of corrosion significantly, although it will not eliminate corrosion in the system entirely.

7.2.2 Heat Exchanger Air-Salt Interface

It was noted in the PHA and FMEA that there is a possibility of air leakage into the molten salt if a hole in the interface occurs. This hole would arise from corrosion, and therefore the risk would be reduced by corrosion control methods, as discussed previously. However, another layer of risk reduction can be applied to this hazard. In the event a hole forms in a fin between air and salt, the leakage of air into salt would no longer depend on corrosion rates, but on the pressure differential between air and salt. The fluid with the highest pressure would migrate through the hole. A risk reduction strategy in this case would be to maintain the pressure of the salt at an equal or higher level than that of the air. Then, the salt would instead migrate into the air side of

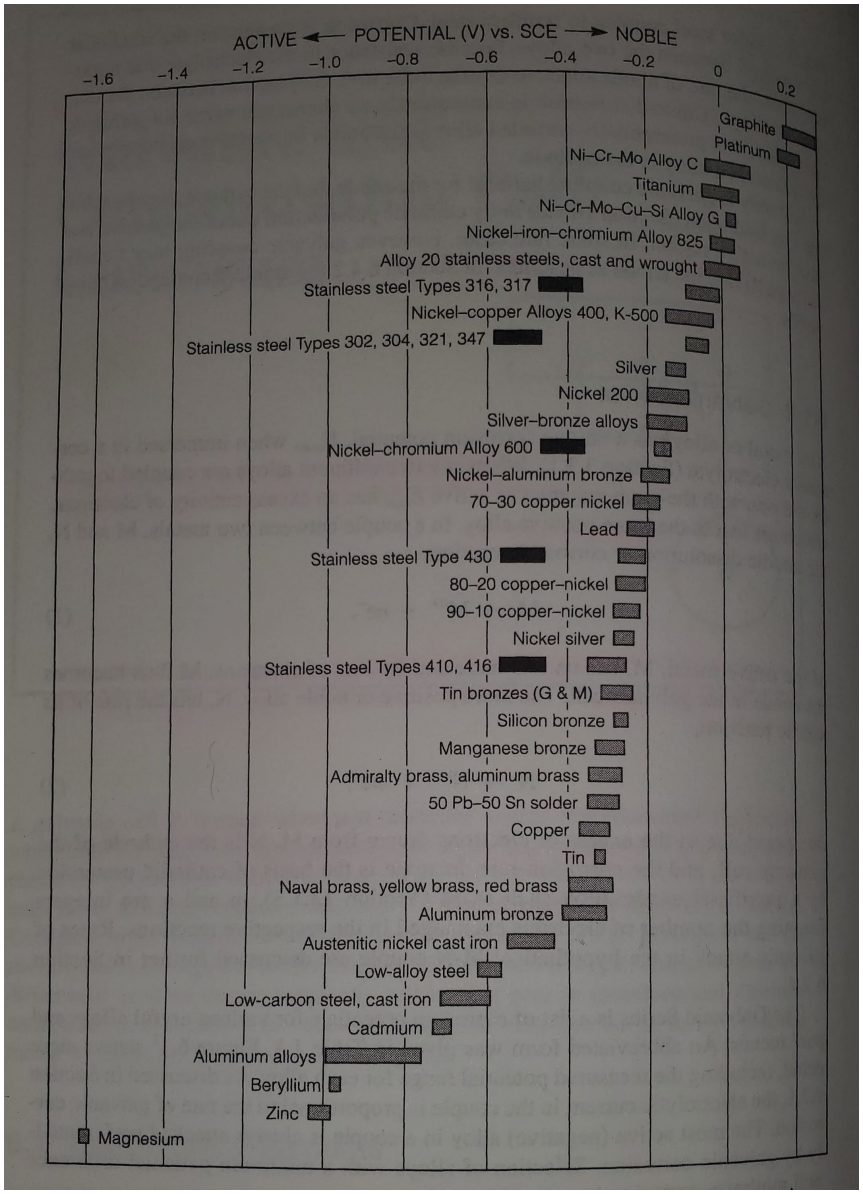

Figure 6: The galvanic series

the heat exchanger. This is a much more acceptable outcome, since this would not compromise the salt matrix. Additionally, it is possible that the salt would solidify upon migration into the air side of the HX, plugging the hole and preventing further loss of fuel salt. This risk reduction strategy would reduce the severity of a hole in the air/salt interface.

7.2.3 Deposits

In any system, there is the possibility of deposits forming on surfaces or corners. These deposits can come from corrosion, or from sediment or fission products which are released into the salt

matrix. There are several ways deposits can be limited in the reactor. Many of these methods would overlap with corrosion control methods, such as purification of salt before loading, corrosion control, or sacrificial material. Minor geometry changes may also serve to limit deposits in the reactor.

Sometimes, a filter is used to collect sediment and unwanted material to avoid deposits. However, a filter in the MsNB would add more risk than it would reduce. A filter would become a large focal point for additional corrosion, since any filter would likely need to be a metal mesh to resist the salt conditions. A filter would also restrict flow, change reactor flow parameters, and provide a possible blockage point. Although a filter may be an acceptable way to limit deposit in other systems, it would not be an effective risk reduction strategy in this design.

7.2.4 Sensors Exposed to Salt

Sensors embedded in reactor internals may end up exposed to the molten salt, if the surrounding structural material is corroded away. In the event the sensors are exposed, it may be desirable to include measures that would prevent the sensors from immediate failure. Thermocouples and neutron detectors can be made from corrosion-resistant materials to limit damage, or the boundary between sensor and salt can be made thicker, to avoid initial exposure of the sensor.

7.2.5 Wall breach and salt release

Wall breaches and salt releases would occur in the MsNB due to corrosion and damage to containment. Corrosion control methods would reduce the likelihood of these events as has already been discussed, but responsive measures can also be designed to reduce the severity of these events should they occur, reducing their risk further.

A wall breach would be an extremely severe event, compromising the reactor and exposing personnel and environment to radioactive salt. Emergency procedures and containment can reduce the likelihood of injury and exposure. A reactor containment for a molten salt reactor should remove factors which can make a salt release more dangerous - such as reactive materials. Water is an example of a material that should be excluded from a reactor containment. When molten salt comes into contact with water, it can cause a steam explosion. A water exclusion zone would reduce the likelihood that escaping salt coming into contact with water, reducing the severity of a water release. In addition, emergency response measures should be planned in advance to not use water. For example, in the event of a fire in the facility, non-water fire extinguishing methods could be used in the reactor area to avoid water contact with salt.

7.2.6 Core Inlet Region

The core inlet region has a flow structure which subjects it to corrosion and deposit, and therefore contained many hazards and possible failures which were above the acceptability threshold. In addition, at the lowest point of the reactor flow, the core inlet region may also collect sediment and deposits at a higher rate than the rest of the reactor environment. Risk reduction for this region is entirely reliant on preventative measures. It is impossible to conduct repairs or address damage in this region, and therefore responsive measures are impossible. The damage that could occur in this area will stem from deposits or corrosion, and therefore the only preventative measures that could be done are those corrosion and deposit control measures already discussed. This highlights the need for a thorough and layered corrosion control method for the MsNB - if corrosion control fails and systems are damaged beyond functionality, it is likely that the core inlet region would be one of the more highly impacted areas. If the core inlet region becomes blocked or damaged, inlet to the core could become halted or altered, shutting down the reactor. Other systems could be similarly impacted.

8 Results

To evaluate the effectiveness of the outlined risk reduction strategies, we can reevaluate the rankings for the highest risk hazards and failures. Tables 19, 20 21, 22, and 23 show the results of these reevaluations. These tables demonstrated the effectiveness of risk reduction strategies - if all are applied, all hazards and failures are reduced to acceptable levels. It should be noted that corrosion hazards were reduced to moderate and not low hazard rankings. This is because corrosion can be minimized, but it is impossible to eliminate corrosion entirely. A moderate risk level is acceptable, and indicates a level of corrosion that will not damage the reactor significantly over its ten-year lifetime.

Table 19: Risk Reduction on PHA for Extremely High Risks

Hazard	**Effects**	**Hazard Category**	**Mitigation**	**New Hazard Category**
Corrosion of Core Wall	Damage to reactor internals, instrumentation damage, impurity addition to salt	4/4 - Extremely High	Corrosion Control	4/2 - Moderate
Corrosion in Upper Distribution Region	Wall damage, reactor breach, damage to control drum containment, salt leakage to internals, corrosion product addition to salt	4/4 - Extremely High	Corrosion Control	4/2 - Moderate
HX fin corrosion	Fin damage, possible hole in fin, subsequent air leak into salt	4/4 - Extremely High	Corrosion Control, thicker fins	4/2 - Moderate

Table 20: Risk Reduction on PHA for Extremely High Risks, continued from table 19

Hazard	**Effects**	**Hazard Category**	**Mitigation**	**New Hazard Category**
HX air leak into salt	Impurity addition to salt causing increased corrosion rates system-wide. Increase in pressure in system, multi-phase flow, unpredictable flow, slowed or halted natural circulation, decreased heat removal	5/4 - Extremely High	Corrosion Control, Salt Pressure higher than Air Pressure, Dry Air	4/2 - Moderate
Corrosion of Downcomer wall	Wall damage, possible breach, salt leakage into control drum assembly and internals, possible salt release and personnel exposure	5/4 - Extremely High	Corrosion Control, multi-layer thickened walls, emergency salt release measures	4/2 - Moderate
Blocked or partially blocked inlet to core	Loss of flow or flow impedance, focal point for corrosion of inlet structure	4/4 - Extremely High	Corrosion Control, structure changes to remove focal points	4/2 - Moderate

Table 21: Risk Reduction on PHA for High Risks

Hazard	**Effects**	**Hazard Category**	**Mitigation**	**New Hazard Category**
Corrosion of reactor internals	Damage to reactor internals, instrumentation damage, impurity addition to salt by corrosion products	3/4 - High	Corrosion Control, thicken cladding on internals, change cladding material	3/2 - Moderate
Corrosion of core inlet structure	Change in flow, stagnant flow regions, possible loss of natural circulation	3/5 - High	Corrosion Control, structure change to remove focal points	3/2 - Moderate
Corrosion in lower distribution region	Wall damage, possible breach, corrosion product addition to salt matrix	3/4 - High	Corrosion Control	3/2 - Moderate
Sensor exposed to salt by corrosion of instrumentation casing	Sensor damage	3/4 - High	Corrosion resistant materials, thicker cladding, thicker boundary between sensor and salt	3/2 - Moderate

Table 22: Risk Reduction on FMEA for RPN = 9 or greater

Failure	**Effect**	**RPN**	**Mitigation**	**New RPN**
Internal damage	Altered core flow, sensor failure	9	Corrosion control, change cladding material, thicken cladding	4
Corrosion of head intrusions	Damaged control drum drives, salt leakage to internals	16	Corrosion control, thicken material, avoid crevices in construction	8
Containment breach	Salt release to facility/environment, loss of fuel salt, reactor shutdown	15	Corrosion control, salt release emergency response measures, isolated reactor containment	8
Holes in an air/salt interface	Air flow into salt, impurity addition and pressure increase, loss of heat removal	12	Corrosion control, keep pressure of salt higher than pressure of air, thicken fin	6

Table 23: Risk Reduction on FMEA for RPN = 9 or greater, continued from table 22

Failure	Effect	RPN	Mitigation	New RPN
Outer wall breach	Salt release to facility/environment, loss of fuel salt, reactor shutdown, major damage	15	Corrosion control, salt release emergency response, isolated reactor containment	8
Inner wall breach	Salt leakage to internals, internal damage and control drum failure, reactor shutdown	12	Corrosion control, multi-layer barrier	6
Clogging in core inlet region	Restricted flow, possible loss of flow	12	Corrosion control, sacrificial material to collect deposits, change structure to avoid focal points	6
Damaged core inlet region	Restricted flow, possible blockage, particulates in salt matrix	9	Corrosion control, change structure to avoid focal points of corrosion	6
Salt release	Personnel and environmental radiation exposure, loss of fuel salt, facility damage, reactor shutdown	15	Corrosion control, isolated reactor containment, emergency salt release measures	8

9 Discussion

9.1 Major takeaways and Implications

The application of the risk reduction strategies discussed earlier reduce the risk levels of concerning hazards to acceptable levels. This reevaluation assumes all applicable risk reduction strategies are applied and work effectively. This is easier said than done, as risk reduction strategies are not perfect and will require significant modeling and experimentation to implement.

Of particular interest in the reevaluation is the level of risk to which each hazard was reduced. Each risk had a high, extremely high, or RPN less than 9 ranking. Although each risk was reduced, none of the risks were reduced to a 'low' rating. This is because these risks still have a level of severity or likelihood that is relatively high. It is important to not discount these risks even when they are reduced to moderate levels, because even low-probability risks can still occur, just at a lower rate. With further design of the MsNB, this analysis can be repeated with more data, quantitative probability analysis, and modeling, to determine what acceptable risk levels are for each type of risk.

9.2 Limitations

There are many limitations to this analysis. A preliminary risk assessment is limited by definition - the design of the MsNB is preliminary, and therefore the risk assessment does not cover all possible hazards in the design. In addition, this analysis was a general look at hazards, and did not even include all details in the current design. This analysis was also performed before any corrosion control system was designed, and therefore corrosion was the main concern throughout the analysis. This analysis was also limited by the preliminary nature of the technology itself. Many risk assessments use accident data and probability analysis to assess occurrence and likelihood ratings. However, molten salt technology is fairly new, and not much data exists to support this type of analysis. Detailed risk assessment will require modeling, to simulate accident scenarios and generate probability data.

10 Conclusions and Future work

Since this reactor is actively being designed, there is much work to be done in the future. This report covered the need for a well-designed corrosion control system, which is certainly an item of future work. This design will need to include modeling of corrosion focal points, experimentation to determine the severity of corrosion in this type of system, and much work to build a thorough control system with enough layers to protect the MsNB for its ten-year lifetime.

In addition to what has been identified in this report, future work is already planned in relation to the MsNB. The establishment of a safety case for the MsNB will be an essential step toward licensing the design. The typical reactor safety case establishes how the operation of the reactor design addresses the following three universally recognized fundamental safety functions when responding to a broad range of events: (1) Control of reactivity, (2) Reactor heat removal, and (3) Containment of radionuclides.

The reactor safety case, and further regulatory guidelines, were established based on typical light-water reactors. Because current experience deals mostly with LWRs, rather than advanced reactor types, it can be difficult for more advanced designs to meet current guidelines. An advanced reactor safety case will be new and challenging, given the different aspects of design and function typical to an advanced design.

The NRC offers guidance on establishing a safety case for an advanced reactor (10; 11). Advanced reactors are expected to "provide the same degree of protection of the public and the environment required for the current generation [LWRs], but also expects that they 'will provide enhanced margins of safety and/or utilize simplified, inherent, passive, or other innovative means to accomplish their safety function'."(10) The NRC recommends the following specific attributes be addressed in advanced designs (10):

- Highly reliable and less complex shutdown and decay heat removal systems
- Longer time constraints to allow more time before reaching adverse conditions
- Simplified safety systems
- Defense-in-depth
- Designs based on existing technology or a suitable technology development program

To this end, future work will focus on developing a safety case which fits within this framework, using risk-informed analyses to inform the design. This safety case will address the three fundamental safety function within the context of the NRC guidance on advanced reactor safety analyses, as discussed. This safety case will focus on high-level critical safety functions, and essential safety systems, controls, and security frameworks.

References

[1] D. Blight, E. Engmann, J. Peterson, J. Richards, W. Sowah, and J. Warner, "Design of the Molten Salt Nuclear Battery - in fulfillment of the course requirements for NE 575," tech. rep., University of Idaho, 2019.

[2] J. P. Carter, T. Casper, K. Geddes, D. Haar, T. Lasley, and S. Lucas, "Microscale Nuclear Battery Shielding and Fuel Cycle (Front-to-Back End)," in fulfillment of course requirement for NE 575, University of Idaho, 2021.

[3] A. I. of Chemical Engineers, ed., Guidelines for hazard evaluation procedures. Hoboken, N.J: CCPS/AIChE/Wiley Interscience, 3rd ed ed., 2008.

[4] B. C. Kelleher, "Purification and Chemical Control of Molten Li2BeF4 for a Fluoride Salt Cooled Reactor," p. 282.

[5] J. Zhang, C. W. Forsberg, M. F. Simpson, S. Guo, S. T. Lam, R. O. Scarlat, F. Carotti, K. J. Chan, P. M. Singh, W. Doniger, K. Sridharan, and J. R. Keiser, "Redox potential control in molten salt systems for corrosion mitigation," Corrosion Science, vol. 144, pp. 44–53, Nov. 2018.

[6] K. Sridharan and T. Allen, "Corrosion in Molten Salts," in Molten Salts Chemistry, pp. 241–267, Elsevier, 2013.

[7] R. Christensen and R. Roper, "Redox Potential Control for the Molten Salt Reactor Concept," in Transactions of the American Nuclear Society - Volume 121, pp. 350–354, AMNS, 2019.

[8] G. Yamazaki, J. Yagi, T. Tanaka, T. Watanabe, and A. Sagara, "Corrosion Mitigation of Ferritic Steels in HF-Containing FLiNaK by Titanium Sacrificial Anodes," Plasma and Fusion Research, vol. 13, pp. 3405079–3405079, June 2018.

[9] D. Jones, A., Principles and Prevention of Corrosion. Prentice Hall, 2nd ed.

[10] C. E. Ader and N. P. Kadambi, "Building a Safety Case for Advanced Reactor Designs," p. 4.

[11] "NRC Approves New Approach to Streamline Advanced Reactor Licensing Process."

Appendix B: DSC Results

The following are the DSC Curves which were obtained for six Flinak samples.

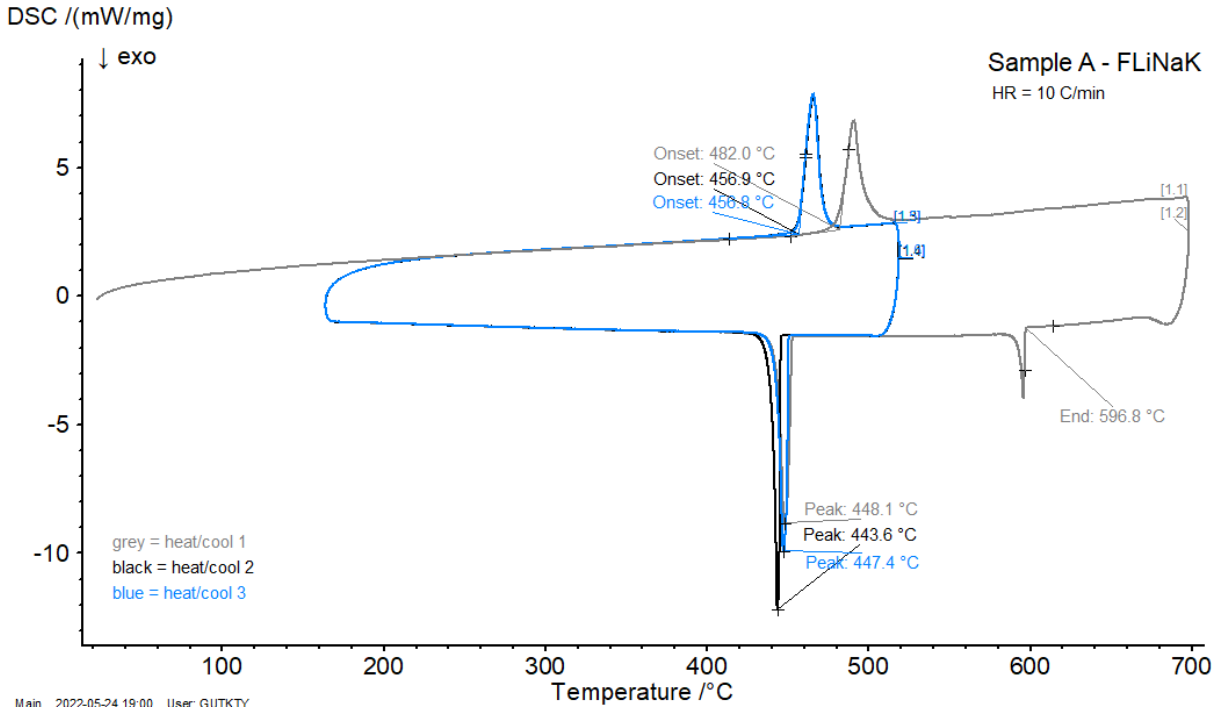

Figure 7.1: DSC curve for sample A, Flinak with no added impurities.

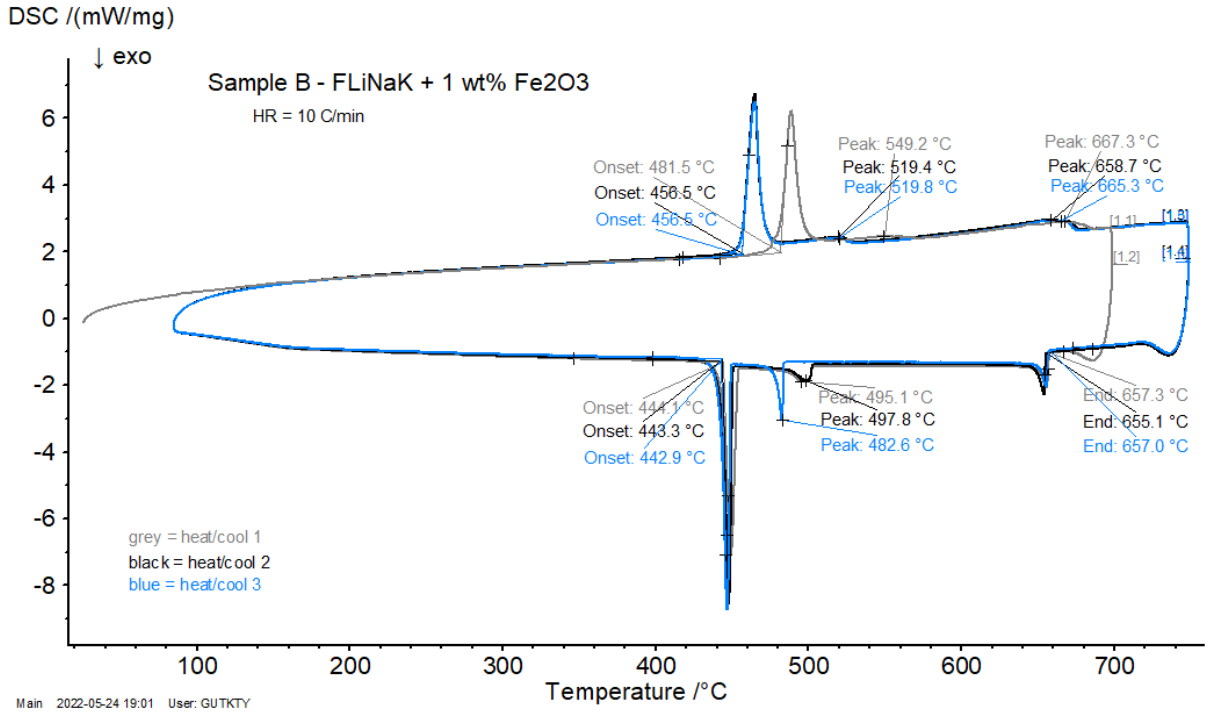

Figure 7.2: DSC curve for sample B, Flinak with 1% Fe_2O_3.

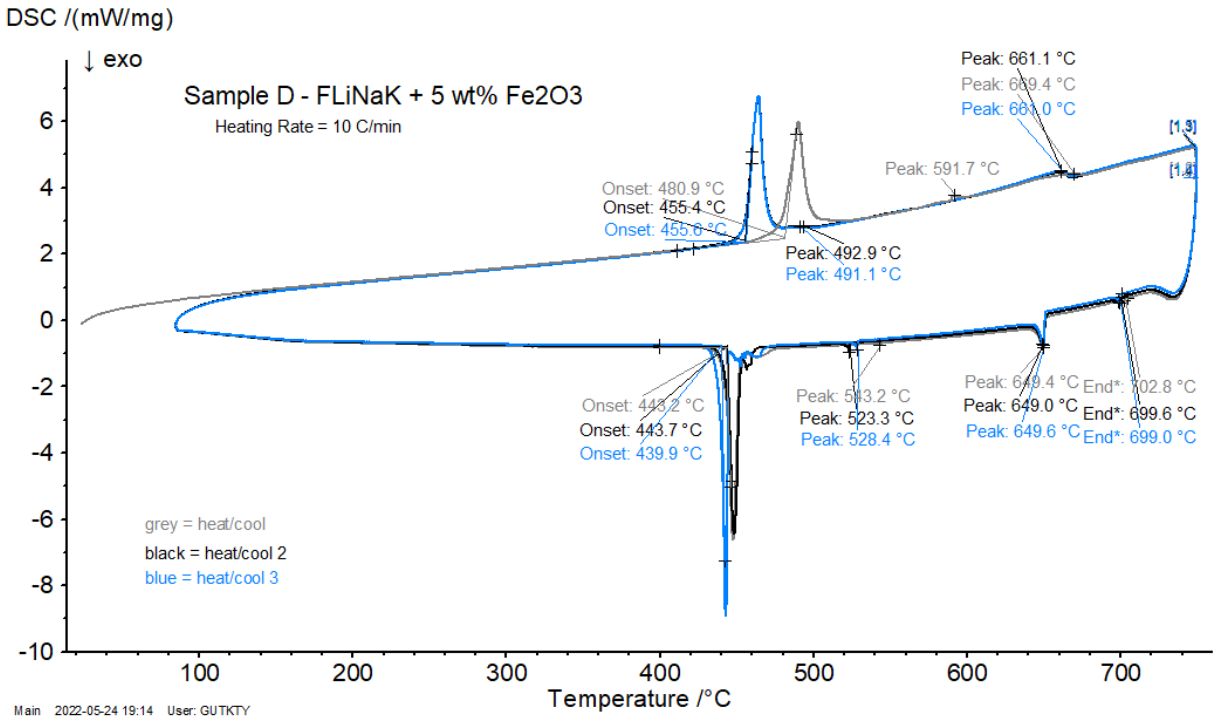

Figure 7.3: DSC curve for sample D, Flinak with 5% Fe_2O_3.

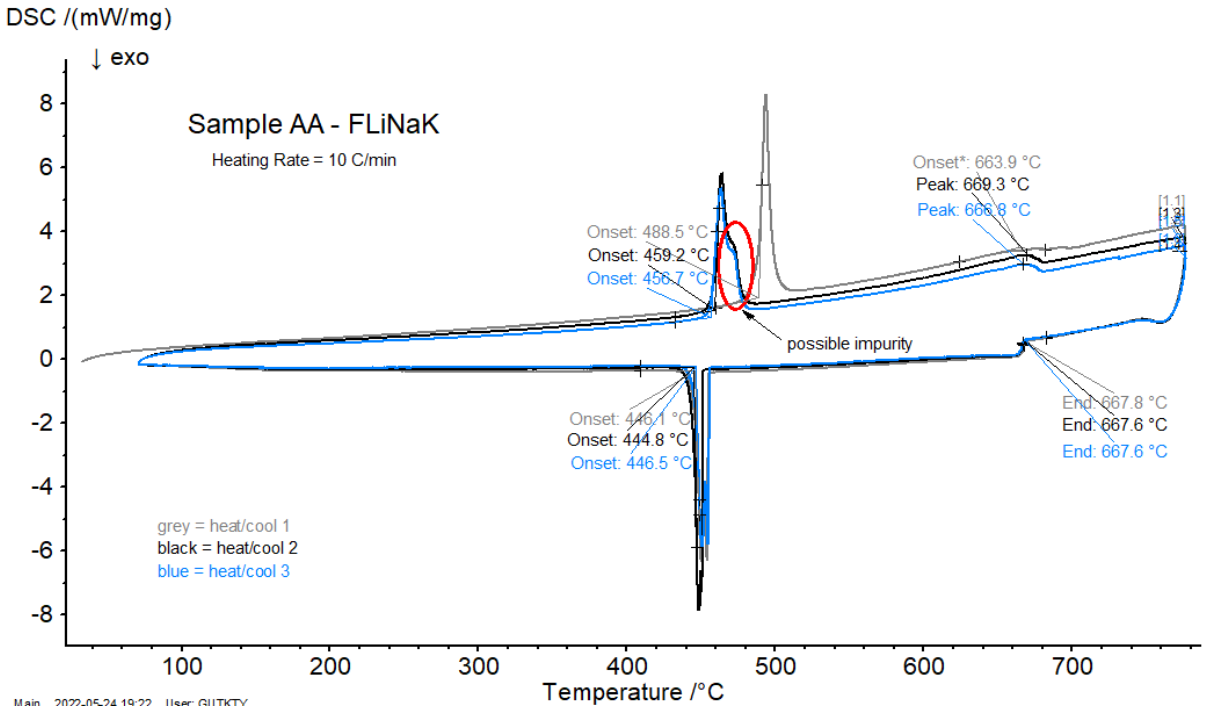

Figure 7.4: DSC curve for sample AA, Flinak with no added impurities.

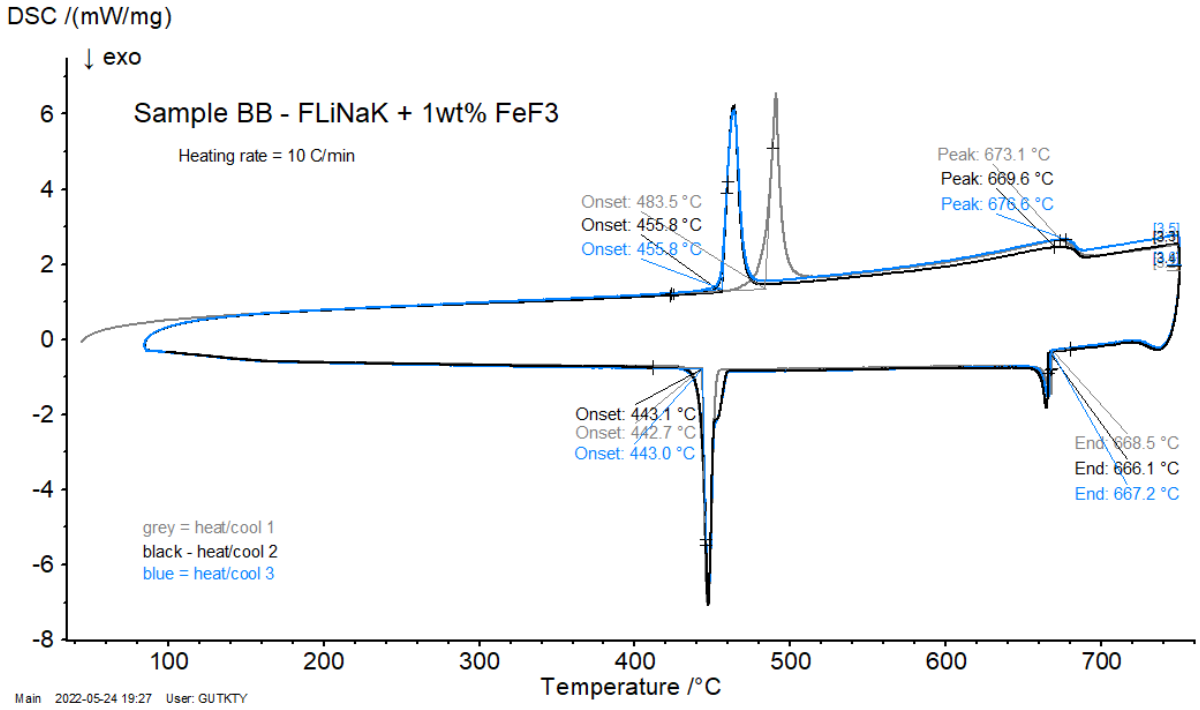

Figure 7.5: DSC curve for sample BB, Flinak with 1% FeF_3.

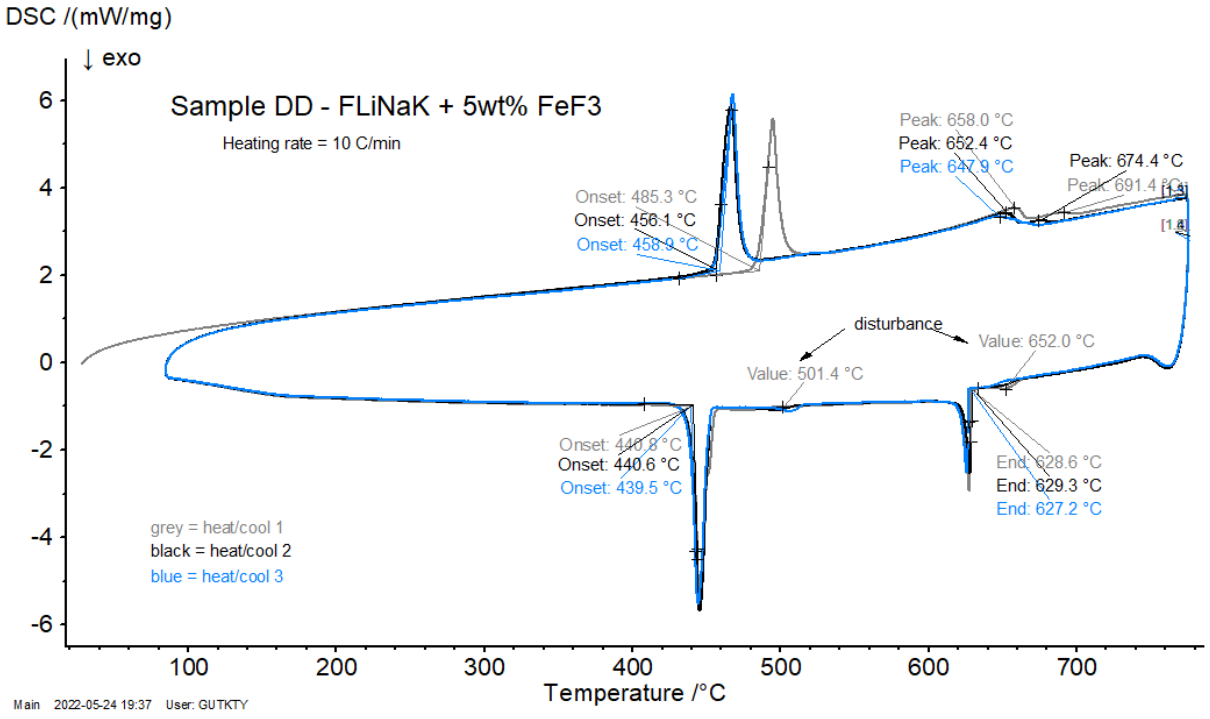

Figure 7.6: DSC curve for sample DD, Flinak with 5% FeF_3.

Appendix C: Generated Report on COMSOL Multiphysics Base Case

The software COMSOL Multiphysics has the capability to generate a detailed report, with parameters, computation, and result details. The software-generated report for the base case of the molten salt corrosion model is included herein.

Base Case - Dummy Electrode

Robin Roper – COMSOL Generated Model Report

Report Generation date

Jul 7, 2022 10:17:54 AM

1 Global Definitions

Date	Jun 27, 2022 12:21:47 PM

GLOBAL SETTINGS

Name	Base Case - Dummy Electrode.mph
Path	C:\Users\CSNRIntern\Desktop\Robin Roper\June - functional\New testing\Base Case - Dummy Electrode.mph
Version	COMSOL Multiphysics 5.6 (Build: 401)

USED PRODUCTS

COMSOL Multiphysics
Corrosion Module

COMPUTER INFORMATION

CPU	Intel64 Family 6 Model 79 Stepping 1, 20 cores
Operating system	Windows 10

1.1 PARAMETERS

PARAMETERS 1

Name	Expression	Value	Description
mfCr	1e-4[1]	1E−4	Initial Cr conc
cO2	0.86[mol/m^3]	0.86 mol/m³	Initial O2 conc
Eq_O2	-0.31[V]	−0.31 V	Eq potential of oxygen rxn
Eq_Cr	-0.44[V]	−0.44 V	Eq potential of Cr rxn
zf	-1	−1	F- ions
zc	2.19	2.19	Avg charge of steel
cf	32435.91[mol/m^3]	32436 mol/m³	fluoride ion concentration
Adis	2.07e-12[mol/cm^2/s]	2.07E−8 mol/(m²·s)	Dissolution Affinity
T	700[C]	700 C	system temp
a	0.5	0.5	
MWsalt	126.02[g/mol]	0.12602 kg/mol	molecular weight of flinak

Name	Expression	Value	Description
rhosalt	2000[kg/m^3]	2000 kg/m³	density of flinak
cs	mfCr*(rhosalt/MWsalt)	1.587 mol/m³	concentration of chromium
musalt	0.01[Pa*s]	0.01 Pa·s	viscosity of flinak
i0	5.2552E-9[A/m^2]	5.2552E−9 A/m²	current
k	10^ - 3[cm/s]	1E−5 m/s	Reaction constant from Guo et. al
F	F_const	96485 C/mol	Faraday's constant
i0_guo	2*F*k*(cs^(1 - a))*(mfCr^a)	0.02431	current from Guo et. al
i0_wu	0.57[mA*cm^ - 2]	5.7 A/m²	current from Wu et. al optimized fitting
a_wu	0.32	0.32	alpha from Wu et. al optimized fitting
diam	0.1[m]	0.1 m	
sdiam	0.2[m]	0.2 m	
D	2*diam*sdiam/(diam + sdiam)	0.13333 m	
vset	0.05[m/s]	0.05 m/s	
Re	rhosalt*vset*D/musalt	1333.3	
i0guo2	9.6e-6[A/cm^2]	0.096 A/m²	from Guo et. al fig 4a

2 Component 1

2.1 DEFINITIONS

2.1.1 Nonlocal Couplings

Average 1

Coupling type	Average
Operator name	aveop1

SELECTION

Geometric entity level	Boundary
Selection	Geometry geom1: Dimension 1: Boundaries 1–2, 10–11

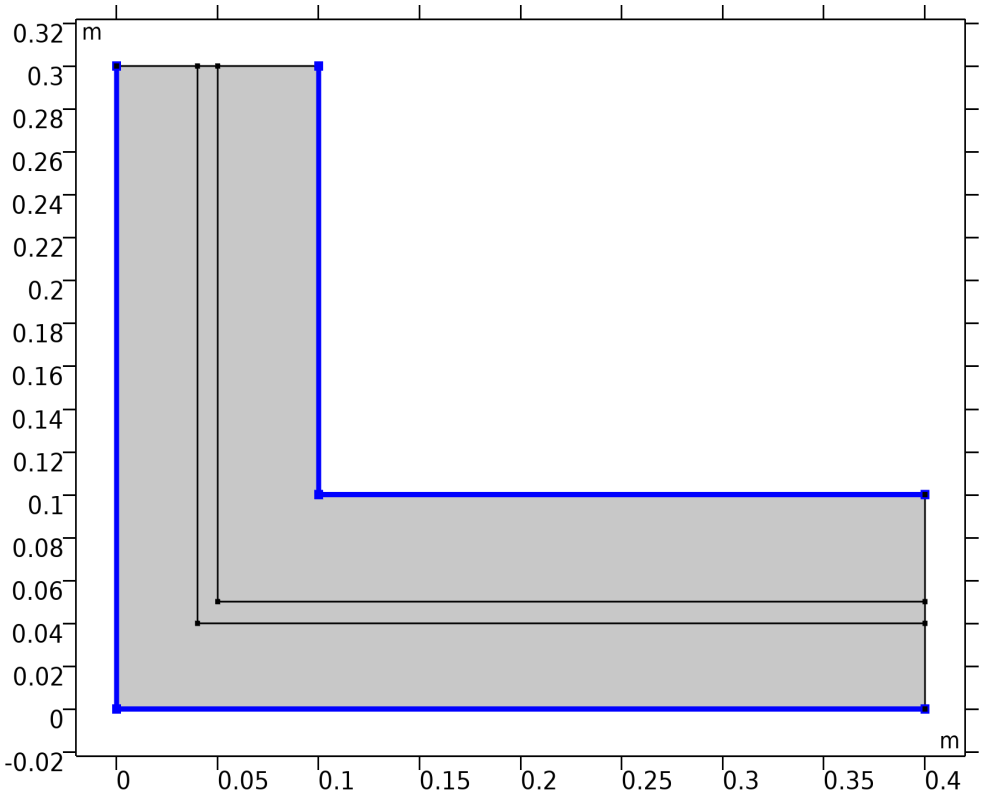

Selection

2.1.2 Coordinate Systems

Boundary System 1

Coordinate system type	Boundary system
Tag	sys1

COORDINATE NAMES

First	Second	Third
t1	n	to

2.1.3 Shared Properties

Model Input 1

Tag	minpt1

DEFINITION

Description	Value
	700[C]

2.2 GEOMETRY 1

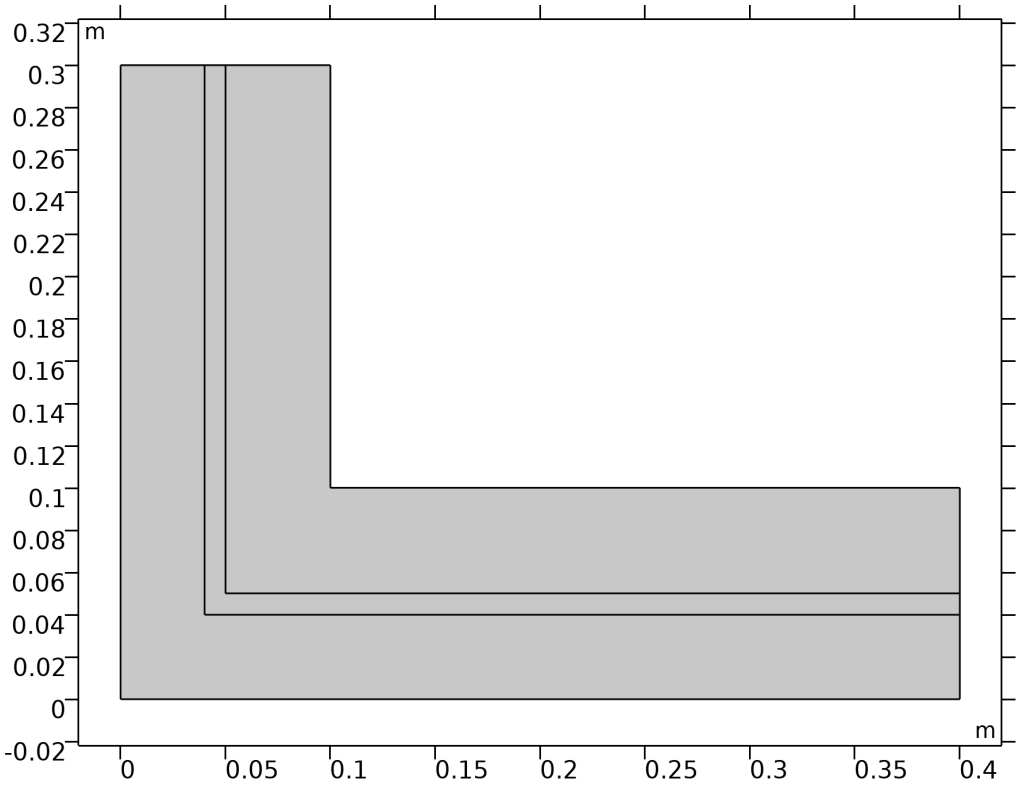

Geometry 1

UNITS

Length unit	m
Angular unit	deg

2.3 TERTIARY CURRENT DISTRIBUTION, NERNST-PLANCK

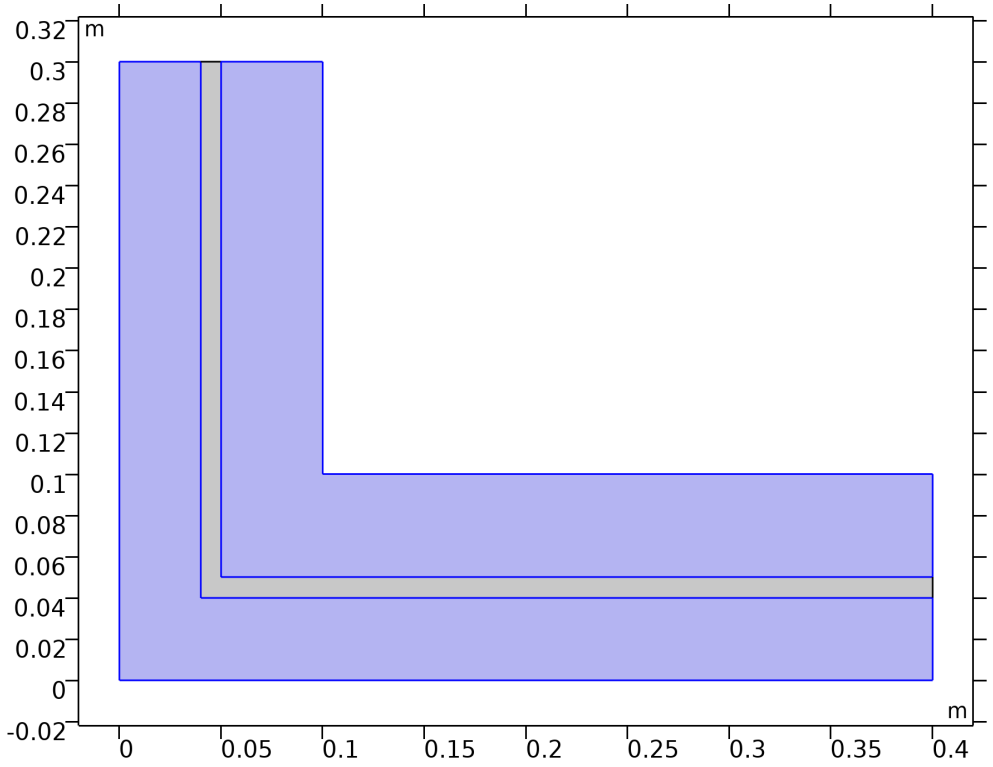

Tertiary Current Distribution, Nernst-Planck

EQUATIONS

$$\nabla \cdot \mathbf{J}_i + \mathbf{u} \cdot \nabla c_i = R_i$$

$$\nabla \cdot \mathbf{i}_\mathrm{l} = F\sum_i z_i R_i + FR_\mathrm{H} - FR_\mathrm{OH} + Q_\mathrm{l}$$

$$\nabla \cdot \mathbf{i}_\mathrm{s} = -F\sum_i z_i R_i - FR_\mathrm{H} + FR_\mathrm{OH} + Q_\mathrm{s}$$

$$\sum_i z_i c_i + c_\mathrm{H} - c_\mathrm{OH} = 0, \quad c_\mathrm{H} c_\mathrm{OH} = K_\mathrm{w}$$

$$\mathbf{J}_i = -D_i \nabla c_i - z_i u_{\mathrm{m},i} F c_i \nabla \phi_\mathrm{l}$$

$$\mathbf{J}_\mathrm{H} = -D_\mathrm{H} \nabla c_\mathrm{H} - u_{\mathrm{m,H}} F c_\mathrm{H} \nabla \phi_\mathrm{l}$$

$$\mathbf{J}_\mathrm{OH} = -D_\mathrm{OH} \nabla c_\mathrm{OH} + u_{\mathrm{m,OH}} F c_\mathrm{OH} \nabla \phi_\mathrm{l}$$

$$\mathbf{i}_\mathrm{l} = F\sum_i z_i \mathbf{J}_i + F\mathbf{J}_\mathrm{H} - F\mathbf{J}_\mathrm{OH}$$

$$\mathbf{i}_\mathrm{s} = -\sigma_\mathrm{s} \nabla \phi_\mathrm{s}$$

$$\phi_\mathrm{l} = \mathrm{phil}, \quad \phi_\mathrm{s} = \mathrm{phis}$$

FEATURES

Name	Level
Electrolyte 1	Domain

Name	Level
No Flux 1	Boundary
Insulation 1	Boundary
Initial Values 1	Domain
Electrode Surface 1	Boundary
Electrode Surface 2	Boundary
Outflow 1	Boundary

2.4 DEFORMED GEOMETRY

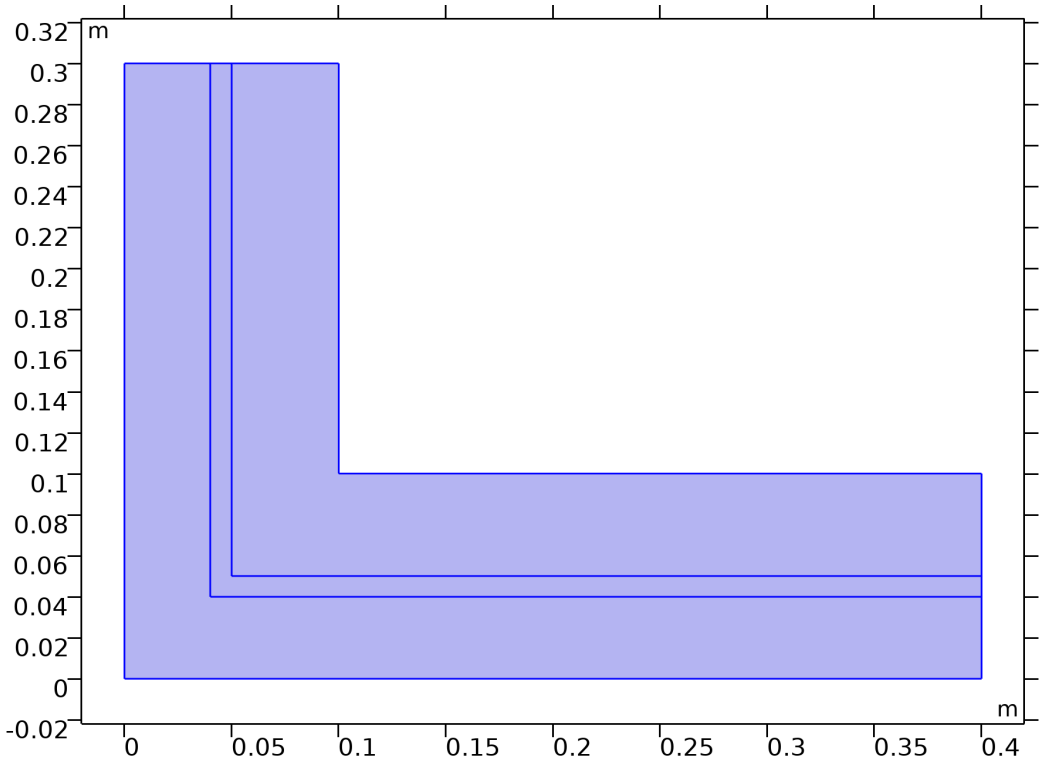

Deformed Geometry

FEATURES

Name	Level
Fixed Mesh 1	Domain
Prescribed Mesh Displacement 1	Boundary

2.5 LAMINAR FLOW

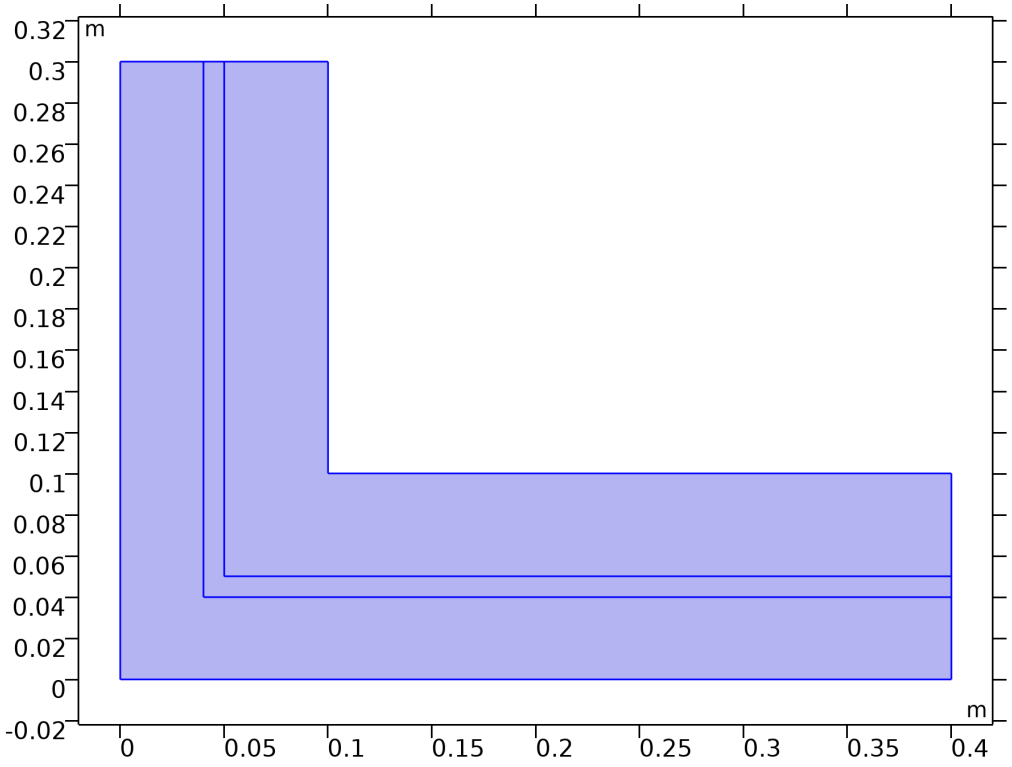

Laminar Flow

EQUATIONS

$$\rho(\mathbf{u}\cdot\nabla)\mathbf{u} = \nabla\cdot[-p\mathbf{I}+\mathbf{K}]+\mathbf{F}$$
$$\rho\nabla\cdot\mathbf{u} = 0$$

FEATURES

Name	Level
Fluid Properties 1	Domain
Initial Values 1	Domain
Wall 1	Boundary
Inlet 1	Boundary
Outlet 1	Boundary

2.6 MESH 1

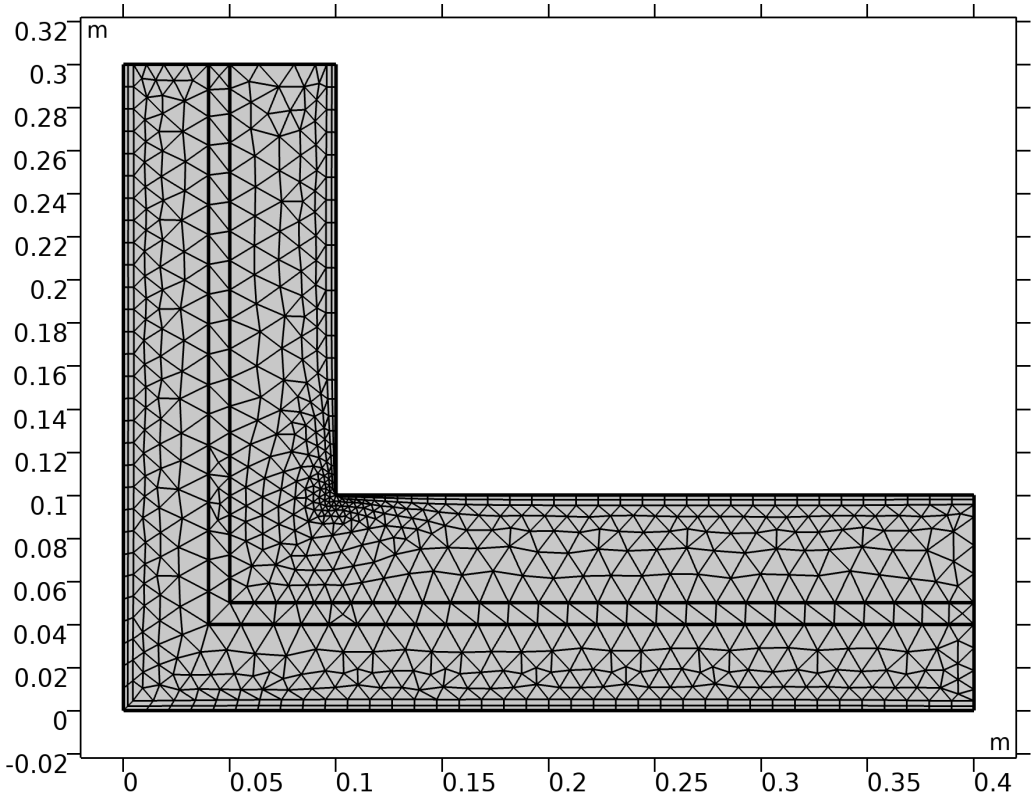

Mesh 1

3 Study 1

COMPUTATION INFORMATION

Computation time	26 min 28 s

3.1 PARAMETRIC SWEEP

Parameter name	Parameter value list	Parameter unit
vset	0.05,0.06,0.07	m/s

STUDY SETTINGS

Description	Value
Sweep type	Specified combinations
Parameter name	vset
Unit	m/s

PARAMETERS

Parameter name	Parameter value list	Parameter unit
vset	0.05,0.06,0.07	m/s

3.2 CURRENT DISTRIBUTION INITIALIZATION

STUDY SETTINGS

Description	Value
Include geometric nonlinearity	Off

PHYSICS AND VARIABLES SELECTION

Physics interface	Discretization
Tertiary Current Distribution, Nernst-Planck (tcd)	physics
Deformed Geometry (dg)	physics
Laminar Flow (spf)	physics

MESH SELECTION

Geometry	Mesh
Geometry 1 (geom1)	mesh1

3.3 TIME DEPENDENT

Times	Unit
range(0,50,500)	h

STUDY SETTINGS

Description	Value
Include geometric nonlinearity	Off

STUDY SETTINGS

Description	Value
Time unit	h
Output times	{0, 50, 100, 150, 200, 250, 300, 350, 400, 450, 500}
Tolerance	User controlled

PHYSICS AND VARIABLES SELECTION

Physics interface	Discretization
Tertiary Current Distribution, Nernst-Planck (tcd)	physics
Deformed Geometry (dg)	physics
Laminar Flow (spf)	physics

MESH SELECTION

Geometry	Mesh
Geometry 1 (geom1)	mesh1

4 Results

4.1.1 Study 1/Parametric Solutions 1

SOLUTION

Description	Value
Solution	Parametric Solutions 1
Component	Component 1 (comp1)

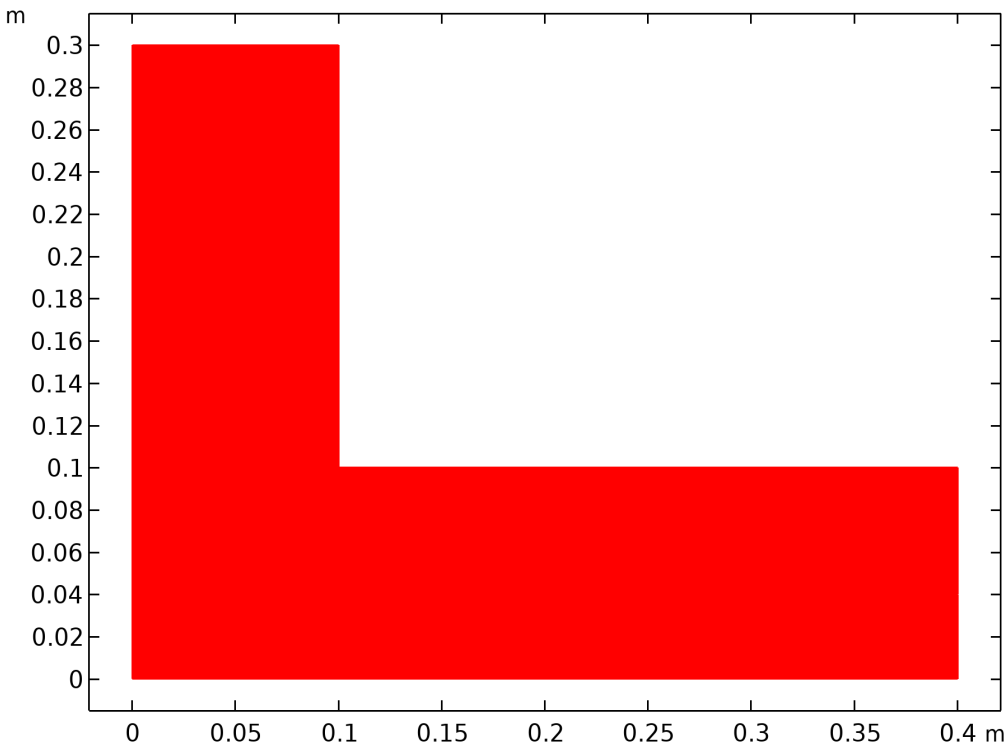

Dataset: Study 1/Parametric Solutions 1

4.2 PLOT GROUPS

4.2.1 Bottom Horizontal all Velocities

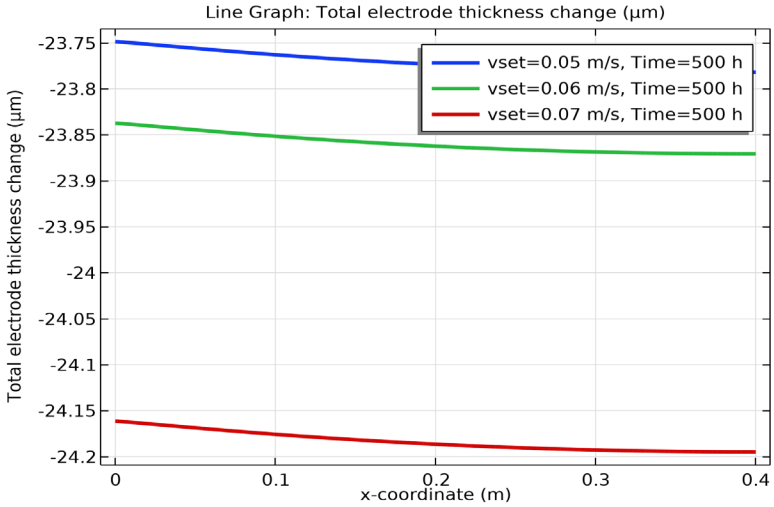

Line Graph: Total electrode thickness change (µm)

4.2.2 Bottom Horizontal 1

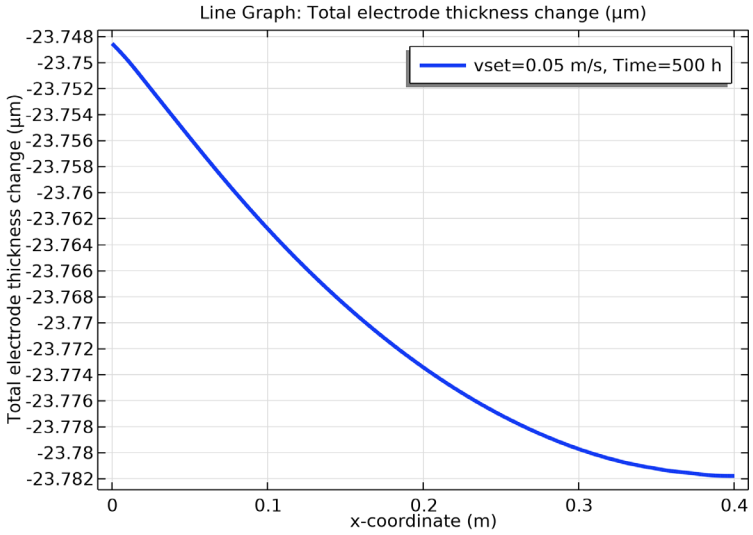

Line Graph: Total electrode thickness change (µm)

4.2.3 Bottom Horizontal derivative

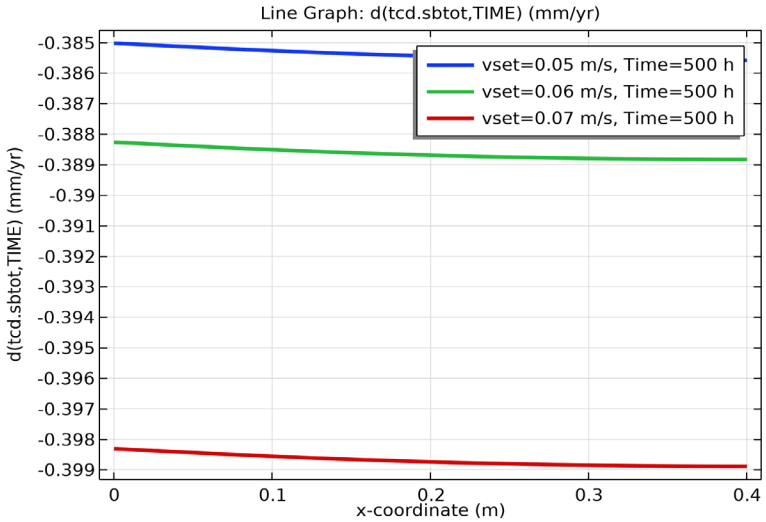

Line Graph: d(tcd.sbtot,TIME) (mm/yr)

4.2.4 Top Horizontal

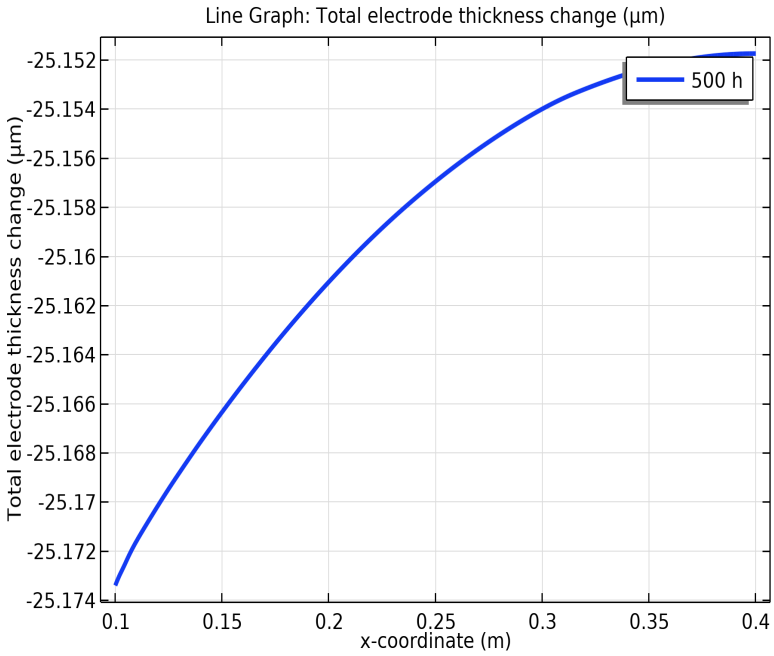

Line Graph: Total electrode thickness change (µm)

4.2.5 Top Horizontal All

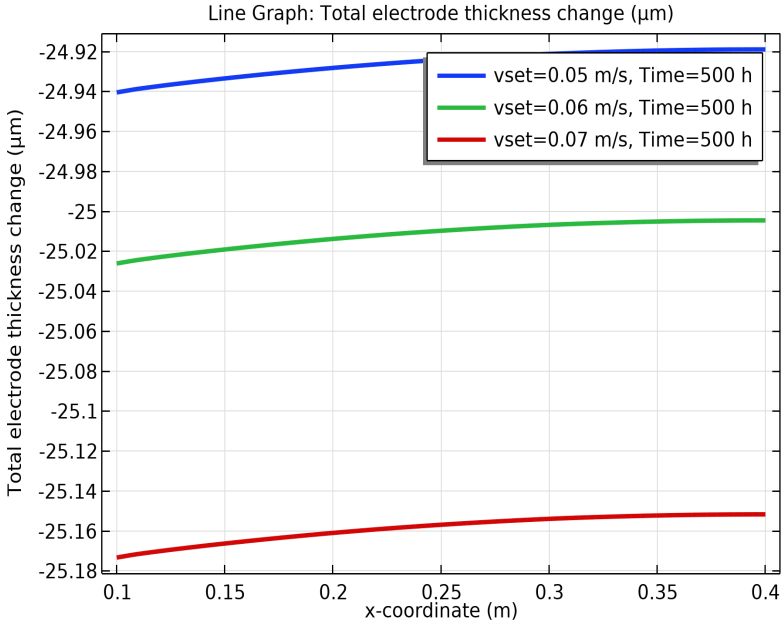

Line Graph: Total electrode thickness change (µm)

4.2.6 Top Horizontal Derivative

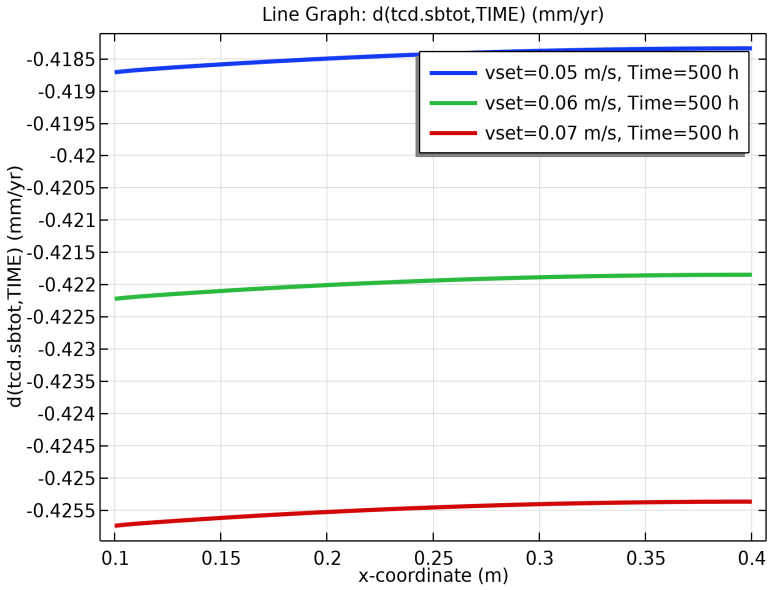

Line Graph: d(tcd.sbtot,TIME) (mm/yr)

4.2.7 Right Vertical

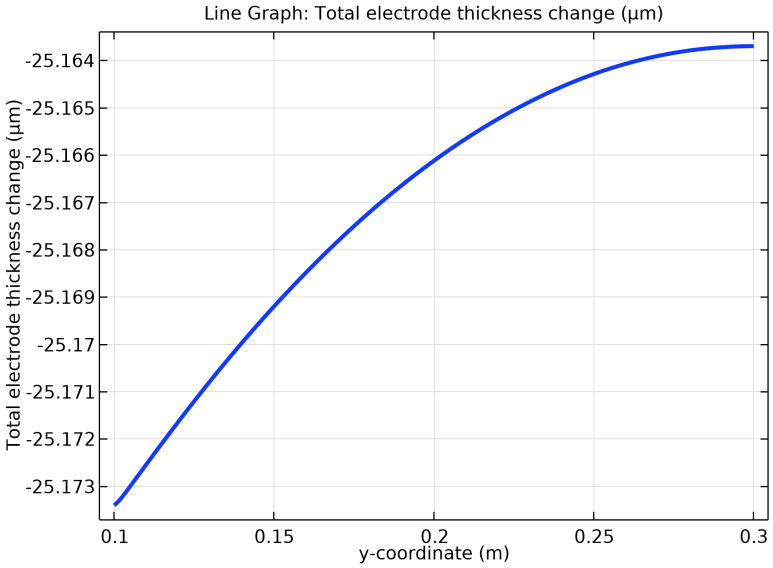

Line Graph: Total electrode thickness change (µm)

4.2.8 Right Vertical All

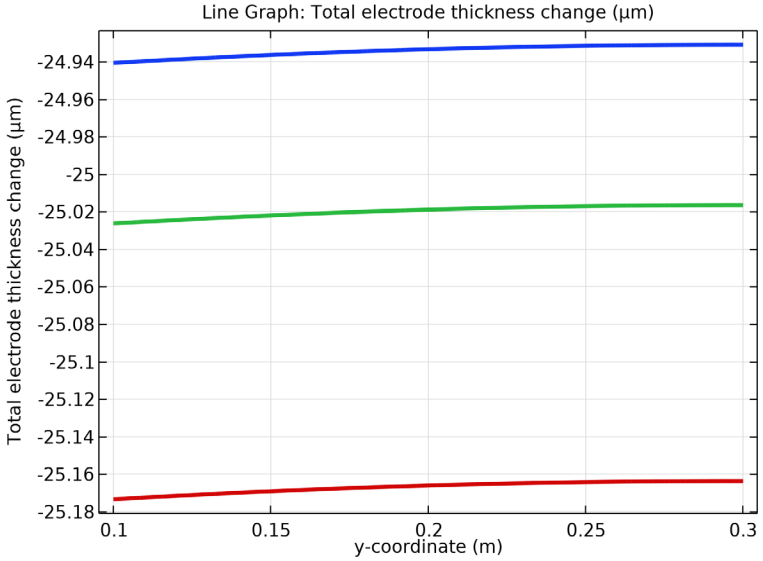

Line Graph: Total electrode thickness change (µm)

4.2.9 Right Vertical Derivative

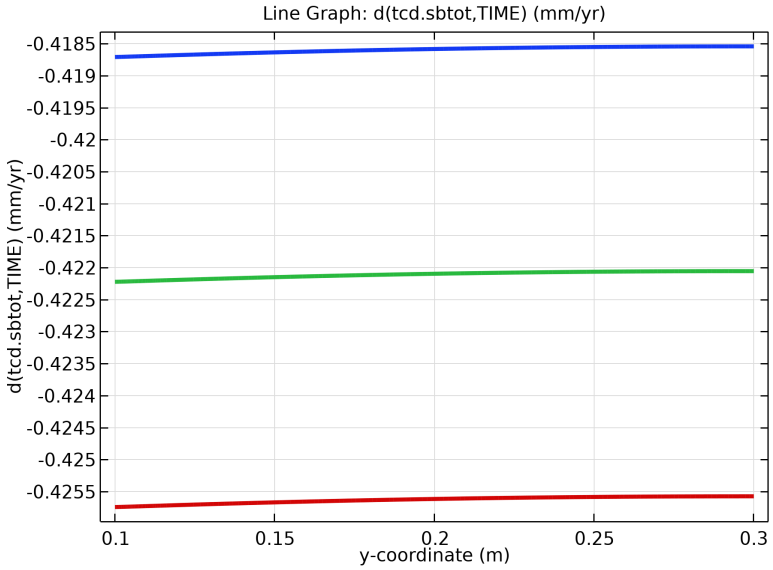

Line Graph: d(tcd.sbtot,TIME) (mm/yr)

4.2.10 Left Vertical

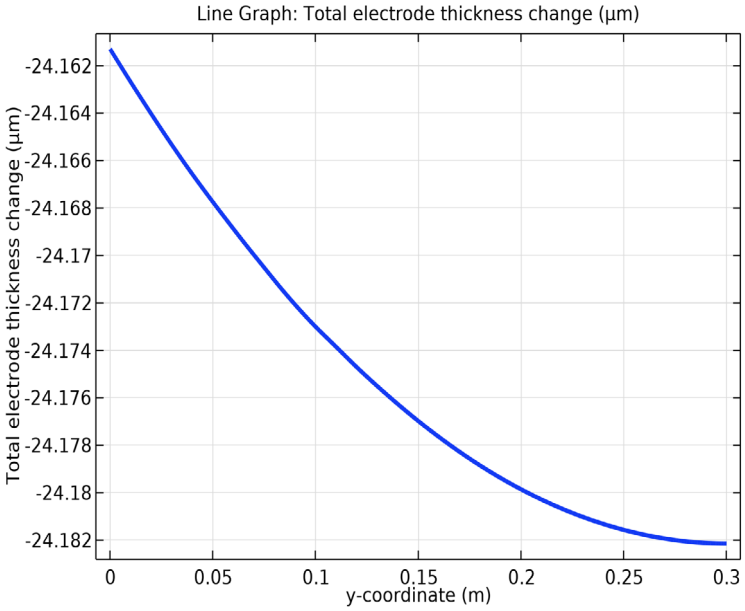

Line Graph: Total electrode thickness change (µm)

4.2.11 Left Vertical All

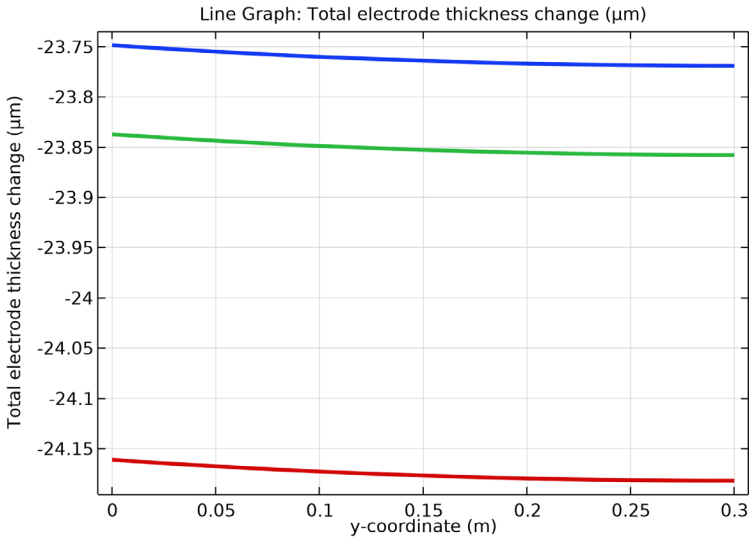

Line Graph: Total electrode thickness change (µm)

4.2.12 Left Vertical Derivative

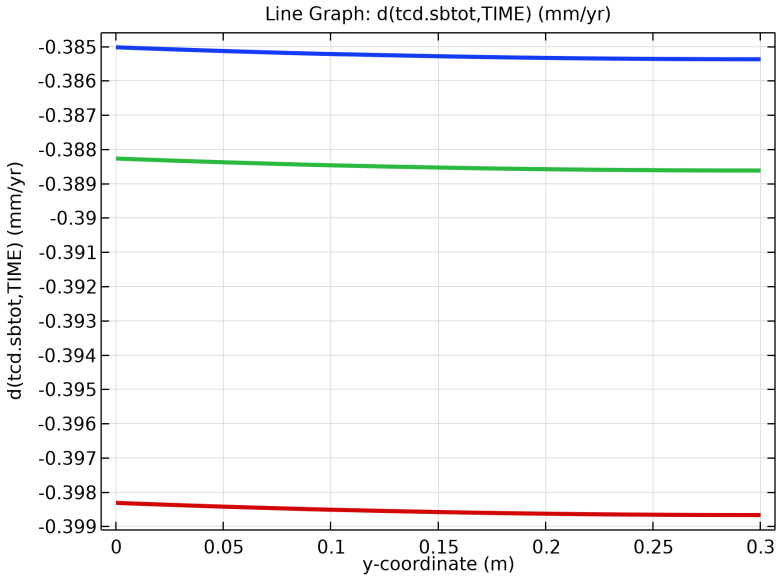

Line Graph: d(tcd.sbtot,TIME) (mm/yr)

4.2.13 Velocity 0.05

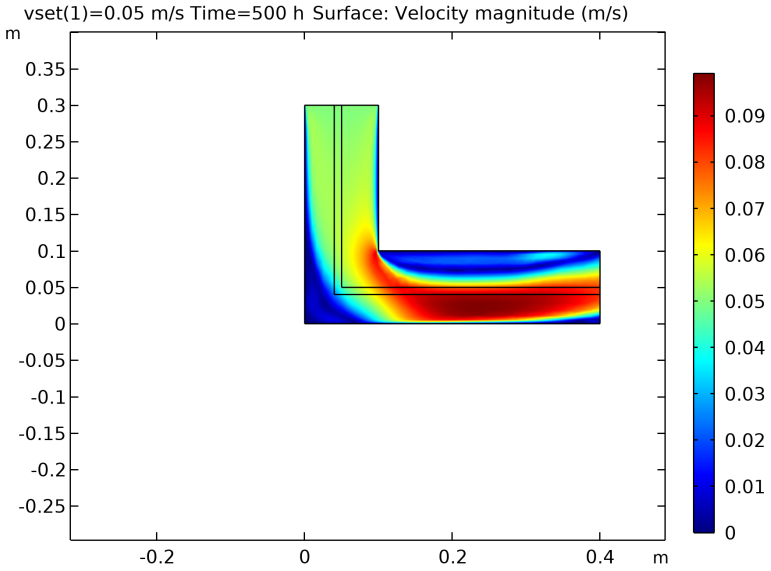

Surface: Velocity magnitude (m/s)

4.2.14 Velocity 0.06

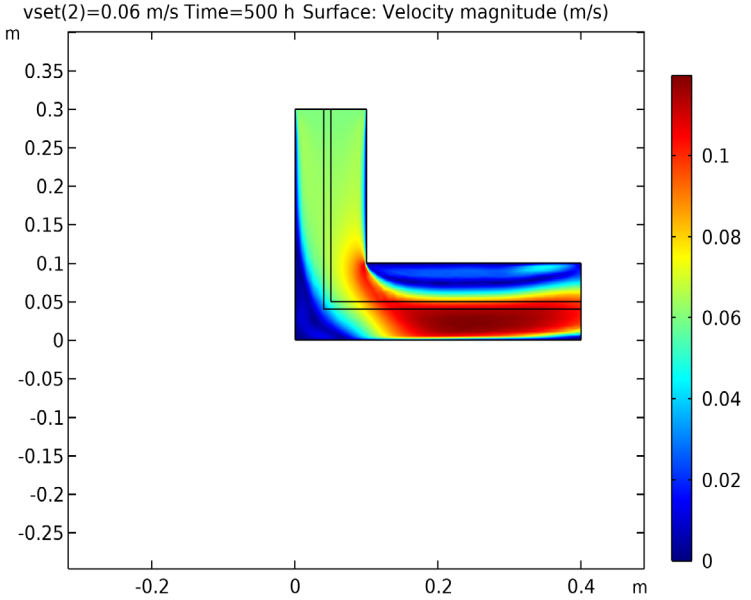

Surface: Velocity magnitude (m/s)

4.2.15 Velocity 0.07

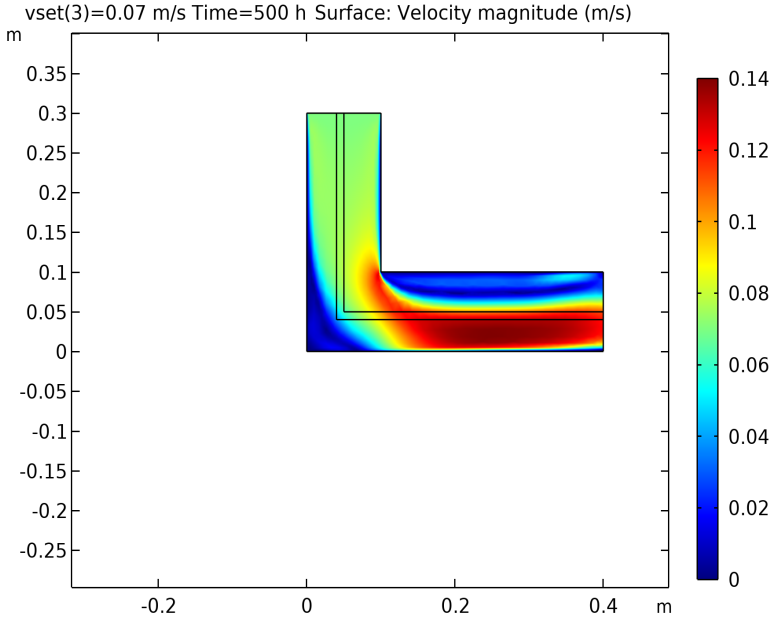

Surface: Velocity magnitude (m/s)

4.2.16 Electrode Thickness Change

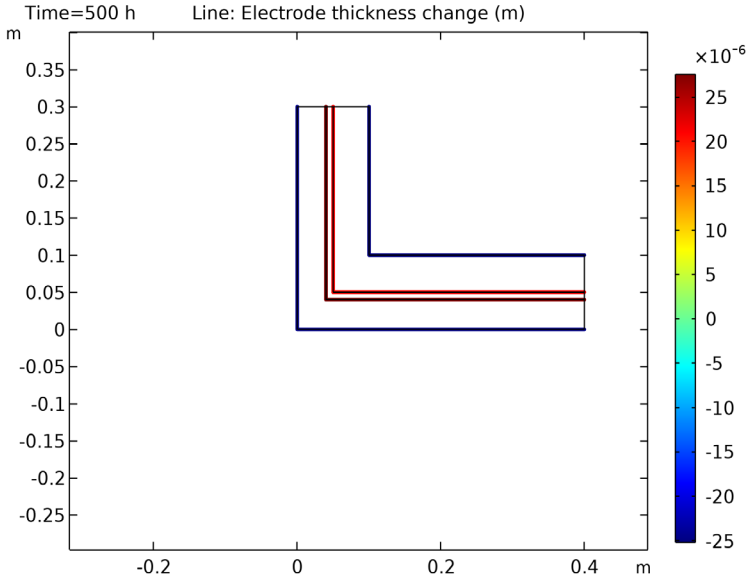

Line: Electrode thickness change (m)

4.2.17 Points by time

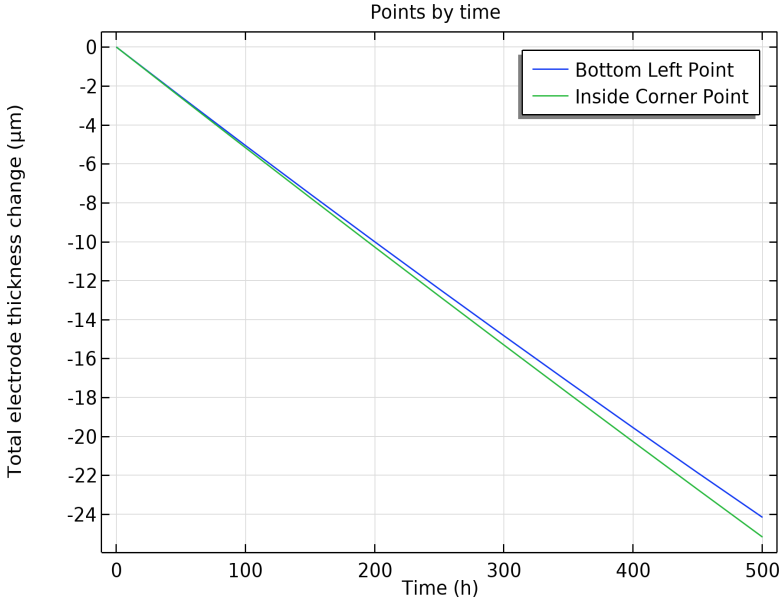

Points by time

4.2.18 Points by time derivative

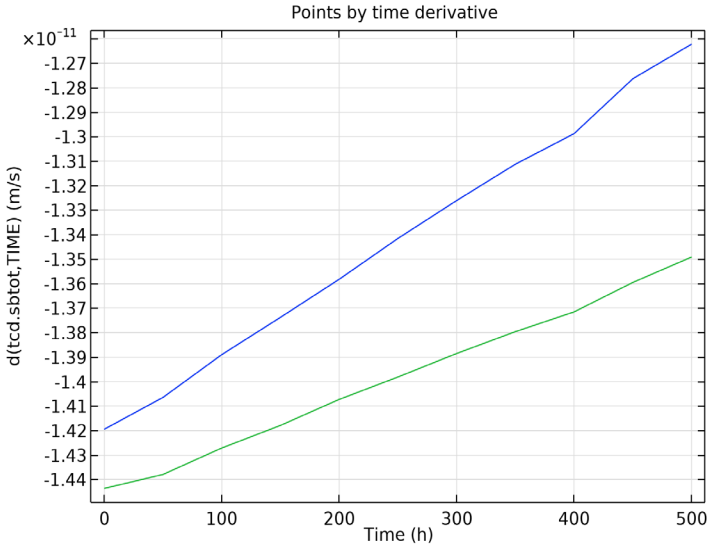

Points by time derivative

4.2.19 Dummy 1.1

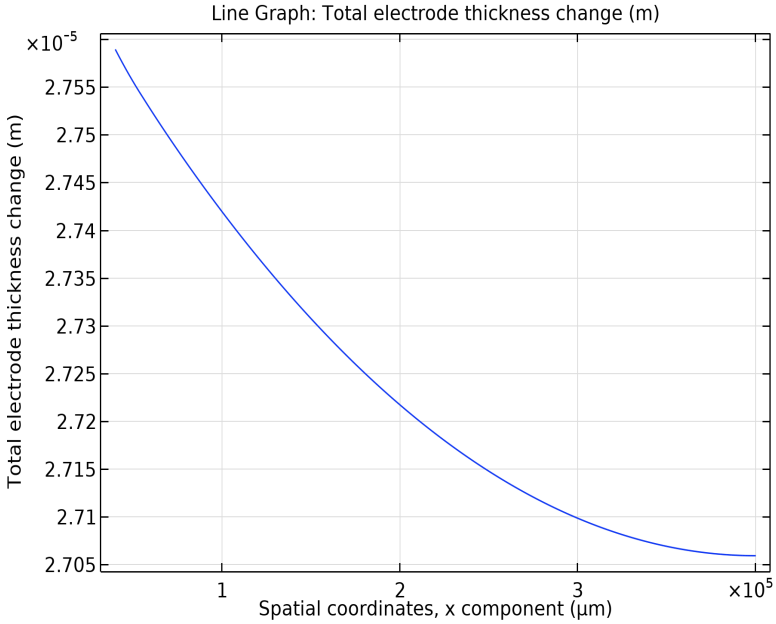

Line Graph: Total electrode thickness change (m)

4.2.20 Dummy 1.2

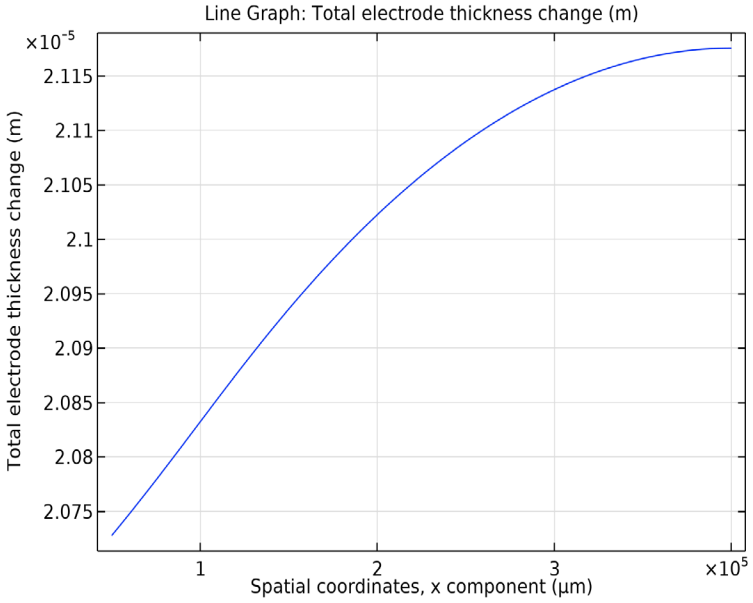

Line Graph: Total electrode thickness change (m)

4.2.21 Dummy 1.3

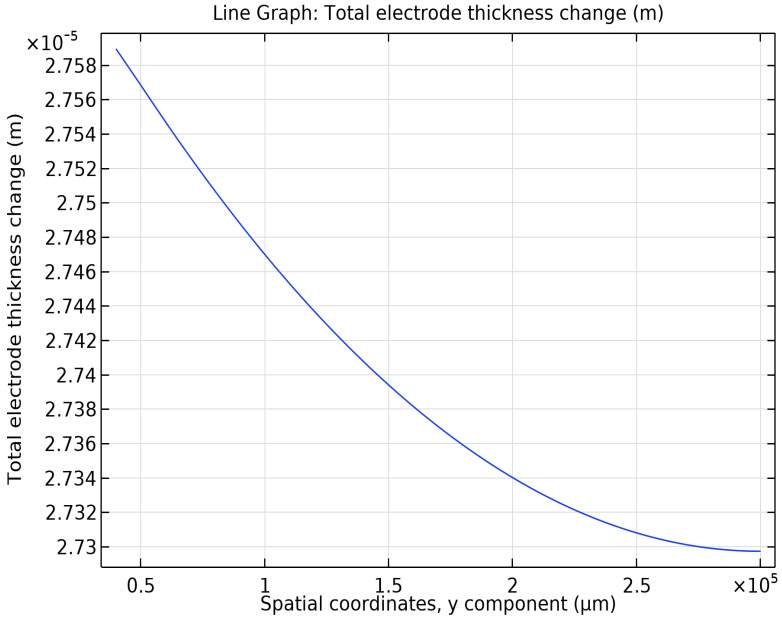

Line Graph: Total electrode thickness change (m)

4.2.22 Dummy 1.4

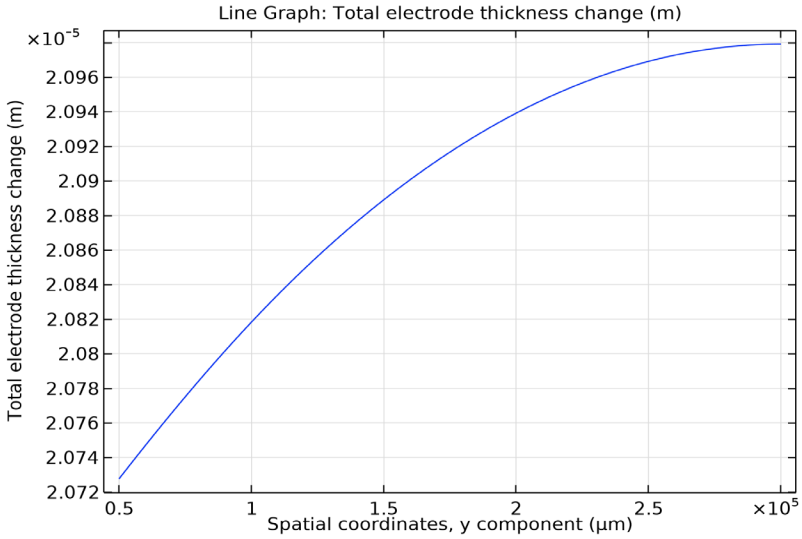

Line Graph: Total electrode thickness change (m)

4.2.23 Velocity - Arrows

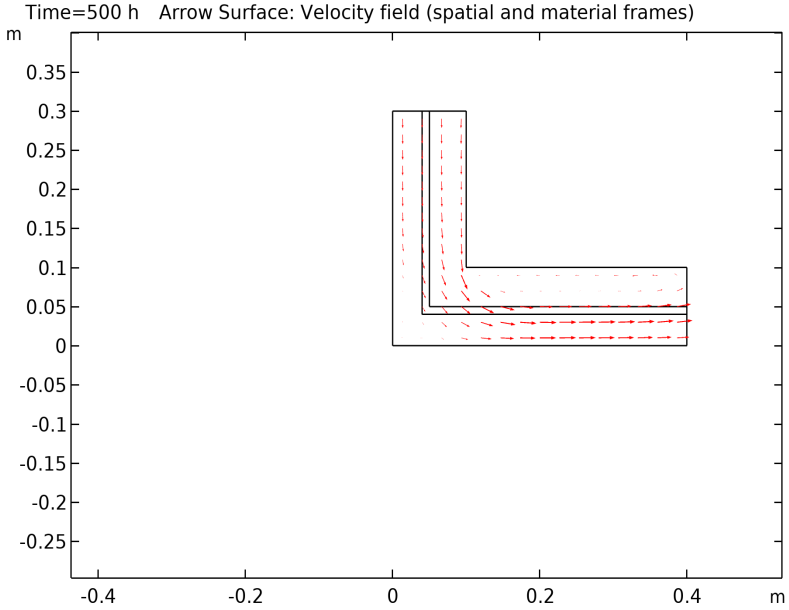

Arrow Surface: Velocity field (spatial and material frames)

4.2.24 Electrolyte Current Density (tcd)

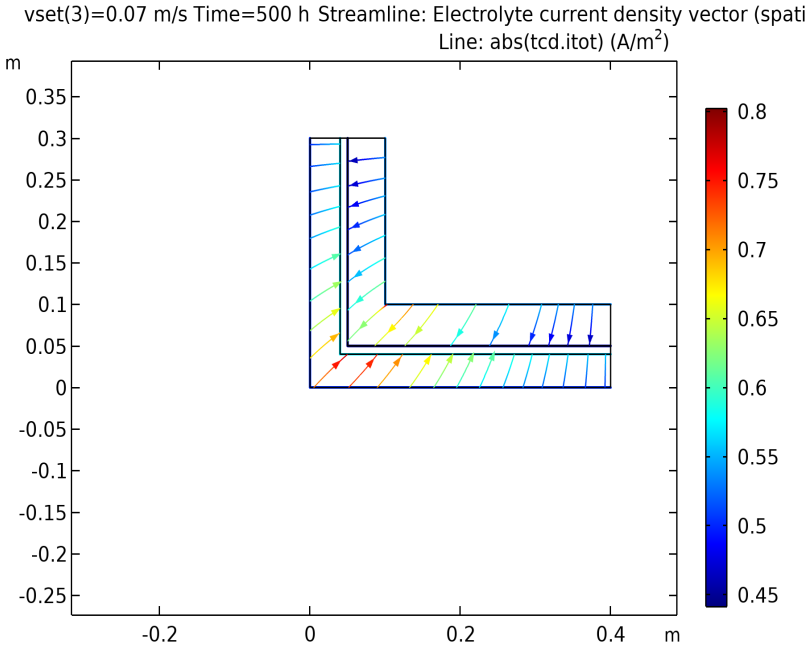

Streamline: Electrolyte current density vector (spatial and material frames) Line: abs(tcd.itot) (A/m^2)

4.2.25 Electrode Potential vs. Adjacent Reference (tcd)

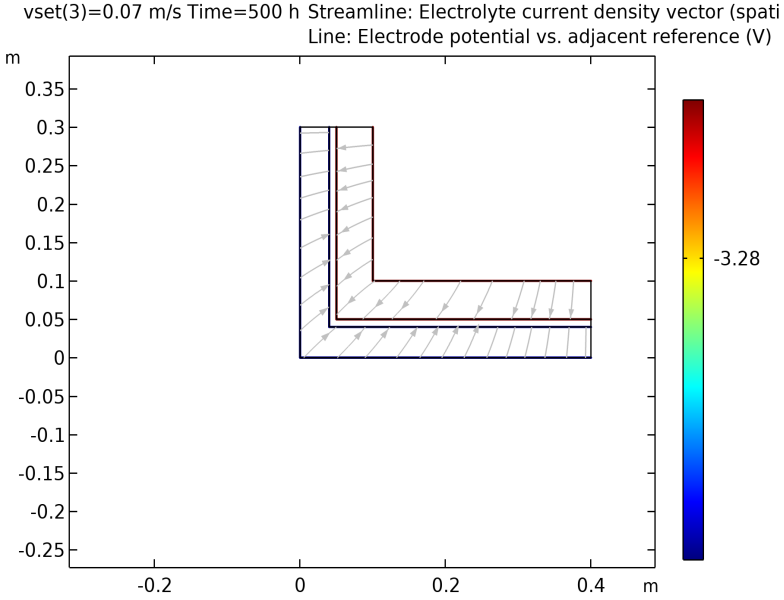

Streamline: Electrolyte current density vector (spatial and material frames) Line: Electrode potential vs. adjacent reference (V)

4.2.26 Total Electrode Thickness Change (tcd)

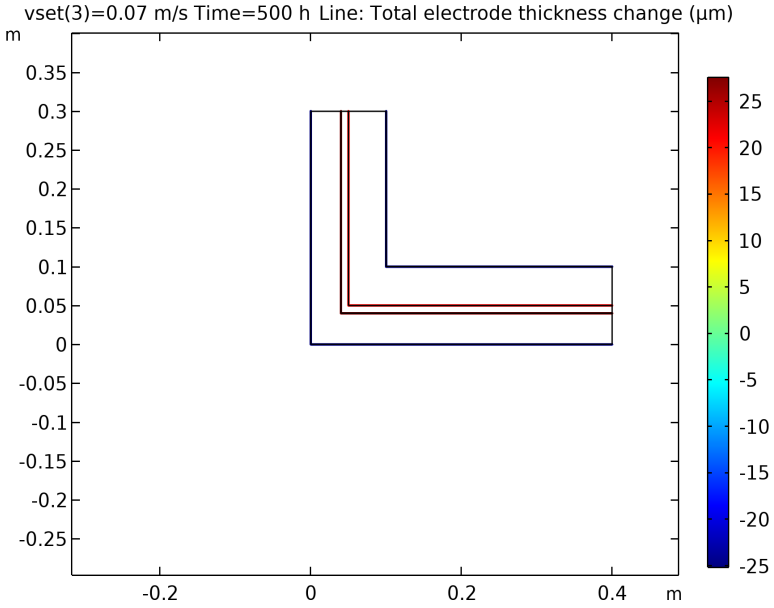

Line: Total electrode thickness change (µm)

4.2.27 Concentration, Cr (tcd)

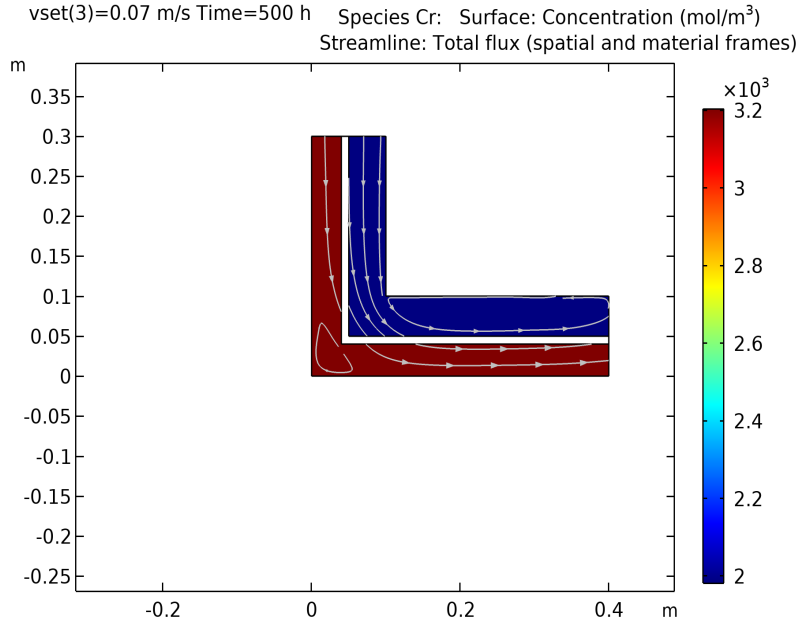

Species Cr: Surface: Concentration (mol/m³) Streamline: Total flux (spatial and material frames)

4.2.28 Concentration, O2 (tcd)

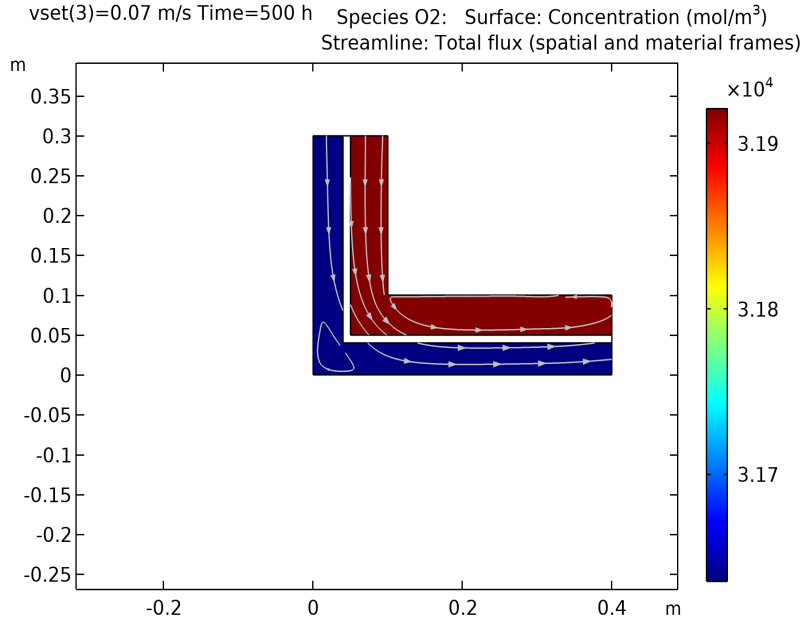

Species O2: Surface: Concentration (mol/m³) Streamline: Total flux (spatial and material frames)

4.2.29 Pressure (spf)

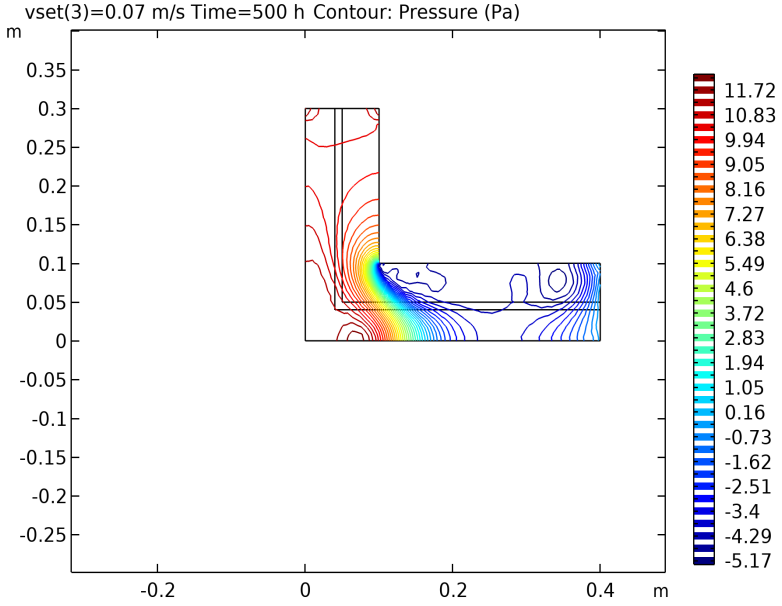

Contour: Pressure (Pa)

4.2.30 Current Density for Horizontal Walls

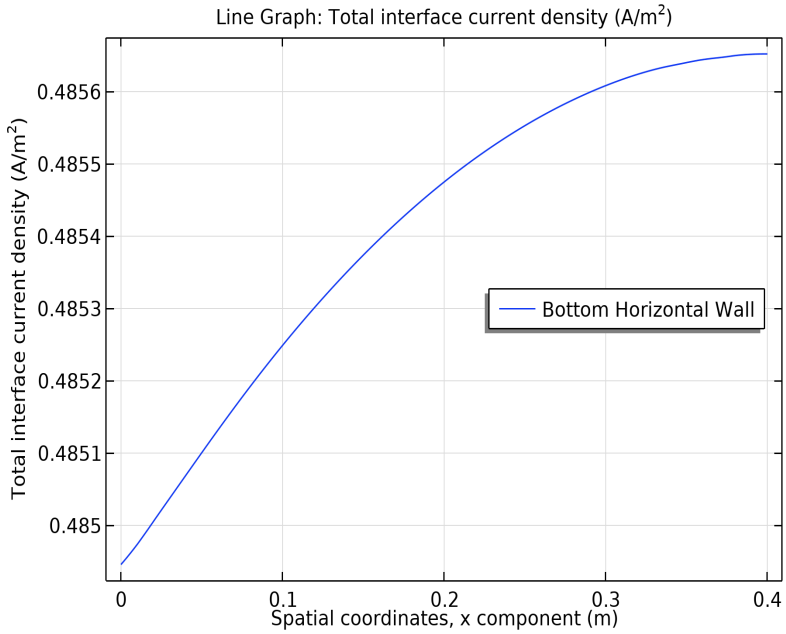

Line Graph: Total interface current density (A/m²)

4.2.31 Current Density for Vertical Walls

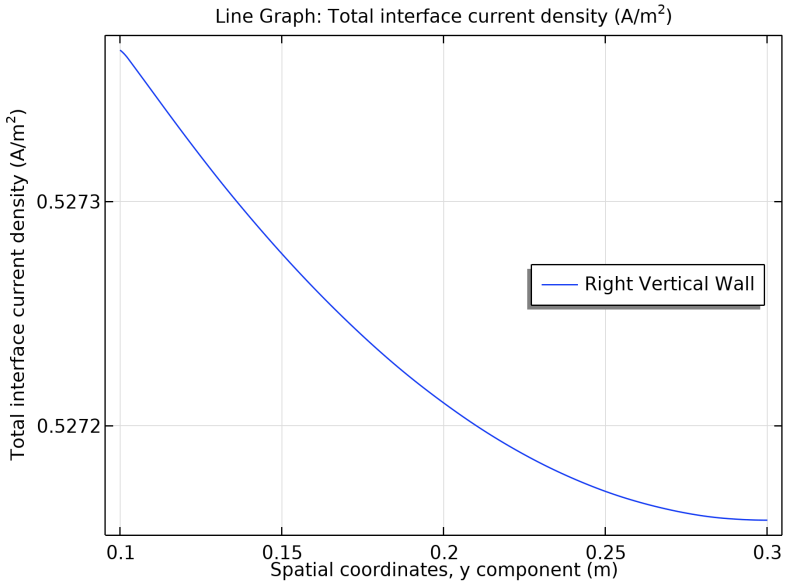

Line Graph: Total interface current density (A/m²)

4.2.32 Current Density for Horizontal Walls 1

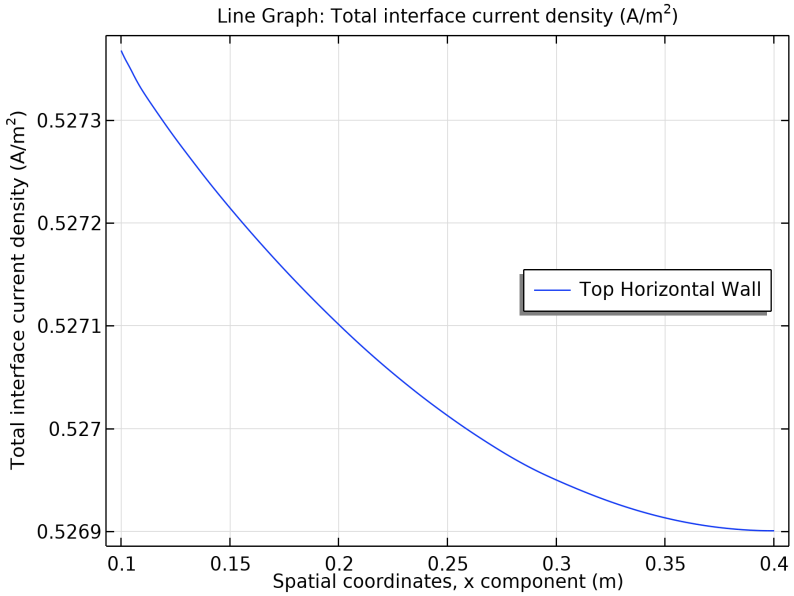

Line Graph: Total interface current density (A/m²)

4.2.33 Current Density for Vertical Walls 1

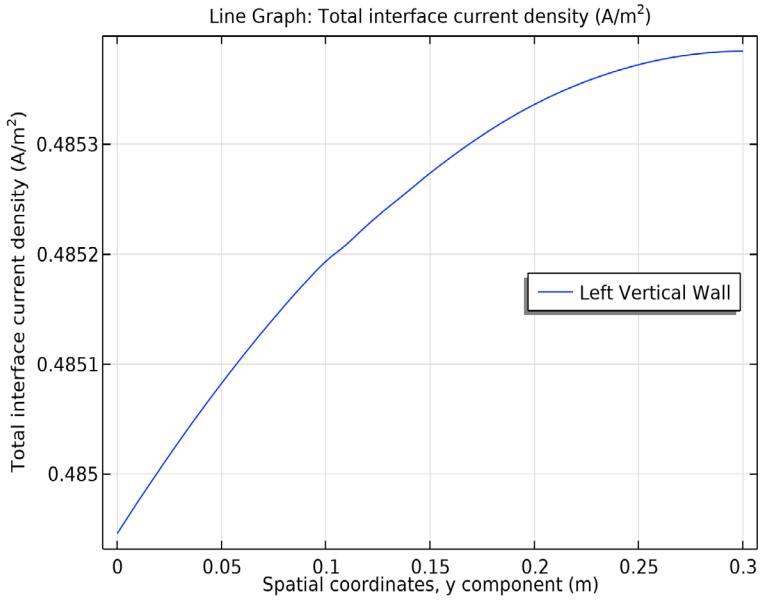

Line Graph: Total interface current density (A/m²)